ISSN 1997-1397 (Print)
ISSN 2313-6022 (Online)

Журнал Сибирского федерального университета

Математика и физика

Journal of Siberian Federal University

Mathematics & Physics

2025 18 (2)

ISSN 1997-1397
(Print)

ISSN 2313-6022
(Online)

2025 18 (2)

ЖУРНАЛ СИБИРСКОГО ФЕДЕРАЛЬНОГО УНИВЕРСИТЕТА
Математика и Физика

JOURNAL OF SIBERIAN FEDERAL UNIVERSITY
Mathematics & Physics

Издание индексируется Scopus (Elsevier), Emerging Sources Citation Index (WoS, Clarivate Analytics), Российским индексом научного цитирования (НЭБ), представлено в международных и российских информационных базах: Ulrich's periodicals directiory, ProQuest, EBSCO (США), Google Scholar, MathNet.ru, КиберЛенинке.

Включено в список Высшей аттестационной комиссии «Рецензируемые научные издания, входящие в международные реферативные базы данных и системы цитирования».

Все статьи представлены в открытом доступе http://journal.sfu-kras.ru/en/series/mathematics_physics.

Журнал Сибирского федерального университета.
Математика и физика.
Journal of Siberian Federal University. Mathematics & Physics.

Учредитель: Федеральное государственное автономное образовательное учреждение высшего образования "Сибирский федеральный университет"(СФУ)
Главный редактор: А.М. Кытманов. Редакторы: В.Е. Зализняк, А.В. Щуплев.
Компьютерная верстка: Г.В. Хрусталева
№ 2. 26.04.2025. Индекс: 42327. Тираж: 1000 экз. Свободная цена
Адрес редакции и издателя: 660041 г. Красноярск, пр. Свободный, 79, оф. 32-03.
Отпечатано в типографии Издательства БИК СФУ
660041 г. Красноярск, пр. Свободный, 82а.
Свидетельство о регистрации СМИ ПИ № ФС 77-28724 от 29.06.2007 г., выданное Федеральной службой по надзору в сфере массовых коммуникаций, связи и охраны культурного наследия
http://journal.sfu-kras.ru
Подписано в печать 15.04.25. Формат 84×108/16. Усл.печ. л. 12,0.
Уч.-изд. л. 11,8. Бумага тип. Печать офсетная.
Тираж 1000 экз. Заказ 23349
Возрастная маркировка в соответствии с Федеральным законом № 436-ФЗ:16+

CONTENTS

A. G. Knyazeva, O. N. Kryukova **149**
Influence of Coupling of Thermokinetic and Mechanical Processes on the Composite Synthesis on the Substrate

O. A. Zolotov, A. I. Chusovitina, V. E. Zalizniak **161**
Stability of a Steady State of Closed Microecosystem «algae – heterotrophic bacteria»

E. V. Timchenko, P. E. Timchenko, A. V. Lyamin, K. A. Kayumov, I. V. Bazhutova, L. T. Volova, O. O. Frolov, A. V. Zotova, F. R. Bazhutov **171**
Raman Spectroscopy Method for Identification of Streptococci

E. K. Guseva, V. I. Golubev, I. B. Petrov, V. P. Epifanov **179**
Elastoplastic Ice Model with the Dynamic Destruction for the Simulation of Nonlinear Processes During the Low-speed Impact

V. I. Erofeev, A. M. Antonov, A. O. Malkhanov **191**
On the Velocities of Rayleigh Surface Waves Propagating along the Houndaries of Generalized Continua

V. S. Petrakova, A. S. Tsipotan **199**
Computer Simulation of Self-assembly of Structure from an Ensemble of Nanoparticles

Yu. V. Klochkov, A. P. Nikolaev, V. A. Pshenichkina, O. V. Vakhnina, A. S. Andreev, M. Yu. Klochkov **209**
Physically Nonlinear Deformation of the Shell Using a Three-field FEM

A. V. Nasedkin, A. A. Nasedkina **218**
Analysis of the Influence of Porosity and Non-Uniform Polarization of Piezoelectric Ceramics on the Efficiency of a Bridge Transducer as Sensor and Actuator

I. Haouam **229**
A Classical Aspect of the Dirac Equation in the Context of Conformable Fractional Derivative

M. Ramanamurty, R. Santhikumar, K. Sobhanbabu **243**
FRW Viscous Cosmological Model with Time Periodically Varying Deceleration Parameter In $\mathbf{f}(\mathbf{R}, \mathbf{T})$Gravity

M. A. Tokareva, A. A. Papin **253**
Filtration of Two Immiscible Liquids in a Viscoelastic Porous Medium

A. Al-Omari **262**
Properties of $m\mathcal{H}$-compact Sets in Hereditary m-Spaces

A. A. Sharif, M. M. Hamood, K. P. Ghadle **273**
Novel Results on Positive Solutions for Nonlinear Caputo-Hadamard Fractional Volterra-Fredholm Integro Differential Equations

M. I. Buzurnyy, I. A. Lopatin **283**
Another Proof of Puiseux's Theorem on Algebraic Functions

СОДЕРЖАНИЕ

А. Г. Князева, О. Н. Крюкова **149**
Влияние связанности термокинетических и механических процессов на синтез композита на подложке

О. А. Золотов, А. И. Чусовитина, В. Е. Зализняк **161**
Устойчивость стационарного состояния замкнутой микроэкосистемы «одноклеточная водоросль –гетеротрофная бактерия»

Е. В. Тимченко, П. Е. Тимченко, А. В. Лямин, К. А. Каюмов, И. В. Бажутова, Л. Т. Волова, О. О. Фролов, А. В. Зотова, Ф. Р. Бажутов **171**
Метод спектроскопии комбинационного рассеяния для идентификации стрептококков

Е. К. Гусева, В. И. Голубев, И. Б. Петров, В. П. Епифанов **179**
Упругопластическая модель льда с динамическим разрушением для моделирования нелинейных процессов во время низкоскоростного удара

В. И. Ерофеев, А. М. Антонов, А. О. Мальханов **191**
О скоростях поверхностных волн Рэлея, распространяющихся вдоль границ обобщенных континуумов

В. С. Петракова, А. С. Ципотан **199**
Компьютерное моделирование самосборки структур из ансамбля наночастиц

М. Ю. Клочков, А. П. Николаев, В. А. Пшеничкина, О. В. Вахнина, А. С. Андреев, Ю. В. Клочков **209**
Физически нелинейное деформирование оболочки при использовании трехпольного МКЭ

А. В. Наседкин, А. А. Наседкина **218**
Анализ влияния пористости и неоднородной поляризации пьезокерамики на эффективность мостового преобразователя как сенсора и актуатора

И. Хауам **229**
Классический аспект уравнения Дирака в контексте согласованной дробной производной

М. Раманамурти, Р. Сантикумар, К. Собханбабу **243**
Вязкая космологическая модель FRW с периодически изменяющимся во времени параметром замедления в $\mathbf{f}(\mathbf{R}, \mathbf{T})$гравитации

М. А. Токарева, А. А. Папин **253**
Фильтрация двух несмешивающихся жидкостей в вязкоупругой пористой среде

А. Аль-Омари **262**
Свойства $m\mathcal{H}$-компактов в наследственных m-пространствах

А. А. Шариф, М. М. Хамуд, К. П. Гэдл **273**
Новые результаты по положительным решениям для нелинейных дробных производных Капуто-Адамара интегро-дифференциальных уравнений Вольтерра-Фредгольма

М. И. Бузурный, И. А. Лопатин **283**
Еще одно доказательство теоремы Пьюизо об алгебраической функции

EDN: EIMYRY
УДК 531+536

Influence of Coupling of Thermokinetic and Mechanical Processes on the Composite Synthesis on the Substrate

Anna G. Knyazeva*
Olga N. Kryukova†
Institute of Strength Physics and Materials Science
Siberian Branch of the Russian Academy of Sciences
Tomsk, Russian Federation

Received 15.09.2024, received in revised form 20.10.2024, accepted 26.11.2024

Abstract. A coupled mathematical model for the process of a composite synthesis from a powder mixture under laser heating conditions is presented. The model takes into account two phenomena that are neglected in traditional models of surface treatment and 3D technologies. They are the heat transfer-deformation behaviour and heat release in chemical reactions. The formation of composition is described by a simplified reaction scheme that includes the total reaction leading to the formation of hardening particles and the total reaction of matrix formation. The influence of stress work on reaction rates is taken into account. The stress-strain state is described in the quasi-static approximation. As a result, it is shown that coupling of processes of different physical nature is important both for determining composition of the composite and for estimating the associated stresses and strains.

Keywords: coupled model, composite synthesis, associated stresses, controlled mode.

Citation: A.G. Knyazeva, O.N. Kryukova, Influence of Coupling of Thermokinetic and Mechanical Processes on the Composite Synthesis on the Substrate, J. Sib. Fed. Univ. Math. Phys., 2025, 18(2), 149–160. EDN: EIMYRY.

Introduction

A large number of publications are devoted to process modelling in modern technologies. The authors often repeat each other and use the term "coupled models" unnecessarily. Coupled models should be understood as such models in which the interaction between physical fields is taken into account. There are many examples of coupled models in physics and continuum mechanics. One can mention models of solid-phase combustion theory in which the interaction of heat transfer and chemical reactions is taken into account [1]. Another example is solid-state diffusion models which take into account the interaction of diffusion of atoms and vacancies, the interrelation between diffusion and stresses [2]. However, when modelling the synthesis of new materials, it is of interest to study the stress and strain fields accompanying the synthesis. Together with the external load they influence the kinetic patterns of phase formation through different channels. Despite the fact that term "coupled model" is used in a huge number of publications, there are not many real coupled models. Results of modelling of the temperature field, residual stresses, processes in the melt bath (singled out as an independent object), crystallization in meso-volumes, powder melting in the beam, mechanical behaviour of synthesized

*anna-knyazeva@mail.ru https://orcid.org/0000-0002-9765-7695
†okruk@ispms.ru https://orcid.org/0000-0002-7522-0249

objects, effective properties from experimentally obtained structural data were presented [3–5]. The aim of this paper is to demonstrate the role of different channels of interaction between processes of different physical nature within the model of synthesis of composite coating on a substrate.

1. General problem formulation

Let us assume that under experimental conditions the mixture of powders from which a coating or a layer of three-dimensional product is formed under the governing of a moving heat source is freely poured on a flat substrate. Chemical reactions may occur in the mixture of powders. Reactions are accompanied by thermal effects. When the melting temperatures are reached the liquid phase appears. Sometimes its appearance in large quantities is undesirable as it may lead to splashing and other negative effects. Therefore, it is convenient to carry out the process in such a way that the area occupied by the liquid phase is small compared to the size of the whole sample or that the proportion of liquid phase anywhere in the sample is negligible. In this case it is possible to neglect melting effects and consider solid-phase processes. Then conventional description of thermokinetic phenomena requires heat conduction equation and kinetic equation:

$$\rho c \frac{\partial T}{\partial t} = -\nabla \cdot J_{\mathrm{q}} + W_{ch} + W_{ext}; \tag{1}$$

$$\frac{d\eta_i}{dt} = \sum_{(k)} \nu_{ik} \Phi_k, \tag{2}$$

where T is the temperature; t is time; ρ is the density; c is the isobaric heat capacity; J_q is the heat flux satisfying the Fourier law $J_{\mathrm{q}} = -\lambda_T \nabla T$; λ_T is the heat transfer coefficient; W_{ch} is the total chemical heat release, $W_{ch} = \sum_{(k)} Q_k \Phi_k$; Q_k is the heat effect of k-reaction (number of which r); Φ_k is the k-th reaction rate; η_i is the concentration of i-component; ν_{ik} is the stoichiometric coefficient of i-component in k-reaction; W_{ext} is the heat source associated with heating by an external energy source (laser, electron beam, electric arc, plasma) which in general case has limited size and it moves along the surface on some specified trajectory.

The boundary conditions at $x = 0$; $x = L_x$; $y = 0$; $y = L_y$ and at the bottom surface of the substrate are related to heat loss by radiation and/or convection. For example, one can write for $x = 0$

$$\lambda_T \frac{\partial T}{\partial x} = \alpha_L \left(T - T_e\right) + \sigma_0 \varepsilon_L \left(T^4 - T_w^4\right), \tag{3}$$

where T_e is the environment temperature; T_w — is the vacuum chamber wall temperature (if the process is carried out in the chamber); α_L is the heat loss coefficient; ε_L — surface emissivity; σ_0 — Stefan-Boltzmann constant.

When synthesis process is described in detail then properties can depend on temperature, composition and porosity. However, in the vast majority of cases such relationships are unknown. Then one should use some effective values. The influence of these values on the process can be studied in special way [6].

However, considering dynamics of synthesis of new materials the role of the associated mechanical processes is of great interest. These processes are not reflected in (1), (2). In general, in order to take into account the properties of the substrate or surrounding layers and, at the same time, the stress-strain state in the model of controlled coating synthesis three-dimensional heat

conduction equations together with equations of equilibrium are required. However, it leads to cumbersome formulations and it is problematic for parametric studies.

Let us take advantage of the fact that a thin flat substrate together with the coating can be considered as a flat (two-dimensional) object whose thickness is much smaller than its width and length. Then averaging the three-dimensional equations over the thicknesses of the substrate and the coating, one can consider a plane stress state and a two-dimensional problem [7–9]. In this case, the two-dimensional heat conduction equation takes the following form

$$(c_\varepsilon \rho)_{eff} \frac{\partial T}{\partial t} = \lambda_{T,eff} \left(\frac{\partial^2 T}{\partial x^2} + \frac{\partial^2 T}{\partial y^2} \right) + \frac{h_R W_{ch} + H}{h_S + h_R} + \frac{W_{ext,eff}}{h_S + h_R} - 3 \left(K \alpha_T \right)_{eff} T \frac{\partial \varepsilon_{kk}}{\partial t}. \quad (4)$$

Equation (4) contains effective properties (index "*eff*") that take into account the properties and thicknesses of the powder layer and the substrate [7] as well as two new terms. One of them takes into account heat losses from the surfaces of the substrate and coating:

$$\frac{H}{h_S + h_R} = \frac{\alpha_{eff}}{h_S + h_R} (T - T_0) + \frac{\sigma_0 \varepsilon_{eff}}{h_S + h_R} \left(T^4 - T_w^4 \right) = \alpha'_{eff} (T - T_0) + \sigma_0 \varepsilon'_{eff} \left(T^4 - T_w^4 \right),$$

where α_{eff}, α'_{eff} — effective heat transfer coefficients $\varepsilon_{eff}, \varepsilon'_{eff}$ — effective emissivities of surfaces, h_S and h_R — substrate and powder layer thicknesses; T_0 — temperature of the environment; T_w — temperature of the walls with which the heat is exchanged by radiation.

The second term $3K_{eff}\alpha_{T,_{eff}} T \partial \varepsilon_{kk} / \partial t$ also contains effective properties (bulk elastic modulus K_{eff} and linear thermal expansion coefficient $\alpha_{T,eff}$). It reflects the coupling of heat transfer and deformation processes. Chemical reactions take place only in the powder. Then multiplier $h_R / (h_S + h_R)$ can be accounted for as corrections to the thermal effects of the reactions $Q'_k = h_R Q_k / (h_S + h_R)$. The external heat source can also be modified. For example, in the case of a laser it is

$$W'_{ext,eff} = \frac{W_{ext,eff}}{h_S + h_R} = \frac{(1 - f_L)}{h_S + h_R} \frac{W_0}{k S_L} f(x, y) = q_0 f(x, y),$$

where S_L — effective heating spot area; W_0 — laser power; f_L — reflection coefficient; k — concentration factor (or correction factor); q_0 — effective power density of the heat source; type of function $f(x, y)$ depends on the mode and frequency of scanning. In this form (with the introduction of q_0 and $f(x, y)$), the source corresponds to any of the aforementioned movable heat sources. In the model (4) that takes into account the coupling of thermal and mechanical processes it is used not isobaric (or isochoric) heat capacity but heat capacity at constant strains c_ε.

2. Equilibrium problem

To determine deformations ε_{ij} one needs to solve the equilibrium problem of a planar object. For the plane stress state the following relations are true

$$\sigma_{zz} = 0, \qquad \sigma_{xy} = \sigma_{xz} = \sigma_{yz} = 0, \quad (5)$$

$$\varepsilon = \begin{vmatrix} \varepsilon_{xx} & \varepsilon_{xy} & 0 \\ \varepsilon_{yx} & \varepsilon_{yy} & 0 \\ 0 & 0 & \varepsilon_{zz} \end{vmatrix}. \quad (6)$$

Then there are two equations of equilibrium:

$$\frac{\partial \sigma_{xx}}{\partial x} + \frac{\partial \sigma_{xy}}{\partial y} = 0; \qquad \frac{\partial \sigma_{yx}}{\partial x} + \frac{\partial \sigma_{yy}}{\partial y} = 0. \quad (7)$$

Components of the strain tensor are related to components of the displacement vector by Cauchy relations

$$\varepsilon_{xx} = \frac{\partial u_x}{\partial x}; \qquad \varepsilon_{yy} = \frac{\partial u_y}{\partial y}; \qquad \varepsilon_{xy} = \frac{1}{2}\left(\frac{\partial u_x}{\partial y} + \frac{\partial u_y}{\partial x}\right), \tag{8}$$

where u_x, u_y — displacement vector components.

The additional relations are the equation

$$\frac{\partial^2 \varepsilon_{xx}}{\partial y^2} + \frac{\partial^2 \varepsilon_{yy}}{\partial x^2} = 2\frac{\partial^2 \varepsilon_{xy}}{\partial x \partial y}. \tag{9}$$

and the Duhamel–Neumann relations

$$\sigma_{ij} = 2\mu_{eff}\varepsilon_{ij} + \delta_{ij}\left[\lambda_{eff}\varepsilon_{kk} - \langle K\omega\rangle\right], \tag{10}$$

where λ, μ — Lamet coefficients ($K = \lambda + 2\mu/3$), $i, j = x, y, z$; ω is a function of concentrations and temperature:

$$\omega = 3\left[\alpha_T\left(T - T_0\right) + \sum_{k=0}^{n}\alpha_k\left(\eta_k - \eta_{k0}\right)\right], \tag{11}$$

α_k — concentration expansion coefficients; index "0" refers to the undeformed state; n — number of components; δ_{ij} — Kronecker delta: $\delta_{ij} = 1$, if $i = j$ and $\delta_{ij} = 0$, if $i \neq j$.

Designation $\langle K\omega\rangle$ means averaging over coating and

$$\langle K\omega\rangle = \frac{1}{h_S + h_R}\left[K_S w_S h_S + K_R w_R h_R\right] =$$

$$= \frac{K_S h_S \alpha_S + K_R h_R \alpha_R}{h_S + h_R}\left(T - T_0\right) + \frac{h_R K_R}{h_S + h_R}\sum_{k=0}^{n}\alpha_k\left(\eta_k - \eta_{k0}\right) =$$

$$= K_{eff}\left[\alpha_{T,eff}\left(T - T_0\right) + \sum_{k=0}^{n}\alpha_{k,eff}\left(\eta_k - \eta_{k0}\right)\right] = K_{eff}\omega_{eff}.$$

In what follows index «eff» and dash «'» in properties and effective parameters are omitted for simplicity.

Then for the plane stress state one can find from (10) that

$$\varepsilon_{xx} = \frac{\sigma_{xx}}{2\mu} - \left[\frac{\lambda}{2\mu}\frac{\sigma_{xx} + \sigma_{yy}}{3K} - \frac{\omega}{3}\right]; \qquad \varepsilon_{yy} = \frac{\sigma_{yy}}{2\mu} - \left[\frac{\lambda}{2\mu}\frac{\sigma_{xx} + \sigma_{yy}}{3K} - \frac{\omega}{3}\right]; \tag{12}$$

$$\varepsilon_{zz} = -\left[\frac{\lambda}{2\mu}\frac{\sigma_{xx} + \sigma_{yy}}{3K} - \frac{\omega}{3}\right]; \qquad \varepsilon_{xy} = \frac{\sigma_{xy}}{2\mu}. \tag{13}$$

The strain tensor and the stress tensor are symmetric, $\varepsilon_{xy} = \varepsilon_{yx}$.

After simple transformations [9] one can obtain from (2), (8) and (9) the system of equations

$$\Delta\sigma_{kk} = -\frac{K\mu}{\lambda + \mu}\Delta\omega, \qquad \Delta\sigma_{yy} = \frac{\partial^2 \sigma_{kk}}{\partial x^2}, \qquad \Delta\sigma_{xy} = -\frac{\partial^2 \sigma_{kk}}{\partial x \partial y}. \tag{14}$$

The remaining component of the stress tensor follows from the obvious relation $\sigma_{xx} = \sigma_{kk} - \sigma_{yy}$. Components of the strain tensor follow from (12)–(13).

At the initial moment of time $t = 0$

$$\sigma_{ij} = 0; \ \varepsilon_{ij} = 0. \tag{15}$$

Since the plate is free on the substrate, the stresses on all its surfaces are zero. However, any end fixation conditions can be set in the model.

3. Kinetics of composite formation

Suppose that a composite material is synthesized on a substrate from a mixture of powders in which the formation of strengthening particles occurs simultaneously with the formation of the matrix composition. It is assumed, as in [6, 9], that the process of composite synthesis can be described by two successive-parallel stages: one of the products of reaction P_2, in which strengthening particles P_1 are formed, goes to the formation of matrix P according to some total reaction:

$$2X \to P_1 + 2P_2, \qquad X + 2P_2 \to P.$$

The presence of different components in the initial mixture X affects the rates of total stages. The rate of the first reaction is Φ_1, second — Φ_2.

Hereinafter concentrations of components for the written out total reaction scheme is denoted by the same letters as the symbols in this scheme. Then system of kinetic equations (2) has the following form

$$\frac{dP_1}{dt} = \Phi_1, \qquad \frac{dP_2}{dt} = 2\left[\Phi_1 - \Phi_2\right], \qquad \frac{dP}{dt} = \Phi_2. \tag{16}$$

The total reagent $X = 1 - P_1 - P_2 - P$.

It is assumed that reaction rates depend on concentrations according to the acting masses law and on temperature according to the Arrhenius law

$$\Phi_1(T) = k_{10} W_1(T) X^2; \qquad \Phi_2(T)_2 = k_{20} W_2(T) P_2^2 X,$$

$$W_1(T) = \exp\left(-\frac{E_{a1}}{RT}\right), \qquad W_2(T) = \exp\left(-\frac{E_{a2}}{RT}\right),$$

where k_{10} and k_{10} are pre-exponential factors, E_{a1} and E_{a2} are activation energies of total reactions, R is the universal gas constant.

Consequently, the total chemical heat release in reactions is written as follows $W_{ch} = Q_1\Phi_1 + Q_2\Phi_2$, where Q_k are heat effects of reactions 1 and 2.

The rate of reactions involving solids can depend not only on temperature but also on stresses. A reaction can be activated not only by changing internal energy but also by mechanical work. Then [10]

$$W_1 = \exp\left[-\frac{E_{a1} - k_{\sigma 1}\Pi}{RT}\right], \qquad W_2 = \exp\left[-\frac{E_{a2} - k_{\sigma 2}\Pi}{RT}\right], \tag{17}$$

where $k_{\sigma 1}, k_{\sigma 2}$ are coefficients of sensitivity of reaction rates to mechanical work (proportional to activation volumes); $\Pi = -\left(\sigma_{xx}\varepsilon_{xx} + \sigma_{yy}\varepsilon_{yy} + 2\sigma_{xy}\varepsilon_{xy}\right)$ — mechanical work.

As a result, the heat conduction equation takes the form

$$c_\varepsilon \rho \frac{\partial T}{\partial t} = \lambda_T\left(\frac{\partial^2 T}{\partial x^2} + \frac{\partial^2 T}{\partial y^2}\right) + Q_1\Phi_1 + Q_2\Phi_2 - H + W_{ext} - 3K\alpha_T T\frac{\partial \varepsilon_{kk}}{\partial t}. \tag{18}$$

Next, let us assume that $W_{ext} = q_0 \exp\left(-\left((x - Vt)^2 + y^2\right)/a_t^2\right)$, $H = \alpha_{eff}(T - T_0) + \sigma_0\varepsilon_0(T^4 - T_w^4)$.

Thus, the thermokinetic problem involves kinetic equations (16) and heat conduction equation (18). Conditions for this part of the problem are

$$t = 0 : T = T_0, \qquad X = 1, \qquad P = P_1 = P_2 = 0;$$

$$y = 0 : \quad \partial T/\partial y = 0, \qquad x = 0, \infty : \quad \partial T/\partial x = 0, \qquad y \to \infty : \quad \partial T/\partial y = 0.$$

4. Problem in dimensionless form

The nature of processes occurring in the plate depends on the ratio of different physical scales which in turn depend on the properties characterizing different physical processes. Properties in the process of reactions continuously change, and it is impossible to find data to describe the change of properties so effective properties were introduced above. Further, in order to study phenomena qualitatively, it is advisable to switch to dimensionless variables. They significantly reduce the number of unknown quantities and allow us to develop a convenient algorithm for the numerical realization of the model.

Let us introduce dimensionless variables

$$\theta = \frac{T - T_*}{T_* - T_0}, \quad \tau = \frac{t}{t_*}, \quad \xi = \frac{x}{x_*}, \quad \eta = \frac{y}{x_*}, \quad e_{ij} = \frac{\varepsilon_{ij}}{\varepsilon_*}, \quad s_{ij} = \frac{\sigma_{ij}}{\sigma_*}, \quad \bar{\Pi} = \frac{\Pi}{\varepsilon_* \sigma_*},$$

where

$$T_* = \frac{Q_1}{c\rho} + T_0, \quad t_* = \frac{c\rho R T_*^2}{k_{01} E_{a1} Q_1} \exp\left(\frac{E_{a1}}{R T_*}\right), \quad x_* = \sqrt{\frac{\lambda t_*}{c\rho}},$$

$$\sigma_* = 3K\alpha_T \left(T_* - T_0\right), \quad \varepsilon_* = \frac{3K\alpha_T \left(T_* - T_0\right)}{2\mu}.$$

As a result, the problem takes the form similar to [9]

$$\frac{\partial \theta}{\partial \tau} = \left[\frac{\partial^2 \theta}{\partial \xi^2} + \frac{\partial^2 \theta}{\partial \eta^2}\right] + \frac{1}{\theta_0}\bar{\Phi}_1 + S_{ch} z_{ch} \frac{1}{\theta_0}\bar{\Phi}_2 + f_1 - S_b \left[\left(\theta + \sigma^{-1}\right)^4 - \left(\sigma^{-1} - \theta_w\right)^4\right] - Bi\left(\theta + 1\right) - \left(\theta + \sigma^{-1}\right)\kappa^{-1}\delta_\varepsilon \frac{\partial e_{kk}}{\partial \tau}, \tag{19}$$

$$\frac{dP}{d\tau} = \gamma \bar{\Phi}_1; \qquad \frac{dP_1}{d\tau} = 2\gamma(\bar{\Phi}_1 - \bar{\Phi}_2); \qquad \frac{dP_2}{d\tau} = \gamma \bar{\Phi}_2, \tag{20}$$

$$\Delta s_{kk} = -\frac{\kappa}{2 - \kappa}\Delta \bar{w}; \qquad \Delta s_{\eta\eta} = \frac{\partial^2 s_{kk}}{\partial \xi^2}; \qquad \Delta s_{\xi\eta} = \frac{\partial^2 s_{kk}}{\partial \xi \partial \eta}; \qquad s_{\xi\xi} = s_{kk} - s_{\eta\eta}. \tag{21}$$

At the initial moment of time

$$\tau = 0 \qquad \theta = -1; \qquad X = 1, \qquad P_1 = 0, \qquad P_2 = 0, s_{ij} = 0. \tag{22}$$

Boundary conditions for the thermokinetic problem are

$$\xi \to 0, L_\xi : \qquad \frac{\partial \theta}{\partial \xi} = 0; \qquad\qquad \eta \to 0, L_\eta : \qquad \frac{\partial \theta}{\partial \eta} = 0; \tag{23}$$

and for the equilibrium problem are

$$\xi = 0, \quad \xi = L_\xi : \qquad s_{ij} = 0; \quad \eta = 0, \quad \eta = L_\eta : \qquad s_{ij} = 0. \tag{24}$$

It is assumed in (19), (20) that

$$f_1 = S_e \exp\left(-\frac{\left(\xi - \bar{V}\tau\right)^2 + \eta^2}{\delta_t^2}\right);$$

$$\bar{\Phi}_1 = X^2 \exp\left[\frac{\theta\sigma - \delta_\varepsilon A_1 \bar{\Pi}}{\beta\left(1 + \theta\sigma\right)}\right]; \qquad \bar{\Phi}_2 = P_2^2 X \exp\left[\frac{\theta\sigma + e_k - \delta_\varepsilon A_2 \bar{\Pi}}{\beta\left(1 + \theta\sigma\right)}\right].$$

$$e_{kk} = e_{\xi\xi} + e_{\eta\eta} + e_{\varsigma\varsigma}; \qquad \bar{\Pi} = -\left(e_{\xi\xi}s_{\xi\xi} + e_{\eta\eta}s_{\eta\eta} + 2e_{\xi\eta}s_{\xi\eta}\right),$$

$$\bar{w} = \left[(\theta + 1) + g_1\left(P_1 - P_{10}\right) + g_2\left(P_2 - P_{20}\right) + g_0\left(P - P_0\right)\right].$$

The remaining values are also reduced to dimensionless form.

In general, solution of the problem depends on a large number of parameters. Their definition in terms of physical scales and the ranges of change is given in Tab. 1. All parameters of the problem have a clear physical meaning and they are described in [6, 9]. The algorithm of numerical solution of the problem is described there and the role of chemical reactions in the total values of stresses and strains is demonstrated. However, some important aspects of the problem formulation are not reflected there.

Ranges of variation of dimensionless parameters were determined using literature data on the properties of various substances (*Ti, Al, Cr, Fe* oxides) and parameters of heat sources and kinetic constants (q_0, V, E_{ai}, Q_i, k_{0i}) [9].

Table 1. Parameters of the model and their ranges of variation

Dimensionless parameter	Range of variation of dimensionless parameter	Dimensionless parameter	Range of variation of dimensionless parameter
$\gamma = \frac{(c\rho)_S RT_*^2}{E_{a1}Q_1}$	$\gamma = 0.009 \div 0.1$	$S_{ch} = \frac{Q_2}{Q_1}$	$S_{ch} = 0.1 \div 1$
$\sigma = \frac{T_* - T_0}{T_*}$	$\sigma = 0.3 \div 0.9$	$z_{ch} = \frac{k_2}{k_1}$	$z_{ch} = 10^{-6} \div 10^{6}$
$\theta_0 = \frac{\sigma}{\beta}$, $\beta = \frac{E_{a1}}{RT_*}$	$\theta_0 = 4 \div 15$	$e_k = 1 - \frac{E_{a2}}{E_{a1}}$	$e_k = 0 \div 0.7$
$S_b = \frac{t_* \sigma_0 \varepsilon_0 (T_* - T_0)^3}{c_S \rho_S}$	$S_b = 10^{-6} \div 10^{-4}$	$S_e = \frac{q_0}{h} \frac{t_*}{(T_* - T_0) c_S \rho_S}$	$S_e = 10^{-8} \div 10^{3}$
$Bi = \alpha_{eff} \frac{t_*}{c_S \rho_S}$	$Bi = 0 \div 4$	$\delta_\varepsilon = \frac{(3K\alpha_T)^2}{2\mu} \frac{(T_* - T_0)}{c\rho}$	$\delta_\varepsilon = 0 \div 0.1$
$\theta_w = \frac{T_* - T_w}{T_* - T_0}$	$\theta_w = 0.4 \div 0.9$	$\delta_t = a_t / x_*$	$\delta_t = 0.03 \div 10^{5}$
$g_i = \frac{(\alpha_i - \alpha_x)}{\alpha_T (T_* - T_0)}$	$g_i = -4 \div 4$	$\bar{V} = V t_* / x_*$	$\bar{V} = 10^{-8} \div 10^{3}$
$A_1 = \frac{k_{\sigma 1} Q_1}{E_{a1}}$ $A_2 = \frac{k_{\sigma 2} Q_1}{E_{a1}}$	$A = 0 \div 20$	–	–

5. Analysis of results

In the course of calculations, parameters were varied within a fairly wide range. In the examples presented below, some of the parameters were fixed [9]: $z_{ch} = 100$, $e_k = -0.2$, $A = 0.4$, $g_0 = 3.72$, $g_1 = -0.62$, $g_2 = 3.24$; $\bar{V} = 0.25$, $S_e = 2.5$, $K_C = 1$; $S_{ch} = 0.5$, $\delta_t = 2$, $\sigma = 0.5$, $\beta = 0.025$, $\gamma = 0.035$, $S_b = 0.0015$,

The synthesis control conditions are fixed. To illustrate the interrelation of processes of different nature let us limit ourselves to a single pass. For chosen control parameters for a single pass after the unsteady stage the process changes to a stationary regime in which the temperature values, the shape of temperature distributions and the accompanying stress and strain distributions remain practically unchanged. However, this cannot be stated for multi-pass processing. The dynamics of the process for different situations is shown in [6–9] and it is not duplicated here. The composition of the composite behind the laser beam, i.e., where the external source is absent, no longer changes. This "quasi-stationary" composition depends both on parameters characterizing the processing conditions and on the interaction of different physical processes.

This is illustrated in Fig. 1. The higher parameter Bi the greater heat loss, the lower temperature and, obviously, the lower yield of the reaction product (Fig. 1 a). The higher sensitivity coefficients to mechanical work the faster reactions start and the higher yield of products.

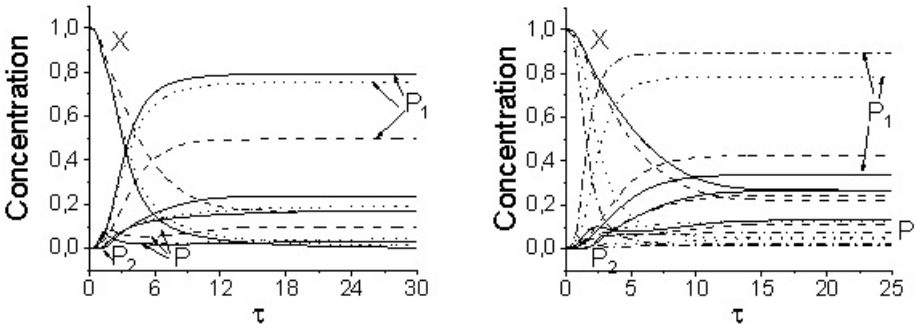

Fig. 1. Time dependence of composition at the point (x=25, y=0) for various conditions of heat exchange with the environment (a) and for various relationships between reaction rate and mechanical work (b). Parameters are $\delta_\varepsilon = 0.05$, $g_k \neq 0$. In figure (a) $\delta_k = 0.05$, solid lines — $Bi = 0$; dashed lines — $Bi = 0.1$; dotted-lines — $Bi = 0.5$. In figure (b) $\delta_\varepsilon = 0.05$; solid lines — $\delta_k = 0$; dashed lines — $\delta_k = 0.05$; dotted-lines — $\delta_k = 0.25$; dashed-dotted-lines — $\delta_k = 0.5$

The values of stresses and strains also depend significantly on the model parameters (Figs. 2–4). With increasing heat losses (curves 1–3) in Fig. 2 a,b stresses and strains decrease due to decreasing temperature, decreasing size of the region where gradients are significant, and slowing down of chemical reactions. The maximum corresponds to the coordinate of the heat source position at a given time. The behaviour of diagonal components of tensors is qualitatively similar to that of invariants s_{kk} and e_{kk}. The shear stresses and strains at the chosen set of parameters are much smaller and their behaviour is different from that of diagonal components (Fig. 2 c,d).

The shape of curves shown in Fig. 2 a,b corresponds to the qualitative temperature distribution (Fig. 3). For $Bi = 0$ (curves 1) the sample warms up in front of the beam due to heat conduction and initiated chemical reactions, and since there are no heat losses from the end the heat is accumulated. Although there are edge effects associated with overheating in experimental studies, $Bi = 0$ hardly corresponds to laser treatment. For $Bi = 0.1$ (curves 2) temperature is much lower but heat conduction still favours heating in front of the heat source which promotes preheating. For $Bi = 0.5$ (curves 3) a temperature profile typical for quasi-stationary laser treatment is observed.

Fig. 4 illustrates the role of concentration stresses and strains which can be comparable to thermal stresses in absolute value [9]. For selected values of parameters the consideration of concentration stresses leads to an increase in the total value of stresses and strains. Shear stresses and strains are highlighted in Fig. 4 c,d

As noted above, there are two types of coupling in the heat conduction equation. It is found that neglecting one of them also changes the result. Thus, if there is no coupling in the traditional sense (Fig. 5, left, $\tau = 30$) but the coefficient of sensitivity of reaction rates to mechanical work is not equal to zero the distributions of all physical quantities along the coordinate are qualitatively and quantitatively different from those when coupling is fully taken into account (Fig. 5, right, $\tau = 60$). The second maximum in stresses and strains is associated with the acceleration of

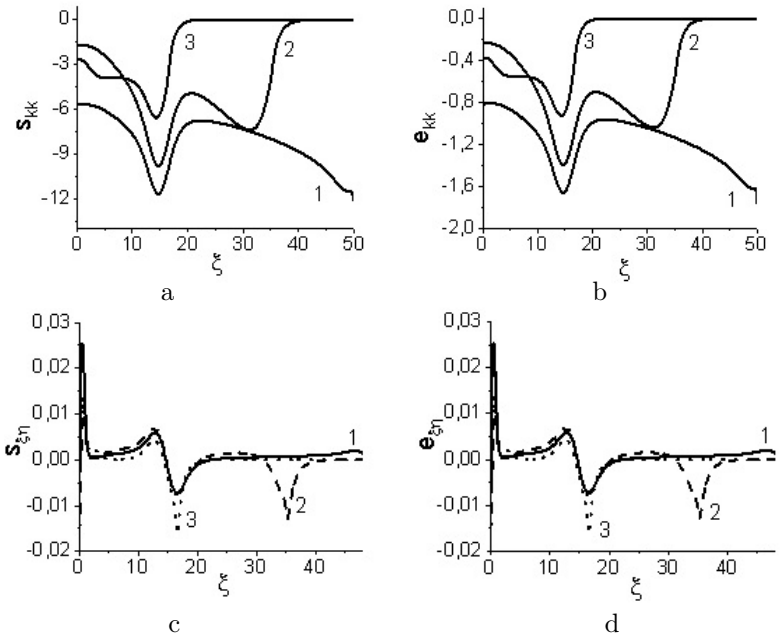

Fig. 2. Distributions along the axis of laser motion at time τ=60 of the first invariants of stress (a) and strain (b) tensors and shear components (c) and (d) of tensors. Parameters are $\delta_\varepsilon = 0.05$, $\delta_k = 0.05$; $g_k \neq 0$; 1 — $Bi = 0$; 2 — $Bi = 0.1$; 3 — $Bi = 0.5$

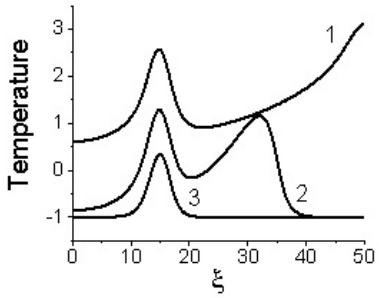

Fig. 3. Temperature distribution at $\tau = 40$ for various conditions of heat exchange with the environment 1 — $Bi = 0$; 2 — $Bi = 0.1$; 3 — $Bi = 0.5$. $\delta_\varepsilon = 0.05$, $\delta_k = 0.05$; $g_k \neq 0$

reactions in front of the moving heat source due to mechanical work. Note that composition for these variants is also different (not shown in the figures). More interesting results are obtained in coupled models when reverse stages of chemical reactions are taken into account.

Conclusion

The paper describes a model of controlled synthesis on a substrate. It is shown that the model has several channels of interaction between different physical phenomena accompanying the synthesis. Even if it is assumed that properties do not depend on composition and temperature it is possible to identify features of coupled models useful for process control in real conditions. For example, acceleration of reactions in front of a heat source. Note that such an approach to study dynamics of synthesis of new materials can be useful for various variants of combined technologies [11–13].

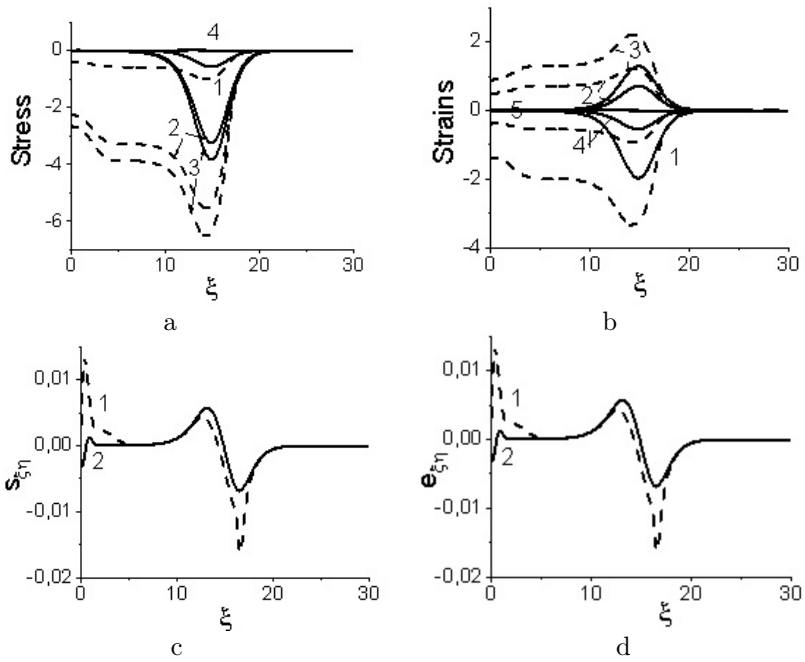

Fig. 4. Distributions along the axis of laser motion at time τ=60 of the first invariants of stress (a) and strain (b) tensors and shear components (c) and (d) of tensors. Parameters are $\delta_\varepsilon = 0.05$, $\delta_k = 0.05$. In figure (a): 1 — $s_{\xi\xi}$, 2 — $s_{\eta\eta}$, 3 — s_{kk}, 4 — $s_{\xi\eta}$. In figure (b): 1 — $e_{\xi\xi}$, 2 — $e_{\eta\eta}$, 3 — $e_{\varsigma\varsigma}$, 4 — e_{kk}, 5 — $e_{\xi\eta}$. Solid lines — $g_i = 0$; dotted lines — $g_i \neq 0$

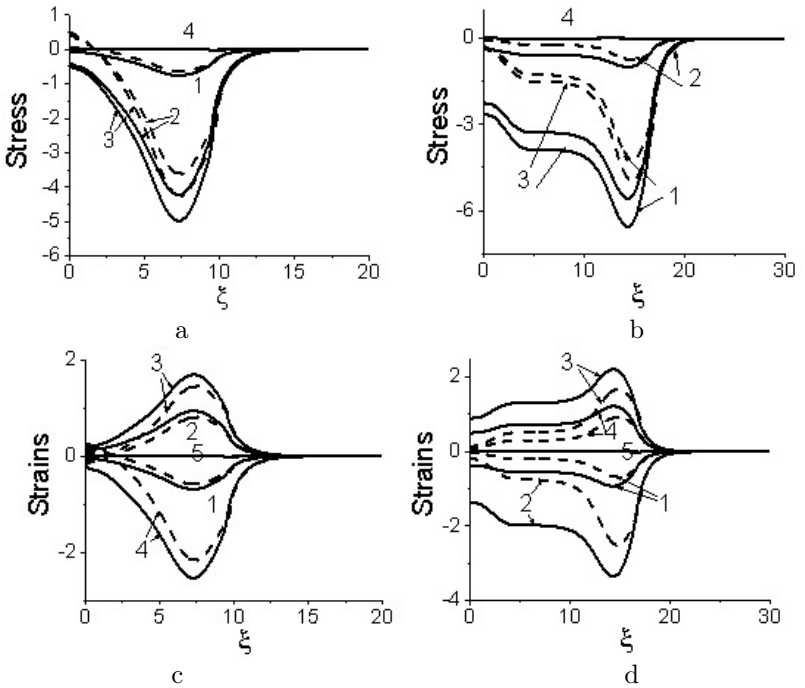

Fig. 5. Distributions along the axis of laser motion of the first invariants of stress (a, b) and strain (c, d) tensors. In figures (a, b) 1 — $s_{\xi\xi}$, 2 — $s_{\eta\eta}$, 3 — s_{kk}, 4 — $s_{\xi\eta}$; $\delta_\varepsilon = 0$, solid line — $\delta_k = 0.25$, dotted line — $\delta_k = 0.5$. In figures (c, d): 1 — $e_{\xi\xi}$, 2 — $e_{\eta\eta}$, 3 — $e_{\varsigma\varsigma}$, 4 — e_{kk}, 5 — $e_{\xi\eta}$; $\delta_\varepsilon = 0.05$. Solid lines — $\delta_k = 0.05$, dotted lines — $\delta_k = 0.25$

This work has been performed according to the Government Research Assignment for ISPMS SB RAS, project FWRW-2022-0003.

References

[1] A.S.Rogachev, A.S.Mukasyan, Combustion for material synthesis, (2014) (in Russian).

[2] G.D.C.Kuiken, Thermodynamics of irreversible processes. Applicationa to diffusion and rheology, 1994.

[3] M.Bayata, W.Dongb, J.Thorborga, A.C.To, J.H.Hattel, A review of multi-scale and multiphysics simulations of metal additive manufacturing processes with focus on modeling strategies, *Additive Manufacturing*, **47**(2021), 102278. DOI: 10.1016/j.addma.2021.102278

[4] H.Gu, C.Wei , L.Li, Q.Han, R.Setchi, M.Ryan, Q.Li, Multi-physics modelling of molten pool development and track formation in multi-track, multi-layer and multi-material selective laser melting, *International Journal of Heat and Mass Transfer*, **151**(2020), 119458. DOI: 10.1016/j.ijheatmasstransfer.2020.119458

[5] Th.A.Mukalay, J.A.Trimble, Kh.Mpofu, R.Muvunzi, Selective laser melting: Evaluation of the effectiveness and reliability of multi-scale multiphysics simulation environments, *Heliyon*, **10**(2024), no. 4. DOI: 10.1016/j.heliyon.2024.e25706

[6] A.G. Knyazeva, O.N. Kryukova, The synthesis of composites with reinforcing particles on a thin substrate, *Materials Physics and Mechanics*, **47**(2021), no. 2, 254–265.

[7] A.G.Knyazeva, Thermomechanical Coupled Model of Coating Synthesis on a Substrate, *PNRPU Mechanics Bulletin*, (2024), no. 1, 58–74 (in Russian). DOI: 10.15593/perm.mech/2024.1.06

[8] A.G.Knyazeva, O.N.Kryukova, Peculiarities of the Reaction Initiation by a Moving Energy Source in a Thin Layer Located on a Substrate, *Khimicheskaya fisika i mesoskopiya*, **26**(2024), no. 1 (in Russian) DOI: 10.15593/perm.mech/2024.1.06

[9] A.G.Knyazeva, O.N.Kryukova, A Coupled Model of Controlled Synthesis, of a Composite on a Substrate, *Lobachevskii Journal of Mathematics*, **43**(2022), no. 7, 1878–1893. DOI: 10.1134/S1995080222100183

[10] A.G.Knyazeva, Hot-spot thermal explosion in deformed solids, *Combust. Explos. Shock-Waves*, **29**(1993), 419–428.

[11] V.N.Antziferov, V.A.Vasin, V.A.Sorokin, I.V.Suminov, Combined technologies of laser processing of materials, 2012 (in Russian).

[12] E.A.Kolubaev, V.E.Rubtsov, A.V.Chumaevsky, Micro-, Meso- and Macrostructural Design of Bulk Metallic and Polymetallic Materials by Wire-Feed Electron-Beam Additive Manufacturing, *Phys Mesomech*, **25**(2022), 479–491. DOI: 10.1134/S1029959922060017

[13] A.G.Malikov, A.A.Golyshev, I.E.Vitoshkin, Recent Trends in Laser Welding and Additive Technologies (Review), *Journal of Applied Mechanics and Technical Physics*, **64**(2023), no. 1, 31–49. DOI: 10.1134/S0021894423010054

Влияние связанности термокинетических и механических процессов на синтез композита на подложке

Анна Г. Князева
Ольга Н. Крюкова
Институт физики прочности и материаловедения
Сибирское отделение Российской академии наук
Томск, Российская Федерация

Аннотация. Представлена связанная математическая модель процесса синтеза композита из порошковой смеси в условиях лазерного нагрева. Модель учитывает два явления, которыми пренебрегают в традиционных моделях обработки поверхности и 3D-технологий: взаимное влияние теплопереноса и деформации и выделение тепла в химических реакциях. Формирование состава описывается упрощенной схемой реакций, включающей суммарную реакцию, приводящую к образованию упрочняющих частиц, и суммарную реакцию формирования матрицы. Учтено влияние работы напряжения на скорость реакции. Напряженно-деформированное состояние описывается в квазистатическом приближении. В результате показано, что связанность процессов различной физической природы важна как для определения состава композита, так и для оценки сопутствующих синтезу напряжений и деформаций.

Ключевые слова: связанная модель, синтез композитов, сопутствующие напряжения, контролируемый режим.

EDN: BKJGVU
УДК 1-76, 574.34, 57.038

Stability of a Steady State of Closed Microecosystem «algae – heterotrophic bacteria»

Oleg A. Zolotov*
Alexandra I. Chusovitina†
Viktor E. Zalizniak‡
Siberian Federal University
Krasnoyarsk, Russian Federation

Received 15.08.2024, received in revised form 20.09.2024, accepted 02.12.2024

Abstract. Two models of closed microecosystem "algae–heterotrophic bacteria" are considered in this paper. Mathematical models are the Cauchy problem for system of non-linear ordinary differential equations. To develop models the Liebig's law of the minimum is consistently used for both specific rate of biomass growth and specific mortality rate of algae and bacteria cells. To describe the specific rate of substrate utilization by algae and bacteria the Andrew model (substrate inhibition) is used. It is assumed that carbon and nitrogen are main biogenic elements. Both models predict stationary state of microecosystem «Clorella vulgaris Pseudomonas sp.» that is in reasonable agreement with experimental data. Stability of the obtained stationary state is examined by means of Lyapunov's indirect method and Lyapunov's direct method based on the proposed form of Lyapunov function.

Keywords: mathematical modelling of ecosystems, closed ecosystem, algae, heterotrophic bacteria, stationary state, stability, Lyapunov indirect method, Lyapunov direct method.

Citation: O.A. Zolotov, A.I. Chusovitina, V.E. Zalizniak, Stability of a Steady State of Closed Microecosystem «algae – heterotrophic bacteria», J. Sib. Fed. Univ. Math. Phys., 2025, 18(2), 161–170. EDN: BKJGVU.

1. Notations

x — biomass concentration of algae model cells, g/l
y — biomass concentration of bacteria model cells, g/l
μ_x, μ_y — specific growth rate of biomass (algae, bacteria), 1/h
$\mu_{x,max}$, $\mu_{y,max}$ — maximal specific growth rate of biomass (algae, bacteria), 1/h
d_x, d_y — specific mortality rate of cells (algae, bacteria), 1/h
$d_{x,min}$, $d_{y,min}$ — specific mortality rate of of cells at optimal conditions (algae, bacteria), 1/h
$d_{x,max}$, $d_{y,max}$ — specific mortality rate of of cells in the absence of nutrition (algae, bacteria), 1/h
$q_x^{(c)}$, $q_y^{(c)}$ — specific consumption rates of carbon (algae, bacteria), 1/h
$q_x^{(n)}$, $q_y^{(n)}$ — specific consumption rates of nirigen (algae, bacteria), 1/h
$q_{x,max}^{(c)}$, $q_{y,max}^{(c)}$ — maximal specific consumption rates of carbon (algae, bacteria), 1/h
$q_{x,max}^{(n)}$, $q_{y,max}^{(n}$ — maximal specific consumption rates of nirogen (algae, bacteria), 1/h
$C_{max}^{(x)}$, $C_{max}^{(y)}$ — carbon concentration whereby $\mu_{x,max}$ and $\mu_{y,max}$ are achieved (algae, bacteria), 1/h

*ozolot_@mail.ru
†chusovitina2001@mail.ru
‡vzalizniak@yandex.ru

$N_{max}^{(x)}$, $N_{max}^{(y)}$ — nitrogen concentration whereby $\mu_{x,max}$ and $\mu_{y,max}$ are achieved (algae, bacteria), 1/h

γ_{xc}, γ_{xn} — stoichiometric coefficients for model cells of algae

γ_{yc}, γ_{yn} — stoichiometric coefficients for model cells of bacteria

C_m, N_m — concentration of mineral forms of carbon and nitrogen in water, g/l

C_b, N_b — concentration of biological forms of carbon and nitrogen (proteins, lipids, carbohydrates) in water, g/l

e — growth efficiency of heterotrophic bacteria

2. Introduction

Closed ecological systems (CES) constitute self-replenishing ecosystems which receive energy from outside but do not exchange matter with the outside environment. These systems have a number of applications. They are unique tools for studying fundamental processes and interactions in ecosystems. They also provide a basis for creating life support systems for space exploration. To gain insight into the functioning of CES mathematical models can be used. The elaboration of main principles of constructing mathematical models can be conveniently performed on the basis of closed microecosystems. Microecosystem (MES) is a small-scale, simplified, often laboratory based experimental ecosystem.

Mathematical models often represent the closed ecosystem as a set of first-order autonomous differential equations. Models based on so called flexible metabolism were suggested [1, 2]. It was found that these models of closed ecosystems tend to become more stable as the number of the described species increased. Various models of closed ecological systems with low species diversity were considered [3]. It was shown that models based on flexible metabolism have a stable stationary state in a wide range of parameters. Model of closed microecosystem «algae-heterotrophic bacteria» was proposed [4]. The Liebig's law of the minimum was consistently used for constructing this model. Concentration of the biomass in stationary state obtained with the use of the proposed model is in reasonable agreement with experimental data.

In a closed system external influences are not possible, and the system can only change due to internal processes. Therefore, once equilibrium is achieved, it will remain as long as the system stays closed. The concentrations of biomass and biogenic elements will remain constant, and the system will be in a state of dynamic equilibrium. Any plausible mathematical model of a CES must produce stable steady state solution. It means that model can describe an arbitrarily long existence of a CES.

In this paper two models of closed microecosystem «algae–heterotrophic bacteria» are considered. Both models predict stationary state of microecosystem that is in reasonable agreement with experimental data. Stability of the obtained stationary state is examined by means of Lyapunov's indirect method and Lyapunov's direct method based on the proposed form of Lyapunov function.

3. Stoichiometric ratios and physical factors influencing population growth

Let us introduce model cells that consist of only from carbon and nitrogen (basic biogenic elements). Values of the stoichiometric coefficients for model cells of algae and bacteria are calculated using given C/N ratio for real cells:

$$\gamma_{sc}/\gamma_{sn} \ - \ \text{given}, \quad \gamma_{sc} + \gamma_{sc} = 1, \quad s = (x, y).$$

Mass of model cell is related to the dry mass of real cell as $m_a = r \cdot m_c$, where coefficient r < 1 is determined from the ratio of the mass of carbon and nitrogen to the dry mass of real cell.

Light intensity is one of the important factors for algal photosynthesis. To describe its effect on algal growth function $f_1(I)$ is introduced. The effect of temperature on production of biomass of algae and bacteria is described by function $f_{2,s}(T)$. Algae and bacteria are able to grow in some pH range of medium. In what follows, it is assumed that ecosystem is kept at optimal light intensity and pH of medium ($f_1(I) = 1, f_{3,x}(pH) = 1, f_{3,y}(pH) = 1$).

4. Models of closed microecosystem «algae – heterotrophic bacteria»

The first model was presented in detail in [4]. It was assumed that specific substrate consumption rate of biogenic elements (C and N) by algae and bacteria is defined using modified Andrew's equation [5]. It was also assumed that specific mortality rate of algae and bacteria depends on the concentration of biogenic elements [6, 7]. The model can be expressed in the form of a system of differential equations

$$\begin{gathered} d\,\mathbf{s}_1/d\,t = \mathbf{f}_1\left(\mathbf{s}_1\right), \\ \mathbf{s}_1 = (x, y, C_b, C_m, N_b, N_m)^T, \quad \mathbf{f}_1\left(\mathbf{s}_1\right) = \left(f_{1,1}\left(\mathbf{s}_1\right), \ldots, f_{1,6}\left(\mathbf{s}_1\right)\right)^T. \end{gathered} \tag{1}$$

Let us consider now second model. Specific growth rate of population can be defined in the form that is equivalent to modified Andrew's equation

$$v_s\left(b\right) = f_{2,s}\left(T\right) \frac{b_{1/2}^{(s)}/b_{\max}^{(s)} + b_{\max}^{(s)}/b_{1/2}^{(s)} - 2}{b/b_{\max}^{(s)} + b_{\max}^{(s)}/b + b_{1/2}^{(s)}/b_{\max}^{(s)} + b_{\max}^{(s)}/b_{1/2}^{(s)} - 4},$$

$$s = (x, y), \; b = (C, N),$$

where $b_{s,1/2}$ — substrate saturation constant (substrate concentration when $\nu(b_{s,1/2}) = 1/2$. Let C_{yb} and N_{yb} be concentrations of organic carbon and nitrogen that can be consumed by bacteria (organic matter in water and in algae). It is assumed that carbon and nitrogen are consumed independently by bacteria. Then consumption rates of organic carbon and nitrogen by bacteria are

$$dC_{yb}/dt = dC_b/dt + \gamma_{xc}\, dx_{eaten}/dt,$$
$$dN_{yb}/dt = dN_b/dt + \gamma_{xn}\, dx_{eaten}/dt,$$

where dC_b/dt and dN_b/d t are consumption rates of organic carbon and nitrogen in water, dx_{eaten}/dt is consumption rates of algae by bacteria. Consumption rates dC_b/dt, dN_b/d and dx_{eaten}/dt are propotional to C_b, N_b and x_{eaten} , respectively. Then

$$dC_b/dx_{eaten} = C_b/x, \quad dN_b/dx_{eaten} = N_b/x.$$

Let us express C_b and N_b from the condition of closeness

$$\gamma_{xc}x + \gamma_{yc}y + C_b + C_m = C_0 = \text{const},$$
$$\gamma_{xn}x + \gamma_{yn}y + N_b + N_m = N_0 = \text{const},$$

and obtain

$$dC_{yb}/dt = \left((C_0 - \gamma_{xc}x - \gamma_{yc}y - C_m)/x + \gamma_{xc}\right) dx_{eaten}/dt = \left((C_0 - \gamma_{yc}y - C_m)/x\right) dx_{eaten}/dt,$$
$$dN_{yb}/dt = \left((N_0 - \gamma_{xn}x - \gamma_{yn}y - N_m)/x + \gamma_{xn}\right) dx_{eaten}/dt = \left((N_0 - \gamma_{yn}y - N_m)/x\right) dx_{eaten}/dt.$$

Using Liebig's law, one can obtain

$$dx_{eaten}/dt = x \cdot \min\left(\frac{1}{C_0 - \gamma_{yc} y - {}_m} dC_{yb}/dt, \frac{1}{N_0 - \gamma_{yn} y - N_m} dN_{yb}/dt\right). \tag{2}$$

Bacteria need for vital activity not only biogenic elements but also energy. Part of consumed organic matter is used for growing bacterial biomass, and the rest part is degraded by bacteria releasing inorganic nutrients and obtaining energy. This process is known as mineralization. It can be described as follows

$$\begin{aligned} dC_{yb}/dt &= \mu_{yc,\max} \nu\left(C_{yb}\right) y = \gamma_{yc} dy_p/dt + dC_{ym}/dt, \\ dN_{yb}/dt &= \mu_{yn,\max} \nu_y\left(N_{yb}\right) y = \gamma_{yn} dy_p/dt + dN_{ym}/dt, \end{aligned} \tag{3}$$

where $\mu_{yc,max}$, $\mu_{yn,max}$ — maximal specific consumption rate of carbon and nitrogen, respectively; dy_p/dt — specific growth rate of heterotrophic bacteria without regard for mortality; dC_{ym}/dt , dN_{ym}/dt — rates of mineralization of carbon and nitrogen. It is proved in the Appendix that if condition (A2) is satisfied then

$$dy_p/dt = \mu_{y,\max} \cdot \min\left(\nu_y(C_{Yb}), \nu_y(N_{Yb})\right) y. \tag{4}$$

Algae consume mineral forms of carbon and nitrogen independently. Then

$$\begin{aligned} dC_{xm}/dt &= \gamma_{xc} \mu_{x,\max} \nu_x\left(C_m\right) x, \\ dN_{xm}/dt &= \gamma_{xn} \mu_{x,\max} \nu_x\left(N_m\right) x, \end{aligned} \tag{5}$$

where dC_{xm}/dt , dN_{xm}/dt — consumption rates of inorganic carbon and nitrogen in water. Using Liebig's law and (5), one can obtain specific growth rate of algae without regard for mortality dx_p/dt as follows

$$dx_p/dt = \min\left((1/\gamma_{xc}) dC_{xm}/dt,\ (1/\gamma_{xn}) dN_{xm}/dt\right) = \mu_{x,\max} \min\left(\nu_x\left(C_m\right), \nu_x\left(N_m\right)\right) x \tag{6}$$

Using (2), (4), (6) and (A3), specific growth rates of algae and bacteria are written in the form

$$\begin{aligned} dx/dt &= dx_p/dt - d_x x - dx_{eaten}/dt, \\ dy/dt &= dy_p/dt - d_y y, \end{aligned} \tag{7}$$

where d_x , d_y – specific mortality rates of algae and bacteria, respectively. Using (3)–(5), the rate of concentration change of mineral forms of carbon and nitrogen is described as follows

$$\begin{aligned} dC_m/dt &= dC_{ym}/dt - dC_{xm}/dt, \\ dN_m/dt &= dN_{ym}/dt - dN_{xm}/dt. \end{aligned} \tag{8}$$

Considering (7) and (8), the following system of differential equations is finally obtain

$$\begin{gathered} d\,\mathbf{s}_2/d\,t = \mathbf{f}_2\left(\mathbf{s}_2\right), \\ \mathbf{s}_2 = (x, y, C_m, N_m)^T, \quad \mathbf{f}_2\left(\mathbf{s}_2\right) = \left(f_{2,1}\left(\mathbf{s}_2\right), \ldots, f_{2,4}\left(\mathbf{s}_2\right)\right)^T. \end{gathered} \tag{9}$$

5. Steady states of closed laboratory microecosystem «Chlorella-Pseudomonas sp»

Results of experimental studies of various closed microecosystems were presented [8]. For example, microecosystem that contains algae *Chlorella 219* and heterotrophic bacteria *Pseudomonas sp* was studied. Biocenosis was illuminated for 24 hours at 28–30°C. Concentrations of

biomass of living algae cells, bacteria cells, dead algae cells and concentration of detritus were determined.

Let us consider time evolution of microecosystem *«Chlorella vulgaris - Pseudomonas sp»* that is described by system of equations (1). It is assumed that microecosystem is kept at optimal illumination and pH at 29°C. Functions $f_{2,x}(T)$ and $f_{2,y}(T)$ are given in [4]. Stoichiometric coefficients, parameters r and parameters of functions for specific substrate consumption rate for *Chlorella vulgaris* and *Pseudomonas sp* are also presented in [4]. The following stationary solution was obtained

$$\mathbf{s}_1^a = (x, y, C_b, C_m, N_b, N_m)|_{t\to\infty} = (x^a, y^a, C_b^a, C_m^a, N_b^a, N_m^a) =$$
$$= (0.02465, 0.00647, 0.0906, 0.00273, 0.0002, 0.00048)\,.$$

Consider now stationary solution for model 2 that follows from system of equations (9). In stationary state $d\mathbf{s}_2/dt = 0$. Then

$$\begin{cases} 0 = dx_{born}/dt - d_x x - dx_{eaten}/dt, \\ 0 = dy_{born}/dt - d_y y, \\ 0 = \beta_C \mu_{y\,\max} \nu(C_0 - \gamma_{yC} y - C_m) y - \gamma_{yC} c dy_{born}/dt - \gamma_{xC} \mu_{x\,\max} \nu(C_m) x, \\ 0 = \beta_N \mu_{y\,\max} \nu(N_0 - \gamma_{yN} y - N_m) y - \gamma_{yN} dy_{born}/dt - \gamma_{xN} \mu_{x\,\max} \nu(N_m) x. \end{cases} \tag{10}$$

Parameters d_x and d_y follow from the first two equations of (10)

$$d_x = \mu_{x\,\max} \min\big(\nu(C_m), \nu(N_m)\big) - \mu_{y\,\max} y \min\left(\frac{\beta_N \nu(N_0 - \gamma_{yN} y - N_m)}{N_0 - \gamma_{yN} y - N_m}, \frac{\beta_C \nu(C_0 - \gamma_{yC} y - C_m)}{C_0 - \gamma_{yC} y - C_m}\right),$$

$$d_y = \mu_{y\,\max} \min\big(\nu(C_0 - \gamma_{yC} y - C_m), \nu(N_0 - \gamma_{yN} y - N_m)\big).$$

It is assumed that *Chlorella* contains 50 % of proteins, 10 % of fats and 40% of carbohydrates. Using average formulae for proteins, fats, carbohydrates and energy values for them [9], estimates of parameters Q_C and Q_N can be obtained: Q_C =12.182 kJ/g and Q_N = 0.595 kJ/g.

Four possible stationary solutions were found

1. $C_m < C_{\max}$, $N_m < N_{\max}$

   $C_m = 0.00049,\ N_m = 0.01794,\ x = 0.023,\ y = 0.004,\ C_b = 0.06,\ N_b = 0.001.$

2. $C_m < C_{\max}$, $N_m > N_{\max}$

   $C_{\rm m} = 0.0000468,\ N_m = 0.06776,\ x = 0.02,\ y = 0.001,\ C_b = 0.01,\ N_b = 0.001.$

3. $C_m > C_{\max}$, $N_m < N_{\max}$

   $C_{\rm m} = 0.827,\ N_m = 0.013,\ x = 0.021,\ y = 0.002,\ C_b = 0.01,\ N_b = 0.001.$

4. $C_m > C_{\max}$, $N_m > N_{\max}$

   $C_{\rm m} = 0.3987,\ N_m = 0.0333,\ x = 0.019,\ y = 0.004,\ C_b = 0.01,\ N_b = 0.001.$

Solution 1 corresponds to the conditions of the experiment. Specific mortality rates are determined from relations (21), using stationary solution 1. They are

$$d_x = 0.0285,\ d_y = 0.0588.$$

Organic form of carbon C_b and nitrogen N_b were not immediately determined in the experiment. Biomass concentration of dead chlorella cells (0.12 g/l) and concentration of detritus (0.12g/l) were determined. It was assumed that dead chlorella cell is chemically identical to living chlorella cell, and detritus contains 35–50 % of carbon and 1–4 % of nitrogen. Then parameters C_b and N_b can be estimated for the experiment. Calculated parameters of the microecosystem are shown in comparison with experimental results in Tab. 1.

Table 1. Stationary state of closed microecosystem «Clorella Pseudomonas sp»

Parameter	Model 1	Model 2	Experiment [9]
$x_r = x/r, g/l$	0.049	0.046	0.05
$y_r = y/r, g/l$	0.011	0.007	0.015
$C_b, g/l$	0.091	0.06	0.097 – 0.115*
$N_b, g/l$	0.0002	0.001	0.007 – 0.01*

* estimate

6. Stability of steady states of closed microecosystem «Chlorella-Pseudomonas sp»

Now turn to investigate the stability of the obtained steady states. First consider the method that allows one to determine whether the equilibrium of the nonlinear system is asymptotically stable or unstable based on the analysis of the linearized system about this equilibrium. This method is sometimes known as Lyapunov indirect method.

Lyapunov indirect method. Let $d\mathbf{s}/dt = \mathbf{A}\mathbf{s}$ be the linearisation of non-linear system $d\mathbf{s}/dt = \mathbf{f}(\mathbf{s})$ about the equilibrium point of non-linear system. Let $\lambda_n, n = 1, \ldots, N$ denote the eigenvalues of matrix $\mathbf{A}$. If $Re(\lambda_n) < 0$ for all n then the equilibrium of non-linear system is asymptotically stable. If there exists n such that $Re(\lambda_n) > 0$ then the origin is unstable.

Real parts of eigenvalues of matrix $\mathbf{A}$ for model 1 are

$$(-724.77, -0.236, -0.128, -0.067,\ 0,\ 0)\,.$$

Real parts of eigenvalues of matrix $\mathbf{A}$ for model 2 are

$$(-0.0025, -775.8166, -0.0001,\ 0)\,.$$

Hence, there are zero eigenvalues. In this case Lyapunov wrote [10] "... one can come to conclusion that ... problem on stability is resolved by the sign of the minimal characteristic number. Consequently, only cases when this number is equal to zero remain open to question. Then the problem can not be resolved until higher then linear terms are taken into account in differential equations". Alternatively, one can use Lyapunov direct method.

Lyapunov direct method. Let $\mathbf{s} = 0$ be an equilibrium point for $d\mathbf{s}/dt = \mathbf{f}(\mathbf{s})$ where $\mathbf{f} : D \to \mathbf{R}^n$ is locally Lipschitz on domain $D \subset \mathbf{R}^n$. Assume there exists a continuously differentiable function $V(\mathbf{s}) : D \to \mathbf{R}$ such that

1. $V(0) = 0$ and $V(s) > 0$ for all $\mathbf{s} \in D$ not equal to zero,
2. $\dfrac{dV}{dt}(\mathbf{s}) = \sum\limits_{n=1}^{N} \dfrac{\partial V}{\partial \mathbf{s}_n} \mathbf{f}_n(\mathbf{s}) \leqslant 0$ for all $\mathbf{s} \in D$.

Then $s = 0$ is stable in the sense of Lyapunov.

To study stability of steady state for model 1 the folloing Lyapunov function is proposed

$$V(\mathbf{s}_1) = \sum_{n=1}^{6} \left(\mathbf{f}_{1,n}(\mathbf{s}_1)\right)^2$$

For model 2 Lyapunov function has similar form:

$$V(\mathbf{s}_2) = \sum_{n=1}^{4} \left(\mathbf{f}_{2,n}(\mathbf{s}_2)\right)^2$$

Hence the first condition is fulfilled in D. To study stability of nonzero stationary state one should use change of variables $\mathbf{s}^* = \mathbf{s} - \mathbf{s}^a$, where $\mathbf{s}^a$ is nonzero stationary state.

Analytical study of the derivative of the Lyapunov function in the vicinity of stationary states was performed for both models using Maple software. Then as a result conditions were established whereby $dV/dt \leqslant 0$. In the case of model 1 the derivative of the Lyapunov function is non-positive for

$$x < 0.135,\ N_m < 0.0085,\ N_b < 0.0495.$$

In the case of model 2 appropriate conditions were established for every stationary state:

1. $C_m < C_{\max}, N_m < N_{\max}$
$$x < 0.035,\quad y < 0.0105.$$
2. $C_m < C_{\max}, N_m > N_{\max}$
$$x < 0.08,\quad y < 0.0065.$$
3. $C_m > C_{\max}, N_m < N_{\max}$
$$0.008 < N_m < 0.01335,\ 0.0009 < y < 0.0029,\quad 0.015 < C_m.$$
4. $C_m > C_{\max}$, $N_m > N_{\max}$
$$N_m > 0.03165,\quad y < 0.035.$$

By this means the stability of obtained stationary states is proved.

Conclusions

Two models of closed microecosystem «algae-heterotrophic bacteria» were considered in this paper. Mathematical models are the Cauchy problem for system of non-linear ordinary differential equations. The Liebig's law of the minimum and the Andrew model for the specific rate of biomass growth were used to develop these models. Both models predict stationary state of microecosystem *«Clorella vulgaris Pseudomonas sp.»* that is in reasonable agreement with experimental data. To study stability of the obtained stationary state Lyapunov indirect method and Lyapunov direct method were used. The form of Lyapunov function that is used in Lyapunov direct method was proposed. Methodology developed in this paper can be used to study stability of stationary states of various closed microecosystems that include algae and heterotrophic species.

Appendix

Energy that bacteria can spend on biomass growth can not exceed energy obtained during the process of degradation of organic matter by bacteria and releasing inorganic nutrients:

$$Q_C dC_{ym}/dt + Q_N dN_{ym}/dt \geq Q_y dy_p/dt \qquad (A1),$$

where Q_C , Q_N – energy values of carbon and nitrogen, respectively; Q_y – energy needed to support vital activity of bacteria. Bacterial growth efficiency e introduced in model 1 can be represented as follows

$$e = dy_p/(dC_{yb} + dN_{yb}) = dy_p/(dY + dC_{ym} + dN_{ym}) = \frac{1}{1 + dC_{ym}/dy_p + dN_{ym}/dy_p}$$

Then maximal value of e is

$$e_{\max} = \frac{1}{1 + dC_{ym,\max}/dy_{p,\max} + dN_{ym,\max}/dy_{p,\max}} \text{ and } dC_{ym,\max}/dy_{p,\max} + \\ + dN_{ym,\max}/dy_{p,\max} = 1/e_{\max} - 1$$

Because $Q_C > Q_N$ one can assume that $e_{\max}$ has the following form

$$e_{\max} = \frac{1}{1 + dC_{ym}(e_{\max})/dy_p(e_{\max})} \text{ and } dC_{ym}(e_{\max})/dY_p(e_{\max}) = 1/e_{\max} - 1.$$

If growth is limited by carbon then maximal growth of bacterial biomass is achieved when $e = e_{max}$. Then

$$Q_C dC_{ym}(e_{\max})/dt = Q_y dy_p(e_{\max})/dt.$$

Let us express Qy and obtain

$$Q_y = Q_C(1/e_{\max} - 1).$$

Then

$$\mu_{yc,\max} y = \gamma_{yc} y_p(e_{\max})/dt + C_{ym}(e_{\max})/dt = \gamma_{yc} dy_p(e_{\max})/dt + (1/e_{\max} - 1) dy_p(e_{\max})/dt = \\ dy_p(e_{\max})/dt(\gamma_{yc} + (1/e_{\max} - 1)).$$

Taking into account that $dYp/dt = \mu_y(e_max)y$ when $e = e_{\max}$, one can obtain expression for $\mu_{yc,\max}$:

$$\mu_{yc,\max} = (\gamma_{yc} + (1/e_{\max} - 1))\, \mu_y(e_{\max})$$

Expression for $\mu_{yc,\max}$ can be obtained in analogous way:

$$\mu_{yn,\max} = (\gamma_{yn} + (Q_C/Q_N)\,(1/e_{\max} - 1))\, \mu_y(e_{\max}).$$

When $e = e_{\max}$ inequality (A1) becomes

$$Q_C dC_{ym}/dt + Q_N dN_{ym}/dt = Q_C\,(1/e_{\max} - 1)\, dY_{p,\max}/dt. \qquad (A2)$$

Let us express bacterial biomass growth that follows from energy requirements

$$dy_e/dt = \frac{Q_C\,(\gamma_{yc} + (1/e_{\max} - 1))\,\nu(C_{yb}) + Q_N\,(\gamma_{YN} + (Q_C/Q_N)\,(1/e_{\max} - 1))\,\nu(N_{yb})}{Q_C\gamma_{yc} + Q_N\gamma_{yn} + Q_C\,(1/e_{\max} - 1)} \mu_y(e_{\max}).$$

Maximal specific growth rate of bacterial biomass $\mu_{y,\max}$ is achieved when $\nu(C_{yb}) = \nu(N_{yb}) = 1$, $(\mu_y(e_{\max}) = \mu_{y,\max})$. Then

$$dy_e/dt = \frac{Q_C\,(\gamma_{yc} + (1/e_{\max} - 1))\,\nu(C_{yb}) + Q_N\,(\gamma_{YN} + (Q_C/Q_N)\,(1/e_{\max} - 1))\,\nu(N_{yb})}{Q_C\gamma_{yc} + Q_N\gamma_{yn} + 2Q_C\,(1/e_{\max} - 1)} \mu_{y,\max} Y,$$

$$dy_{yb}/dt = (\gamma_{yc} + (1/e_{\max} - 1))\, \frac{Q_C\gamma_{yc} + Q_N\gamma_{yn} + Q_C(1/e_{\max} - 1)}{Q_C\gamma_{yc} + Q_N\gamma_{yn} + 2Q_C(1/e_{\max} - 1)} \mu_{y,\max}\nu(C_{yb})Y = \qquad (A3)$$

$$= \beta_C \mu_{y,\max}\nu(C_{yb})Y,$$

$$dN_{yb}/dt = (\gamma_{yn} + (Q_C/Q_N)\,(1/e_{\max} - 1))\, \frac{Q_C\gamma_{yc} + Q_N\gamma_{yn} + Q_C(1/e_{\max} - 1)}{Q_C\gamma_{yc} + Q_N\gamma_{yn} + 2Q_C(1/e_{\max} - 1)} \mu_{y,\max}\nu(N_{yb})Y \\ = \beta_N \mu_{y,\max}\nu(N_{yb})Y.$$

Finally, using Liebig's law, one can obtain

$$dy_p/dt = \mu_{y,\max} y \min\left(\nu(C_{yb}), \nu(N_{yb}), (dy_e/dt)(1/t)\right) =$$

$$= \mu_{y,\max} y \min\left(\nu(C_{yb}), \nu(N_{yb}), \frac{Q_C\left(\gamma_{yc} + (1/e_{\max} - 1)\right)\nu(C_{yb}) + Q_N\left(\gamma_{yn} + \frac{Q_C}{Q_N}(1/e_{\max} - 1)\right)\nu(N_{yb})}{Q_C\gamma_{yc} + Q_N\gamma_{yn} + 2Q_C(1/e_{\max} - 1)}\right).$$

Let us transform given above expression

$$dy_p/dt = \mu_{y,\max} y \min\left(\nu(C_{yb}), \nu(N_{yb}), \frac{Q_C\gamma_{yc} + Q_C(1/e_{\max} - 1)}{Q_C\gamma_{yc} + Q_C(1/e_{\max} - 1) + Q_N\gamma_{yn} + Q_C(1/e_{\max} - 1)}\nu(C_{yb}) + \right.$$

$$\left. + \frac{Q_C\gamma_{yn} + Q_C(1/e_{\max} - 1)}{Q_C\gamma_{yc} + Q_C(1/e_{\max} - 1) + Q_N\gamma_{yn} + Q_C(1/e_{\max} - 1)}\nu(N_{yb})\right).$$

Let us note that this expression has the form

$$dy_p/dt = \mu_{y,\max} y \min\left(\nu(C_{yb}), \nu(N_{yb}), a\nu(C_{yb}) + (1-a)\nu(N_{yb})\right).$$

Then

$$dy_p/dt = \mu_{y,\max} y \min\left(a\nu(C_{yb}) + (1-a)\nu(C_{yb}), (1-a)\nu(N_{yb}) + a\nu(N_{yb}), a\nu(C_{yb}) + (1-a)\nu(N_{Yy})\right).$$

Taking into account that

$$a\nu(C_{Yb}) + (1-a)\nu(C_{Yb}) < a\nu(C_{Yb}) + (1-a)\nu(N_{Yb}),$$
$$(1-a)\nu(N_{Yb}) + a\nu(N_{Yb}) < a\nu(C_{Yb}) + (1-a)\nu(N_{Yb}),$$

one can finally obtain (15).

References

[1] M.Yu.Saltykov, S.I.Bartsev, Y.P.Lankin. Dependence of cosed ecosystem models' stability on the number of species, Journal of Siberian Federal University. Biology, **4**(2011), no. 2, 197–208 (in Russian).

[2] M.Yu.Saltykov, S.I.Bartsev, Yu.P.Lankin, Stability of closed ecology life support systems (CELSS) models as dependent upon the properties of methabolism of the described species. Advances in Space Research, **49**(2012), 223–229. DOI: 10.1016/j.asr.2011.10.002

[3] S.Bartsev, A.Degermendzhi, The evolutionary mechanism of formation of biosphere closure. Mathematics, **11**(2023), 3218. DOI: 10.3390/math11143218

[4] V.E.Zalizniak, O.A.Zolotov, Mathematical model of closed microecosystem «algae – heterotrophic bacteria». Mathematical Biology and Bioinformatics, **19**(2024), no. 1, 96–111 (in Russian). DOI: 10.17537/2024.19.96

[5] Andrews J.F. A mathematical model for the continuous culture of microorganisms utilizing inhibitory substrates. Biotechnology and Bioengineering, **10**(1968), 707–723.

[6] S.Takano, B.J.Pawlowska, I.Gudelj, T.Yomo, S.Tsuru, Density-dependent recycling promotes the long-term survival of bacterial populations during periods of starvation. ASM Journals/mBio, **8**(2017), e02336–16. DOI: 10.1128/mbio.02336-16.

[7] V.V.Zelenev, A.H.C. van Bruggen, A.M. Semeno, "BACWAVE" a spatial–temporal model for traveling waves of bacterial populations in response to a moving carbon source in soil. Microbial Ecology, **40**(2000), 260–272. DOI: 10.1007/s002480000029

[8] B.G.Kovrov, G.N.Fishtein, A distribution of biomass in synthetic closed microbial biocenosis depending on a species structure. Izvestiya Sibirskogo otdeleniya Akademii nauk SSSR. Seriya biologicheskaya, **5**(1980), no. 1, 35–40 (in Russian).

[9] A.A.Paul, D.A.T.Southgate, McCance and Widdowsons' The Composition of Foods, Stationery Office Books, London, 1978.

[10] A. M.Lyapunov The General Problem of the Stability of Motion, Gosudarstvennoe Izdatel'stvo Tehniko-Teoreticheskoj Literatur, Moscow–Leningra, 1950 (in Russian).

Устойчивость стационарного состояния замкнутой микроэкосистемы «одноклеточная водоросль – гетеротрофная бактерия»

Олег А. Золотов
Александра И. Чусовитина
Виктор Е. Зализняк
Сибирский федеральный университет
Красноярск, Российская Федерация

Аннотация. В работе предлагаются две модели замкнутой микроэкосистемы «одноклеточная водоросль–гетеротрофная бактерия». Математическая модель формулируется в виде задачи Коши для системы нелинейных обыкновенных дифференциальных уравнений. Для построения модели последовательно использовался закон минимума Либиха, как для описания скорости роста биомассы элементов микроэкосистемы, так и для описания скорости отмирания клеток водоросли и бактерии. Для описания удельной скорости потребления биогенных элементов водорослью и бактерией использовалась функция Эндрюса (ингибирование избытком субстрата). Предполагается, что биогенными элементами являются углерод и азот. Вычисленные с использованием предложенных моделей концентрации биомассы микроэкосистемы «Clorella vulgaris-Pseudomonas sp» в стационарном состоянии хорошо согласуются с данными эксперимента. Устойчивость стационарного состояния исследуется с использованием метода первого приближения и метода функций Ляпунова.

Ключевые слова: математическое моделирование экосистем, замкнутая экосистема, одноклеточная водоросль, гетеротрофная бактерия, стационарное состояние, устойчивость, метод первого приближения, метод функций Ляпунова.

EDN: LTNPWW
УДК 543.424

Raman Spectroscopy Method for Identification of Streptococci

Elena V. Timchenko*
Pavel E. Timchenko†
Institute of Computer Science and Cybernetics
Samara, Russian Federation
Artem V. Lyamin‡
Karim A. Kayumov
Center for Genetic Laboratory Technologies of SamSMU
Samara, Russian Federation
Irina V. Bazhutova§
Institute of Professional Education of SamSMU
Samara, Russian Federation
Larisa T. Volova¶
Samara State Medical University
Samara, Russian Federation
Oleg O. Frolov‖
Alena V. Zotova**
Institute of Computer Science and Cybernetics
Samara, Russian Federation
Filipp R. Bazhutov
Lomonosov Moscow State University
Moscow, Russian Federation

Received 10.08.2024, received in revised form 15.09.2024, accepted 24.10.2024

Abstract. In the modern world, various infammatory diseases of the oral cavity have become widespread, in particular periodontitis. Streptococcs are one of the potential participants in the infammatory process. In this work, three streptococcal strains were studied by Raman spectroscopy. As a result, spectral differences were established and criteria for identifying groups of samples were introduced.

Keywords: raman spectroscopy, streptococcus, periodontitis.

Citation: E.V. Timchenko, P.E. Timchenko, A.V. Lyamin, K.A. Kayumov, I.V. Bazhutova, L.T. Volova, O.O. Frolov, A.V. Zotova, F.R. Bazhutov, Raman Spectroscopy Method for Identification of Streptococci, J. Sib. Fed. Univ. Math. Phys., 2025, 18(2), 171–178.
EDN: LTNPWW.

*lazer-optics.timchenko@mail.ru https://orcid.org/0000-0002-0539-7989
†timpavel@mail.ru https://orcid.org/0000-0003-3089-7966
‡a.v.lyamin@samsmu.ru https://orcid.org/0000-0002-5905-1895
§docba@mail.ru https://orcid.org/0000-0003-3200-5538
¶l.t.volova@samsmu.ru https://orcid.org/0000-0002-6599-7732
‖frolov679@mail.ru
**zotova_alena@bk.ru

Introduction

In the modern world, various inflammatory diseases of the oral cavity have become widespread, in particular periodontitis [1, 2]. The main cause of periodontitis and peri-implantitis is tissue infection by microorganisms of the oral cavity. One of the known potential participants in the pathological process is streptococci, which are detected in periodontal pockets in almost 100 percent of cases [3–6]. At the same time, streptococci remain one of the most difficult to identify microorganisms, even when using modern methods. Currently, an actively used physical method for diagnosing microorganisms, including streptococci, is matrix-assisted laser desorption/ionization time-of-flight mass spectrometry (MALDI-TOFMS). No new technology for microorganism identifications without problems and the same is true for MALDI TOFMS. Among the most common errors are the inability to perform an accurate differentiation in those microorgan-isms that have a genotypic/protein profile similarity and an absence of reliable data in the database [7]. In this regard, the urgent task is the detection of species identification of streptococci.

As an alternative method for identifying streptococci, the method of Raman spectroscopy (RS), which has found wide application in biomedical practice [8], can be used. RS allows the analysis of vibrational modes of molecules and can distinguish between similar molecules, which gives hope for solving the problem of identifying closely related bacterial species.

Previously, other authors conducted a similar study, but it focused on the species identification of pneumococcus, as the main causative agent of generalized infections (pneumonia and meningitis) [9]. Given the increasing role of streptococci as causative agents of diseases of various localizations, further research in this direction is required. The aim of the study was a spectral study of strains of three closely related species of streptococci Streptococcus mitis, Streptococcus oralis and Streptococcus pneumoniae using Raman spectroscopy for rapid assessment of bacterial strains in the diagnosis of periodontitis.

Materials and methods of research

4 strains of S.mitis, 4 strains of *S.oralis* and 3 strains of *S.pneumoniae* were used as research objects. All isolates were obtained from the clinical material of patients with oral diseases. The growth of crops was obtained on 5 procent blood agar (HiMedia, India), with the addition of mutton blood (HEM LLC, Russia). Incubation of crops was carried out under microaerophilic conditions. Identification was performed using MALDI-ToF mass spectrometry on a Microflex device (Bruker, Germany). For all strains, an additional study was conducted to determine sensitivity to bile and optochine. Daily cultures of streptococcus were suspended in saline solution to obtain an inoculum with a density of 0.5 McFarland units.

For each species, the spectra were obtained: S.pneumoniae (45 Raman spectra), S.oralis (60 Raman spectra), S.mitis (56 Raman spectra). The Raman spectroscopy method described in detail in [10, 11] was used as the main method for analyzing S.mitis, S.oralis, and S.pneumoniae strains. The Raman spectra were captured using a Sharmrock SR-303i spectrograph with an integrated ANDOR DV-420A-OE digital camera (resolution 0.15 nm in wavelength) cooled to –60°C, including a semiconductor laser (LML-785.0RB-04), an optical raman scattering module (PBL 785).

The normalization of the spectra was carried out by the Extended multiplicative signal correction (EMSC) method. The smoothing of the spectra was carried out by the Maximum Likelihood

Estimation Savitzky-Golay filter (MLE-SG) method [12] with the parameter s = 4. To exclude the contribution of autofluorescence to the Raman spectra, a modified method of subtracting the fluorescent component by polynomial approximation Improved Modified Multi-Polynomial Fitting (ExModPoly) with a polynomial degree of 8 was used. The analysis of the Raman spectra of the samples was carried out in the range 450–1800 cm^{-1}.

Results

Fig. 1 shows the averaged Raman spectra of all the studied samples. As can be seen from Fig. 1, the main analytical indicators are manifested at the level of 527 cm^{-1} (S-S di sulfide stretching in proteins, phosphatidylserine or (S-S) gauche-gauche trans (amino acid cysteine)), 621 cm^{-1} (C-C mode of twisting phenylalanine (proteins)), 1280 cm^{-1} (amide III, CH_2, causing vibrations of the glycine backbone or side chains of proline), 1333 cm^{-1} (guanine), 1445 cm^{-1} (CH_2 bending modes, deformation of C-H proteins, deformation of CH_2/CH_3 in lipids), 1525 microns-1 (amide II), 1692 microns-1 (Stretching CO), 1749 cm^{-1} (C=O, lipids). On the CR line 621 cm^{-1} (C-C twisting mode of phenylalanine (proteins)) The samples of the *S.mitis* group show a noticeable increase in peak intensity. On the CR line of 1280 cm^{-1} corresponding to Amide III, CH_2 wagging vibrations from glycine backbone or proline sidechains, changes in the intensity amplitude of all the studied groups occur. On the CR line of 1445 cm^{-1} (CH_2 bending modes, deformation C-H bending proteins, deformation CH_2/CH_3 in lipids), the group of samples *S.oralis* has the highest intensity. On the Raman scattering line of 1525 cm^{-1} (Amide II), the group of samples it *S.pneumoniae* has the highest intensity.

Fig. 1 shows the averaged Raman spectra of the samples

On the line 1692 cm^{-1} group of samples *S.mitis* it has a noticeably smaller amplitude. Also, on the line 1749 cm^{-1} (C=O, lipids), the group of samples it S.oralis has the highest intensity. Further, in this work, a nonlinear regression analysis of the spectra was carried out, consisting in their decomposition into the sum of asymmetric Gauss lines to increase the information content of the obtained Raman spectra and subsequent analysis using linear discriminant analysis. The amplitude of the a lines was taken as the criterion variable, depending on the values of the independent regressors dx and x0, which determine the initial conditions of the analysis. The composition of spectral lines was determined on the basis of automatic multi-iterative modeling of 161 Raman spectra and tested based on the results of literature analysis. When modeling the spectral contour, the position of x0 and the half-width of the line (HWHM) dx were fixed for the lines used as a template. During the simulation, the line intensity was selected in the range from 0 to the value of the local maximum of the spectrum in the x0 region. HWHM was limited in the range from 1 to 13 cm^{-1}. This made it possible to achieve high stability of the results when modeling the contour and take into account all shifts of the Raman lines. For additional analysis after separation of the spectral lines of the studied samples, the method of linear discriminant analysis in the RS-tool program was chosen. The drawn lines or areas in the LD-1 and LD-2 space can represent class boundaries, which allows you to predict which group a particular sample belongs to based on its LD-1 and LD-2 values. The points in the graph corresponding to group 1 are concentrated in the area where LD-2 is significantly less than 2. This may indicate specific spectral features inherent in this group. For group 2, we notice the concentration of samples in the upper left part (LD-1 $<$ –8 and LD-2 $>$ 1), which also indicates unique characteristics that distinguish it from other groups. Group 3, in turn, occupies the upper right corner, where the values LD-1 $>$–9.

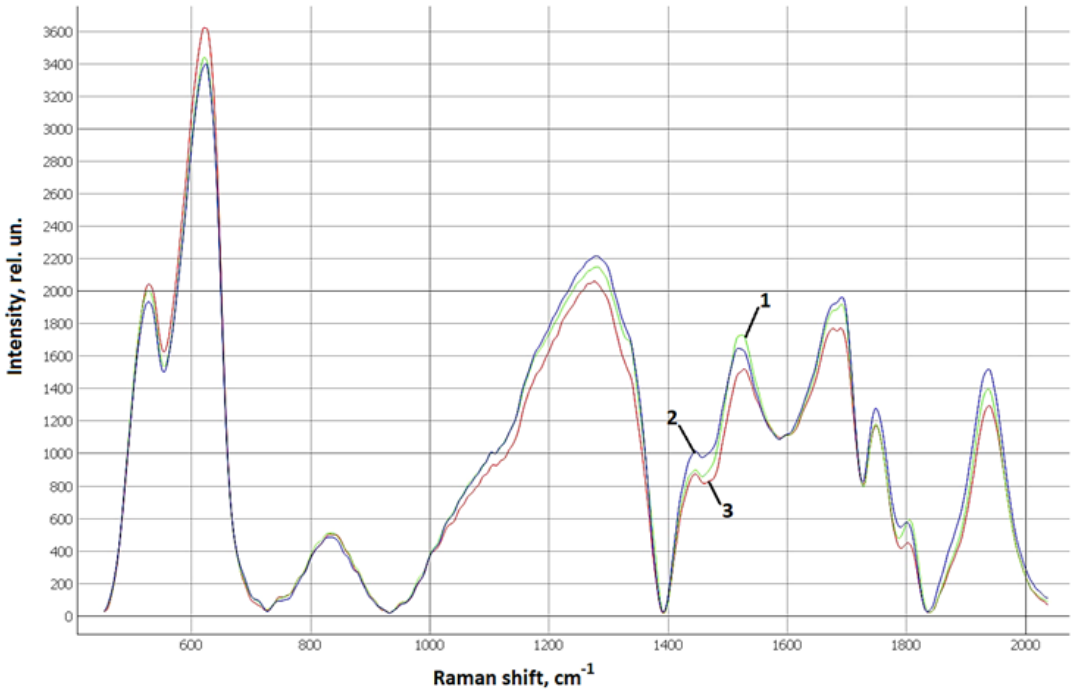

Fig. 1. Averaged Raman spectra of the studied sample groups: 1 — *S.pneumoniae, 2 — S.oralis, 3 — S.mitis*

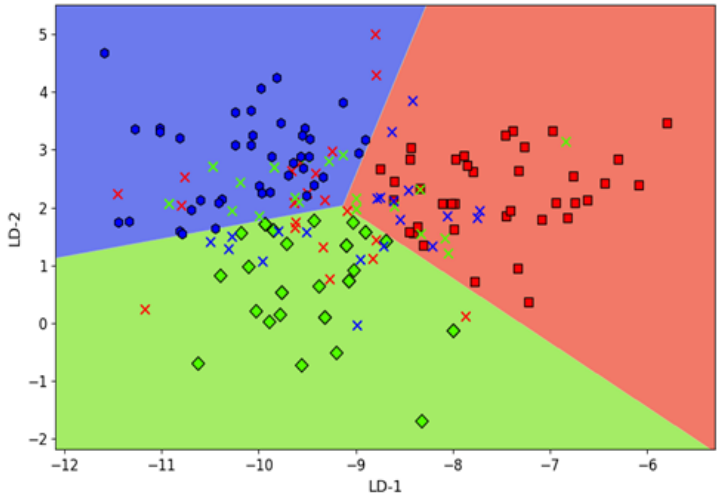

Fig. 2. The results of linear discriminant analysis are a graph of the values of the linear discriminant function

Fig. 3 shows the coeficients of the matrix of the factor structure for the most significant lines of the KR, which have a physical meaning of the correlation between the variables in the model and the discriminating function. The higher the modulo value of LD-1 for a variable, the more it determines the difference in the discriminative model between groups of samples.

It can be noted that the variable with the highest value of SHAP ($_{+}7.63$) is $_{k}528.73_{a}$, which indicates its significant influece on the classification. In general, values decrease, which may indicate that variables with high values contribute more to differences between groups than variables with lower values. The smallest value of SHAP ($_{+}0.22$) belongs to the variable $_{k}1338.65_{a}$, which indicates its insignificand contribution to the model.

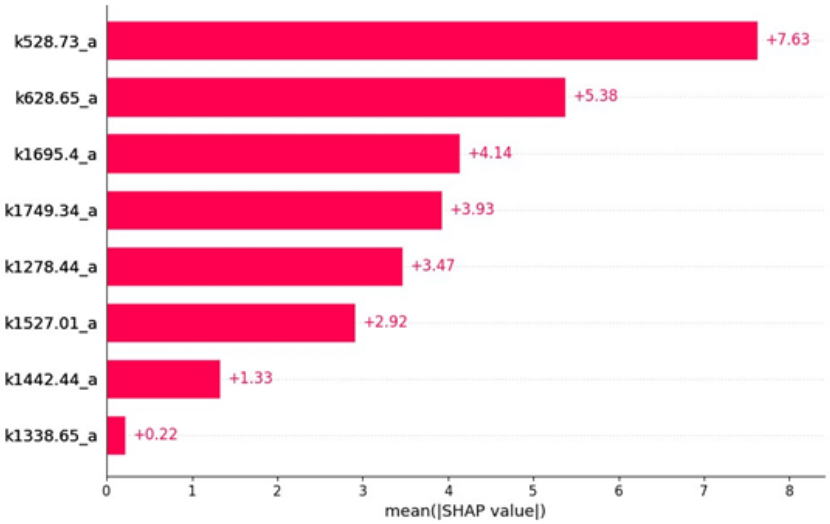

Fig. 3. The contribution of variables to the intensity of lines

The results of the classification of groups are shown in Fig. 4. It can be seen that the number of correctly classified values is approximately equal for each of the groups. For groups 1 and 3, the number of correctly classified values was 9 out of 12, for groups 2–8 out of 12.

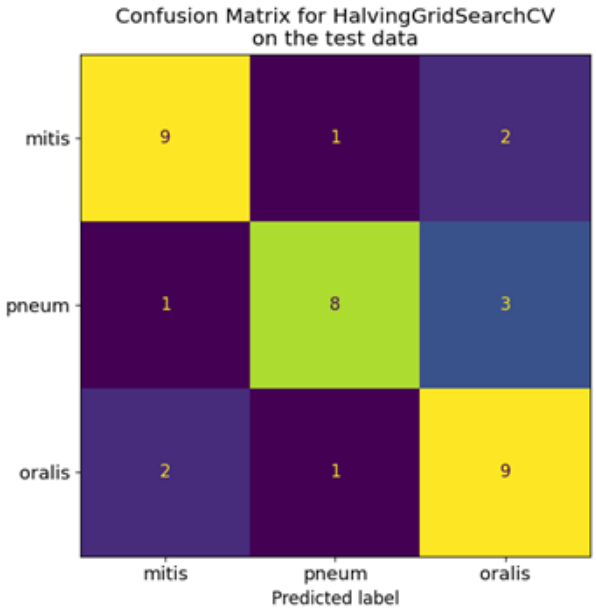

Fig. 4. The Confusion Matrix

Fig. 5 shows the ROC-curves for each sample group. The specificity of the developed algorithm calculated using ROC analysis was 81–91 percent, depending on the defined group. The curves show the ratio of true positive and false positive results, which is important for understanding the accuracy of the classification.
For furthe analysis, AUC (Area Under Curve) values were calculated, which makes it possible to quantify the classification ability of the algorithm. The AUC values for each group were:
mitis (AUC=0.91)
pneunom (AUC=0.89)
oralis(AUC=0.81)
microaverage (AUC=0.86)
macroaverage (AUC=0.87)
The AUC index above 0.8 in all cases indicates the high classification ability of the algorithm, confirming its potential usefulness in practical applications for the diagnosis and classification of varios conditions.

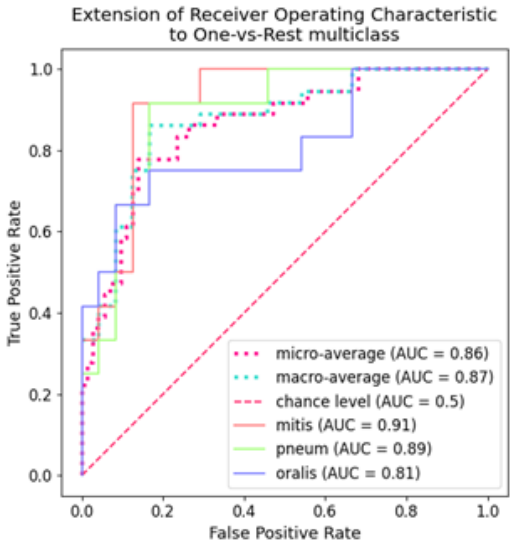

Fig. 5. ROC-curves for all sample groups

Conclusion

In this work, spectral differences of *S.mitis, S.oralis, S.pneumoniae* strains are established. The main spectral differences are visible at 527 cm^{-1} (S-S di sulfide stretching in proteins, Phosphatidylserine or v(S-S) gauche-gauche-trans (aminoacid cysteine)), 621 cm^{-1} (C-C twisting mode of phenylalanine (proteins)), 1280 cm^{-1} (Amide III, CH_2 wagging vibrations from glycine backbone or proline side chains), 1333 cm^{-1} (Guanine), 1445 cm^{-1} (CH_2 bending modes, deformation C-H bending proteins, deformation CH_2/CH_3 in lipids), 1525 cm^{-1} (Amide II), 1692 cm^{-1} (Stretching CO), 1749 cm^{-1} (C=O, lipids). As a result of this study, criteria were introduced for the identification of groups of samples based on the intensity of the lines of the averaged Raman spectra and the conducted discriminant analysis. Thus, for strains of *S.pneumoniae*, the values LD-2 < 2 correspond, for strains *S.oralis* the values LD-1 <-8 and LD-2 >1 correspond, and for strains *S.mitis* the values LD-1 >-9 preferentially. Using ROC analysis, the specificity

of the developed algorithm was calculated, which amounted to 81–91 percent, depending on the defined group. The results obtained will allow further rapid analysis of different types of streptococcal strains using Raman spectroscopy.

References

[1] N.A.Tuneva, N.V.Bogacheva, U.O.Tuneva, Problems of dential implantation, *Vyatka medical Bulletin*, **62**(2019), no. 2, 86–93 (in Russian).

[2] A.I.Nikolaev, L.M.Tsepov, Practical therapeutic dentistry, Medpress-inform, 2019.

[3] L.Y.Orekhova, Periodontal diseases, Poly Media Press, 2004, 218–220

[4] I.V.Bazhutova, D.D.Ismatullin, A.V.Lyamin, D.A.Trunin, Species diversity of streptococci in pertodontal diseases, *Immunopathology, allergology, infectology*, (2023), no. 1, 81–86. DOI: 10.14427/jipai.2023.1.81

[5] D.D.Ismatullin, P.V.Bochkareva, I.V.Bazhutova, A.V.Lyamin, R.R.Galieva, A.V.Zhestkov, M.O.Zolotov, Species diversity of streptococci in local and systemic infections, *Clinical laboratory diagnostics*, **68**(2023), no. 10, 597–603 (in Russian). DOI: 10.51620/0869-2084-2023-68-10-597-603

[6] N.A.Tuneva, N.V.Bogacheva, Comparative assessment of microbial contamination in periodontitis and peri-implantitis, *Bulletin of the Perm University. Ser. Biology*, (2021), no. 2, 101–109. DOI: 10.17072/1994-9952-2021-2-101-109 (in Russian).

[7] M.Ercibengoa, MALDI-TOF MS breakpoint limitations for streptococcus mitis group species typing, *Clinical Laboratory*, **63**(2017), no. 11-12, 1935–1938. DOI: 10.7754/Clin.Lab.2017.170619)

[8] A.Carden, R.M.Rajachar, M.D.Morris, D.H.Kohn, Ultrastructural Changes Accompanying the Mechanical Deformation of Bone Tissue: A Raman Imaging Study, *Calcif Tissue Int.*, **72**(2003), 166–175.

[9] S.Berus, E.Witkowska, K.Niciski, E.Sadowy, W.Puzia, P.Ronkiewicz, A.Kamiska, Surface-enhanced Raman scattering as a discrimination method of Streptococcus spp. And alternative approach for identifying capsular types of S. Pneumonia isolates, *Spectrochimica Acta. Part A: Molecular and Biomolecular Spectroscopy*, **233**(2020). DOI: 10.1016/j.saa.2020.118088

[10] P.E.Timchenko, E.V.Timchenko, L.T.Volova, O.O.Frolov, Use of Raman spectroscopy for the assessment of dentin materials during their fabrication, *Journal of Optical Technology*, **88**(2021), no. 9, 485–488. DOI: 10.1364/JOT.88.000485

[11] P.E.Timchenko, E.V.Timchenko, L.T.Volova, O.O.Frolov Spectral Analysis of Organic Components of Demineralized Bone Biografts, *Optics and Spectroscopy (English translation of Optika i Spektroskopiya)*, **126**(2019), no. 6, 769–775. DOI: 10.1134/S0030400X19060262

[12] P.E.Timchenko, E.V.Timchenko, L.T.Volova, M.A.Zybin, O.O.Frolov, G.G.Dolgushov, Optical Assessment of Dentin Materials, *Optical Memory and Neural Networks*, **29**(2020), no. 4, 354–357. DOI: 10.3103/S1060992X20040116

Метод спектроскопии комбинационного рассеяния для идентификации стрептококков

Елена В. Тимченко
Павел Е. Тимченко
Институт информатики и кибернетики
Самара, Российская Федерация
Артём В. Лямин
Карим А. Каюмов
Центр генетических лабораторных технологий СамГМУ
Самара, Российская Федерация
Ирина В. Бажутова
Институт профессионального образования СамГМУ
Самара, Российская Федерация
Лариса Т. Волова
Самарский государственный медицинский университет
Самара, Российская Федерация
Олег О. Фролов
Алёна В. Зотова
Институт информатики и кибернетики
Российская Федерация
Филипп Р. Бажутов
Московский государственный университет имени М. В. Ломоносова
Москва, Российская Федерация

Аннотация. В современном мире широкое распространение приобрели различные воспалительные заболевания полости рта, в частности пародонтит. Одним из потенциальных участников воспалительного процесса являются стрептококки. В данной работе методом спектроскопии комбинационного рассеяния были изучены три штамма стрептококков. В результате были установлены спектральные отличия, введены критерии для идентификации групп образцов.

Ключевые слова: спектроскопия комбинационного рассеяния, стрептококки, пародонтит.

EDN: GBYSKG
УДК 519.63

Elastoplastic Ice Model with Dynamic Damage for Simulation of Non-linear Processes During a Low-speed Impact

Evgeniya K. Guseva*
Vasily I. Golubev†
Igor B. Petrov‡
Computational Physics Department
Moscow Institute of Physics and Technology
Dolgoprudny, Russian Federation
Viktor P. Epifanov§
Ishlinsky Institute for Problems in Mechanics RAS
Moscow, Russian Federation

Received 10.09.2024, received in revised form 25.10.2024, accepted 16.12.2024

Abstract. Estimation of ice deformations during dynamic loading plays a primary role in understanding many processes occurring in the Arctic region. However, the problem of choosing the most suitable model is complicated due to the complex structural changes in ice that affect its behaviour. In order to reconstruct observed damage localization, the dynamic von Mises–Schleicher criterion is applied to calculate the borders of the hydrostatic core in an elastoplastic specimen. This helps to account for the change in ice strength based on the stress magnitude. In the core, under conditions of uniform compression ice may pulverize. It results in microfracturing and recrystallization of ice. Additionally, inner and surface splits are introduced using the principal stress criterion. The model is verified with the use of numerical modelling of the laboratory experiment that consists of a direct low-speed impact. The main focus of this work is to study how non-linear processes influence the dynamics of the collision. The grid-characteristic method is used to accurately reconstruct waves formation. As a result, the formation of non-linear waves was observed. It causes further fracturing during propagation through the ice. Moreover, the conducted analysis of deformation curves confirmed that numerical results agree with the experimental data.

Keywords: ice rheology, non-linear waves, hydrostatic core, Von Mises–Schleicher yield criterion, fractures, low-speed impact.

Citation: E.K. Guseva, V.I. Golubev, I.B. Petrov, V.P. Epifanov, Elastoplastic Ice Model with Dynamic Damage for Simulation of Non-linear Processes During a Low-speed Impact, J. Sib. Fed. Univ. Math. Phys., 2025, 18(2), 179–190. EDN: GBYSKG.

Study of ice mechanical behaviour under dynamic loading remains a relevant problem that becomes especially important for the solution of practical tasks in the Arctic region. However, studying ice is complicated due to its non-linear behaviour during even for small deformations. Additionally, formulation of an adequate model is challenging because ice behaviour depends on many natural and structural factors [1] such as temperature and strain rate. Viscoelastic and elastoplastic models are commonly used for mathematical modelling, and the latter one is often applied in cases with large deformations [2, 3]. However, it is still uncertain which model would work better in specific cases. Furthermore, the influence of non-linear waves generated during impact is often assumed but not usually identified. Therefore, the main aim of this work is to

*guseva.ek@phystech.su https://orcid.org/0000-0003-2194-5081
†golubev.vi@mipt.ru https://orcid.org/0000-0003-3113-7299
‡petrov@mipt.ru https://orcid.org/0000-0003-3978-9072
§evp@ipmnet.ru https://orcid.org/0000-0002-9196-4264

study the role of wave processes occurring during impact on the dynamics of ice at low collision speeds (approximately up to 7 m/s) which are common of many processes in the Arctic region. To achieve this, the grid-characteristic method is used, which proved to be effective for many dynamic processes in complex media [4, 5].

The goal of this work is to develop the most suitable ice model with the use of laboratory experiments on the low-velocity direct impact conducted at the Ishlinsky Institute for Problems in Mechanics of the Russian Academy of Sciences. One particular feature that needs to be reflected is the observed localization of destruction in the high stress zone (contact patch) and the elastic behaviour far from the impact [2, 6]. Various criteria [7] are used to identify the hydrostactic core where ice structure can change under triaxial compression, and where microfracturing and recrystallization are observed. One of the standard choices for isotropic ice that was used in the conducted experiment is the von Mises criterion. Its advantage lies in the possibility of being modified by using a function for the calculation of yield strength. The von Mises–Schleicher criterion introduces linear relationship betwee this parameter and stress [8]. Thus, the observed changes in ice resistance to loading during collision are taken into account.

Another significant issue is the change in ice behaviour from the ductile behaviour and brittle failure when the deformation rates increase [1]. The considered low-velocity impacts fall into the transitional zone where both phenomena can be observed. Existing successful compound models [9] often require significant computational resources and determination of many parameters. Therefore, a simpler approach is proposed in this work to account for crack formation, where cracks appear according to the principal stress criterion [10]. As a result, this work proposes an elastoplastic model with the hydrostatic core, and boundaries of the core are calculated using the von Mises-Schleicher criterion and fracturing.

1. Problem formulation

1.1. Laboratory experiment

The laboratory experiment conducted using the procedure given in [11]. The scheme of the experiment is shown in Fig. 1. Frozen from distilled water, polycrystalline ice disc 3 was placed on the hard metal stand 4 with the ability to slide freely on its surface. A hard steel spherical indenter 2 with a piezoelectric accelerometer was hung with an inextensible string above ice surface attached to the carrier 6 with the trigger 1. The second sensor was set on the rear side of the sample along the striking axis. The whole set was placed on the metal plate 5 in a cooling chamber with the constant temperature $-10°C$. As a result of the measurements, oscillograph patterns were obtained as demonstrated in Fig. 1.

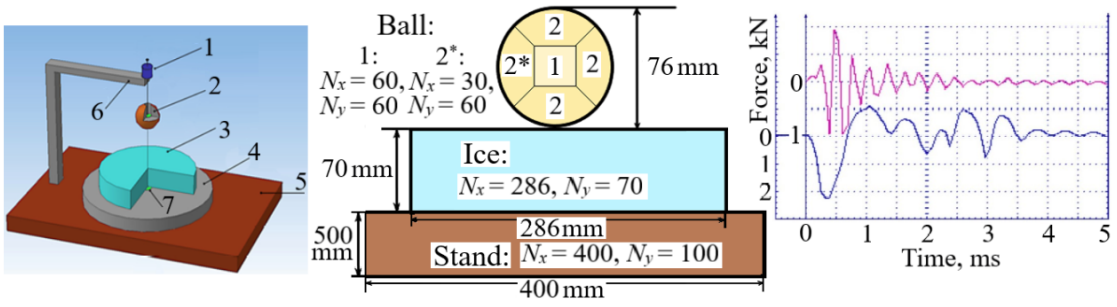

Fig. 1. On the left: the design of the laboratory experiment; in the middle: computational domain; on the right: results of the laboratory experiment (the blue line for sensor in the ball, magenta line for sensor in the ice)

1.2. Quantitative analysis procedure

In order to conduct quantitative comparison of the simulations and the experiment the acceleration of indentor obtained from the force F in Fig. 1 was further processed. The instantaneous velocity of the ball was obtained with integration using the Simpson rule: $v(t) = 0.56 + \frac{1}{m}\int\limits_0^t F(\tau)\,d\tau$, with mass of the ball $m = 1.76$ kg. However, the calculated velocity did not reach zero, presumably due to the influence of tangential velocity. To deal with this problem the transformation was conducted: $v(t) = 0.56\left(1 - \frac{v - 0.56}{\min(v - 0.56)}\right)$. Additionally, the coordinate of the ball was estimated: $x(t) = \int\limits_0^t v(\tau) sign(v(\tau))\,d\tau$. Here additional function $sign(v(t))$ was introduced. It was equal to 1 during loading before velocity reaches zero and –1 during unloading. Finally, in order to estimate the model deformation representing the curves positions in relation to the experiment the graph extremums were taken as the control points. They were the maximum value of the ball coordinate $x_{\max}$ which also represents the depth of the forming dent, and the time when the velocity reaches zero $t_{v=0}$.

1.3. Computational domain

Computations were conducted in the plane setting in order to be able to thoroughly study the model qualities. Although the model evaluation in three-dimensional case is still required calculations still managed to reconstruct ice complex non-linear behaviour. The formulated computational domain in this work is presented in Fig. 1 with numbers of grid cells along the horizontal (N_x) and the vertical (N_y) axes. In order to construct structured grids the ball was divided into 5 parts, where domain 2 corresponds to the rotation of the domain 2^*. Full adhesion contact condition was used between areas 1–2. Free slippage condition was applied to the contact areas between the ball, the disc and the stand. Consider the dynamic ball-ice contact. If the distance between grids is less than the set value (0.05 mm) then corresponding nodes are considered to be in contact. Moreover, when normal to the surface stresses change their sign in the nodes these nodes become free. Thus, it is possible to reconstruct the effect of "glueing" and "unsticking" of the contact patch observed in the real experiments. On the left, right and bottom sides of the stand no reflection boundary was set. All other boundaries were considered to be free. Impact velocity equal to 0.56 $\frac{m}{s}$ was used as an initial condition set in the cells of the ball. All grids were moved by the Lagrange corrector. The time step equal to 25 ns was chosen to fulfil the stability condition of the calculations. The initial distance between the ball and the disc was set to be 0.05 mm. The simulations were performed untill the ball stopped contacting with the ice or when the ball did not rebound from the ice.

In order to translate the set up shown in Fig. 1 into three-dimensional case for future simulations the computational domain should have rotational symmetry over the striking axis. Thus, new grids would be the surfaces of revolution of the plane grids. However, for construction of structured grids in the ice disc one needs to divide it into five parts, similarly to the grids in the ball in two-dimensional case. To keep the grid step in the impact zone equal to 1 mm as in the plain setting the number of grid nodes should be increased considerably. Ice grid in Fig. 1 has around 20 thousand nodes and if the horizontal size of the central square of the ice is set to 120–150 mm then the number of nodes can reach 1–1.6 million. The number of nodes in other four sectors can be limited to around 0.7–1 million. Therefore, the total number of nodes for the ice can equal 2.6 million which is 130-fold increase with respect to the plain grid. Similar estimations can be done for the stand and the ball. For the ball, in particular, seven grids can be constructed: one central square and six sectors. Using the numbers of grid steps that correspond to Fig. 1, the total number of nodes would increase form the initial 11 thousands to almost 1

million. Thus, during the three-dimensional modelling the number of performed operations and the real time of each calculation can increase 130-fold which would require the usage of parallel computing. Even these rough estimations incentivize the usage of the plain setting to study basic qualities of the model and its parameters.

2. Governing system of equations

In order to represent the ice of polycrystalline structure that was studied in the experiment the commonly used in practice isotropic linear elasticity model [12] is chosen as the governing system of equations:

$$\rho\dot{\mathbf{v}} = \nabla\cdot\sigma + \mathbf{f}, \tag{1}$$

$$\dot{\sigma} = \lambda(\nabla\cdot\mathbf{v})I + \mu(\nabla\otimes\mathbf{v} + (\nabla\otimes\mathbf{v})^T). \tag{2}$$

Here, the unknown velocity $\mathbf{v}$ and stress tensor σ are calculated at each time step using the Lame parameters λ, μ and density ρ. These parameters can be used to calculate speeds of pressure and shear waves: $c_p = \sqrt{\dfrac{\lambda+2\mu}{\rho}}$ and $c_s = \sqrt{\dfrac{\mu}{\rho}}$. As a result, c_p, c_s and ρ fully define the behaviour of system (1)–(2). External volumetric forces can be introduced with $\mathbf{f}$. For the simulations, the material parameters for hard steel are used for the ball and the metal stand: $c_p = 5700\,\frac{m}{s}$, $c_s = 3100\,\frac{m}{s}$, $\rho = 7800\,\frac{kg}{m^3}$. Ice parameters were estimated using the Berdennicov formula ($E = (87.6 - 0.21T - 0.0017T^2)\cdot 10^8$ Pa, [13]) with the same temperature as in the laboratory experiment and the constant Poisson coefficient $\nu = 0.295$. Then parameters for ice are $c_p = 3600\,\frac{m}{s}$, $c_s = 1942\,\frac{m}{s}$, $\rho = 917\,\frac{kg}{m^3}$.

3. Computational method and scheme

Nowadays, there is no standard method to solve ice problems related to dynamic loading [14]. Although the finite element methods [15], coupling methods [16] and various mesh-free methods such as peridynamics [17] are gaining popularity. However, a lot of them still have disadvantages. They are mainly related to the representation of fracturing. As the focal point of this work is the study of wave phenomena linked to the occurring damage the grid-characteristic method was chosen to solve equations (1)–(2). This method allows one to accuratly reproduce dynamic processes as proven in [4,5]. The method uses the hyperbolicity of system (1)–(2) in order to conduct coordinate-wise and process-wise splitting and change of the variables to the Riemann invariants. As a result, the initial system can be reduced to a system of independent one-dimensional transport equations. In this case, each equation is solved using the third approximation order grid-characteristic scheme monotonized by the grid-characteristic monotonicity criterion [18].

4. Nonlinear rheological models

Splitting on physical processes allows one to take into account non-linear behaviour. All such models modify the elastic solution after each calculation step. The introduced compound model consists of the elastoplastic ice with the hydrostatic core and fractures.

4.1. Elastoplasticity model

Plasticity is described as the Prandtl–Reuss flow rule [19] that corrects the stress deviator $\left(s_{ij}^{el} = \sigma_{ij}^{el} - \dfrac{\sigma_{ll}^{el}}{\delta_{mm}}\delta_{ij}\right)$ to return the stress tensor to the von Mises yield surface $\left(\text{if } \frac{1}{2}s_{ij}^{el}s_{ij}^{el} - k^2 > 0\right)$:

$$s_{ij} = s_{ij}^{el} \frac{\sqrt{2}k}{\sqrt{s_{pq}^{el} s_{pq}^{el}}},$$

The defining parameter of the model is the maximum shear stress k. The initial state of the ice is considered to be elastoplastic. During the collision, calculated elastic variables are used to check the fulfilment of criteria for formation of the hydrostatic core at each time step. Then, the elastoplasticity in the ice is realized outside of the core.

4.2. Hydrostatic core

In order to account for structural changes in ice the approach formulated in [10] is used. The damage is divided into static and dynamic part. The static damage is represented as the formation of the hydrostatic core. It is a zone where the ice is under the triaxial compression due to loading of the ball. Here complex structural changes such as microfracturing and recrystallization can occur. Boundaries of this zone are defined on the basis of the von Mises-Schleicher criterion. It is a modified version of the von Mises criterion that allows for taking into account the change in the ice strength during collision. This is realized as follows. The constant shear stress value is replaced with a linear function $k_0 + ap$, where $p = \dfrac{\sigma_{ll}}{\delta_{mm}}$ is the instantaneous value of pressure in the node. In order to represent material inside the core the sand model [10] is used. It considers that damaged material could not sustain tension. Thus, all positive principal stresses are set to zero. Moreover, instead of elastoplastic stress tensor correction elastic parameters are changed, and the Lame parameter μ is decreased by a factor of 100 to represent the almost liquid state of the ice.

4.3. Fracture model

The dynamic damage is described by taking fracturing into account [10]. If the principal stresses exceeded the spallation strength k_s in some node of the ice disc grid then a unit fracture is formed. The size of the fracture is not defined within the cell, and it is considered to be less then spacial step. As a result, the growth of cracks is described as the increase in the number of such unit fractures. Free boundary conditions are used in each damaged node in order to reconstruct the observed reflections from fractures. This allows for the reconstruction of time-dependent behaviour of ice by observing the complex interactions between wave and damage processes.

4.4. The compound model algorithm

To sum up the process of the model implementation the following procedure is conducted at each time step of simulations. At first, the elastic values of unknown variables $\mathbf{v}^{el}$ and σ^{el} are calculated and corresponding coordinate-wise splitting boundary and interface conditions are implemented. Then, the von Mises–Schleicher criterion is used to determine the boundaries of the core. If condition $\frac{1}{2} s_{ij}^{el} s_{ij}^{el} - (k_0 + ap)^2 > 0$ is fulfilled then correction of principal stresses and elastic parameters is performed in each grid node of the ice in accordance with the core model. In the nodes outside the core stress tensor deviator is corrected when the von Mises criterion $\frac{1}{2} s_{ij}^{el} s_{ij}^{el} - k^2 > 0$ is satisfied as the elatoplastic model suggests. Finally, the principal stress condition for fracturing is checked in each node, and fractures appear in corresponding nodes. After all corrections are performed grids are moved.

5. Simulation results

As a result of simulations, wave, stress and damage patterns (Figs. 2–4) are obtained and used for the comparison with the experiment. Moreover, graphs of the ball velocity and coordinate

are used for quantitative evaluations (Figs. 5–6).

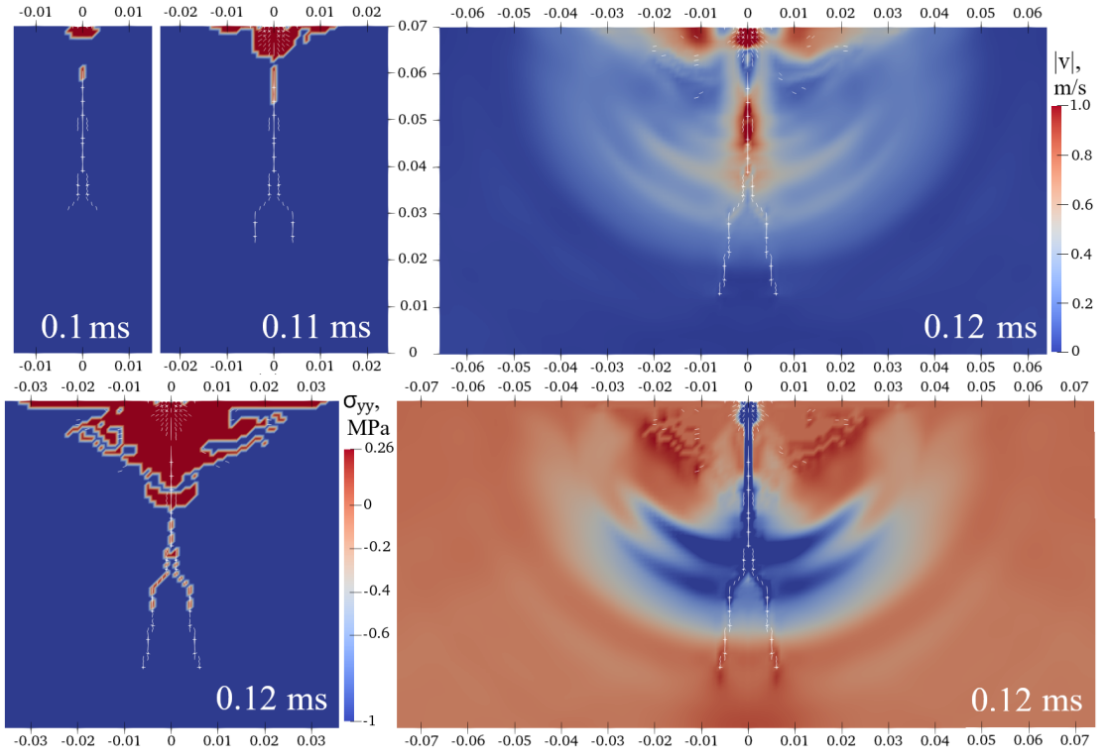

Fig. 2. Left column: damage patterns, core (red) and fractures (white). Right column: nonlinear wave ($|\mathbf{v}|$) and stress (vertical stress projection σ_{yy}) patterns. Coordinates are in meters, $k = k_0 = k_s = 0.3$ MPa, $a = 0.1$

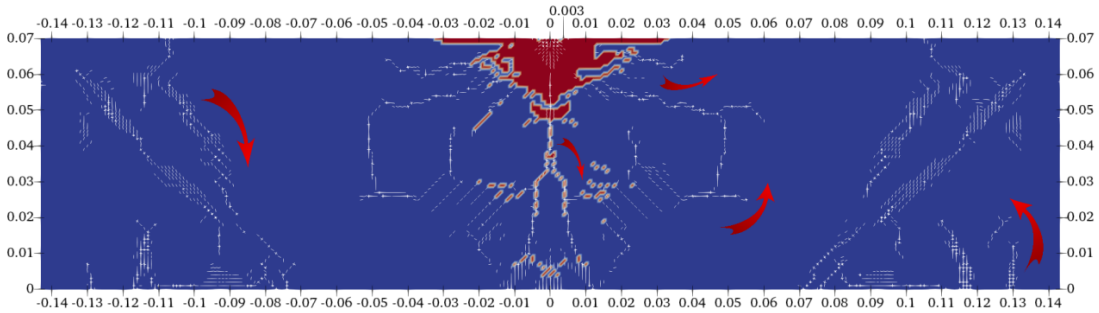

Fig. 3. Damage patterns, core (red) and fractures (white) at 0.23 ms, $k = k_0 = k_s = 0.3$ MPa, $a = 0.1$. Arrows show the direction of fracture growth. Radius of the contact patch is 3 mm. Coordinates are in meters

5.1. Qualitative comparison with the experiment

Simulations show that behaviour of the model can be drastically changed with different damage parameters. For big values of k_0 and k_s damage (core and fractures) is usually localized near the impact zone (similar to patterns at 0.1 ms in Fig. 2). At the initial stages of collision,

the first cracks start to appear in the area with the biggest stress on the contact patch. Vertical cracks form near the boundary of the patch, and their number increases as this boundary moves along with the ball indentation. Moreover, the core forms directly under the surface fractures. Its size usually corresponds to the diameter of the contact. Similar localization of fracture can be observed in real experiments [20, 21]. Additionally, a median fracture can be formed with the propagation of the impact wave. Its growth starts at a distance from the contact, and it is additionally stimulated by the reflected wave. Sometimes this crack can be split into two parts, forming an arch similar to Fig. 2 at 0.12 ms. However, further inner spalling does not occur.

When k_s is decreased, the principal stress criterion starts to be fulfilled in a greater number of nodes, and fracture begin to spread through the disc. As shown in Fig. 2, at certain points of time the number of cracks can increase exponentially starting from the impact zone. This phenomenon is seemingly caused by inference between the reflected impact waves and waves generated from the contact patch due to the surface fracture and waves that propagate in the ball. The rapid growth of fractures invokes non-linear waves that create further damage far from the impact zone. With the forward travel of the wave fractures grow from the core, and side cracks can appear. After reflection cracks begin to form from the rear surface. The damage patterns are fully developed by the time of the unloading as in Fig. 3.

A similar phenomenon can be observed when the value of k_0 is small and the fractures are localized or not taken into account completely as in Fig. 4. This case clearly demonstrates the influence of a on the results. When $a = 0$, the core usually has homogeneous structure and not many discontinuities. On the contrary, non-zero a can change the form of the core, and it begins to resemble fractures (Fig. 4). However, when a is too big, the von Mises–Schleicher criterion is rarely satisfied and the core is localized at the impact zone. When $a < 1$, the centre of the core is usually formed in the nearest neighbourhood of the contact patch. The rapid increase in the core area can also generate non-linear waves that cause patterns similar to conical (middle picture) and side (top and middle pictures) cracks and horizontally oriented clusters of fractures (bottom picture). Additionally, the spread of the core zones starting from the rear surface of the ice can also be recreated (bottom picture). As a result, the appearance of non-linear waves represents a distinct interaction between the wave and damage processes that was usually assumed but not clearly demonstrated in previous works.

5.2. Quantitative comparison with the experiment

The influence of model parameters on wave patterns and fracture patterns is studied on the basis of deformation curves in Fig. 5. The velocities obtained from the laboratory experiment can be divided into three stages: the inlet section (up to about 0.2 ms), the main stage of impact (from 0.2 to 0.6 ms) and the time near the rebound (from 0.6 to 0.8 ms). The gradual decrease of the velocity during the first and last stages may be related to the temperature effects and surface tension that influence the formation of the dent and the hardening processes. The inlet section was not reconstructed during the simulation. However, it is in the case of small values of k_0 when it is possible to qualitatively represent the experiment by the time of unloading. This is demonstrated by similar slopes of the calculated and experimental curves and tapering of the velocity.

Moreover, Fig. 5 shows the distinction in behaviour between the small and big values of k_0. Small value of k_0 leads to a larger core, higher amplitudes of coordinates, less monotone velocity, and bigger times when the velocity reaches minimum. This trend appears both with (second row) and without (first row) fractures. Thus, it is possible to find the optimal parameters of the model to reach agreement with the experiment. As a result, the closest to the experiment curve is in the case without fractures: $k = 0.03$ MPa, $k_0 = 0.08$ MPa, $a = 0.5$. However, when the value of k_0 is big the von Mises–Schleicher criterion stops to be satisfied, and the curves for various a almost coincide.

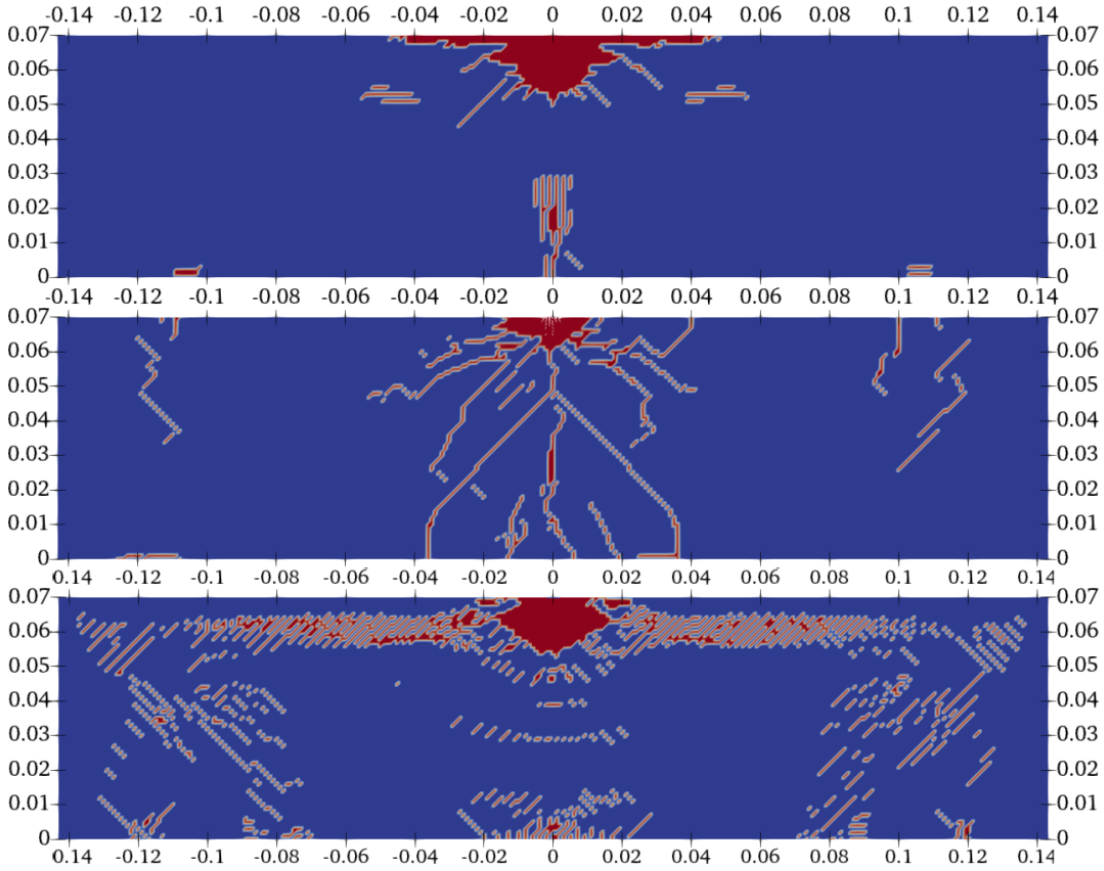

Fig. 4. Damage patterns: core (red) and fractures (white). Picture at the top: no fractures, $k = 0.08$ MPa, $k_0 = 0.1$ MPa, $a = 0.1$, 0.4 ms. Picture at the top middle: with fractures, $k = 0.08$ MPa, $k_0 = 0.1$ MPa, $k_s = 0.3$ MPa, $a = 0.5$, 0.9125 ms. Picture at the bottom: no fractures, $k = 0.3$ MPa, $k_0 = 0.08$ MPa, $a = 0.5$, 0.3 ms

Similar trends can be observed when a and k are varied. However, the introduction of a generally results in significant oscillations and less monotonous graphs of velocity. Nonetheless, the change in a allows for the achievement of the optimal parameters of the model as shown in Fig. 6 for small enough values of k_0. These parameters can be predicted using the intersection between numerical results with the experimental values of $x_{\max}$ and $t_{v=0}$. Therefore, this allows for the usage of optimization algorithms and machine learning to train the model. Furthermore, this approach can be used for both variations of the model with and without fractures. As it is shown in Fig. 5 (third row), the calculated curves are very similar, especially for small values of a. However, the influence of the spallation strength k_s is ambiguous. Thus, a more thorough evaluation is still required. As a result, the model proved to be able to reconstruct many aspects of ice behaviour during the impacts. Although the deformation curves do not coincide completely with the experimental ones, the simulations represent the experiment during the main stage of the collision. Moreover, the model allows for the optimization of its parameters. It is one of the main directions for further work.

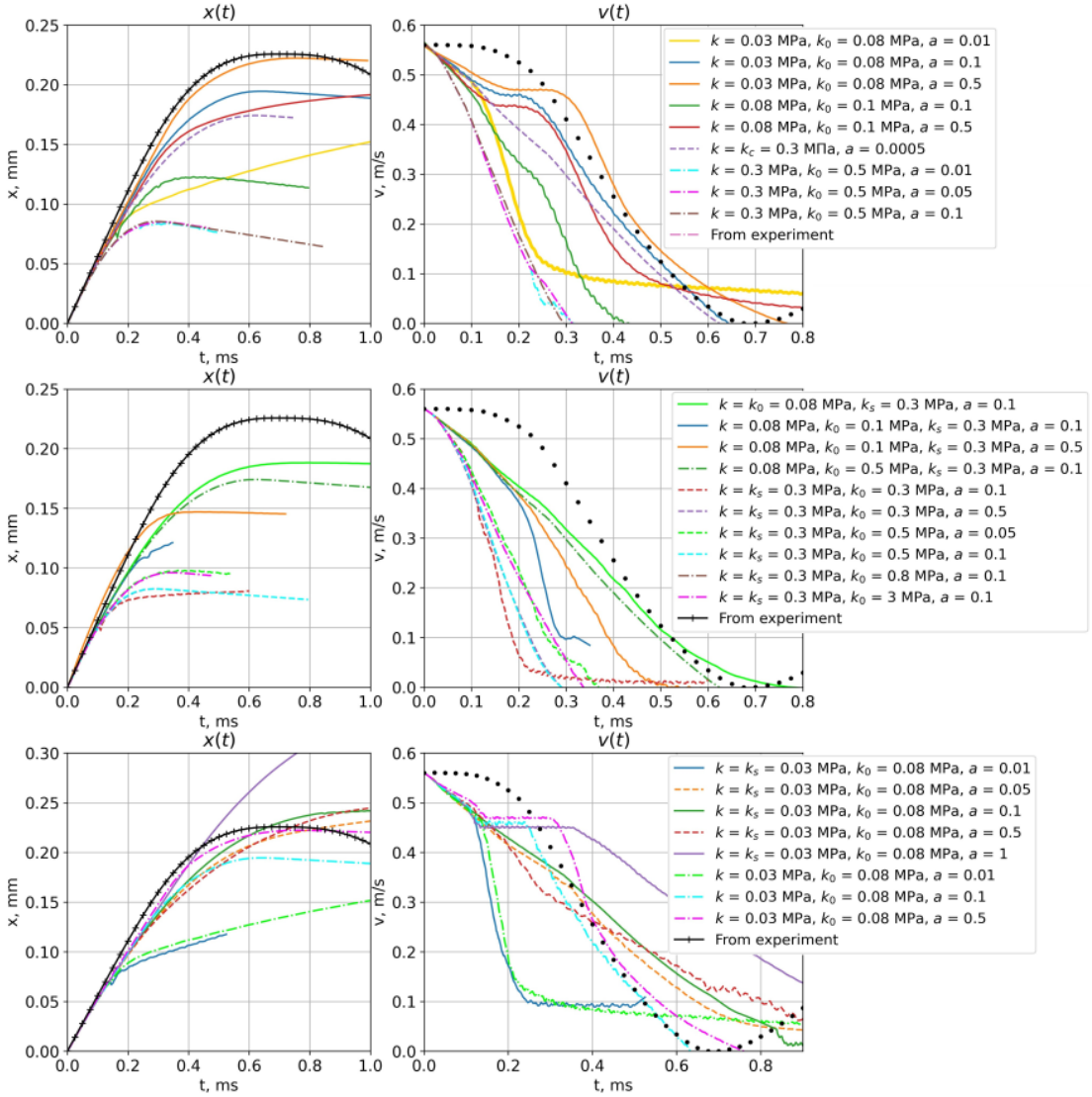

Fig. 5. Ball coordinate (x) and velocity (v) during the collision for various parameters of the model. First row — no fractures, second row— with fractures, third — comparison of the cases with and without fractures

Conclusion

As a result of this work, the compound model is used to describe ice behaviour during a low-speed impact by a spherical indentor. The observed localization of damage and the change in ice local resistance to loading are accounted for by the determination of the hydrostatic core in the elastoplastic sample using the dynamic von Mises–Schleicher yield criterion. Fracturing is introduced using the maximum principle stress criterion. Thus, it is possible to reconstruct ice complex and time-dependent behaviour with the obtained formation of non-linear waves that cause further damage. Moreover, both core and fractures could represent different types of cracks, such as median, side and conical fractures. The cracks formed on the contact patch from the rear surface and far from the impact zone. The qualitative analysis of deformation curves proves

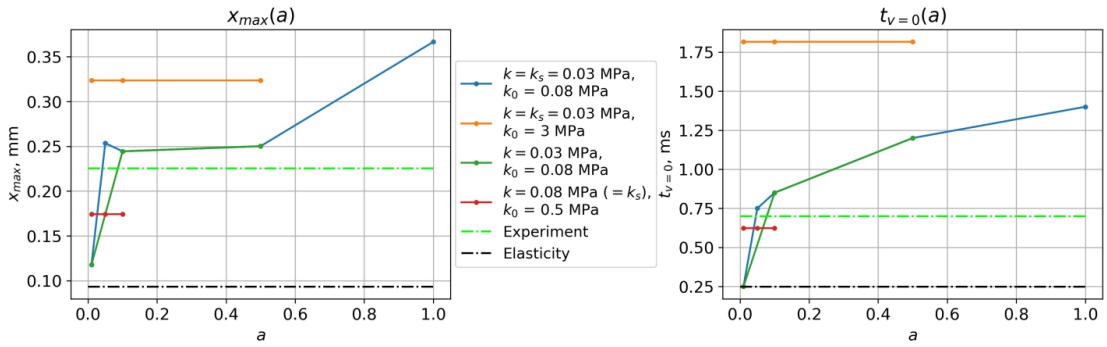

Fig. 6. Maximum ball coordinate and velocity in relation to parameter a. For reference, the values obtained with the use of standard elasticity model for ice are marked by black line

the ability of the model to reach an agreement with the experiment. Therefore, a more detailed optimization of parameters of the model both in a plane and space setting is the main direction for further work.

The reported study was carried out with the financial support of the Russian Science Foundation, project no. 23-21-00384.

References

[1] S.T.Ince, A.Kumar, J.K.Paik, A new constitutive equation on ice materials, *Ships Offshore Struct.*, **12**(2017a), no. 5, 610–623. DOI: 10.1080/17445302.2016.1190122

[2] I.Jordaan, Some issues in ice mechanics, *Proceedings of the ASME 2015 34th International Conference on Ocean, Offshore and Arctic Engineering*, **8**(2015), OMAE2015–42042. DOI: 10.1115/OMAE2015-42042

[3] M.Mokhtari, B.J.Leira, A critical review of constitutive models applied to Ice-Crushing simulations, *Journal of Marine Science and Engineering*, **12**(2024), no. 6, 1021. DOI: 10.3390/jmse12061021

[4] A.V.Favorskaya, I.B.Petrov, Calculation of seismic stability of buildings in the Far North using the Grid-Characteristic Method, *Lobachevskii Journal of Mathematics*, **45**(2024b), no. 1, 213–222. DOI: 10.1134/S1995080224010153

[5] N.I.Khokhlov, I.B.Petrov, Application of the grid-characteristic method for solving the problems of the propagation of dynamic wave disturbances in high-performance computing systems, *Proceedings of the Institute for System Programming of RAS*, **31**(2019), no. 6, 237–252. DOI: 10.15514/ISPRAS-2019-31(6)-16

[6] P.Barrette, J.Pond, I.Jordaan, Ice damage and layer formation in small-scale indentation experiments, Ice in the Environment: Proceedings of the 16th International Association for Hydraulic Engineering and Research (IAHR) International Symposium on Ice, 2002, 246–253.

[7] W.Zhang, J.Li, L.Li, Q.Yang, A systematic literature survey of the yield or failure criteria used for ice material, *Ocean Engineering*, **254**(2022), 111360. DOI: 10.1016/j.oceaneng.2022.111360

[8] A.M.Kovrizhnykh, Plane Stress Equations for the Von Mises-Schleicher Yield Criterion, *Journal of Applied Mechanics and Technical Physics*, **45**(2004), 894–901. DOI: 10.1023/B:JAMT.0000046039.92532.fd

[9] M.Mokhtari, E.Kim, J.Amdahl, A non-linear viscoelastic material model with progressive damage based on microstructural evolution and phase transition in polycrystalline ice for design against ice impact, *International Journal of Impact Engineering*, **176**(2023b), 104563. DOI: 10.1016/j.ijimpeng.2023.104563

[10] A.Favorskaya, V.Golubev, D.Grigorievyh, Explanation the difference in destructed areas simulated using various failure criteria by the wave dynamics analysis, *Procedia Computer Science*, **126**(2018), 1091–1099. DOI: 10.1016/j.procs.2018.08.046

[11] V.P.Epifanov, Ice destruction from impact interactions, *Akademiia Nauk SSSR Doklady*, **284**(1985), no. 3, 599–603. DOI: 10.1007/978-3-031-54589-4_29

[12] V.Novatskii, Theory of Elasticity, Mir, Moscow, 1975 (in Russian).

[13] V.P.Berdennikov, Izuchenie modulya uprugosti lda, *Trudi GGI*, **7**(1948), no. 61, 13–23 (in Russian).

[14] D.Grinevich, V.Buznik, G.Nuzhnyi, Review of numerical methods for simulation of the ice deformation and fracture, *Proceedings of VIAM*, **8**(2020), 109–122 (in Russian). DOI: 10.18577/2307-6046-2020-0-8-109-122

[15] H.Jang, S.Hwang, J.Yoon, J.H.Lee, Numerical analysis of Ice-Structure impact: Validating material models and yield criteria for prediction of impact pressure, *Journal of Marine Science and Engineering*, **12**(2024), no. 2, 229. DOI: 10.3390/jmse12020229

[16] R.Sun, Z.Li, Y.Shi, Numerical simulation of ice loading characteristics of ships in a wave-current environment in a broken ice area, *Journal of Physics Conference Series*, **2756**(2024), no. 1, 012030.

[17] Y.Song, L.Zhang, S.Li, Y.Li, A Multi-Yield-Surface Plasticity State-Based Peridynamics Model and its Applications to Simulations of Ice-Structure Interactions, *Journal of Marine Science and Application*, **22**(2023), no. 3, 395–410. DOI: 10.1007/s11804-023-00344-8

[18] E.K.Guseva, V.I.Golubev, I.B.Petrov, Linear, Quasi-Monotonic and Hybrid Grid-Characteristic Schemes for Hyperbolic Equations, *Lobachevskii J. Math.*, **44**(2023), 296–312. DOI: 10.1134/S1995080223010146

[19] O.T Bruhns, The Prandtl-Reuss equations revisited, *Z. Angew. Math. Mech.*, **94**(2014), no. 3, 187–202.

[20] V.P.Epifanov, Physical mechanisms of ice contact fracture, *Dokl. Phys.*, **52**(2007), no. 1, 19–23. DOI: 10.1134/S1028335807010053

[21] V.P.Epifanov, Contact fracture behavior of ice, *Ice and Snow.*, **60**(2020), no. 2, 274–284 (in Russian). DOI: 10.31857/S2076673420020040

Упругопластическая модель льда с динамическим разрушением для моделирования нелинейных процессов во время низкоскоростного удара

Евгения К. Гусева
Василий И. Голубев
Игорь Б. Петров
Кафедра вычислительной физики
Московский физико-технический институт
Долгопрудный, Российская Федерация
Виктор П. Епифанов
Институт проблем механики им. Ишлинского РАН
Москва, Российская Федерация

Аннотация. Определение деформации льда в процессе приложения динамических нагрузок играет первостепенную роль для понимания многих процессов, происходящих в Арктическом регионе. Однако решение задачи выбора наиболее подходящей модели усложняется из-за происходящих структурных изменений, влияющих на поведение льда. Для отражения наблюдаемой локализации разрушений применяется динамический критерий Мизеса–Шлейхера для выделения гидростатического ядра в упругопластическом образце льда. Таким образом, также учитывается изменение прочности льда в зависимости от величины напряжений. В ядре в условиях всестороннего сжатия лед может крошиться, возможно образование микротрещин и рекристаллизация. Дополнительно учитывается трещинообразование в объеме материала с помощью критерия по главным напряжениям. Модель верифицируется на основе моделирования лабораторного эксперимента по низкоскоростному прямому удару. Основной особенностью данной работы является изучение влияния нелинейных процессов на динамику столкновения. Применение сеточно-характеристического метода позволяет точно разрешать образующиеся волны. В результате удалось продемонстрировать образование нелинейной волны, вызывающей трещинообразование при прохождении через лед. К тому же, анализ деформационных кривых подтвердил возможность согласования расчетов с экспериментом.

Ключевые слова: реология льда, нелинейные волны, критерий текучести Мизеса–Шлейхера, трещины, низкоскоростной удар.

EDN: FSMZDD
УДК 534.1

On the Velocities of Rayleigh Surface Waves Propagating along Boundaries of Generalized Continua

Vladimir I. Erofeev*
Artem M. Antonov†
Alexey O. Malkhanov‡
Mechanical Engineering Research Institute RAS
Branch of Federal Research Center A. V. Gaponov–Grekhov
Institute of Applied Physics of the Russian Academy of Sciences
Nizhny Novgorod, Russian Federation

Received 07.10.2024, received in revised form 15.11.2024, accepted 24.12.2024

Abstract. It is demonstrated that mathematical models of gradient-elastic medium and reduced Cosserat medium, in contrast to the model of classical deformable solid, allow one to describe experimentally observed dispersion of Rayleigh surface wave, i.e., relationship between phase velocity of surface wave and frequency. At the same time, according to the model of gradient-elastic half-space, velocity of surface wave cannot exceed the velocity of shear wave but at certain values of frequency it can reach it. According to reduced Cosserat model, velocity of surface wave exceeds the velocity of shear wave as well as velocity of propagation of surface wave in classical half-space and gradient-elastic half-space.

Keywords: gradient-elastic half-space, reduced Cosserat model, surface wave, dispersion, phase velocity, frequency.

Citation: V.I. Erofeev, A.M. Antonov, A.O. Malkhanov, On the Velocities of Rayleigh Surface Waves Propagating along Boundaries of Generalized Continua, J. Sib. Fed. Univ. Math. Phys., 2025, 18(2), 191–198. EDN: FSMZDD.

In 1885, English scientist Lord Rayleigh (John William Strutt) theoretically demonstrated that waves can propagate along the flat boundary of a solid elastic half-space with vacuum or with sufficiently rarefied medium (for example, air), and their amplitudes rapidly decrease with depth [1]. These waves called Rayleigh surface waves. They depend on the frequency range and have different applied directions.

It became obvious that Rayleigh waves in the low-frequency range (1–100 Hz) are the main type of waves observed during earthquakes. Therefore, they have been studied in detail in seismology for almost 140 years [2].

The main features of propagation of Rayleigh waves are as follows: absence of dispersion, i.e., the wave speed does not depend on its frequency and it is constant for each material; the speed is slightly less than the speed of the bulk shear wave by a factor 0.87 – 0.96; the displacement vector has longitudinal and transverse components, and the transverse component always exceeds the longitudinal component [3].

A series of works by V. V. Krylov [4–10] was devoted to the study of elastic vibrations of the earth generated by trains and motor vehicles. Very high level of ground vibrations generated by high-speed trains moving at a speed higher than the speed of Rayleigh surface waves in the ground was theoretically predicted. For these works V. V. Krylov was honoured with the Rayleigh Medal in 2000 awarded by the Acoustical Institute of Great Britain and often called the Nobel

*erof.vi@yandex.ru https://orcid.org/0000-0002-6637-5564
†artem.antonov@autorambler.ru
‡malkhanov@gmail.com https://orcid.org/0000-0001-5210-8281

Prize in Acoustics. Krylov's theory was experimentally confirmed in 1997–1998 (with his direct participation) on a new high-speed line in Sweden (Gothenburg-Malmo), where on some sections of the route the speed of Rayleigh waves was only 45 m/s, and a train speed of 160 km/h was enough to observe the effect. The discovered effect became known as "ground vibration shock" (by analogy with the well-known sonic boom from a supersonic aircraft). The generation sources became known as "trans-Rayleigh trains" [11].

It should be noted that the existence of critical speeds of load movement along rail guides above which bending waves are generated in the guides was discussed back in the first half of the 1980s [12–14]. However, the critical speeds calculated at that time showed the practical unattainability of the effect of generating bending waves in the guides by a vehicle. It turned out to be easier for the load to overcome the speed of the Rayleigh wave in the soil located under the rail guide and the guide itself with the system of sleepers and ballast acted as an intermediary between the source of wave generation and the environment in which these waves arose.

At present, problems of stability of motion of high-speed objects along rail guides and problems of generation of bending and bending-torsional waves in rail guides are recognized as relevant, and results of their solution serve as methodological and computational support for experiments on high-speed acceleration (or braking) of payloads on rocket tracks citeerofeev15,erofeev16,erofeev17,erofeev18, erofeev19, erofeev20.

The mechanics of a homogeneous isotropic deformable solid excludes the possibility of surface wave propagation with a speed greater than the speed of shear wave. However, along with the classical continuum model generalized continuum models are also quite widely used in the mechanics of deformable solid [21–24].

The study of generation of Rayleigh waves by sources moving along the boundaries of non-classical elastic half-spaces was presented [25]. The purpose of the work was to determine how the velocities of shear waves and Rayleigh surface waves are related for materials described by the equations of mechanics of generalized (non-classical) continua such as Cosserat continuum [26] and its modifications [27, 28]) and the gradient-elastic medium [29–31].

1. Dispersion properties of surface waves in generalized continua

As generalized continua, the gradient-elastic medium and the reduced Cosserat medium are further considered.

Vector equations of the dynamics of studied media are written with respect to displacements as follows

- for a gradient-elastic medium

$$\rho\ddot{\mathbf{u}} - (\lambda+\mu)grad\, div\, \mathbf{u} - \mu\Delta\mathbf{u} + 4\mu L^2\Delta(\Delta\mathbf{u} + \widetilde{\nu} grad\, div\, \mathbf{u}) = 0 \tag{1}$$

  where $\mathbf{u}$ — vector of displacements, λ and μ — Lame elastic constants, L — the ratio of the curvature modulus to the shear modulus, $\widetilde{\nu}$ — dimensionless constant;

- for the reduced Cosserat medium

$$(\lambda+2\mu)\nabla(\nabla\cdot\mathbf{u}) - \mu\nabla*(\nabla*\mathbf{u}) - J\frac{\partial^2}{\partial t^2}\nabla*(\nabla*\mathbf{u}) = \rho\frac{\partial^2\mathbf{u}}{\partial t^2}, \tag{2}$$

  where J — constant which characterize the inertial properties of a macrovolume, ρ — density of the material.

By introducing a scalar φ and vector ψ potentials, solutions of equations (1) and (2) are sought. In this case, displacement vector $\mathbf{u}$ can be written in the form

$$\mathbf{u} = \nabla\varphi + \nabla * \psi. \tag{3}$$

Note that for a plane problem the vector potential has only one non-zero component which is denoted by ψ. Then, two equations are obtained from equations (1) and (2):

- for a gradient-elastic medium

$$\Delta\varphi - \frac{1}{c_1^2}\frac{\partial^2\varphi}{\partial t^2} = 0, \quad \Delta(1 - L^2\Delta)\psi - \frac{1}{c_2^2}\frac{\partial^2\psi}{\partial t^2} = 0, \tag{4}$$

- for the reduced Cosserat medium

$$\Delta\varphi - \frac{1}{c_1^2}\frac{\partial^2\varphi}{\partial t^2} = 0, \quad \Delta\psi + G\Delta\frac{\partial^2\psi}{\partial t^2} - \frac{1}{c_2^2}\frac{\partial^2\psi}{\partial t^2} = 0, \tag{5}$$

  where $G = J/\mu$.

The solution of equations (4) and (5) is sought in the form of harmonic waves propagating in the direction of the axis . Moreover, one should select only those solutions which correspond to a decrease in wave amplitudes with depth. Then one can obtained

- for a gradient-elastic medium

$$\varphi = Ae^{\zeta y + i(\omega t - kx)}, \quad \psi = B_1 e^{\eta_1 y + i(\omega t - kx)} + B_2 e^{\eta_2 y + i(\omega t - kx)}, \tag{6}$$

- for the reduced Cosserat medium

$$\varphi = Ae^{\zeta y + i(\omega t - kx)}, \quad \psi = Be^{\eta y + i(\omega t - kx)}. \tag{7}$$

Taking into account the absence of stresses at the boundary $y = 0$, the following dispersion equation for a gradient-elastic medium are obtained

$$\begin{gathered}
16(1-\beta\varsigma)(1+\alpha-\varsigma)[1+2\alpha+2\sqrt{\alpha(1+\alpha-\varsigma)}] = \\
= (2-\varsigma)^2[(1-3\alpha^2)^2 + \alpha(3-\alpha)(1+\alpha-\varsigma) + (1-\alpha^2)(1+\alpha-\varsigma)^2 + \alpha(1+\alpha-\varsigma)^3 + \\
+2(1-3\alpha^2)(3-\alpha)\sqrt{\alpha(1+\alpha-\varsigma)} + 2(1-3\alpha^2)(1-\alpha)(1+\alpha-\varsigma) - \\
-2(1-3\alpha^2)(1+\alpha-\varsigma)\sqrt{\alpha(1+\alpha-\varsigma)} + 2(3-\alpha)(1-\alpha)(1+\alpha-\varsigma)\sqrt{\alpha(1+\alpha-\varsigma)} - \\
-2(3-\alpha)(1+\alpha-\varsigma)^2\alpha - 2(1-\alpha)(1+\alpha-\varsigma)^2\sqrt{\alpha(1+\alpha-\varsigma)}].
\end{gathered} \tag{8}$$

Here $\varsigma = c_R^2 = \dfrac{\omega^2}{k^2c_2^2}$, $\alpha = L^2k^2$, $\beta = \dfrac{1-2\nu}{2-2\nu}$, ν — Poisson ratio. When $L = 0$, equation eqrefeq:8 is reduced to the dispersion equation of the Rayleigh surface wave in the classical case [3]. Analysis of equation (8) showed that for gradient-elastic medium, the dispersion properties of the Rayleigh surface wave in the "wave number – frequency" plane are described by two curves. The first curve (the lower one) comes from the origin of coordinates. The origin of the second curve is shifted upward along the frequency axis. In this case the surface wave has two modes, and each mode has dispersion since velocities of both modes depend on frequency. When frequency increases the speed of each mode of the surface wave increases, and as frequency tends to infinity ($\omega \to \infty$) the velocity of the lower mode goes from below to the horizontal asymptote

$C_R = \sqrt{2}\, c_2$, where $c_2 = \sqrt{\dfrac{\mu}{\rho}}$. The speed of the upper mode of the surface wave increases from the classical values for Rayleigh waves $(0,87\breve{}0,96)c_2$, reaches a maximum, and then goes to the horizontal asymptote $C_R = \sqrt{2}\, c_2$ when $(\omega \to \infty)$. The value of the maximum velocity increases with increasing Poisson ratio. For example, for materials with Poisson ratio close to 0.5 the surface wave velocity at the peak of the curve is 4% greater than the maximum surface wave velocity for materials with Poisson ratio close to 0.2. Analysis of the second equation of system (4) shows that volume shear wave in gradient-elastic medium also has dispersion. This follows from the non-linear relationship between frequency and the wave number $\omega^2 = c_2^2 k^2 (1 + L^2 k^2)$. It allows one to calculate the phase velocity

$$V_\phi^2 = \frac{\omega^2}{k^2} = c_2^2 (1 + L^2 k^2). \tag{9}$$

It is easy to see from (9) that for any non-zero value of the wave number (or frequency) $V_{ph} > c_2$ and, consequently, c_2 is not the true velocity of the dispersive shear wave but it serves only as its lower limit. Therefore, the Rayleigh wave velocity C_R should be compared not with c_2 but with V_{ph}.

This result demonstrates that velocity of the surface wave cannot exceed the phase velocity of the shear wave, reaching it at certain frequency values.

Similarly, taking into account the absence of stresses at the boundary $y = 0$, one can obtain dispersion equation for reduced Cosserat medium

$$\eta \left[\eta^3 - 8\eta^2 + \left(24 - 16 \frac{\varsigma}{1 - \frac{J}{\mu}\omega^2} \right) \eta - 16 \left(2 - \frac{1}{1 - \frac{J}{\mu}\omega^2} - \varsigma \right) \right] = 0. \tag{10}$$

where $\varsigma = \dfrac{c_2^2}{c_1^2}$, $\eta = \dfrac{c_R^2}{c_2^2}$.

Analysis of equation (10) showed that here, too, unlike the classical case [3], the Rayleigh surface wave has dispersion. In the "wave number – frequency" plane, there are two dispersion branches: lower and upper. With increasing frequency, the speed of the surface wave related to the lower dispersion branch decreases and at infinity the square of the speed of the surface wave $c_R^2 \to 0.7\, c_2^2$. The velocity of the surface wave related to the upper dispersion branch increases with increasing frequency. For dimensionless frequencies $\omega > 9$ this growth becomes unlimited. Consequently, the upper dispersion branch describes wave processes in the interval of dimensionless frequencies $0 < \omega < 9$, then the process ceases to be wave-like.

Analysis of the second equation of system (5) shows that bulk shear wave in the reduced Cosserat medium also has dispersion. This follows from the non-linear relationship between frequency and the wave number $\omega^2 = \dfrac{k^2 c_2^2}{1 + \frac{Gk^2}{c_2^2}}$ which allows one to calculate the phase velocity

$$V_{ph\tau}^2 = \frac{\omega^2}{k^2} = \frac{c_2^2}{1 + \frac{Gk^2}{c_2^2}}. \tag{11}$$

Comparing the frequency dependence of the velocity of the surface wave related to the upper dispersion branch and the phase velocity of the shear wave given in (11), one can see that velocity of the surface wave in the entire frequency range exceeds the phase velocity of the shear wave which converges to c_2 for $\omega \to 0$ and decreases monotonically to zero when $C_R^2 \to 0.8 c_2^2$ for $\omega \to \infty$.

The frequency dependencies of $V_{ph\tau 1}^2$ (the square of the phase velocity of the shear wave in a gradient-elastic medium) and $V_{ph\tau 1}^2$ (the square of the phase velocity of the shear wave in the

reduced Cosserat medium) are shown in Fig. 1. It is evident from the graphs that phase velocity of the shear wave in the gradient-elastic medium exceeds phase velocity of the shear wave in the reduced Cosserat medium in the entire frequency range.

The frequency dependences of C^2_{R1} (the square of the Rayleigh wave velocity in a gradient-elastic half-space), C^2_{R2} (the squared Rayleigh wave velocity in a reduced Cosserat medium (lower dispersion branch)), C^2_{R3} (the Rayleigh wave velocity in the classical isotropic elastic half-space) are shown in Fig. 2. It is evident from the graphs that at low frequencies the maximum propagation velocity of Rayleigh waves is observed in the reduced Cosserat medium. At the same time, when frequency increases the Rayleigh wave velocity in the reduced medium decreases, and the Rayleigh wave velocity in the gradient-elastic half-space increases and exceeds the wave velocity in the Cosserat medium over the entire frequency range. It is also evident from the graphs that Rayleigh wave velocity in the classical half-space exceeds the wave velocity in the Cosserat medium when frequency increases. At the same time, the surface wave velocity in the classical medium is independent of frequency. Therefore, waves in this medium do not have dispersion. Considering the upper dispersion branch of the Rayleigh wave velocity, one can see that velocity of the surface wave in the reduced Cosserat medium exceeds the surface wave velocities in the classical medium and in the gradient-elastic medium.

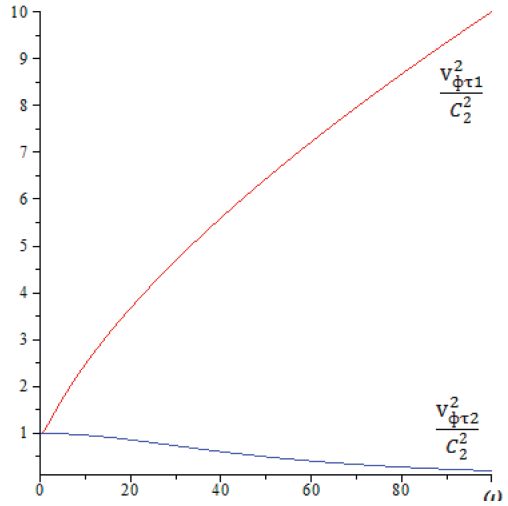

Fig. 1. Frequency dependences of phase velocities of shear waves

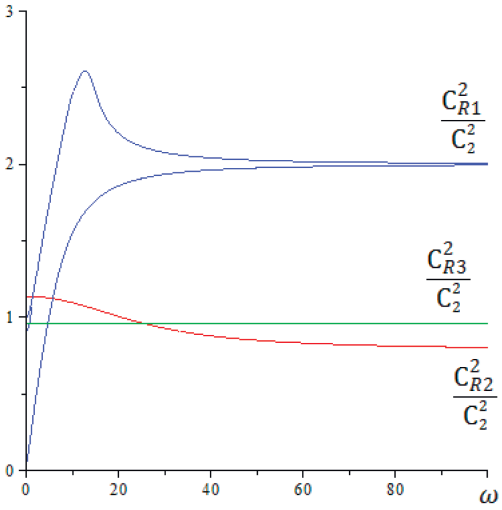

Fig. 2. Frequency dependences of velocities of surface waves

Conclusion

It is shown that velocity of the surface wave propagating along the free boundary of the gradient-elastic half-space is a function of frequency, i.e., the wave has dispersion, and it can exceed the velocity of the bulk shear wave calculated as the square root of the ratio of the shear modulus to the density of material. However, in the medium under consideration the shear wave also has dispersion and the value of the specified velocity is only the lower limit of its phase velocity. Thus, in a gradient-elastic medium the phase velocity of the surface wave cannot exceed the phase velocity of the bulk shear wave but at certain values of the wave number it can reach it. Rayleigh surface waves propagating along the free boundary of the half-space of the Cosserat medium (reduced model) also have dispersion. In the "phase velocity – frequency" plane for such waves there are lower and upper dispersion branches. When frequency increases

the phase velocity of the wave related to the lower dispersion branch decreases. The phase velocity of the wave related to the upper dispersion branch increases when frequency increases. The phase velocity of the surface wave exceeds the phase velocity of the bulk shear wave in the entire frequency range.

The work was carried out with financial support from the Russian Science Foundation (project no. 20-19-00613).

References

[1] Lord Rayleigh, On waves propagated along the plane surface of an elastic solid, *Proceedings of the London Mathematical Society*, **s1-17**(1885), no. 2, 4–11. DOI: 10.1112/plms/s1-17.1.4

[2] K.Aki, P.G.Richards, Quantitative seismology: theory and methods. 2 nd edition, University Science Books, Sausalito, California, 2002.

[3] I.A.Viktorov, Sound surface waves in solids, Nauka, Moscow, 1981 (in Russian).

[4] V.V.Krylov, On the theory of railway-induced ground vibrations, *Journal de Physique IV*, **4**(1994), no. C5, 769–772. DOI: 10.1051/jp4:19945167

[5] V.V.Krylov, C.C.Ferguson, Calculation of low-frequency ground vibrations from railway trains, *Applied Acoustics*, **42**(1994), 199–213. DOI:10.1016/0003-682X(94)90109-0

[6] V.V.Krylov, Generation of ground vibrations by superfast trains, *Applied Acoustics,* **44**(1995), 149-164. DOI:10.1016/0003-682X(95)91370-I

[7] V.V.Krylov, Vibrational impact of high-speed trains: effect of track dynamics, *Journal of the Acoustical Society of America*, **101**(1996), no. 6, 3121–3134. DOI:10.1121/1.417123

[8] V.V.Krylov, Spectra of low-frequency ground vibrations generated by high-speed trains on layered ground, *Journal of Low Frequency Noise, Vibration and Active Control*, **16**(1997), no. 4, 257–270.

[9] V.V.Krylov, Effect of track properties on ground vibrations generated by high-speed trains, *Acustica-Acta Acustica*, **84**(1998), no.1, 78–90.

[10] V.V.Krylov, Ground vibration boom from high-speed trains, *Journal of Low Frequency Noise, Vibration and Active Control*, **18**(1999), no. 4, 207–218.

[11] V.V.Krylov (ed), Noise and vibration from high speed trains, Thomas Telford Publishing, London, 2001.

[12] A.I.Vesnitsky, Waves in systems with moving boundaries and loads, Fizmatlit, Moscow, 2001 (in Russian).

[13] A.I.Vesnitsky, Selected works on mechanics, Nash Dom Publ., Nizhny Novgorod, 2010 (in Russian).

[14] G.G.Denisov, V.V.Novikov, E.K.Kugusheva, On the problem of stability of one-dimensional infinite elastic systems, *Applied Mathematics and Mechanics*, **49**(1985), no. 6, 164–168 (in Russian).

[15] S.V.Butova, S.I.Gerasimov, V.I.Erofeev, V.G.Kamchatnyi, Stability of high-speed objects moving along a rocket track guide, *Journal of Machinery Manufacture and Reliability*, **44**(2015), no. 1–5. DOI: 10.3103/S1052618815010021

[16] S.I.Gerasimov, V.I.Erofeev, Calculation of flexural-and-torsional vibrations of a rocket track rail, *Journal of Machinery Manufacture and Reliability*, **45**(2016), no. 3, 211–213. DOI: 10.3103/S1052618816030055

[17] S.I.Gerasimov, V.I.Erofeev, V.G.Kamchatnyi, I.A.Odzerikho, The sliding contact condition in stability analysis of stage motion for a rocket sled track facility, *Journal of Machinery Manufacture and Reliability*, **47**(2018), no. 3, 221–226. DOI:10.3103/S105261881803007X

[18] S.I.Gerasimov, V.I.Erofeev, D.A.Kolesov, E.E.Lisenkova, Dynamics of deformable systems carrying moving (review of publication and dissertation research), *Bulletin of Science and Technical Development*, **160**(2021), no. 1, 25–47. DOI: 10.18411/vntr2021-160-3

[19] S.A.Astakhov, V.I.Biryukov, A.V.Kataev, Evaluation of the efficiency of various methods of braking the stored equipment on a limited length during high-speed track tests of aviation and rocket technology products, *Bulletin of the Moscow Aviation Institute*, **29**(2022), no. 2, 20–34 (in Russian).

[20] S.A.Astakhov, V.I.Biryukov, A.V.Kataev, Experimental determination of vibration conductivity by structural elements of a rocket carriage during high-speed track tests of aircraft, *Siberian Aerospace Journal*, **24**(2023), no. 1, 44–63 (in Russian).

[21] H.Altenbach, G.A.Maugin, V.Erofeev (Editors). Mechanics of Generalized Continua, *Advanced Structured Matherials*, **7**(2011), Springer-Verlag, Berlin-Heidelberg

[22] H.Altenbach, S.Forest, A.Krivtsov (Editors). Generalized Continua as Models with Multi-Scale Effects or Under Multi-Field Actions, *Advanced Structured Matherials*, **22**(2013) Springer-Verlag, Berlin-Heidelberg

[23] H.Altenbach, V.A.Eremeyev (Editors), Generalized Continua - from the Theory to Engineering Applications, Springer, Wien, 2013

[24] H.Altenbach, S.Forest (Editors) Generalized Continua as Models for Classical and Advanced Materials *Advanced Structured Matherials*, **42**(2016), Springer-Verlag, Switzerland

[25] A.M.Antonov, V.I.Erofeev, A.O.Malkhanov, Excitation of waves by a high-speed source moving along the border gradient-elastic half-space, *IOP Conference Series: Materials Science and Engineering*, **971**(2020), no. 3, 032068. DOI:10.1088/1757-899X/971/3/032068

[26] E. et F. Cosserat, Theorie des corps deformables, Paris, Librairie Scientifique A. Hermann et Fils, 1909.

[27] W.Nowacki, Theory of asymmetric elasticity, Pergamon Press, Oxford, 1986.

[28] L.M.Schwartz, D.L.Jonson, S.Feng, Vibrational models in granular materials, *Physical Review Letters*, **52**(1984), no. 10, 831–834. DOI: 10.1103/PhysRevLett.52.831

[29] J. Le Roux, Etude geometrique de la flexion, dans les deformations infinitesimaleg d'nn milien continu, *Ann. Ecole Norm. Super.*, **28**(1911), 523–579. DOI: 10.24033/asens.643

[30] J. Le Roux, Recherchesg sur la geometrie beg deformatios finies, *Ann. Ecole Norm. Super.*, **30**(1913), 193–245. DOI: 10.24033/asens.659

[31] T.J.Jaramillo, A Generalization of the Energy Function of Elasticity Theory, Dissertation, Departament of Mathematics, University of Chicago, Chicago, 1929.

О скоростях поверхностных волн Рэлея, распространяющихся вдоль границ обобщенных континуумов

Владимир И. Ерофеев
Артем М. Антонов
Алексей О. Мальханов
Институт проблем машиностроения РАН – филиал ФГБНУ
«Федеральный исследовательский центр Институт прикладной физики
им. А. В. Гапонова–Грехова РАН»
Нижний Новгород, Российская Федерация

Аннотация. Показано, что математические модели градиентно-упругой среды и редуцированной среды Коссера, в отличие от модели классического деформируемого твердого тела, позволяют описать наблюдаемую экспериментально дисперсию поверхностной волны Рэлея, т.е. зависимость фазовой скорости от поверхностной волны частоты. При этом, согласно модели градиентно-упругого полупространства, скорость поверхностной волны не может превосходить скорости сдвиговой волны, но при определенных значениях частоты может ее достигать. Согласно же редуцированной модели Коссера скорость поверхностной волны превышает скорость сдвиговой волны, а также скорость распространения поверхностной волны в классическом полупространстве и градиентно-упругом полупространстве.

Ключевые слова: градиентно-упругое полупространство, редуцированная модель Коссера, поверхностная волна, дисперсия, фазовая скорость, частота.

Journal of Siberian Federal University. Mathematics & Physics 2025, 18(2), 199–208

EDN: GAYLEB
УДК 51-73

Computer Simulation of Self-assembly of Structure from an Ensemble of Nanoparticles

Viktoriya S. Petrakova*
Institute of Computational Modeling
Siberian Branch of Russian Academy of Sciences
Krasnoyarsk, Russian Federation
Alexey S. Tsipotan†
Siberian Federal University
Krasnoyarsk, Russian Federation

Received 25.09.2024, received in revised form 09.11.2024, accepted 08.01.2025

Abstract. Self-assembly is one of the methods utilized to create intricate geometry-based structures at the nanoscale. Earlier research in this field has shown that the formation of multiparticle structures using this technique is primarily achievable through gradual assembly, where a new particle is connected with a previously formed cluster. But step-by-step construction requires additional expenses and may result in defects within the already formed structures. If step-by-step assembly is not appropriate, a structure can be formed from a ensemble of particles without additional influence, but it is uncertain whether the probability of structure formation and the process selectivity are high. The paper presents a mathematical model that demonstrates how to derive a structure from an ensemble of particles, describes its implementation through software, and proposes the result of computational experiments.

Keywords: mathematical model, nanostructure self-assembly, computational experiment, Langevin dynamics.

Citation: V.S. Petrakova, A.S. Tsipotan, Computer Simulation of Self-assembly of Structure from an Ensemble of Nanoparticles, J. Sib. Fed. Univ. Math. Phys., 2025, 18(2), 199–208. EDN: GAYLEB.

Introduction

Scientific and technological interest is heightened in terms of the study of nanometric structures and their application in the creation of devices [1]. This is especially important in electronics, where smaller components allow for smaller devices with faster signal transmission. At the same time, many-particle systems play an important role in the description of many processes, the elements of which interact with each other through the environment, represented by both physical and chemical characteristics and a superposition of forces acting on the ensemble. Here there is an important feature for multiparticle systems: when faced with forces that affect the ensemble directly or indirectly through the environment, some particles can aggregate into structures. The term self-organization or self-assembly is used to describe such a process [2].

Self-assembly processes are the subject of theoretical and experimental studies in many application. The area of practice application is related to the binary solvents, mixing different kinds of particles, creating multilayer systems, achieving multistage self-assembly, and controlling the self-assembly of external fields, such as, for example, inertial forces [3–5]. The use of self-assembly is especially interesting for describing the aggregation of ultrasmall nanoparticles, like nanodiamonds [6, 7], quantum dots and supramolecules [8], and metal particles [9]. There is much

*vika-svetlakova@yandex.ru
†cipotana@mail.ru

less work on theoretical modeling of such systems. Molecular Brownian dynamics, Monte Carlo methods, dissipative particle dynamics, and self-consistent field theory are commonly utilized as tools for mathematical and numerical modeling to explore self-organizing structures.

From the point of view of mathematical and computer modeling of self-assembly processes, the most important is the construction of physically meaningful and computationally simple models. The choice of model is determined by the approximations necessary to simplify the initially complex phenomenon. The existing experience of the authors in the application of Brownian particle dynamics for modeling self-assembly processes in the volume of a solution indicates the possibility of reproducing and predicting real processes and phenomena in both simple and more complex systems. Thus, earlier in [10,11], an universal method was proposed for the formation of nanostructures under the action of an external quasi-resonant field due to the self-organization of nanoparticles. The first experiments [12,13] showed the fundamental possibility of pair formation from colloidal quantum dots. Numerical calculations [14] showed the possibility of creating more complex structures using staged self-assembly. This work is devoted to a mathematical and computer model of self-organization of aggregates from an ensemble of particles for estimating the parameters of the medium and field at which such an assembly becomes possible, as well as to a numerical analysis of the simulated process.

The article is organized as follows. Section 2 is devoted to the mathematical formulation of the problem and its implementation. Section 3 presents the results of computational experiments. Section 4 proposes conclusions and discussion of the results.

1. Mathematical formulation

Assume that under laser radiation field an ensemble of N nanoparticles having mass m_j of radius R_j and resonant frequency $\omega 0_j$, $j = 1, \ldots, N$ is considered. For every $j-$th dipole particle at any moment in time, we define:

$\bar{r}_j = \left(r_j^x, r_j^y, r_j^z\right)$ – radius-vector of the particle's center of mass;

$\bar{v}_j = \left(v_j^x, v_j^y, v_j^z\right)$ – vector of translational velocity of the particle's center of mass;

$\bar{\omega}_j = \left(\omega_j^x, \omega_j^y, \omega_j^z\right)$ – particle rotational velocity vector;

$\bar{d}_j = \left(d_j^x, d_j^y, d_j^z\right)$ – dipole moment vector.

The problem is to estimate the probability of assembling structures from an ensemble of particles for fixed parameters of the medium and field, in a time not exceeding the duration of one laser pulse ($T \leqslant 10$). The difference from our previous works lies in the solution of a multiparticle problem, when we are not limited to step-by-step assembly or a small number of particles (for example, see [14]). Here we are primarily interested in the possibility of assembling structures consisting of more than two particles and the selectivity of the process.

1.1. Langevin dynamics to describe the motion of an ensemble of particles

In this section we briefly describe the model used to describe many-particle interactions. It is based on a description of interaction through Langevin dynamics, a physical concept developed for statistical modeling of molecular systems. It represents stochastic dynamics in which particles move under the influence of a force directed towards the most probable regions of state space, determined by the parameters of the environment. To avoid repeating complete model conclusions regarding our previous works for pairs and triplets of particles [14,15], only the main equations and comments regarding the many-particle problem will be given here.

a) translation motion

Let us separately describe the translational and rotational motion of an ensemble of particles. Given that the ensemble size is much smaller than the wavelength of the incident radiation, we can assume that the external electric field $\vec{E}$ is uniform

$$\vec{E} = 1/2\ \vec{E}_0 \exp(i\omega^r t) + c.c.$$

and not to take into account delays. Here ω^r is the frequency of laser radiation. One of the widely used methods for describing the translational motion of an ensemble of particles is Langevin dynamics [11], expressed in the form of system

$$\begin{cases} d\bar{r}_j/dt = \bar{v}_j, \\ m_j d\bar{v}_j/dt = \bar{F}_j, \end{cases} \tag{1}$$

where $\bar{F}_j$ is the superposition of forces acting on the j-th particle, including friction forces and stochastic forces that take into account the temperature parameters of the medium. As the $\bar{F}_j$ we will consider the sum of the following components

$$\bar{F}_j = \vec{F}_j^v + \vec{F}_j^e + \vec{F}_j^d - \vec{F}_j^f + \vec{F}_j^c, \tag{2}$$

where $\vec{F}_j^d = -\nabla(W_j^d)$ is the electrodynamic force; $\vec{F}_j^v = -\nabla(W_j^v)$ is van der Waals force; $\vec{F}_j^e = -\nabla(W_j^e)$ is electrostatic repulsion force; $\vec{F}_j^f$ is viscous friction force; $\vec{F}_j^c$ is stochastic hydrodynamic force. Here $W_j^d, W_j^v,\ W_j^e$ are the energies of dipole-dipole, van der Waals and Coulomb interactions of an ensemble of particles at the position point of that particle, determined by (3)–(5) respectively.

$$W_j^d = \frac{1}{4\pi\varepsilon_0} \sum_{k\neq j} \frac{(\vec{d}_j, \vec{d}_k)|\vec{r}_{jk}|^2 - 3(\vec{d}_j, \vec{r}_{jk})(\vec{d}_k, \vec{r}_{jk})}{|\vec{r}_{jk}|^5}; \tag{3}$$

$$W_j^v = -\frac{A_H}{6} \sum_{k\neq j} \left(\frac{2{R_j}^2}{h_{jk}^2 + 4R_j h_{jk}} + \frac{2{R_j}^2}{h_{jk}^2 + 4R_j h_{jk} + 2{R_j}^2} + \ln \frac{h_{jk}^2 + 4R_j h_{jk}}{h_{jk}^2 + 4R_j h_{jk} + 2{R_j}^2} \right); \tag{4}$$

$$W_j^e = 2\pi\varepsilon_r\varepsilon_0 R_j {\phi_0}^2 \sum_{k\neq j} \ln\left[1 + \exp(-h_{jk}k_0)\right]. \tag{5}$$

Here A_H is the Hamaker constant; h_{jk} is interparticle gap; ϕ_0 is potential at the Helmholtz boundary; ε_r is dielectric constant of the medium; k_0 is screening constant.

For spherical particles the Stokes formula allows calculate the force of viscous friction $\vec{F}_f$

$$\vec{F}_j^f = 6\pi\eta R_j \vec{v}_j, \tag{6}$$

where η is the dynamic viscosity of the medium. The interaction of particles with a medium with fluctuating density usually leads to a random change in their trajectory. To take Brownian motion into account, consider a random force $\vec{F}_j^c$ described by a Gaussian distribution. Suppose a particle or particle's cluster experiences a random force over Δt. Before each integration step, the values of the projections of the random force $\vec{F}_j^c$ on the coordinate axes are selected from a Gaussian distribution with zero mean and standard deviation $\sigma^2 = 12\pi\eta RkT/\Delta t$.

b) rotational movement

The rotational motion of an ensemble of particles, arising as a result of the interaction of particles with induced dipole moments $\vec{d}_j$ in a uniform constant laser field in a viscous environment is determined by the action of the torque $\vec{N}_j$:

$$\vec{N}_j = \left[\vec{d}_j \times \vec{E}\right] + \vec{M}_j^{rot}, \tag{7}$$

where $[\vec{a} \times \vec{b}]$ is the vector product and $\vec{M}_j^{rot}$ is the torque caused by the forces of hydrodynamic resistance to the rotation of the structure

$$\vec{M}_j^{rot} = \left[\vec{F}_j^{tr} \times \vec{r}_j\right],$$

where $\vec{F}_j^{tr}$ is the superposition of forces acting on the particle with the exception of the force of electrodynamics interaction. One of the techniques to describe the rotation of a structure mathematically involves identifying it with rotation by a moving (local) coordinate system, which is fixed to the structure. For the connection between the moving and inertial coordinate systems, Euler angles are considered [15]. Using the equation of moments [16], we determine the rotation of the structure in the local coordinate system according to the presence or absence of momentum.

$$\frac{\mathrm{d}\vec{L}_j}{\mathrm{d}t} + \left[\vec{w}_j^{loc} \times \vec{L}_j\right] = \vec{N}_j^{loc}. \tag{8}$$

Here $\vec{L}_j$ is the angular momentum of the dipole structure, defined as $\vec{L}_j = J_j \vec{w}_j^{loc}$; $\vec{N}_j^{loc}$ is the rotational moment determined in the local coordinate system (CS). The position of the moving CS relative to the inertial one is determined by Euler's kinematic equations [16].

Remark 1. The initial distribution of dipole moments can be determined from a system of linear algebraic equations:

$$\vec{d}_j = \mathcal{X}_{0j}\left(\vec{E} + \sum_{k \neq j} \vec{E}_k\right),$$

where $\mathcal{X}_{0j}$ is the linear polarizability of j-th isolated particle, $\vec{E}_k$ is the field created by that particle of the ensemble at the location of k-th particle [15].

Remark 2. The "gluing" of particles into a pair or the formation of more complex multiparticle structures was considered to be the achievement of an interparticle gap between the gluing components of less than half the radius of the particle. After gluing, the center of mass of the formed structure is determined depending on the geometric arrangement of the particles forming it; mass as the sum of the masses of the parts forming the structure and dipole moment as a superposition of the forming dipole moments.

Remark 3. When modeling the translational motion of structures consisting of several nanoparticles, the same formulas (1)–(6) were used as for an ensemble of particles, except for the Stokes formula for calculating viscous friction forces for formed pairs of particles. Instead, we used the approximation of the pair by a cylinder of the appropriate radius and a generalization of the Stokes formula proposed in [15]. In turn, rotational motion for pairs of particles and more complex agglomerates, in contrast to isolated particles, requires the introduction and consideration of a local CS, rigidly related to the structure. Technical issues of modeling the rotation of a pair are discussed in [15].

1.2. Numerical solution and system scaling

For the numerical implementation of the system of differential equations, the Runge–Kutta method of the 4-th order was used. For the simulation, we considered an ensemble of CdTe particles in an aqueous solution. The parameters of particles, medium and field are described in Tab. 1. Note that the program for modeling the interaction of dipole particles is implemented in the C++ programming language, and the maximum accuracy of representing a real number during operation is ensured by the double type and is 15 significant digits. Therefore, it is necessary that the ratio of the maximum number to the minimum number does not exceed 10^{15}. Based on this restriction, we scaled the basic units of measurement of the International System of Units (SI):

$$\text{m} = 10^9\ m^*;\ \ \text{kg} = 10^{23}\ kg^*;\ \ \text{s} = 10^9\ s^*;\ \ \text{A} = 10^{13}\ A^*.$$

The values of the corresponding scaled quantities with descriptions and initial values are presented in Tab. 1.

Table 1. Description of constants and scaled quantities

Description	**Designation**	**Value**	**Scaled value**
Particle radius	R	$1.5{\cdot}10^{-9}\ m$	$1.5\ m^*$
Particle mass	m	$8.2485{\cdot}10^{-23}\ kg$	$8.2485\ kg^*$
Planck's constant	$\hbar$	$1.054{\cdot}10^{-34}\ J\cdot s$	$1.054\cdot 10^{-2}\ J^*\cdot s^*$
External field wavelength	λ	$690{\cdot}10^{-9}\ m$	$690\ m^*$
Resonance wavelength	λ_0	$525{\cdot}10^{-9}\ m$	$525\ m^*$
Uniform line width	G	$1.6{\cdot}10^{13}\ Hz$	$1.6\cdot 10^4\ Hz^*$
Dielectric constant in vacuum	ε_0	$8.82{\cdot}10^{-12}\ F/m$	$8.82\ F^*/m^*$
Relative dielectric constant of water	ε_r	81	81
Potential at the Helmholtz boundary	ϕ_0	$2.34{\cdot}10^{-3}\ V$	$2.34\cdot 10^{-2}\ V^*$
Viscosity	η	$0.8902{\cdot}10^{-3}\ Pa\cdot s$	$0.8902\cdot 10^2\ Pa^*\cdot s^*$
Screening constant	k_0	$0.1{\cdot}109\ m^{-1}$	$0.1\ m^{*-1}$
Boltzmann's constant	k_b	$1.38{\cdot}10^{-23}\ J/K$	$1.38\ J^*/K^*$
Hamaker constant	A_H	$50k_bT$	$50k_bT$
Transition dipol moment in a two-level system	$\lvert d_{12}\rvert^2$	$1.91\cdot 10^{-44}\ J\cdot m^3$	$19.1\ J^*\cdot m^{*3}$
Temperature	T	$300\ K$	$300\ K^*$
Speed of light	$_0$	$2.99{\cdot}10^8\ m/s$	$2.99\cdot 10^8\ m^*/s^*$
Field intensity	I	$10^{10}\ W/m^2$	$10^6\ W^*/m^{*2}$
Electric field strength	$\lvert\vec{E}\rvert$	$2.27{\cdot}10^6 V/m$	$2.27\cdot 10^{-2}\ V^*/m^*$

Assume also that in Cartesian coordinates the electric field strength vector $\vec{E} = (E^x, E^y, E^z)$ is determined by the radiation intensity and two angles α and β as follows:

$$\begin{cases} E^x = E\sin\alpha\sin\beta, \\ E^y = E\sin\alpha\cos\beta, \\ E^z = E\cos\alpha. \end{cases} \tag{9}$$

2. Results of numerical simulation

Fig. 1 shows an example of modeling the interaction of an ensemble of dipole particles for 10 ns from 10 particles. The initial location of the particles was set randomly within the cube with a 100 nm edge. As a result of the simulation, a pair is formed at 7 ns. No other structures were formed.

Fig. 2 shows the probability of assembly of at least one structure depending on the direction of laser radiation for different numbers of particles in 10 ns. Note that structures other than pairs were not formed for any combination of angles and initial numbers of particles. Fig. 3 shows the dependence of the average assembly time of the first pair of particles on their initial number. Fig. 4 shows a visualization of the change in the probability of structure assembly with an increase in the initial number of particles in the system at certain angles of incidence of laser radiation.

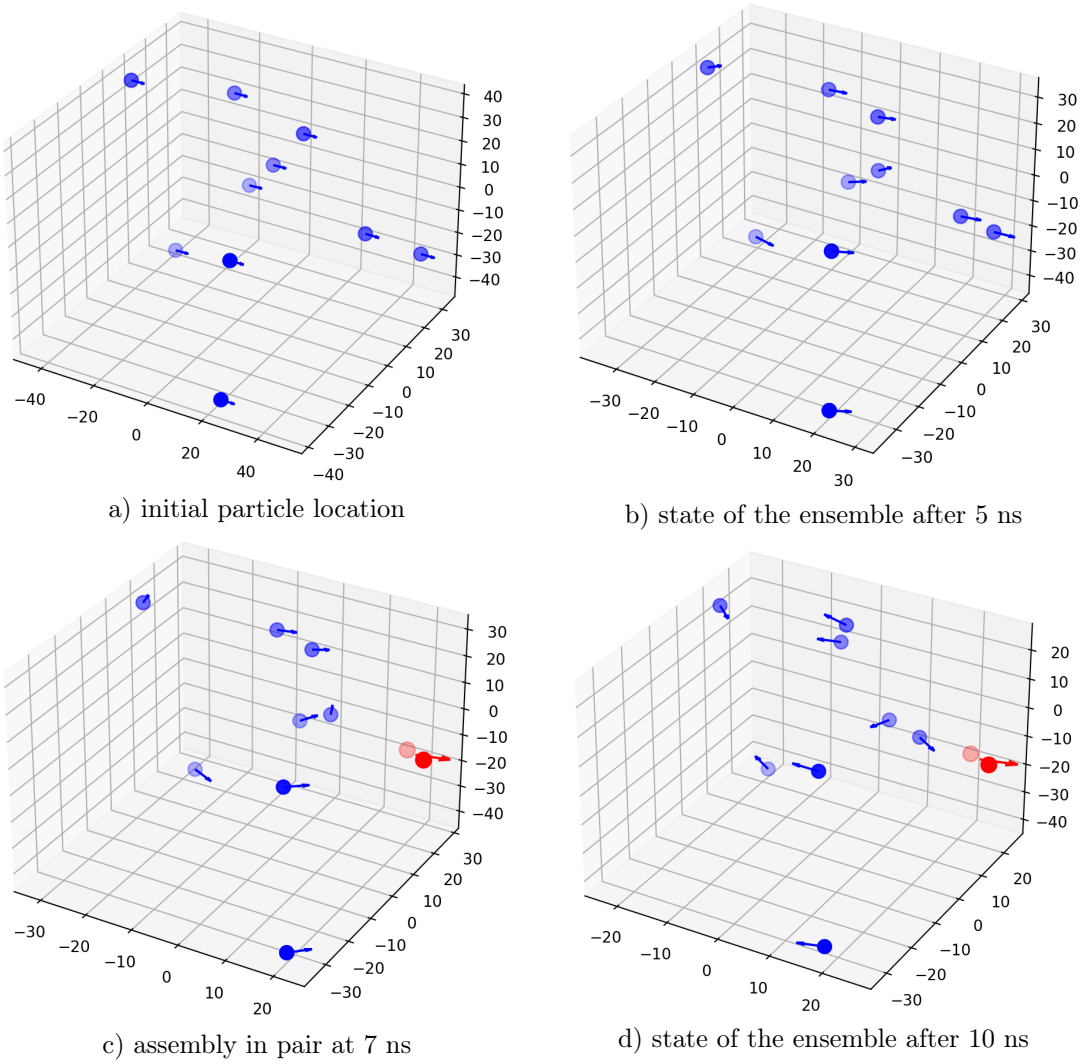

a) initial particle location

b) state of the ensemble after 5 ns

c) assembly in pair at 7 ns

d) state of the ensemble after 10 ns

Fig. 1. An example of modeling the interaction of an ensemble of 10 dipole particles

3. Conclusions and discussion

The article is devoted to a numerical assessment of the possibility of self-assembly of agglomerates from an ensemble of nanoparticles under certain environmental and field parameters. Previously obtained results, described, for example, in [12–14], show that with certain conditions of the environment, self-organization of particles of a given geometry becomes possible. It was shown that the probability of such an assembly depends significantly on the initial distance between particles. The described difficulty can be overcome by changing the concentration of particles, which, in the presence of random fluctuations, leads to the assembly of structures. However, it remained not obvious whether the process stay selective with respect to the field parameters, for which purpose the corresponding computational experiments were carried out. To implement the assessment, a mathematical model was built, described in Section 2.

Briefly describe the obtained results. Figures 2 and 4 show that, regardless of the initial number of particles, the maximum probability of assembly is achieved when the laser is positioned

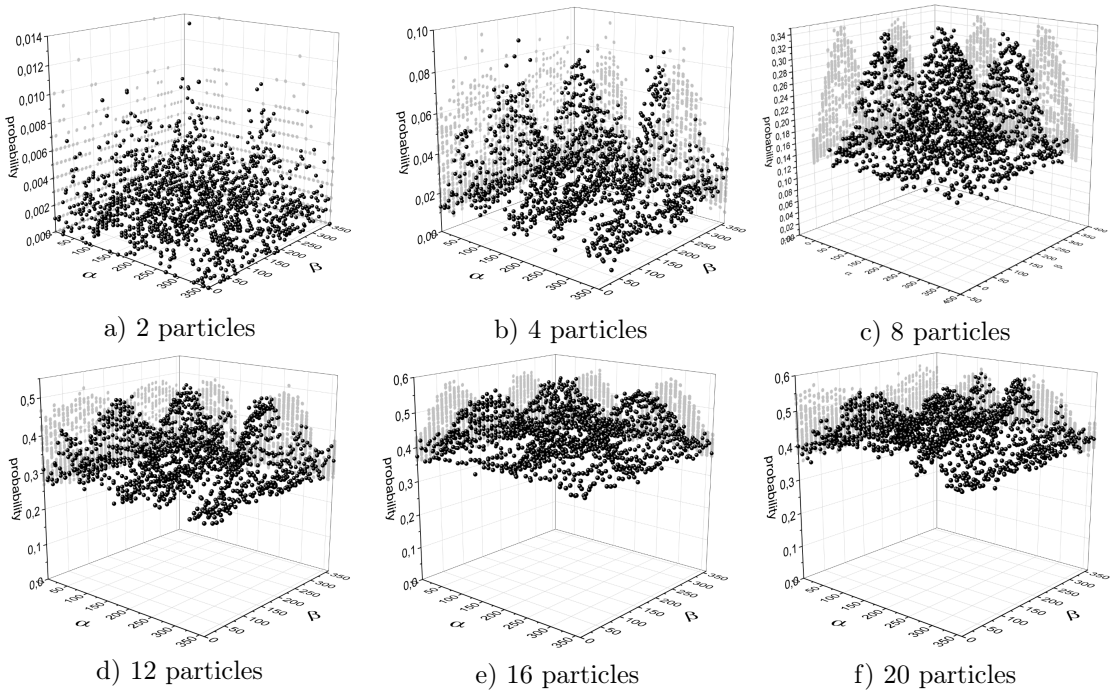

a) 2 particles b) 4 particles c) 8 particles

d) 12 particles e) 16 particles f) 20 particles

Fig. 2. Probability of pair assembly depending on the direction of laser radiation for different numbers of particles in 10 ns

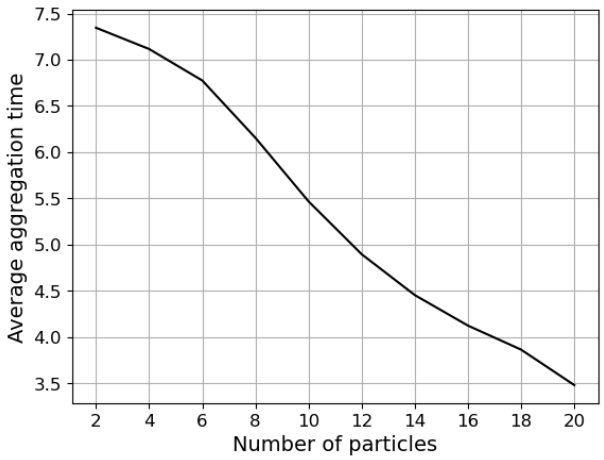

Fig. 3. Dependence of the average assembly time of the first pair of particles on their initial number

along the x axis, while with a different direction of the laser beam, assembly also occurs, but with a lower probability. Note that, due to the symmetry of the process, there should be no obvious advantage in the direction of laser radiation for assembly, that is, at high concentrations and random arrangement of particles, the process should be non-selective in the direction of laser radiation. This phenomenon most likely arises due to the peculiarities of the software modeling, since the initial location of particles along the y, z axes was chosen randomly throughout the entire

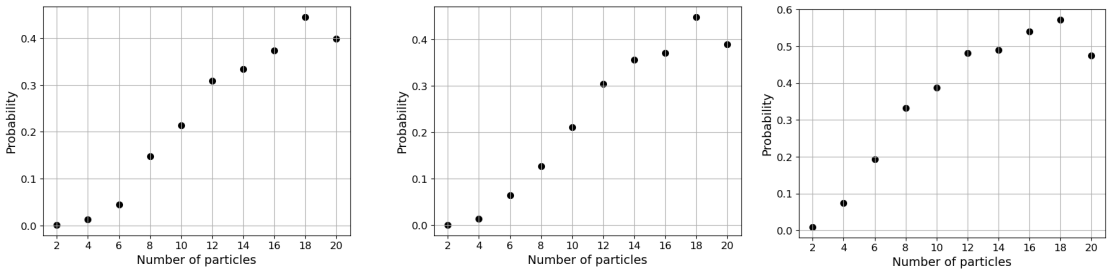

a) $\alpha = 0;\ \beta = 0$ b) $\alpha = 90;\ \beta = 0$ c) $\alpha = 90;\ \beta = 90$

Fig. 4. Probability of structure assembly for different numbers of dipole particles for certain field parameters

computational domain, and along the x axis — in a narrower part of the domain, depending on the number of particles so that nanoparticles occupied the computational space area uniformly. This was done so that when the area was randomly filled, it did not occur that some particles were generated already at the distance at which gluing was performed. Note that from Figures 2 and 4 it is clear that the difference between the maximum and minimum probability of aggregation narrows with increasing particle concentration.

We also note that at the chosen wavelength of the external field, corresponding to the assembly of pairs of particles [12], structures other than pairs are not assembled. In this case, with an increase in the number of particles in the ensemble, the growth rate of the assembly probability slows down, as can be seen from Fig. 4. This can be explained by the superiority of the electrostatic repulsion forces over the electrodynamics interaction forces at a small interparticle gap, as was shown in [13]. Note also that at $N = 20$, the average distance between particles along one axis is of the order of the particles' diameter, where the use of the dipole-dipole approximation becomes incorrect. Fig. 3 shows a similar behavior of the average assembly time of the first pair depending on the initial number of particles.

Thus, the results of computational modeling demonstrated the possibility of self-assembly of pairs from an ensemble of free isolated dipole particles with a high probability exceeding 50% at high concentrations in the volume. At the same time, the problem of the possibility of assembling more complex structures from an ensemble of particles and pairs, as well as taking into account relaxation processes when turning off laser radiation, remains a question for future research.

V. Petrakova thanks the Krasnoyarsk Mathematical Center and financed by the Ministry of Science and Higher Education of the Russian Federation in the framework of the establishment and development of regional Centers for Mathematics Research and Education (Agreement no. 075-02-2024-1378). The studies for A. Tsipotan was carried out within the framework of the state assignment of the Federal State Autonomous Educational Institution of Higher Education "Siberian Federal University" (number FSRZ-2023-0008).

References

[1] M.Nasrollahzadeh, M.Sajadi, M.Sajjadi, Z.Issaabad, An Introduction to Nanotechnology, *Interface Science and Technology*, **28**(2019), 113–143. DOI: 10.1016/B978-0-12-813586-0.00004-3

[2] K.Deng, Zh.Luo, L.Tana, Z.Quan, Self-assembly of anisotropic nanoparticles into functional superstructures, *Chem. Soc. Rev.*, **49**(2020), 6002–6038. DOI: 10.1039/d0cs00541j

[3] P.Pula, A.Leniart, P.Majewski, Solvent-assisted self-assembly of block copolymer thin films, *Soft Matter*, **18**(2022), 4042–4066. DOI: 10.1039/d2sm00439a

[4] P.Kundu, D.Samanta, R.Leizrowice, et al., Light-controlled self-assembly of non-photoresponsive nanoparticles, *Nature Chem*, **7**(2015), 649–652. DOI: 10.1038/nchem.2303

[5] Y.,Dou B.Wang, M.Jin, Y.Yu, G.Zhou, L.Shui, A review on self-assembly in microfluidic devices, *J. of Micromechanics and Microengineering*, **27**(2017), 113002. DOI: 10.1088/1361-6439/aa84db

[6] D.Dordrecht, Nanodiamonds: Applications in Biology and Nanoscale Medicine, London, Springer, 2010.

[7] A.Vul, E.Eydelman, M.Inakuma, E.Osawa, Correlation between viscosity and absorption of electromagnetic waves in an aqueous UNCD suspension, *Diamond Relat. Mater*, **16**(12)(2007), 2023–2028. DOI: 10.1016/j.diamond.2007.08.003.

[8] J.Wang, P.Jiang, Z.Han, L.Qiu, C.Wang, B.Zheng, J.Xia, Fast Self-Assembly Kinetics of Quantum Dots and a Dendrimeric Peptide Ligand, *Langmuir*, **28**(21)(2012), 7962–7966. DOI: 10.1021/la301227r

[9] S.Watanabe, M Y.ino, Y.Ichikawa, M.Miyahara, Spontaneous Formation of Cluster Array of Gold Particles by Convective Self-Assembly, *Langmuir*, **28**(36)(2012), 12982–12988. DOI: 10.1021/la302811y

[10] V.Slabko, G.Khachatryan, A.Aleksandrovsky, Self-organized aggregation of small metal particles controlled by an external light field, *JETP Letters*, **84**(6)(2006), 300–304. DOI: 10.1134/S0021364006180056

[11] V.Slabko, A.Tsipotan, A.Aleksandrovsky, Resonant light-controlled self-assembly of ordered nanostructures, *Photonics and Nanostructures, Fundamentals and Applications*, **10**(4)(2012), 636–643. DOI: 10.1016/j.photonics.2012.06.002

[12] V.Tkachenko, A.Tsipotan, A.Aleksandrovsky, V.Slabko, Three-dimensional model of quantum dots' self-assembly under the action of laser radiation, *Computer Optics*, **41**(4)(2017), 577–580.

[13] A.Tsipotan, M.Gerasimova, V.Slabko, A.Aleksandrovsk, Laser-induced wavelength-controlled self-assembly of colloidal quasi-resonant quantum dots, *Optics Express*, **24**(10)(2016), 11145–11150. DOI: 10.1364/OE.24.011145

[14] V.Kornienko, A.Tsipotan, A.Aleksandrovsky, V.Slabko, Brownian dynamics of the self-assembly of complex nanostructures in the field of quasi-resonant laser radiation, *Photonics and Nanostructures - Fundamentals and Applications*, **35**(2019), 100707. DOI: 10.1016/j.photonics.2019.100707

[15] V.Petrakova, A.Tsipotan, V.Slabko, The mathematical model of quantum dots pair orientation under laser radiation field, *Computer Optics*, **46**(4)(2022), 555–560. DOI: 10.18287/2412-6179-CO-1062

[16] H.Goldstein, Classical Mechanics, MA: Addison-Wesley, 1980.

Компьютерное моделирование самосборки структур из ансамбля наночастиц

Виктория С. Петракова
Институт вычислительного моделирования СО РАН
Красноярск, Российская Федерация
Алексей С. Ципотан
Сибирский федеральный университет
Красноярск, Российская Федерация

Аннотация. Самосборка — один из методов, используемых для создания сложных геометрических структур на наноуровне. Более ранние исследования в этой области показали, что формирование многочастичных структур с использованием этого метода в первую очередь достижимо путем поэтапной сборки, когда новая частица присоединяется к ранее образованному кластеру. Но поэтапное формирование требует дополнительных затрат и может привести к дефектам уже полученных конструкций. Если поэтапная сборка невозможна, то структура может быть сформирована из ансамбля частиц без дополнительного воздействия, но неясно, высока ли вероятность структурообразования и является ли процесс селиктивным. В статье представлена математическая модель, которая демонстрирует, как получить структуру из ансамбля частиц, описывает ее реализацию с помощью программного обеспечения и предлагает результаты вычислительных экспериментов.

Ключевые слова: математическая модель, самосборка наноструктур, вычислительный эксперимент, динамика Ланжевена.

Journal of Siberian Federal University. Mathematics & Physics 2025, 18(2), 209–217

EDN: MGVVRP
УДК 539.3

Physically Nonlinear Deformation of the Shell Using a Three-field FEM

Mikhail Yu. Klochkov*
Volgograd State Technical University
Volgograd, Russian Federation
Anatoly P. Nikolaev†
Volgograd State Agricultural University
Volgograd, Russian Federation
Valeria A. Pshenichkina‡
Volgograd State Technical University
Volgograd, Russian Federation
Olga V. Vakhnina§
Aleksandr S. Andreev¶
Yuri V. Klochkov‖
Volgograd State Agricultural University
Volgograd, Russian Federation

Received 10.08.2024, received in revised form 15.09.2024, accepted 24.10.2024

Abstract. A method has been developed for implementing an algorithm for determining the stress-strain state (SSS) of a thin shell based on the finite element method (FEM) in a three-field formulation under step loading. A quadrangular fragment of the median surface of the thin shell is accepted as the finite element. Nodal unknowns at the loading step used: increments of kinematic quantities (increments of displacements and their derivatives); increments of deformation quantities (increments of deformations and curvatures of the median surface); increments of force values (increments of forces and moments). The approximation of kinematic quantities was carried out using bicubic shape functions based on Hermite polynomials of the third degree, and force and deformation quantities using bilinear functions. To account for the physical nonlinearity of the shell material, the defining equations are used in two versions: the first is the defining equations of the theory of plastic flow and the second is the defining equations based on the proposed hypothesis of proportionality a component of deviators of strain increments and stress increments. The stiffness matrix of the finite element is formed on the basis of a nonlinear Lagrange functional for the loading step, expressing the equality of possible and actual work of given loads and internal forces, with the complementary condition that the actual work of the increments of internal forces is equal to zero on the difference in increments of deformation quantities determined by geometric relations and using approximating expressions. An example of calculation is given using the resulting finite element stiffness matrix.

Keywords: finite element in the three-field formulation, physical nonlinearity of the material, variants of the governing equations, nonlinear Lagrange functional with condition.

*m.klo4koff@yandex.ru https://orcid.org/0000-0001-6751-4629
†anpetr40@yandex.ru https://orcid.org/0000-0002-7098-5998
‡vap_hm@list.ru https://orcid.org/0000-0001-9148-2815
§ovahnina@bk.ru https://orcid.org/0000-0001-9243-7287
¶aandreev.07.1988@gmail.com https://orcid.org/0000-0002-3763-0394
‖klotchkov@bk.ru https://orcid.org/0000-0002-1027-1811

Citation: Yu.V. Klochkov, A.P. Nikolaev, V.A. Pshenichkina, O.V. Vakhnina, A.S. Andreev, M.Yu. Klochkov, Physically Nonlinear Deformation of the Shell Using a Three-field FEM, J. Sib. Fed. Univ. Math. Phys., 2025, 18(2), 209–217. EDN: MGVVRP.

Shell structures are widely used in various areas of engineering — in shipbuilding, aircraft manufacturing, in the creation of chemical engineering objects, in the aerospace industry and in many other branches of engineering. Nonlinear behavior of the material occurs in many areas of the considered thin-walled elements of engineering structures. To determine the stress-strain state in such areas, numerical calculation methods are usually used, among which the most widely used is the FEM in the formulation of the displacement method, when displacements and their derivatives of different orders are taken as nodal unknowns. A disadvantage of the FEM in the displacement method version is the lack of compatibility in terms of deformations at the boundaries between adjacent elements. To overcome this drawback, the FEM began to be used in a mixed version, where kinematic unknowns (displacements and their derivatives) and force unknowns (forces and moments) are used as nodal unknowns, where, when using bilinear approximation, convergence in force parameters at the boundaries of adjacent finite elements was ensured [1, 2].

The finite element method in a mixed version is used in studies of the stability of nonlinearly deformed elastic structures [3–5], as well as in determining the stress-strain state of structures taking into account the physical nonlinearity of the material [6–12]. In elastic-plastic deformation, the total strains are determined by differentiating the strain energy function with respect to stresses. Plastic strain is determined by the difference between the total and elastic strains. Displacements and stresses are taken as unknown quantities. When using the three-field FEM version [13], plastic multipliers are added to the nodal unknowns.

In this paper, a finite element in the form of a quadrangular fragment of the middle surface of a thin shell with three fields of nodal unknowns: kinematic, deformation and force is developed. In the first variant, the equations of the theory of plastic flow are used as the governing equations at the loading step. In the second variant, the governing equations at the loading step are obtained without separating the strain increments into elastic and plastic parts, based on the hypothesis of proportionality of the components of the deviators of strain increments and stress increments. To obtain the stiffness matrix of the finite element at the loading step, a nonlinear Lagrange functional is used with the condition of zero work of the increments of internal forces on the difference in the strain increments determined by geometric relations and found using approximating expressions directly.

1. Geometrical relationships of a thin shell

The position of an arbitrary point M^0 of the mid-surface of the shell is determined by the radius vector

$$\vec{R}^0 = x^m(\theta^\alpha)\vec{i}_m, \tag{1.1}$$

where x^m, $\vec{i}_m$ are the coordinates and orthants of the Cartesian coordinate system; θ^α are the curvilinear coordinates of the point.

The basis vectors of the point M^0 are defined by the expressions

$$\vec{a}^0_\alpha = \vec{R}^0_{,\alpha};\ \vec{a}^0_3 = \frac{\vec{a}^0_1 \times \vec{a}^0_2}{|\vec{a}^0_1 \times \vec{a}^0_2|} = \frac{\vec{a}^0_1 \times \vec{a}^0_2}{\sqrt{a^0}}. \tag{1.2}$$

The derivatives (1.2) are written as components in the same basis

$$\underset{3\times1}{\{\vec{a}^0_{,1}\}} = \underset{3\times3}{[m]}\,\underset{3\times1}{\{\vec{a}^0\}};\quad \underset{3\times1}{\{\vec{a}^0_{,2}\}} = \underset{3\times3}{[n]}\,\underset{3\times1}{\{\vec{a}^0\}}, \tag{1.3}$$

where $\underset{1\times3}{\{\vec{a}^0_{,\alpha}\}}^T = \{\vec{a}^0_{1,\alpha}\ \vec{a}^0_{2,\alpha}\ \vec{a}^0_{3,\alpha}\};\ \underset{1\times3}{\{\vec{a}^0\}}^T = \{\vec{a}^0_1\ \vec{a}^0_2\ \vec{a}^0_3\}$.

The displacement vector of the point M^0 and its derivatives are defined in the basis of the same point

$$\vec{v} = v^\rho\vec{a}^0_\rho + v\vec{a}^0_3;\quad \vec{v}_{,\alpha} = f^\rho_\alpha\vec{a}^0_\rho + f_\alpha\vec{a}^0_3;\quad \vec{v}_{,\alpha\beta} = f^\rho_{\alpha\beta}\vec{a}^0_\rho + f_{\alpha\beta}\vec{a}^0_3, \tag{1.4}$$

where the components $f^\rho_\alpha,\ \ f_\alpha,\ \ f^\rho_{\alpha\beta},\ f_{\alpha\beta}$ are defined using (1.3).

Deformations and curvatures of the median surface at the point M^0 are determined by the relations [14]

$$\Delta\varepsilon_{\alpha\beta} = \frac{1}{2}(\vec{a}^0_\alpha\cdot\vec{v}_{,\beta}+\vec{a}^0_\beta\cdot\vec{v}_{,\alpha});\ \Delta\varkappa_{\alpha\beta} = \frac{1}{2}[\vec{a}^0_\alpha(\vec{a}_{3,\beta}-\vec{a}^0_{3,\beta})+\vec{a}^0_\beta(\vec{a}_{3,\alpha}-\vec{a}^0_{3,\alpha})+\vec{a}^0_{3,\alpha}\cdot\vec{v}_{,\beta}+\vec{a}^0_{3,\beta}\cdot\vec{v}_{,\alpha}]. \tag{1.5}$$

where $\vec{a}_{3,\alpha} = \dfrac{1}{\sqrt{a^0}}(\vec{a}_{1,\alpha}\times\vec{a}_2+\vec{a}_1\times\vec{a}_{2,\alpha});\ \vec{a}_\alpha = \vec{a}^0_\alpha + \vec{v}_{,\alpha};\ \vec{a}_{\alpha,\rho} = \vec{a}^0_{\alpha,\rho} + \vec{v}_{,\alpha\rho}$.

On the basis of (1.5) we can form a matrix relation

$$\underset{6\times1}{\{\Delta\varepsilon\}} = \underset{6\times3}{[L]}\,\underset{3\times1}{\{\Delta U\}}, \tag{1.6}$$

where $\underset{1\times6}{\{\Delta\varepsilon\}}^T = \{\Delta\varepsilon_{11}\ \Delta\varepsilon_{22}\ 2\Delta\varepsilon_{12}\ \Delta\varkappa_{11}\ \Delta\varkappa_{22}\ 2\Delta\varkappa_{12}\};\ \underset{1\times3}{\{\Delta U\}}^T = \{\Delta v^1\Delta v^2\Delta v\}$.

2. Defining equations

In the first variant, the equations of plastic flow theory were used, according to which the incremental strains at an arbitrary point of the shell are composed of elastic and plastic strains

$$\Delta\varepsilon^\zeta_{\alpha\beta} = \Delta\varepsilon^{\zeta e}_{\alpha\beta} + \Delta\varepsilon^{\zeta P}_{\alpha\beta}. \tag{2.1}$$

The elastic strain increments are determined by the relations [15]

$$\Delta\varepsilon^{e\zeta}_{\alpha\beta} = \frac{1}{2\mu}\Delta\sigma_{\alpha\beta} - g_{\alpha\beta}\lambda P_{\Delta\sigma}\frac{3}{2}\frac{1-2\nu}{2\mu}, \tag{2.2}$$

where $\lambda,\ \mu$ are the Lame parameters; ν is the transverse strain coefficient; $P_{\Delta\sigma} = \Delta\sigma_{\rho\tau}g^{\rho\tau}$ — first invariant of the stress increment tensor; $g_{\alpha\beta},\ g^{\alpha\beta}$ — components of the metric tensor.

Plastic strain increments in the flow theory are determined on the basis of the hypothesis of proportionality of plastic strain increments to the components of the stress deviator

$$\Delta\varepsilon^{\zeta P}_{\alpha\beta} = \frac{3}{2\sigma_i}\varphi(\sigma_{\alpha\beta} - \frac{1}{3}g_{\alpha\beta}P_\sigma)\Delta\sigma_i, \tag{2.3}$$

where $\varphi = \dfrac{1}{E_k} - \dfrac{1}{E_1}$; E_1 is the modulus of the initial section of the strain diagram; E_k is the tangent modulus of the strain diagram; $\Delta\sigma_i = \dfrac{\partial\sigma_i}{\partial\sigma_{\rho\tau}}\Delta\sigma_{\rho\tau} = \underset{1\times3}{\{S\}}^T\underset{3\times1}{\{\Delta\sigma\}}$; σ_i — stress intensity; $\underset{1\times3}{\{\Delta\sigma\}}^T = \{\Delta\sigma_{11}\Delta\sigma_{22}\Delta\sigma_{12}\}$.

Based on (2.1), (2.2) and (2.3) a matrix relation is formed

$$\underset{3\times1}{\{\Delta\varepsilon^{\zeta}\}} = \underset{3\times3}{[C_1]}\,\underset{3\times1}{\{\Delta\sigma\}}. \tag{2.4}$$

In the second version of the defining relations, the hypothesis of separation of strain increments into elastic and plastic parts is not used. The defining equations are obtained on the basis of the hypothesis of proportionality of the components of the deviators of strain increments and stress increments

$$\Delta\varepsilon_{\alpha\beta} - \frac{1}{3}g_{\alpha\beta}P_{\Delta\varepsilon} = K(\Delta\sigma_{\alpha\beta} - \frac{1}{3}g_{\alpha\beta}P_{\Delta\sigma}), \tag{2.5}$$

where $K = \dfrac{3}{2E_{x\partial}}$; $P_{\Delta\varepsilon} = P_{\Delta\sigma}\dfrac{1-2\nu}{E}P_{\Delta\sigma}$; $P_{\Delta\sigma} = \Delta\sigma_{\rho\tau}g^{\rho\tau}$ is the first invariant of the stress increment tensor.

Based on (2.5) a matrix relation is formed

$$\underset{3\times1}{\{\Delta\varepsilon^{\zeta}\}} = \underset{3\times3}{[C_2]}\,\underset{3\times1}{\{\Delta\sigma\}}. \tag{2.6}$$

At an arbitrary point M^0 we introduce lines of increments of deformations and curvatures of the medial surface and lines of increments of internal forces and moments of the shell section, the relations between which are determined taking into account (2.4), (2.6) on the basis of the Kirchhoff–Lava hypothesis

$$\underset{6\times1}{\{\Delta S\}} = \underset{6\times6}{[h_\alpha]}\,\underset{6\times1}{\{\Delta\varepsilon\}}. \tag{2.7}$$

where

$$\underset{6\times1}{\{\Delta S\}}^T = \{\Delta N^{11}\ \Delta N^{22}\ \Delta N^{12}\ \Delta M^{11}\ \Delta M^{22}\ \Delta M^{12}\};$$
$$\{\Delta\varepsilon\} = \{\Delta\varepsilon_{11}\ \Delta\varepsilon_{22}\ 2\Delta\varepsilon_{12}\ \Delta\varkappa_{11}\ \Delta\varkappa_{22}\ 2\Delta\varkappa_{12}\}.$$

3. Stiffness matrix of the finite element

The finite element is taken in the form of a curvilinear quadrilateral fragment of the median surface with nodes i, j, k, l. The relations between kinematic, deformation and force parameters for the finite element are regulated at the loading step by a nonlinear variational Lagrangian functional with condition

$$\begin{aligned}\Pi_{LU} = \int\limits_F \left[\underset{1\times6}{\{S\}}^T + \frac{1}{2}\underset{1\times6}{\{\Delta S\}}^T\right]\underset{6\times1}{\{\Delta\varepsilon\}}dF - \int\limits_F \underset{1\times3}{\{\Delta U\}}^T\left[\underset{3\times1}{\{q\}} + \frac{1}{2}\underset{3\times1}{\{\Delta q\}}\right]dF + \\ + \frac{1}{2}\int\limits_F \underset{1\times6}{\{\Delta S\}}^T\left[\underset{6\times1}{\{\Delta\varepsilon^g\}} - \underset{6\times1}{\{\Delta\varepsilon^a\}}\right]dF,\end{aligned} \tag{3.1}$$

where the first expression means the possible and actual work of internal forces on the deformation values of the loading step. The second expression defines the possible and actual work of the given forces on the loading step. The third expression means the actual work of internal forces of the loading step on the difference of deformation values determined by geometrical formulae (through displacements) with subsequent approximation of displacements and deformation values found by their direct approximation.

The following kinematic nodal unknowns in the local $\{\Delta v_y^s\}$ and global $\{\Delta v_y^g\}$ coordinate systems are used for the finite element under consideration

$$\begin{aligned}
\underset{1\times 36}{\{\Delta v_y^s\}^T} &= \{\Delta v^{1i}\dots\Delta v^{1l}\Delta v^{1i}_{,\xi}\dots\Delta v^{1l}_{,\xi}\Delta v^{1i}_{,\eta}\dots\Delta v^{1l}_{,\eta}\Delta v^{2i}\dots\Delta v^{2l}\\
&\Delta v^{2i}_{,\xi}\dots\Delta v^{2l}_{,\xi}\Delta v^{2i}_{,\eta}\dots\Delta v^{2l}_{,\eta}\Delta v^{i}\dots\Delta v^{l}\Delta v^{i}_{,\xi}\dots\Delta v^{l}_{,\xi}\Delta v^{i}_{,\eta}\dots\Delta v^{l}_{,\eta}\};\\
\underset{1\times 36}{\{\Delta v_y^g\}^T} &= \{\Delta v^{1i}\dots\Delta v^{1l}\Delta v^{1i}_{,\alpha}\dots\Delta v^{1l}_{,\alpha}\Delta v^{1i}_{,\beta}\dots\Delta v^{1l}_{,\beta}\Delta v^{2i}\dots\Delta v^{2l}\\
&\Delta v^{2i}_{,\alpha}\dots\Delta v^{2l}_{,\alpha}\Delta v^{2i}_{,\beta}\dots\Delta v^{2l}_{,\beta}\Delta v^{i}\dots\Delta v^{l}\Delta v^{i}_{,\alpha}\dots\Delta v^{l}_{,\alpha}\Delta v^{i}_{,\beta}\dots\Delta v^{l}_{,\beta}\},
\end{aligned} \tag{3.2}$$

between which there is a matrix relation

$$\underset{36\times 1}{\{\Delta v_y^s\}} = \underset{36\times 36}{[T]}\ \underset{36\times 1}{\{\Delta v_y^g\}}. \tag{3.3}$$

The strain $\{\Delta E_y\}^T$ and force nodal unknowns $\{\Delta S_y\}^T$ were taken as follows lines

$$\begin{aligned}
\underset{1\times 24}{\{\Delta E_y\}^T} &= \{\underset{1\times 6}{\{\Delta E_y^i\}^T}\underset{1\times 6}{\{\Delta E_y^j\}^T}\underset{1\times 6}{\{\Delta E_y^k\}^T}\underset{1\times 6}{\{\Delta E_y^l\}^T}\};\\
\underset{1\times 24}{\{\Delta S_y\}^T} &= \{\underset{1\times 6}{\{\Delta S_y^i\}^T}\underset{1\times 6}{\{\Delta S_y^j\}^T}\underset{1\times 6}{\{\Delta S_y^k\}^T}\underset{1\times 6}{\{\Delta S_y^l\}^T}\},
\end{aligned} \tag{3.4}$$

where $\underset{1\times 6}{\{\Delta E_y^\lambda\}^T} = \{\Delta\varepsilon_{11}^\lambda\Delta\varepsilon_{22}^\lambda 2\Delta\varepsilon_{12}^\lambda\Delta\varkappa_{11}^\lambda\Delta\varkappa_{22}^\lambda 2\Delta\varkappa_{12}^\lambda\}$ — a string of strain and curvature increments at the nodal point; $\underset{1\times 6}{\{\Delta S_y^\lambda\}^T} = \{\Delta N^{11\lambda}\Delta N^{22\lambda}\Delta N^{12\lambda}\Delta M^{11\lambda}\Delta M^{22\lambda}\Delta M^{12\lambda}\}$ — line of force and moment increments at the nodal point λ; $\lambda = i,\ j,\ k,\ l$.

The approximation of the increments of displacements of the internal point of the finite element was carried out by the expression

$$\lambda = \underset{1\times 36}{\{\varphi(\xi,\eta)\}^T}\underset{36\times 1}{\{\Delta v_y^s\}}, \tag{3.5}$$

where the symbol λ is Δv^1, Δv^2, Δv^2, Δv; the elements of the function $\{\varphi(\xi,\eta)\}$ are Hermite polynomials of degree three.

On the basis of (3.5) the matrix relations are formed

$$\underset{3\times 1}{\{\Delta U\}} = \underset{3\times 36}{[A]}\ \underset{36\times 1}{\{\Delta v_y^s\}};\quad \underset{6\times 1}{\{\Delta\varepsilon\}} = \underset{6\times 3}{[L]}\underset{3\times 1}{\{\Delta U\}} = \underset{6\times 3}{[L]}\ \underset{3\times 36}{[A]}\ \underset{36\times 1}{\{\Delta v_y^s\}} = \underset{6\times 36}{[B]}\ \underset{36\times 1}{\{\Delta v_y^s\}}. \tag{3.6}$$

Bilinear functions are used for approximation of deformations and forces on the basis of which matrix expressions are formed

$$\underset{6\times 1}{\{\Delta\varepsilon\}} = \underset{6\times 24}{[H]}\ \underset{24\times 1}{\{\Delta E_y\}};\quad \underset{6\times 1}{\{\Delta S\}} = \underset{6\times 24}{[H]}\ \underset{24\times 1}{\{\Delta S_y\}}. \tag{3.7}$$

Taking into account the approximating expressions (2.7), (3.3), (3.6), (3.7), the functional (3.1) is written by the expression

$$\begin{aligned}
\Pi_{LU} = \underset{1\times 36}{\{\Delta U_y^g\}^T}\ \underset{36\times 36}{[T]}^T\int\limits_F \underset{36\times 6}{[B]}\ \underset{6\times 1}{\{S\}}dF + \frac{1}{2}\underset{1\times 36}{\{\Delta\varepsilon_y\}^T}\int\limits_F \underset{36\times 6}{[H]}^T\underset{6\times 6}{[h_\alpha]}\ \underset{6\times 24}{[H]}\,dF\underset{1\times 24}{\{\Delta\varepsilon_y\}}-\\
-\underset{1\times 36}{\{\Delta U_y^g\}^T}\ \underset{36\times 36}{[T]}^T\int\limits_F \underset{36\times 3}{[A]}^T\ \underset{3\times 1}{\{q\}}dF - \frac{1}{2}\underset{1\times 36}{\{\Delta U_y^g\}^T}\ \underset{36\times 36}{[T]}^T\int\limits_F \underset{36\times 3}{[A]}^T\underset{3\times 1}{\{\Delta q\}}dF+\\
+\underset{1\times 24}{\{\Delta S_y\}^T}\frac{1}{2}\int\limits_F \underset{24\times 6}{[H]}^T\ \underset{6\times 36}{[B]}\,dF\ \underset{36\times 36}{[T]}^T\underset{36\times 1}{\{\Delta U_y^g\}} - \underset{1\times 24}{\{\Delta S_y\}^T}\frac{1}{2}\int\limits_F \underset{24\times 6}{[H]}^T\underset{6\times 24}{[H]}\,dF\underset{24\times 1}{\{\Delta\varepsilon_y\}}.
\end{aligned} \tag{3.8}$$

Minimising the functional (3.8) by nodal unknowns leads to the matrix equations

$$\frac{\partial \Pi_{LU}}{\partial \{\Delta\varepsilon_y\}^T} \equiv \underset{24\times24}{[a]}\ \underset{24\times1}{\{\Delta\varepsilon_y\}} - \underset{24\times24}{[d]}\ \underset{24\times1}{[\Delta S_y]} = 0; \tag{3.9}$$

$$\frac{\partial \Pi_{LU}}{\partial \{\Delta S_y\}^T} \equiv \underset{24\times36}{[b]}\ \underset{36\times1}{\{\Delta U_y\}} - \underset{24\times24}{[d]}^T\underset{24\times1}{[\Delta\varepsilon_y]} = 0; \tag{3.10}$$

$$\frac{\partial \Pi_{LU}}{\partial \{\Delta U_y^g\}^T} \equiv \underset{36\times24}{[b]}^T\ \underset{24\times1}{[\Delta S_y]} - \underset{36\times1}{\{f_{\Delta q}\}} + \underset{36\times1}{\{R\}} = 0, \tag{3.11}$$

where $\underset{24\times24}{[a]} = \int\limits_F \underset{24\times6}{[H]}^T\underset{6\times6}{[h_\alpha]}\ \underset{6\times24}{[H]}\,dF$; $\underset{24\times24}{[d]} = \frac{1}{2}\int\limits_F \underset{24\times6}{[H]}^T\ \underset{6\times24}{[H]}\,dF$; $\underset{24\times36}{[b]} = \frac{1}{2}\int\limits_F \underset{24\times6}{[H]}^T\ \underset{6\times36}{[B]}\,dF\ \underset{36\times36}{[T]}$; $\underset{36\times1}{\{f_{\Delta q}\}} = \underset{36\times36}{[T]}\ \int\limits_F \underset{36\times3}{[A]}^T\underset{3\times1}{\{\Delta q\}}dF$; $\underset{36\times1}{\{R\}} = -\ \underset{36\times36}{[T]}\ \int\limits_F \underset{36\times3}{[A]}^T\underset{3\times1}{\{q\}}dF + \underset{36\times36}{[T]}\ \int\limits_V \underset{6\times36}{[B]}\ \underset{36\times1}{\{S\}}dV$.

From the systems (3.9), (3.10) we obtain the relations

$$\underset{24\times1}{\{\Delta\varepsilon_y\}} = \underset{24\times24}{[d]}^{-1}\ \underset{24\times36}{[b]}\ \underset{36\times1}{\{\Delta U_y^g\}};\ \underset{24\times1}{\{\Delta S_y\}} = \underset{24\times24}{[d]}^{-1}\ \underset{24\times24}{[a]}\ \underset{24\times1}{\{\Delta\varepsilon_y\}}. \tag{3.12}$$

By considering (3.12), the stiffness matrix of the finite element is obtained from the system (3.11)

$$\underset{36\times36}{[K]}\ \underset{36\times1}{\{\Delta U_y^g\}} = \underset{36\times1}{\{f_{\Delta q}\}} - \underset{36\times1}{\{R\}}, \tag{3.13}$$

where $\underset{36\times36}{[K]} = \underset{36\times24}{[b]}^T\left[\underset{24\times24}{[d^T]^{-1}}\right]\underset{24\times24}{[a]}\ \underset{24\times24}{[d]}^{-1}\ \underset{24\times36}{[b]}$ — finite element stiffness matrix, which is used to form the shell stiffness matrix.

After determining the kinematic nodal unknowns of the shell, the deformation and force nodal unknowns are determined by (3.12).

4. Calculation example

As an example, the calculation of a shell with a medial surface in the form of a truncated ellipsoid of rotation loaded with internal pressure of intensity $q = 6$ MPa. Due to axial symmetry, the ellipsoid was modelled by a ribbon of discretisation elements oriented along the shell meridian. The left end of the shell was rigidly clamped, the right end was free of clamping (Fig. 1). The initial data had the following values: ellipsoid parameters $a = 1.3$ m; $b = 0.9$ m; thickness $h = 0.02$ m; axial coordinate varied in the range $0 \leqslant x \leqslant 1.2$ m. Mechanical characteristics of the shell material: duralumin alloy $E = 7.49 \cdot 10^4$ MPa; $\nu = 0.32$. The yield strength of the material is $\sigma_T = 200$ MPa. The deformation diagram was modelled by a two-link broken line with linear hardening defined by the dependence

$$\sigma_i = 200 + 18087(\varepsilon_i - 0,0023496). \tag{4.1}$$

The calculations were performed with control of the convergence of the computational process both by the number of sampling elements and by the number of loading steps. Tab. 1 shows the results of ellipsoidal shell calculation with the number of sampling elements equal to 200 and different numbers of loading steps. The table shows the values of normal stresses in the support and free ends of the shell on the inner σ^{in}, outer σ^{out} and midline σ^{midl} surfaces of the shell. Analyses of the tabular data allow us to conclude that the computational process is stable as the number of loading steps increases. Due to the unloaded right end of the ellipsoid, σ_{xx}^{midl} must be

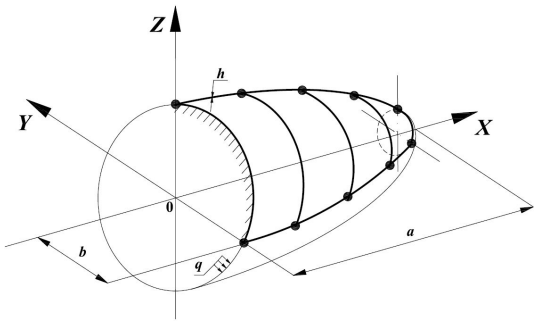

Fig. 1. Calculation diagram of an ellipsoidal shell

equal to zero. As Tab. 1 shows, the numerical values of σ_{xx}^{midl} are quite close to zero. The ring stresses σ_{tt}^{midl} at the free end of the ellipsoid can be calculated using the Laplace formula

$$\frac{\sigma_{xx}}{R_1} + \frac{\sigma_{tt}}{R_t} = \frac{q}{t}, \tag{4.2}$$

where $R_1,\ R_t$ are the radii of the principal curvatures.

Given that at the free end $\sigma_{xx} = 0$, the analytical value of σ_{tt} can be obtained from (4.2).

$\sigma_{tt} = \dfrac{q}{t} R_t = \dfrac{6}{0.02} \cdot 0.6708 = 201.2$ MPa. Comparing the analytical value of σ_{tt}, presented in the rightmost column of Table 1, with the numerical value of σ_{tt}^{midl}, we can conclude that the calculation error $\delta = 3.38\%$ is within acceptable limits when performing engineering calculations.

Table 1. Numerical values of stresses depending on the number of loading steps

Point coordinates, x, m	σ, MPa	Number of loading steps				Analytical solution
		12	22	32	42	
0,00	σ_{xx}^{in}	322.6	321.1	319.8	320.1	—
	σ_{xx}^{out}	–230.4	–228.4	–227.2	–227.9	—
	σ_{xx}^{midl}	168.7	167.0	165.1	165.5	—
1,20	σ_{xx}^{in}	0.039	0.025	0.032	0.033	—
	σ_{xx}^{out}	0.041	0.030	0.036	0.036	—
	σ_{xx}^{midl}	0.036	0.023	0.030	0.030	0,00
	σ_{tt}^{in}	200.7	199.5	200.1	200.2	—
	σ_{tt}^{out}	189.5	188.3	188.9	1889	—
	σ_{tt}^{midl}	195.0	193.8	194.4	194.4	201.2

Conclusion

In the developed FEM algorithm in the three-field variant, when using bilinear approximations for deformation and force quantities to be sought, their coherence is ensured not only at the nodes of adjacent finite elements, but also along their boundaries. In addition, the developed algorithm can control the location of an internal point with coordinates $\varepsilon_i,\ \sigma_i$ on the deformation diagram, which opens up the possibility of finding unloading zones under complex loading of shell structures.

References

[1] Yu.Klochkov, A.Nikolaev, V.Pshenichkina, O.Vakhnina, M.Klochkov, Three-field fem for analysis of thin elastic shells, *Magazine of Civil Engineering*, **17**(2024), no. 3(127), 12710.

[2] Yu.V.Klochkov, V.A.Pshenichkina, A.P.Nikolaev, S.S.Marchenko, O.V.Vakhnina, M.Yu.Klochkov, Calculation of shells of revolution with the use of a mixed fem with a vector approximation procedure, *Journal of Machinery Manufacture and Reliability*, **53**(2024), no. 1, 10–21. DOI: 10.1134/S1052618824010059

[3] M.Cervera, M.Chiumenti, R.Codina, Mixed stabilized finite element methods in nonlinear solid mechanics: Part I: Formulation, *Comput. Meth. Appl. Mech. Eng.*, **199**(2010), no. 37-40, 2559–2570. DOI: 10.1016/j.cma.2010.04.006

[4] M.Cervera, M.Chiumenti, R.Codina, Mixed stabilized finite element methods in nonlinear solid mechanics: Part III: Compressible and incompressible plasticity, *Comput. Meth. Appl. Mech. Eng.*, **285**(2015), no. 1, 752–775. DOI: 10.1016/j.cma.2014.11.040

[5] N.A.Nodargi, P.Bisegna, A novel high-performance mixed membrane finite element for the analysis of inelastic structures, *Comput. Struct.*, **182**(2017), 337–353.
DOI: 10.1016/j.compstruc.2016.10.002

[6] F.S.Liguori, A.Madeo, G.Garcea, A mixed finite-element formulation for the elasto-plastic analysis of shell structures, *Materials Research Proceedings*, **26**(2023), 227–232.

[7] F.S.Liguori, A.Madeo, G.Garcea, A dual decomposition of the closest point projection in incremental elasto-plasticity using a mixed shell finite element, *International Journal for Numerical Methods in Eng.*, **123**(2022), 6243–6266.

[8] A.Bilotta, L.Leonetti, G.Garcea, An algorithm for incremental elastoplastic analysis using equality constrained sequential quadratic programming, *Comput. Struct.*, **102-103**(2012), 97–107.

[9] A.Bilotta, G.Garcea, L.Leonetti, A composite mixed finite element model for the elasto-plastic analysis of 3D structural problems, *Finite Elcm. Anal. Des.*, **113**(2016), 43–53.
DOI: 10.1016/j.finel.2016.01.002

[10] L.A.M.Mendes, L.M.S.S.Castro, Hybrid-mixed stress finite element models in elastoplastic analysis, *Finite Elem. Anal. Des.*, **45**(2009), no. 12, 863–875.
DOI: 10.1016/j.finel.2009.06.021

[11] N.A.Nodargi, P.Bisegna, State update algorithm for isotropic elastoplasticity by incremental energy minimization, *Int. J. Numer. Methods Eng.*, **105**(2015), no. 3, 163–196.
DOI: 10.1002/nme.4966

[12] N.A.Nodargi, E.Artioli, F.Caselli, P.Bisegna, State update algorithm for associative elastic-plastic pressure-insensitive materials by incremental energy minimization, *Fracture and Structural Integrity*, **29**(2014), 111–127. DOI: 10.3221/IGF-ESIS.29.11

[13] A.Bilotta, L.Leonetti, G.Garcea, Three field finite elements for the elastoplastic analysis of 2D continua, *Finite Elem. Anal. Des.*, **47**(2011), no. 10, 1119–1130.
DOI: 10.1016/j.finel.2011.05.002

[14] A.Sh.Dzhabrailov, A.P.Nikolaev, Y.V.Klochkov, N.A.Gureeva, Accounting for displacement as a solid in the FEM algorithm for the calculation of shells of rotation, *Izvestia of the Russian Academy of Sciences. Mechanics of Solid State*, **6**(2023), 23–38 (in Russian).

[15] L.I.Sedov, Mechanics of Continuous Medium, Moscow, Nauka, Vol. 1, 1994 (in Russian).

Физически нелинейное деформирование оболочки при использовании трехпольного МКЭ

Михаил Ю. Клочков
Волгоградский государственный технический университет
Волгоград, Российская Федерация
Анатолий П. Николаев
Волгоградский государственный аграрный университет
Волгоград, Российская Федерация
Валерия А. Пшеничкина
Волгоградский государственный технический университет
Волгоград, Российская Федерация
Ольга В. Вахнина
Александр С. Андреев
Юрий В. Клочков
Волгоградский государственный аграрный университет
Волгоград, Российская Федерация

Аннотация. Разработана методика реализации при шаговом нагружении алгоритма определения напряженно-деформированного состояния (НДС) тонкой оболочки на основе метода конечных элементов (МКЭ) в трехпольной формулировке. В качестве конечного элемента принят четырехугольный фрагмент срединной поверхности тонкой оболочки. Узловыми неизвестными на шаге нагружения использованы: приращения кинематических величин (приращения перемещений и их производных); приращения деформационных величин (приращения деформаций и искривлений срединной поверхности); приращения силовых величин (приращения усилий и моментов). Аппроксимация кинематических величин осуществлялась с использованием бикубических функций формы на основе полиномов Эрмита третьей степени, а величин силовых и деформационных — с использованием билинейных функций. Для учета физической нелинейности материала оболочки использованы определяющие уравнения в двух вариантах: первый — определяющие уравнения теории пластического течения и второй — определяющие уравнения на основе предложенной гипотезы о пропорциональности компонент девиаторов приращений деформаций и приращений напряжений. Матрица жесткости конечного элемента сформирована на основе нелинейного функционала Лагранжа для шага нагружения, выражающего равенство возможных и действительных работ заданных нагрузок и внутренних усилий, с дополняющим условием равенства нулю действительной работы приращений внутренних усилий на разности приращений деформационных величин, определяемых геометрическими соотношениями и с использованием аппроксимирующих выражений. С использованием полученной матрицы жесткости конечного элемента дается пример расчета.

Ключевые слова: конечный элемент в трехпольной формулировке, физическая нелинейность материала, варианты определяющих уравнений, нелинейный функционал Лагранжа с условием.

EDN: NKANAC
УДК 519.3

Analysis of the Influence of Porosity and Non-Uniform Polarization of Piezoelectric Ceramics on the Efficiency of a Bridge Transducer as Sensor and Actuator

Andrey V. Nasedkin*
Anna A. Nasedkina†
Southern Federal University
Rostov on Don, Russian Federation

Received 10.09.2024, received in revised form 22.10.2024, accepted 26.12.2024

Abstract. Flexible piezoelectric transducers, and the transducers with bridge shaped end-caps in particular, have found wide application as acoustic emitters and energy harvesting devices. In this paper, we investigate the possibilities of using porous piezoceramics as an active element of a bridge transducer. Particular attention is paid to taking into account the non-uniform polarization of porous piezoceramics with the use of simplified models. A finite element analysis of the bridge piezoelectric transducer under steady-state oscillations is performed in resonant and non-resonant modes of its operation. It is found that the use of porous piezoceramics increases the efficiency of the transducer during oscillations near the first frequency of electrical antiresonance.

Keywords: electroelasticity, bridge piezoelectric transducer, porous piezoceramics, non-uniform polarization, resonant frequency, sensor, actuator, finite element method.

Citation: A.V. Nasedkin, A.A. Nasedkina, Analysis of the Influence of Porosity and Non-Uniform Polarization of Piezoelectric Ceramics on the Efficiency of a Bridge Transducer as Sensor and Actuator, J. Sib. Fed. Univ. Math. Phys., 2025, 18(2), 218–228. EDN: NKANAC.

Piezoelectric transducers are widely used in various technical devices. In order to improve their efficiency for specific applications, it is necessary to ensure high values of individual parameters or quality factors. This paper presents the results of the study of a piezoelectric transducer consisting of a piezoelectric ceramic plate polarized by thickness with two metal bridge-shaped end-caps. Here, for the initial device we consider a bridge piezoelectric transducer with a plate made of dense piezoelectric ceramics, which was previously studied in [1].

As modern research has shown, bridge transducers can be effectively used as part of energy havesting devices [2–5], current sensors [6] and emitters. Various types of bridge transducers have been analyzed in [7–11], etc. Original approaches for optimizing the bridge transducer design were proposed in [12, 13].

Another type of piezoelectric transducers similar to bridge transducers are axisymmetric transducers, which are also called Cymbal Transducers, because their end-caps are shaped like cymbal plates. Cymbal transducers have been studied in more details than bridge transducers. In practical applications they are actively used as sensors or sources of renewable energy [2, 4], as well as actuators or emitters [14].

*avnasedkin@sfedu.ru https://orcid.org/0000-0002-3883-2799
†aanasedkina@sfedu.ru https://orcid.org/0000-0003-1258-4886

Improvement of the characteristics of piezoelectric devices can be achieved by using piezoelectric composites as active materials of transducers. In particular, it is possible to use porous piezoceramics, that are more compliant and have lower acoustic impedance, but at the same time have some high electromechanical coupling coefficients with the values close to those of dense piezoceramics. However, for porous piezoceramics, the influence of the inhomogeneity of the polarization field in the vicinity of the pores on its effective properties has not been sufficiently studied yet. Precise application of porous piezoceramics also requires an account of the porosity structure microfeatures and optimization of individual material constants, geometry and boundary conditions for a specific device.

Some of the above issues were investigated in [16–18] for Cymbal transducers with a disk made of porous piezoceramics. In this paper, the efficiency of using porous piezoceramic materials for a bridge piezoelectric transducer is studied in a similar manner. For the active element materials we consider conventional dense piezoceramics and porous piezoceramics PZT-4 with the effective moduli calculated using uniform and non-uniform polarization models [19].

1. General problem statement

1.1. Geometrical and physical data

Let us consider a bridge transducer with the geometric parameters adopted in [1]. This transducer consists of a piezoceramic plate of length $L = 12.7$ (mm), width $b = 12.7$ (mm), and thickness $h_p = 1$ (mm). The end surfaces of the plate relative to its thickness are covered with electrodes, and the piezoceramic material of the plate is polarized by thickness. On some of the end surfaces there are metal bridge caps of width b equal to the width of the plate. Each cover has a thickness $h_c = 0.3$ (mm) and a maximum lift height $h_m = 0.35$ (mm). The maximum lift surfaces are flat and have length $l_m = 3$ (mm), and the sections of the bridge caps connected to the plate have lengths $l_c = 1.85$ (mm).

This geometry, as well as the external influences and fixing conditions adopted further, make it possible to consider one fourth of the device with the corresponding symmetry conditions during finite element modeling. In Fig. 1, the symmetry surface of the fourth part of the transducer is shown in the Oxz plane, related to the Cartesian coordinate system $Oxyz$. Along the Oy axis, all elements of the device quarter occupy the region $-b/2 \leqslant y \leqslant 0$.

For metal overlays, we will accept the properties of brass as an elastic isotropic material with density of $\rho_m = 8400$ (kg/m^3), Young's modulus $E_m = 9.5 \cdot 10^{10}$ (N/m^2) and Poisson's ratio $\nu_m = 0.35$.

The central plate of the transducer is made of PZT-4 piezoceramics with the main direction of polarization along the thickness. For PZT-4 piezoceramics, we will accept different material properties. We will consider dense piezoceramics with stiffness moduli $c^E_{\alpha\beta}$, piezoelectric moduli $e_{i\beta}$ and dielectric permittivity coefficients ε^S_{ij}, as well as porous piezoceramics with effective stiffness moduli $c^{E\,\mathrm{eff}}_{\alpha\beta}$, effective piezomoduli $e^{\mathrm{eff}}_{i\beta}$ and effective permittivity moduli $\varepsilon^{S\,\mathrm{eff}}_{ij}$. Here and below, Greek indices may vary from 1 to 6, and Latin indices vary from 1 to 3: $\alpha, \beta = 1, 2, \ldots, 6$, $i, j = 1, 2, 3$. For the moduli of dense piezoceramics, we use the standard notations of the theory of piezoelectricity (electroelasticity) [20]. In particular, the superscripts indicate at what constant fields the material moduli of electroelasticity used in various constitutive relations were determined. Thus, the superscript E means the constancy of the electric field, D means the constancy of the electric induction field, S means the constancy of the strain fields, and T means

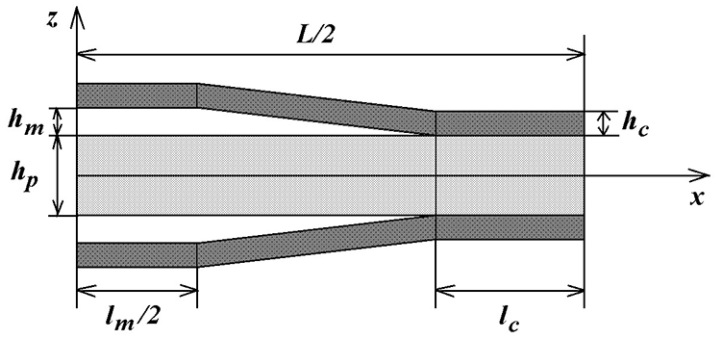

Fig. 1. Geometry of the longitudinal cross-section of the bridge transducer for $x \geqslant 0$, $y = 0$

the constancy of the mechanical stress fields.

The moduli of the porous piezoceramics were determined from the initial moduli of the dense piezoceramics as a result of numerical calculations using the effective moduli method in the ANSYS finite element package. For this purpose, a cubic representative volume V was used, regularly divided into n_e^3 piezoelectric cubic finite elements, where n_e is the number of finite elements along a separate axis of the Cartesian coordinate system. Based on a given percentage of porosity p, $n_p = [pn_e^3/100]$ elements were randomly selected from among these elements, where [...] is the integer part of the number, and these elements were assigned the material properties of the pores, i.e. negligibly small elastic stiffnesses, piezomoduli and permittivities equal to the permittivity of vacuum $\varepsilon_0 = 8.85 \cdot 10^{-12}$ (F/m). The number n_e was determined by the convergence of the results of calculations of effective moduli, and as a result of numerical experiments it was taken to be equal to 45.

Four sets of material properties were used to calculate the piezoelectric transducer. In the basic variant (variant 0), the piezoelectric ceramics were assumed solid and uniformly polarized along the Oz axis. In variant 1, porous piezoceramics were considered with moduli calculated for a piezoelectric ceramic matrix uniformly polarized along the Oz axis.

In variant 2, the finite element method was used to solve the problem of dielectric electrostatics, simulating the polarization process of porous piezoceramics in a simplified formulation, and the polarization vectors $\mathbf{P}^{em}$ were found for each finite element with number m. Then, the heterogeneity of the properties of the piezoceramic matrix was determined by element coordinate systems in which the z^{em} axis for individual finite element with number m was directed along the vector $\mathbf{P}^{em}$. In this variant, the moduli were considered equal to the moduli of dense ceramics $c^E_{\alpha\beta}$, $e_{i\beta}$, ε^S_{ij}, but in the elementcoordinate system $Ox^{em}y^{em}z^{em}$, and then they were recalculated to the values $c^{Eem}_{r\alpha\beta}$, $e^{em}_{ri\beta}$, ε^{Sem}_{rij} in the global coordinate system in accordance with the formulas for transforming the components of the tensors when rotating the coordinate systems.

Finally, in the most realistic version 3, the properties of the piezoceramic matrix for each finite element varied linearly between the corresponding values of the properties of unpolarized ceramics ($s^{np}_{\alpha\beta}$, $d^{np}_{i\beta} = 0$, ε^{np}_{ij}) and the properties of polarized ceramics $s^{Eem}_{r\alpha\beta}$, $d^{em}_{ri\beta}$, ε^{Tem}_{ij}, in accordance with the formulas

$$s^{Eem}_{\alpha\beta} = (1-\chi_p)s^{np}_{\alpha\beta} + \chi_p s^{Eem}_{r\alpha\beta}, \quad d^{em}_{i\beta} = \chi_p d^{em}_{ri\beta}, \quad \varepsilon^{Tem}_{ij} = (1-\chi_p)\varepsilon^{np}_{ij} + \chi_p \varepsilon^{Tem}_{rij}, \tag{1}$$

$$\chi_p = \begin{cases} |\mathbf{P}^{em}|/P_{sat} & |\mathbf{P}^{em}| \leqslant \kappa_p P_{sat}, \\ \kappa_p & |\mathbf{P}^{em}| > \kappa_p P_{sat}. \end{cases} \tag{2}$$

Here $s^{np}_{\alpha\beta}$, $s^{Eem}_{r\alpha\beta}$ are the components of the compliance matrices of unpolarized and polarized ceramics, which are inverse to the corresponding stiffness matrices with components $c^{np}_{\alpha\beta}$ and $c^{Eem}_{r\alpha\beta}$, $\varepsilon^{np}_{ij} = \varepsilon^{np}$, $d^{em}_{ri\beta} = e^{em}_{ri\zeta} s^{Eem}_{r\zeta\beta}$, $\varepsilon^{Tem}_{rij} = \varepsilon^{Sem}_{rij} + d^{em}_{ri\zeta} e^{em}_{rj\zeta}$, $P_{sat} = (\varepsilon^{np} - \varepsilon_0) E_c$, E_c is the value of the polarization field from the electrostatics problem simulating the polarization process, κ_p is the parameter determining the possibility of "superpolarization", which we set equal to 1.2. Further, after finding the moduli $s^{Eem}_{r\alpha\beta}$, $d^{em}_{ri\beta}$, ε^{Tem}_{rij} from (1), (2), it is easy to go to the moduli $s^{Eem}_{r\alpha\beta}$, $d^{em}_{ri\beta}$, ε^{Tem}_{rij} from the main calculation constitutive relations using the corresponding formulas.

The technique for finding effective moduli from solutions of static boundary value problems of electroelasticity with linear essential boundary conditions for displacements and electric potential for homogenous polarized piezoceramics is well known and has been described in many papers. For non-uniformly polarized piezoceramics, we relied on the approaches presented in [19]. However, we supplemented the model $s^E d\varepsilon^T$ with (1), (2) when finding the moduli of unpolarized ceramics by Hill's averaging not only the original moduli $c^E_{\alpha\beta}$, ε^S_{ij}, but also the moduli $c^D_{\alpha\beta}$, ε^T_{ij}, as well as by restricting the value of κ_p in the "superpolarization" model. The results of calculations of the complete set of effective moduli of porous piezoceramics PZT-4 for three variants considering heterogeneities are given in Tab. 1.

Table 1. Initial moduli of dense piezoceramics PZT-4 and effective moduli of porous piezoceramics for three polarization models ($c^{E\,\mathrm{eff}}_{\alpha\beta} \cdot 10^{10}$ in N/m^2, $e_{i\beta}$ in C/m^2, $\tilde{\varepsilon}^{S\,\mathrm{eff}}_{ii} = \varepsilon^{S\,\mathrm{eff}}_{ii}/\varepsilon_0$)

No.	p (%)	$c^{E\,\mathrm{eff}}_{11}$	$c^{E\,\mathrm{eff}}_{12}$	$c^{E\,\mathrm{eff}}_{13}$	$c^{E\,\mathrm{eff}}_{33}$	$c^{E\,\mathrm{eff}}_{44}$	e^{eff}_{31}	e^{eff}_{33}	e^{eff}_{15}	$\tilde{\varepsilon}^{S\,\mathrm{eff}}_{11}$	$\tilde{\varepsilon}^{S\,\mathrm{eff}}_{33}$
0	0	13.90	7.78	7.43	11.5	2.56	–5.2	15.1	12.7	730	635
1	10	11.69	6.32	5.98	9.57	2.22	–4.24	13.41	10.92	657.5	0.85
1	20	9.53	4.92	4.61	7.73	1.88	–3.30	11.68	9.15	583.8	565.8
1	30	7.45	3.61	3.34	5.95	1.55	–2.40	9.86	7.40	510.0	427.4
1	40	5.47	2.45	2.24	4.35	1.21	–1.56	7.98	5.66	431.2	358.5
1	50	3.69	1.49	1.34	2.88	0.88	–0.83	5.89	3.99	352.3	288.4
2	10	11.69	6.32	5.95	9.54	2.22	–4.12	13.45	10.90	653.4	566.3
2	20	9.56	4.92	4.56	7.66	1.87	–3.07	11.74	9.10	576.0	497.5
2	30	7.41	3.60	3.26	5.87	1.53	–2.04	9.96	7.30	496.9	428.5
2	40	5.42	2.42	2.14	4.26	1.19	–1.14	8.06	5.55	416.2	359.2
2	50	3.64	1.47	1.26	2.84	0.86	–0.40	6.02	3.88	333.8	288.9
3	10	11.66	6.28	5.96	9.56	2.23	–3.83	13.53	10.69	666.6	567.9
3	20	9.48	4.85	4.55	7.69	1.90	–2.60	11.78	8.71	602.4	504.0
3	30	7.34	3.50	3.26	5.94	1.57	–1.56	9.92	6.79	531.0	441.3
3	40	5.36	2.31	2.13	4.32	1.24	–0.72	7.86	4.95	455.9	376.8
3	50	3.58	1.37	1.25	2.91	0.90	–0.13	5.66	3.26	371.5	308.9

As can be seen from Tab. 1, polarization models have the least effect on the effective elastic moduli, and the greatest effect on the effective piezoelectric moduli, especially on the transverse piezoelectric modulus e^{eff}_{31}.

1.2. System of equations for harmonic vibrations

For a bridge transducer, we will use the equations of electroelasticity, which in the steady-state oscillation mode $\exp(j\omega t)$ with frequency $f = \omega/(2\pi)$ for the amplitude values of the displacements $u_k(\mathbf{x})$ and the electric potential $\varphi(\mathbf{x})$ we will represent in the form

$$\sigma_{kl,l} + \rho\omega^2 u_k = 0, \quad D_{k,k} = 0, \tag{3}$$

$$T_\alpha = (1 + jQ_d^{-1})c^E_{\alpha\beta}S_\beta - e_{k\alpha}E_k, \quad D_k = e_{k\beta}S_\beta + \varepsilon^S_{kl}E_l, \tag{4}$$

$$\varepsilon_{kl} = (u_{k,l} + u_{l,k})/2, \quad E_k = -\varphi_{,k}. \tag{5}$$

Here σ_{kl} are the components of the stress tensor; ε_{kl} are the components of the strain tensor; $\{T_1, T_2, T_3, T_4, T_5, T_6\} = \{\sigma_{11}, \sigma_{22}, \sigma_{33}, \sigma_{23}, \sigma_{13}, \sigma_{12}\}$, $\{S_1, S_2, S_3, S_4, S_5, S_6\} = \{\varepsilon_{11}, \varepsilon_{22}, \varepsilon_{33}, 2\varepsilon_{23}, 2\varepsilon_{13}, 2\varepsilon_{12}\}$; D_k are the components of the electric induction vector; E_k are the components of the electric field strength vector; ρ is the density; Q_d is the mechanical quality factor for the frequency-independent method of accounting for damping; j is the imaginary unit.

For porous piezoceramics in (3) the density must be recalculated considering the porosity, and in (4) it is necessary to use effective moduli.

Equations (3)–(5) for mechanical fields with $e_{k\beta} = 0$ are equations of elasticity theory with the same method of taking into account damping, and therefore they also describe the vibrations of elastic end-caps in a piezoelectric transducer.

Next, we will consider two types of bridge transducers for different applications. Transducer type A is focused on the problems of energy harvesting from mechanical low-frequency pressures, and transducer type B must operate in resonant mode and generate acoustic waves in the external medium under electrical effects. The problems for these two types of transducers differ in the fixing conditions and external influences.

2. Bridge transducer type A

In the transducer of type A the lower plateau $z = -H$ ($H = h_c + h_m + h_p/2$) was rigidly fixed, and the upper plateau $z = H$ was subjected to pressure oscillating with frequency f of amplitude $p = F/(l_m b)$, where F is the total force. The electroded boundaries of the piezoceramic plate are equipotential, i.e. $\varphi = \Phi_i$, $z = \pm h_p/2$, where the electric potential values Φ_i are constant for each of the two electrodes. These electrodes in transducer A were connected by an external electric circuit with resistance R. The overall quality factor Q_d of the entire device was taken to be equal to 1000.

For the transducer A, the steady-state oscillation mode in the non-resonant frequency range $f \in (0, 2]$ (Hz) was considered, which corresponds to its use as an energy harvesting device. When the transducer was loaded with pressure with a total force $F = 800$ (N), the maximum induced electric potential difference ΔV between the electrodes was determined when they were connected by an electric circuit with a resistance $R = 2$ (kΩ). The results of calculating problem (3)–(5) for the induced electric potential difference and axial displacement at the upper central point of the transducer $\{0, 0, H\}$ depending on the porosity are shown in Fig. 2. Here and below, curves with numbers 1–3 are constructed for porous piezoceramics with effective moduli from the corresponding variants 1–3 of the polarization models.

As can be seen from Fig. 2 (a), the use of porous piezoceramics in the transducer plate with bridge end-caps demonstrates the worst properties to preserve energy compared to dense. Accounting for the heterogeneity of the polarization field slightly reduces the values of the induced difference in the electrical potential compared to the model of homogeneous polarization. Meanwhile, the amplitudes of axial displacements $|u_z|$ at the upper center point of the transducer $\{0, 0, H\}$ increase with the growth of porosity (Fig. 2 (b)), which is quite natural, since porous material is more supple than the corresponding solid. Polarization models practically do not affect the amplitude of maximum axial displacements.

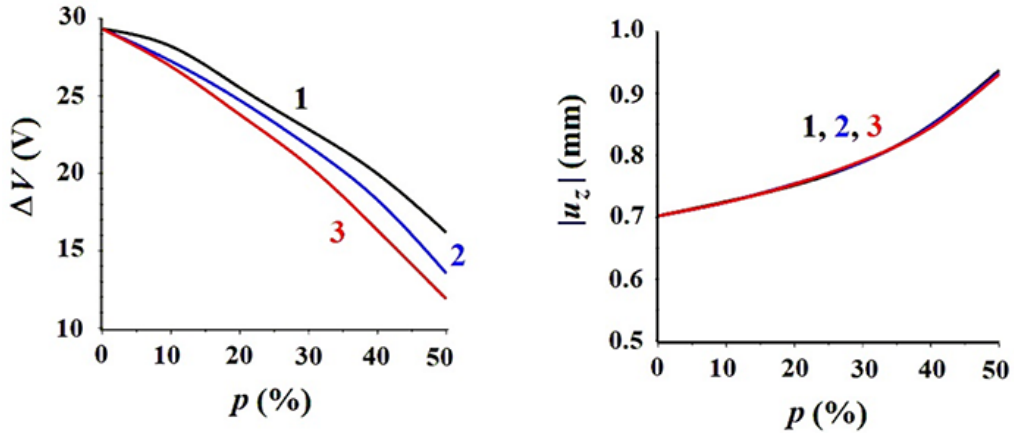

(a) (b)

Fig. 2. Induced electric potential difference (a) and axial displacement at the top central point (b) for transducer A made from different variants of porous piezoceramics

3. Bridge transducer type B

In the transducer B almost all external surfaces are considered stress-free, but at the extreme edges of the plate $x = L/2$, $y = \pm h_p/2$ the axial displacement $u_z = 0$ is fixed. We will consider two cases of generating acoustic vibrations in the transducer. In the first case, the oscillations are generated by applying a difference in electrical potentials $\Delta V = |\Phi_2 - \Phi_1|$ between the electrodes $\Gamma_{\varphi 2} = \{z = h_p/2\}$ and $\Gamma_{\varphi 1} = \{z = -h_p/2\}$. In the second case, the external influence is the electric current I or the charge $Q = -\int\limits_{\Gamma_{\varphi 2}} D_3\, d\Gamma$ on one electrode, for example, on the electrode $\Gamma_{\varphi 2}$, with zero potential $\Phi_1 = 0$ on the other electrode, for example, on $\Gamma_{\varphi 1}$. (Here $I = \pm j\omega Q$, and since we are considering problems for the amplitude values of displacements and electric potential, the factor $\exp(j\omega t)$ is omitted everywhere.)

The transducer of type B is designed to operate as an emitter of acoustic waves into the external medium when it is electrically excited. The investigations of its gain-frequency characteristics in the steady-state oscillation mode were carried out in two stages. At the first stage, problems were solved in ANSYS to determine the electrically active first frequencies of electrical resonances f_{r1} and antiresonances f_{r2}, and at the second stage, the amplitude-frequency characteristics were constructed based on the results of calculations obtained on intervals including the corresponding frequencies of electrical resonances and antiresonances.

Note that the frequencies of electrical resonances f_{rk} and the frequencies of electrical antiresonances f_{ak} are the resonance frequencies of the device and can lead to classical resonance phenomena under various electrical influences: the difference in electrical potentials or current.

Namely, if we consider the specification of potential difference $\Delta V \exp(i2\pi ft)$ on electrode surfaces with the frequency $f = \omega/(2\pi)$ and with fixed amplitude ΔV, then in such problem at electric resonance frequencies f_{rk}, $k = 1, 2, \ldots$, in the absence of damping, resonance phenomena may occur for displacements, electric current amplitudes I and electric admittance $Y = I/(\Delta V)$:

$$|I| \to \infty, \quad |Y| \to \infty, \quad f \to f_{rk}. \tag{6}$$

Another option is to excite oscillations by a harmonically changing electric current

$I\exp(i2\pi ft)$ with a fixed amplitude I (electric charge $Q = iI/(2\pi f)$. In such a problem, resonance phenomena can be observed at the frequencies of electric antiresonance f_{ak} for displacements, amplitudes of the electrical potential difference ΔV and electric resistance (impedance) $Z = \Delta V/I = Y^{-1}$:

$$|\Delta V| \to \infty, \quad |Z| \to \infty, \quad f \to f_{ak}. \tag{7}$$

Our two cases of external electrical influences correspond exactly to the capabilities of the bridge transducer to operate at the frequencies of electrical resonances (6) and antiresonances (7). In modal analysis in ANSYS, we solve problems with homogeneous boundary conditions twice. First, we set zero potentials on both electrodes and find the eigenvalues, among which the frequencies of electrical resonances may be. Then we change the boundary conditions on one of the electrodes, making it free, i.e. with zero total charge. From this problem, we find the eigenvalues, the set of which contains the frequencies of electrical antiresonances. Comparing the two resulting sets and selecting electrically active frequencies with close ordinal numbers, but differing from each other, we find the desired frequencies of the first electrical resonances and antiresonances.

Conducting modal analysis allows us to construct amplitude-frequency characteristics more accurately, since the boundaries of frequency sub-intervals will be close to possible resonance frequencies (or equal to them, in problems without taking damping into account). For further analysis, we will select the amplitude-frequency characteristics of the axial displacement $|u_z|$ at the top central point $\{0, 0, H\}$, as well as the output charge or potential difference.

Some calculation results are shown in Figs. 3 and 4. Curve numbers 1–3 in these figures denote the same types of porous piezoceramics as in Fig. 2. Solid curves with numbers 1–3 are plotted for materials with a porosity of 40%, and dashed curves are plotted for materials with a porosity of 20%. Green curves with number 0 are plotted for the dense piezoceramics material PZT-4 (with zero porosity $p = 0$). The amplitude-frequency characteristics in Fig. 3 and in Fig. 4 are plotted for different electrical effects: Fig. 3 corresponds to the problem with a given oscillating potential difference with a modulus $\Delta V = 100$ (V), and Fig. 4 corresponds to the problem with a given electric charge $Q = -4.25 \cdot 10^{-8}$ (Ω) on one electrode with the second electrode grounded. The quality factor Q_d of the material of the metal end-caps was taken to be equal to 1000, and the quality factor of the piezoceramics was considered to be equal to 500.

The main results are presented in Fig. 3 (a) and 4 (a), which show the amplitude-frequency characteristics of the displacement at the central upper point of the transducer. Fig. 3 (b) and 4 (b) illustrate the resonance phenomena (6), (7). Thus, in the V-problem, for a given fixed amplitude of the potential difference ΔV, an increase in the amplitudes of the electric charge is observed at the first frequencies of electric resonance (Fig. 3 (b)), and in the Q-problem, for a given fixed amplitude of the electric charge Q, an increase in the amplitudes of the potential difference is observed at the first frequencies of electric antiresonance (Fig. 4 (b)).

As can be seen from Fig. 3 (a) and 4 (a), the porosity dependences of the maximum displacement amplitudes in these two problems are quite different. The models of inhomogeneity of porous piezoceramics also affect the values of the oscillation amplitudes, but not very significantly. When setting the potential difference (Fig. 3 (a)) the amplitudes of the axial displacement maxima at resonance frequencies decrease with increasing porosity. The dependences of the axial displacement maxima change significantly when the transducer oscillations are excited by an electric charge (Fig. 4 (a)). Here the displacement maxima increase with increasing porosity.

Note that in all cases at the first resonance frequencies, the axial displacements of the transducer in the central end regions are an order of magnitude greater than the longitudinal dis-

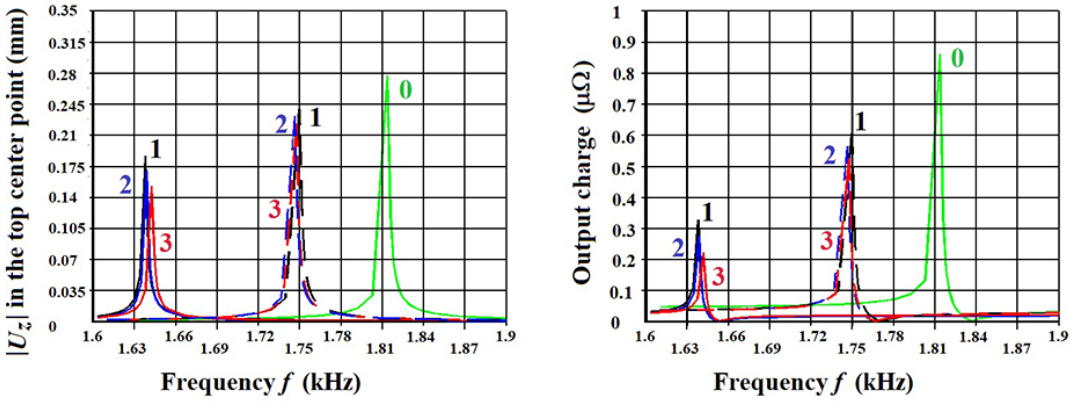

(a) (b)

Fig. 3. Displacements at the upper central point (a) and the output electric charge (b) in the V-problem under the action of a potential difference

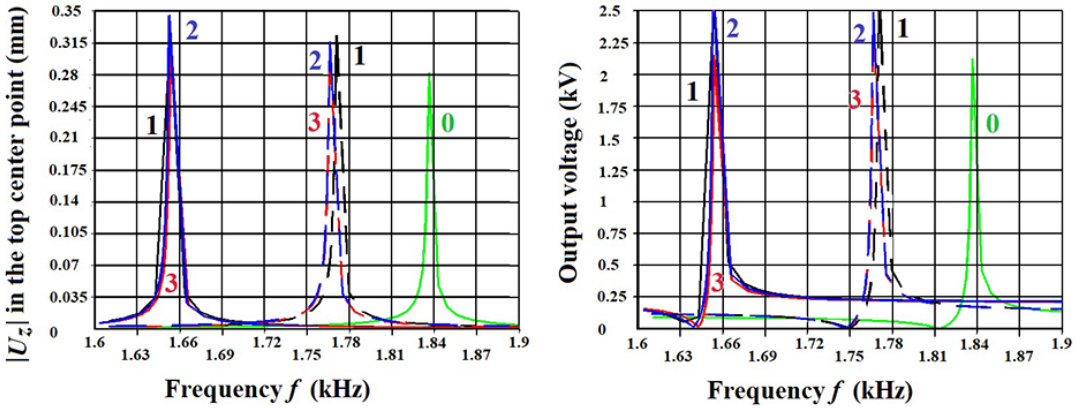

(a) (b)

Fig. 4. Displacements at the upper central point (a) and the output potential difference (b) in the Q-problem under the action of an electric charge

placements of its side surfaces. Thus, the bridge transducer at the first resonance frequency effectively generates axial oscillations. At the same time, calculations of the amplitude-frequency characteristics at a higher resonant frequency showed a lower efficiency of excitation of axial displacements. Nevertheless, in general, if we also take into account the lower acoustic impedance of porous piezoceramics compared to dense ones, we can conclude that the use of the considered porous piezoceramics as active materials for acoustic wave emitters is promising.

It can also be noted that the behavioral features of bridge transducers made of porous piezoceramics as sensors and actuators are similar to the behavioral features of the Symbol transducer [17, 18]. In [17, 18], porous piezoceramics with metallized surface pores were also considered, but non-uniform polarization models were not taken into account. For the porous Symbol transducer, in [17, 18], an advantage was found in using porous piezoceramics with metallized surface pores for energy harvesting and in the V-problem for actuator applications. Therefore, it

can be concluded that porous piezoceramics with metallized surface pores for similar applications will also be effective for a bridge transducer. However, the technological processes for creating such porous piezoceramics have not yet been fully developed.

Conclusion

Thus, here, a bridge piezoelectric transducer consisting of a piezoceramic plate with two bridge-like metal end-caps was investigated using computer modelling methods. The use of porous piezoceramics as the active material of the transducer and the consideration of various models of non-uniform polarization were analyzed.

Two types of bridge piezoelectric transducers are considered. The first transducer is intended for use as a "green energy" piezoelectric generator. It generated electric fields in the transducer under low-frequency mechanical influences. For this device, the use of porous ceramics showed lower efficiency of electromechanical conversion compared to dense ceramics.

The second type of transducer worked as an emitter of acoustic waves. It converted electrical influences near the first resonance frequency into mechanical vibrations. In this case, when the transducer was excited by the potential difference at the first frequencies of electrical resonances, qualitatively similar results were obtained for the use of porous piezoceramics as for the bridge piezogenerator. However, the bridge transducer made of porous piezoceramics showed its efficiency when working at the first antiresonance frequency when its vibrations were excited by electric current. It also turned out that considering the inhomogeneity of polarization of porous piezoceramics is essential for precision modeling of a bridge converter, but taking into account the inhomogeneity does not affect the qualitative characteristics.

This research was supported by the Russian Science Foundation, project no. 22-11-00302.

References

[1] L.Luo, Y.Tang, F.Wang, C.He, H.Luo, Displacement amplification and electric characteristics of modified rectangular cymbal transducers using electroactive materials, *Solid State Commun.*, **143**(2007), 321–325. DOI: 10.1016/j.ssc.2007.05.037

[2] H .Wang, A.Jasim, X.Chen, Energy harvesting technologies in roadway and bridge for different applications - A comprehensive review, *Appl. Energy.* **212**(2018), 1083–1094. DOI: 10.1016/j.apenergy.2017.12.125

[3] L.Yao, H.D.Zhao, Z.Y.Dong, Y.F.Sun, Y.F.Gao, Laboratory testing of piezoelectric Bridge transducers for asphalt pavement energy harvesting, *Key Eng. Mater.*, **492**(2012), 172–175. DOI: 10.4028/www.scientific.net/kem.492.172

[4] H.Zhao,L.Qin, J.Ling, A comparative analysis of piezoelectric transducers for harvesting energy from asphalt pavement, *J. Ceram. Soc. Jpn.*, **120**(2012), no. 1404, 317–323. DOI: 10.2109/jcersj2.120.317

[5] H.Zhao, J.Ling, J.Yu, Test and analysis of bridge transducers for harvesting energy from asphalt pavement , *Int. J. Transp. Sci. Technol.*, **4**(2015), no. 1, 17–28. DOI: 10.1260/2046-0430.4.1.17

[6] W.Hea, Y.Lu, C.Qu, J.Peng, A non-invasive electric current sensor employing a modified shear-mode cymbal transducer, *Sensors Actuat. A* , **241**(2016), 120–123 DOI: 10.1016/j.sna.2016.02.015

[7] A.Daniels, M.Zhu,.A.Tiwari, Design, analysis and testing of a piezoelectric flex transducer for harvesting biokinetic energy, *J. Phys.: Conf. Ser.*, **476**(2013), 012047. DOI: 10.1088/1742-6596/476/1/012047

[8] A.Jasim, H.Wang, G.Yesner, A.Safari, A.Maher, Optimized design of layered bridge transducer for piezoelectric energy harvesting from roadway, *Energy*, **141**(2017), 1133–1145. DOI: 10.1016/j.energy.2017.10.005

[9] Y.Kuang, A.Daniels, M.Zhu, A sandwiched piezoelectric transducer with flex end-caps for energy harvesting in large force environments, *J. Phys. D: Appl. Phys.* **50**(2017), 345501. DOI: 10.1088/1361-6463/aa7b28

[10] B.Ren, S.W.Or, X.Zhao, H.Luo, Energy harvesting using a modified rectangular cymbal transducer based on 0.71Pb $(Mg_{1/3}Nb_{2/3})$ O_3–0.29 $PbTiO_3$ single crystal, *J. Appl. Phys.*, **107**(2010), 034501. DOI: 10.1063/1.3296156

[11] G.Yesner, A.Jasim, H.Wang, B.Basily, A.Maher, A.Safari, Energy harvesting and evaluation of a novel piezoelectric bridge transducer , *Sensors Actuat. A*, **285**(2019), 348–354. DOI: 10.1016/j.sna.2018.11.013

[12] L.Luo, D.Liu, M.Zhu, J.Ye, Metamodel-assisted design optimization of piezoelectric flex transducer for maximal bio-kinetic energy conversion, *J. Intell. Mater. Syst. Struct.*, **28**(2017), no. 18, 2528–2538. DOI: 10.1177/1045389X17689943

[13] L.Luo, D.Liu, M.Zhu, Y.Liu, L.Ye, Maximum energy conversion from human motion using piezoelectric flex transducer: A multi-level surrogate modeling strategy, *J. Intell. Mater. Syst. Struct.*, **29**(2018), no, 15, 3097–3107. DOI: 10.1177/1045389X18783075

[14] S.Guo, W.Li, L.Sang, C.Sun, X.Z.Zhao, Finite element analysis of underwater cymbal transducers with large displacement and fast response time, *Integr. Ferroelectr.*, **78**(2006), no. 1, 103–111. DOI: 10.1080/10584580600660025

[15] J.Y.Pyun, Y.H.Kim, K.K.Park, Design of piezoelectric acoustic transducers for underwater applications, *Sensors*, **23**(2023), 1821. DOI: 10.3390/s23041821

[16] A.V.Nasedkin, A.A.Nasedkina, A. Rajagopal, Analysis of cymbal transducer from porous piezoceramics PZT-4 with various material properties based on ANSYS, *Advanced Materials. Springer Proceedings in Physics*, **207**(2018), 533–547. DOI: 10.1007/978-3-319-78919-4_42

[17] A.V.Nasedkin, A.A.Nasedkina, M.E.Nassar, Finite element calculation of disk transducer with cymbal-shaped end-caps and active element from porous piezoceramics with extreme conductivity of pore surfaces, *Problems of Strength and Plasticity*, **85**(2023), no. 1, 63–76 (in Russian). DOI: 10.32326/1814-9146-2023-85-1-63-76

[18] A.V.Nasedkin, A.A.Nasedkina, M.E.Nassar, Finite element investigation of disk transducers from porous piezoceramics of complex structure with cymbal end-caps in external medium, 2023 Days on Diffraction (DD), St. Petersburg, Russia, IEEE Publ., 2023, 156–161. DOI: 10.1109/DD58728.2023.10325699

[19] A.V.Nasedkin, A.A.Nasedkina, Y.V.Tolmacheva, Computer homogenization of porous piezoceramics of different ferrohardness with random porous structure and inhomogeneous polarization field, *Comput. Contin. Mech.*, **16**(2023), no. 4, 476–492 (in Russian). DOI: 10.7242/1999-6691/2023.16.4.40

[20] E.Dieulesaint, D.Royer, Elastic Waves in Solids: Application to Signal Processing, J.Wiley, New York, 1980.

Анализ влияния пористости и неоднородной поляризации пьезокерамики на эффективность мостового преобразователя как сенсора и актуатора

Андрей В. Наседкин
Анна А. Наседкина
Южный федеральный университет
Ростов-на-Дону, Российская Федерация

Аннотация. Гибкие пьезоэлектрические преобразователи с мостовыми накладками нашли широкие применения в качестве акустических излучателей и устройств накопления энергии. В настоящей работы исследуются возможности использования пористой пьезокерамики в качестве активного элемента мостового преобразователя. Особое внимание уделяется учету неоднородности поляризации пористой пьезокерамики с применением упрощенных моделей, пригодных для практики. Проведен конечно-элементный анализ работы мостового пьезопреобразователя при установившихся колебаниях в нерезонансных и в резонансных режимах его работы. Было установлено, что использование пористой пьезокерамики повышает эффективность преобразователя при колебаниях вблизи первой частоты электрического антирезонанса.

Ключевые слова: электроупругость, мостовой пьезопреобразователь, пористая пьезокерамика, неравномерная поляризация, резонансная частота, сенсор, актуатор, метод конечных элементов.

EDN: PPVCEQ
УДК 530.1

A Classical Aspect of the Dirac Equation in the Context of Conformable Fractional Derivative

Ilyas Haouam*
Laboratoire de Physique Mathématique et de Physique Subatomique (LPMPS)
Université Fréres Mentouri
Constantine 25000, Algeria

Received 24.04.2024, received in revised form 29.05.2024, accepted 14.01.2025

Abstract. In this article, in the context of the conformable fractional derivative (CFD) and employing Ehrenfest's theorem, we investigate the classical limit of the Dirac equation within conformable fractional quantum mechanics. This leads to obtaining deformed classical equations. Here, we assess the effectiveness of Ehrenfest's theorem in deriving the classical limit considering CFD. Also, we examine the correspondence principle under the influence of CFD. Additionally, we obtain the conformable fractional continuity equation.

Keywords: conformable fractional Dirac equation, conformable fractional continuity equation, Ehrenfest's theorem, classical limit, correspondence principle, conformable quantum mechanics.

Citation: I. Haouam, A Classical Aspect of the Dirac Equation in the Context of Conformable Fractional Derivative, J. Sib. Fed. Univ. Math. Phys., 2025, 18(2), 229–242. EDN: PPVCEQ.

1. Introduction and preliminaries

The Dirac equation is a relativistic quantum mechanical equation that specifically describes massive particles with spin-$\frac{1}{2}$, such as electrons. It is a fundamental equation in quantum mechanics, providing a framework for understanding the behavior of these particles within the realm of relativistic effects. The classical limit of the Dirac equation can be investigated by neglecting the influences of quantum mechanics. In doing so, we can describe the system's conduct using classical physics, providing insights into the classical aspects of the system. In the classical limit, phenomena inherent to quantum mechanics, such as interference, superposition and entanglement, are expected to diminish at the macroscopic scale, however, this demise is not easy to explain. In this scenario, the quantum system adheres to the classical laws of physic. The classical limit is commonly defined in terms of the limit of a vanishing Planck's constant, i.e., $\hbar \to 0$ as scaled with the system's action. In this context, Hamilton's principle adopts its classical expression, and all operators commute. In the following, we present some scenarios and approaches that help explain the exploration of the classical limit of the Dirac equation. So, one can initiate the exploration by examining the solutions of the equation under conditions of large distances and durations, or under the conditions of large energies and momenta. Within these limits, the effects of quantum mechanics become negligible [1]. Put differently, the classical limit emerges if the system possesses a big quantum number, undergoes significant interactions with its surroundings, or if its de Broglie wavelength becomes significantly smaller compared to other relevant length measurements. A frequent example illustrating the classical limit of a quantum system is the Bohr correspondence principle [2], which asserts that in the limit of large quantum numbers, a quantum system exhibits conduct similar to the corresponding classical

*ilyashaouam@live.fr; ilyas.haouam@tmp.umc.edu.dz https://orcid.org/0000-0001-6127-0408

system. Also, the Ehrenfest's theorem is considerably used when exploring the classical limit of quantum mechanical systems [3]. This theorem establishes a connection between the evolution of expected values of observables and classical equations of motion. It serves as an effective tool for understanding the conduct of such systems. Through its application, we observe the way quantum mechanical influences dissipate, giving way to classical dynamics [4]. In the context of the Dirac equation, this theorem remains used to explore its classical limit, there, the quantum influences will be very small, leading simplify the Dirac equation to its classical counterpart. In this work, we aim to investigate whether it can be asserted that Ehrenfest's theorem is applicable to the classical limit of the Dirac equation within conformable fractional quantum mechanics (CFQM) and under some conditions.

Extensive research in the literature [5–14] has delved into the alignment between quantum and classical aspects. We also emphasize that other concepts may overlap with the concept of the classical limit, such as the semiclassical and non-relativistic limits. Note that the semiclassical limit of a quantum mechanical system, can be attained if external potentials vary slowly, like in the case of the electrostatic potential [15]. On the other hand, the non-relativistic limit of a relativistic quantum mechanical system as the Dirac equation [16, 17], is the limit where the speed of the particle is much less than the speed of light, i.e., $v \ll c$ or low energy in front of the rest energy, consequently, this limit permits to neglect the relativistic influences. However, the non-relativistic and classical limits are related but distinct concepts, they address different aspects of the system's behavior. It is important to highlight that in many physical situations, the classical limit and the non-relativistic limit can align, leading to similar descriptions of the system's conduct.

On the other side, the concept of a fractional derivative has been receiving a lot of attention in recent years, [18–20]. The fractional derivative, dating back to as early as calculus itself, traces its origins to 1695 when L'Hospital posed inquiries to Leibniz about $\frac{d^n f}{dx^n}$ when n equals $\frac{1}{2}$. However, Leibniz responded that this would be "an apparent paradox, from which one day useful consequences will be drawn" [21]. Since then, researchers have endeavored to elucidate the concept of fractional derivatives, predominantly employing integral formulations. Various definitions have emerged over time, including those by Riemann–Liouville, Caputo, Riesz, Weyl, Grьnwald, Riesz–Caputo, Chen, and Hadamard, [22–24]. Among these, the Riemann–Liouville and Caputo formulations stand out as the most prevalent. For further insight into diverse mathematical aspects of fractional calculus, refer to the seminal works in [25, 26]. The fractional derivative has played an essential role across various domains including physics, chemistry, biology, and engineering. See, for example, [27–29].

However, a few years ago, Khalil et al. [30] introduced a new concept of derivative known as the conformable fractional derivative (CFD). Since then, extensive studies have been conducted on the development of CFD calculus, exploring its properties. For example, conformable fractional versions of fundamental mathematical tools such as the chain rule, exponential functions, Gronwall's inequality, integration by parts, Taylor power series expansions, Laplace or Fourier transforms, linear differential systems [31, 32], divergence theorem [33], spherical harmonics [34], Nikiforov–Uvarov Method [35] and $\mathcal{PT}$ symmetry [36] have been proposed and discussed. Also, applications in various physical contexts [37–50].

Our objective in this study is to investigate some aspects of the Dirac equation within the CFQM including classical limit by using the Ehrenfest's theorem and continuity equation. This work came as a continuation of some works on the classical and non-relativistic limits we did before [8, 12, 16, 17, 51]. As an example, in [12], we studied the classical limit and Ehrenfest's theorem of the noncommutative Dirac equation in the context of minimal uncertainty in momentum. There, we explored the comparison between the classical and non-relativistic limits. Furthermore, in [8], we have investigated Ehrenfest's theorem from the Dirac equation in a noncommutative phase-space.

The rest of the paper is outlined as follows. In Section 2, the CFQM is briefly reviewed. In Section 3, the CL of the Dirac equation in the context of CFD using the Ehrenfest's theorem is explored, where in sub-Section 3.1, a conformable fractional Dirac equation in presence of an electromagnetic field is found. In sub-Section 3.2, based on the Ehrenfest's theorem, conformable fractional classical equations are obtained. Also, in Section 4, a conformable fractional four-vector current density is obtained. Then, in Section 5, the correspondence principle is examined in the context of CFD by using quantum and classical versions of the harmonic oscillator. We present the conclusion and remarks in Section 6.

2. Brief overview on the conformable fractional quantum mechanics

Let shortly review the postulates and basic formulas of the conformable fractional quantum mechanics [30] we use in this work. So, for a smooth function in x, the conformable fractional derivative is expressed as follows:

$$D_x^\alpha f(x) = \lim_{\epsilon\to 0} \frac{f\left(x+\epsilon|x|^{1-\alpha}\right)-f(x)}{\epsilon} = |x|^{1-\alpha}\,\partial_x f(x), \tag{1}$$

where $0<\alpha\leqslant 1$ is assumed. Note that D^α is the conformable fractional derivative operator. At $x=0$, the fractional derivative is $D_x^\alpha f(0) = \lim_{x\to 0} D_x^\alpha f(x)$. But, the conformable partial derivative of f in x_i is defined by [33]:

$$\frac{\partial^\alpha}{\partial x_i^\alpha} f(x_1,\ldots,x_m) = \lim_{\epsilon\to 0} \frac{f\left(x_1,\ldots,x_{i-1},x_i+\epsilon|x_i|^{1-\alpha},\ldots,x_m\right)-f(x_1,\ldots,x_m)}{\epsilon}. \tag{2}$$

The application of the CFD in quantum mechanics is given in some literatures [37–39, 46], leading to CFQM. However, its postulates, basics and essential properties have been well constructed [30, 39, 41]. The CFD satisfies the following properties:

The linearity:

$$D_x^\alpha\{af(x)+bg(x)\} = aD_x^\alpha f(x) + bD_x^\alpha g(x), \tag{3}$$

the Leibniz rule:

$$D_x^\alpha\{f(x)g(x)\} = [D_x^\alpha f(x)]\,g(x) + f(x)\,D_x^\alpha g(x), \tag{4}$$

the chain rule:

$$D_x^\alpha f(g(x)) = \frac{df}{du}\,(D_x^\alpha u), \tag{5}$$

where f, g be α-differentiable functions. All of the classical derivative rules, such as sum, product, division, etc. are same as the conformable derivative. Also, the inner product in Hilbert space related to CFQM is given as follows:

$$\langle f|\,g\rangle = \int_{-\infty}^{\infty} g^*(x)\,f(x)\,|x|^{\alpha-1}\,dx. \tag{6}$$

The definition of the expectation value of a physical operator $\mathcal{O}$ in relation to the state ψ is as follows:

$$\langle\psi|\,\mathcal{O}\psi\rangle = \int_{-\infty}^{\infty} \psi^*(x,t)\,\mathcal{O}\psi(x,t)\,|x|^{\alpha-1}\,dx, \tag{7}$$

but $\mathcal{O}$ to be a Hermitian operator, one may obey

$$\langle\psi|\,\mathcal{O}\psi\rangle = \langle\mathcal{O}\psi|\,\psi\rangle. \tag{8}$$

The fractional integral is defined as

$$\mathcal{J}_{\alpha|x}^{\alpha} f(x) = \int_{\alpha}^{x} |\mathcal{W}|^{\alpha-1} f(\mathcal{W}) \, d\mathcal{W}, \tag{9}$$

where $f(x)$ is any continuous function. Furthermore, the relation between the CFD and the fractional integral is as follows:

$$\begin{cases} D_x^{\alpha} \mathcal{J}_{\alpha|x}^{\alpha} f(x) = f(x), \\ \mathcal{J}_{\alpha|x}^{\alpha} D_x^{\alpha} f(x) = f(x) - f(a). \end{cases} \tag{10}$$

Note that the coordinate realization of α-position $\hat{x}_\alpha$, and α-momentum $\hat{p}_\alpha$ are

$$\hat{x}_\alpha = x, \quad \hat{p}_\alpha = -i\hbar_\alpha^{\alpha} D_x^{\alpha}, \tag{11}$$

here one can merely check that both position and momentum operators are Hermitian. Then, from the de Broglio relation $p = \dfrac{\hbar}{\lambda}$ and Planck relation $E = \dfrac{\hbar}{T}$, we have [39] $\hat{x}_\alpha \psi = x\psi$, $\hat{p}_\alpha \psi = p^\alpha \psi$, which yield the following the x-representation:

$$\hat{x}_\alpha = x, \quad \hat{p}_\alpha = -i\hbar_\alpha^{\alpha} D_x^{\alpha} \text{ and } \hat{\mathscr{H}}_\alpha = -i\hbar_\alpha D_t^{\alpha}, \tag{12}$$

with

$$D_x^{\alpha} = |x|^{1-\alpha} \frac{\partial}{\partial x}, \text{ and } D_t^{\alpha} = |t|^{1-\alpha} \frac{\partial}{\partial t}, \tag{13}$$

where $\hbar_\alpha = \dfrac{h}{(2\pi)^{\frac{1}{\alpha}}}$, and $\hat{\mathscr{H}}_\alpha$ is a α-Hamiltonian operator. Note that the α-position operator has dimension of length while the α-momentum operator has dimension of momentum$^\alpha$ and α-Hamiltonian operator has dimension of energy$^\alpha$. In CFQM, the commutator of the α-position operator and α-momentum operator is

$$[\hat{x}_\alpha, \hat{p}_\alpha] = i\hbar_\alpha^{\alpha} |\hat{x}|^{1-\alpha}. \tag{14}$$

...Also, in Section 4, a conformable fractional four-vector current density is obtained. Then, the correspondence principle is examined in the context of CFD by comparing the quantum and classical versions of the harmonic oscillator. Finally, we present the conclusion and remarks in Section 6."

3. Classical limit of the conformable fractional Dirac equation

In this section, we extend the Dirac equation to the CFQM and subsequently employ it to investigate some classical aspects.

3.1. 3D conformable fractional Dirac equation

The conformable fractional form of the Dirac equation is given as follows [39, 46]:

$$\left\{ i\hbar^{\alpha} \gamma^{\mu} \partial_{\mu}^{\alpha} - m^{\alpha} c^{\alpha} \right\} \psi(x^{\mu}) = 0, \tag{15}$$

where $0 < \alpha \leqslant 1$, which we call the fractional and $\gamma^\mu = \left(\gamma^0, \gamma^k\right)$ are the Dirac matrices. Now, by multiplying equation (14) from the left by γ^0 and separating the time and the spatial parts, one can have

$$\left\{ i\hbar^{\alpha} \left(\gamma^0\right)^2 \partial_0^{\alpha} - i\hbar^{\alpha} \gamma^0 \gamma^k \partial_k^{\alpha} - \gamma^0 m^{\alpha} c^{\alpha} \right\} \psi(\overrightarrow{x}, t) = 0, \tag{16}$$

with $\left(\gamma^0\right)^2 = 1$. Then, supposing that

$$\psi\left(\overrightarrow{x}, t\right) = \psi\left(\overrightarrow{x}\right) e^{-\frac{i}{\hbar^\alpha} E^\alpha \frac{t^\alpha}{\alpha}}, \tag{17}$$

with $i\hbar^\alpha \frac{1}{c}\partial_0^\alpha = i\hbar^\alpha \frac{1}{c} D_t^\alpha$, the time-independent Dirac equation in interaction with an electromagnetic four-potential $A^\mu = \left(\Phi_\alpha, \overrightarrow{A}_\alpha\right)$ (in SI units) reads

$$\left\{c^\alpha \overrightarrow{\alpha} \cdot \left(\hat{\overrightarrow{p}}_\alpha - e\overrightarrow{A}_\alpha\left(\overrightarrow{x}\right)\right) + e\Phi_\alpha + \beta m^\alpha c^{2\alpha}\right\}\psi\left(\overrightarrow{x}\right) = E^\alpha \psi\left(\overrightarrow{x}\right), \tag{18}$$

where $\psi\left(\overrightarrow{x}, t\right) = \begin{pmatrix} \phi\left(\overrightarrow{x}, t\right) & \chi\left(\overrightarrow{x}, t\right) \end{pmatrix}^T$ is the bispinor in the Dirac representation. The Dirac matrices $\overrightarrow{\alpha} = \gamma^0 \overrightarrow{\gamma}$ and $\beta = \gamma^0$ satisfy the following anticommutation relations

$$\{\alpha_i, \alpha_j\} = 2\delta_{ij},\ \{\alpha_i, \beta\} = 0, \quad \alpha_i^2 = \beta^2. \tag{19}$$

Then in more elegant simple form, we have

$$\left\{c^\alpha \overrightarrow{\alpha} \cdot \hat{\overrightarrow{\Pi}}_\alpha + e\Phi_\alpha + \beta m^\alpha c^{2\alpha}\right\}\psi\left(\overrightarrow{x}\right) = E^\alpha \psi\left(\overrightarrow{x}\right), \tag{20}$$

where the minimal substitution $\hat{\overrightarrow{p}}_\alpha - e\overrightarrow{A}_\alpha\left(\overrightarrow{x}\right) = \hat{\overrightarrow{\Pi}}_\alpha$. Next, we move to employ the obtained conformable fractional Dirac equation (20) to explore the classical limit through Ehrenfest's theorem.

3.2. Ehrenfest's theorem in the context of CFQM

Ehrenfest's theorem, originating from the Dirac equation, establishes that the time evolution of expected values of observables in quantum mechanics aligns with classical equations of motion. Essentially, it suggests that the average conduct of a quantum system corresponds to classical physics. Additionally, it is noteworthy that this theorem applies to all quantum systems. However, in the present context, we are computing the time derivatives of position and kinetic momentum operators for Dirac particles interacting with an electromagnetic field in the context of CFQM. However, the equation of motion for an arbitrary operator $\hat{\mathcal{F}}$ is expressed as follows:

$$\frac{d\hat{\mathcal{F}}}{dt} = \frac{\partial \hat{\mathcal{F}}}{\partial t} + \frac{i}{\hbar}\left[\hat{\mathscr{H}}, \hat{\mathcal{F}}\right], \tag{21}$$

where $\hat{\mathscr{H}}$ is the Hamiltonian operator. Now, let start with the operator of position

$$\frac{d\hat{\overrightarrow{x}}}{dt} = \frac{\partial \hat{\overrightarrow{x}}}{\partial t} + \frac{i}{\hbar}\left[\hat{\mathscr{H}}_\alpha, \hat{\overrightarrow{x}}\right] = \frac{i}{\hbar}\left[\hat{\mathscr{H}}_\alpha, \hat{\overrightarrow{x}}\right], \tag{22}$$

and the Hamiltonian operator from equation (20) is given as:

$$\hat{\mathscr{H}}_\alpha = c^\alpha \overrightarrow{\alpha} \cdot \hat{\overrightarrow{\Pi}}_\alpha + e\Phi_\alpha + \beta m^\alpha c^{2\alpha}, \tag{23}$$

subsequently, the commutator expressed in equation (22) is as follows:

$$\begin{aligned}\left[\hat{\mathscr{H}}_\alpha, \hat{\overrightarrow{x}}\right] = c^\alpha\left[\hat{\overrightarrow{\alpha}} \cdot \hat{\overrightarrow{p}}_\alpha, \hat{\overrightarrow{x}}\right] - ec^\alpha\left[\hat{\overrightarrow{\alpha}} \cdot \overrightarrow{A}_\alpha, \hat{\overrightarrow{x}}\right] + e\left[\Phi_\alpha, \hat{\overrightarrow{x}}\right] \\ + m^\alpha c^{2\alpha}\left[\hat{\beta}, \hat{\overrightarrow{x}}\right],\end{aligned} \tag{24}$$

The position operator $\hat{x}$ is diagonal with respect to the spinor indices, i.e., $\hat{\overrightarrow{x}}\psi = \overrightarrow{x}\psi$ and contains no differentiation, thus $\left[\hat{\beta}, \hat{\overrightarrow{x}}\right] = \left[\hat{\overrightarrow{\alpha}}, \hat{\overrightarrow{x}}\right] = 0$, then for three arbitrary vectors $\overrightarrow{A}_1$, $\overrightarrow{A}_2$ and $\overrightarrow{A}_3$ we use the identity

$$\left[\overrightarrow{A}_1\overrightarrow{A}_2,\overrightarrow{A}_3\right]=\left[\overrightarrow{A}_1,\overrightarrow{A}_3\right]\overrightarrow{A}_2+\overrightarrow{A}_1\left[\overrightarrow{A}_2,\overrightarrow{A}_3\right]. \tag{25}$$

Then, we obtain

$$\left[\hat{\overrightarrow{\alpha}}\cdot\hat{\overrightarrow{p}}_\alpha,\hat{\overrightarrow{x}}\right]=-i\hbar_\alpha^\alpha\left|\hat{x}\right|^{1-\alpha}\hat{\overrightarrow{\alpha}}, \tag{26}$$

also

$$\left[\overrightarrow{A}_\alpha,\hat{\overrightarrow{x}}\right]=\left[\Phi_\alpha,\hat{\overrightarrow{x}}\right]=0, \tag{27}$$

because both $\overrightarrow{A}_\alpha$, Φ_α are functions of x.

Therefore, we obtain

$$\frac{d\hat{\overrightarrow{x}}}{dt}=\frac{1}{\hbar}\hbar_\alpha^\alpha c^\alpha\left|\hat{x}\right|^{1-\alpha}\hat{\overrightarrow{\alpha}}. \tag{28}$$

Let us subsequently examine how the operator (28) acts on the Dirac spinor. By focusing on individual components ψ, we obtain

$$\frac{d\hat{x}}{dt}\psi=\pm\frac{1}{\hbar}\hbar_\alpha^\alpha c^\alpha\left|\hat{x}\right|^{1-\alpha}\psi, \tag{29}$$

where the eigenvalues of $\hat{\overrightarrow{\alpha}}$ are ±1. This result has no classical analogue, as the Dirac particle, despite the effects considered, continues to move at the speed of light c^α.

So, to better understand the behaviour of a particle velocity obtained from the classical limit of Dirac equation within the framework of CFQM, we plot equation (29)

Fig. 1 represents the variation of the velocity with respect to the fractional parameter α for different values of x. But, Fig. 2 represents the variation of the velocity with respect to x for different values of the fractional parameter α. However, the velocity as a function of the fractional parameter behaves as a Gaussian where it is symmetric around the central value of the distribution ($\alpha=0.6$). The curve peaks at the mean and decreases symmetrically on either side, i.e., zero and unity. Also, in Fig. 2, the effect of the fractional parameter on the variation of the velocity is shown, which appears to be considerable at $\alpha=0.6$.

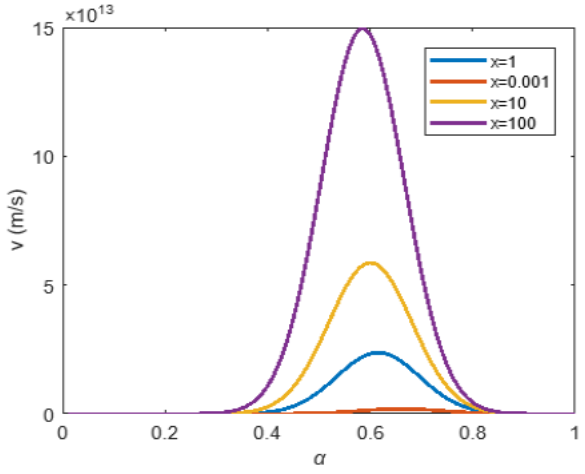

Fig. 1. Velocity versus α for x=0.001,1,10,100

Now, the equation of motion for the kinetic momentum operator $\hat{\overrightarrow{\Pi}}=\hat{\overrightarrow{p}}-\frac{e}{c}\overrightarrow{A}$ is

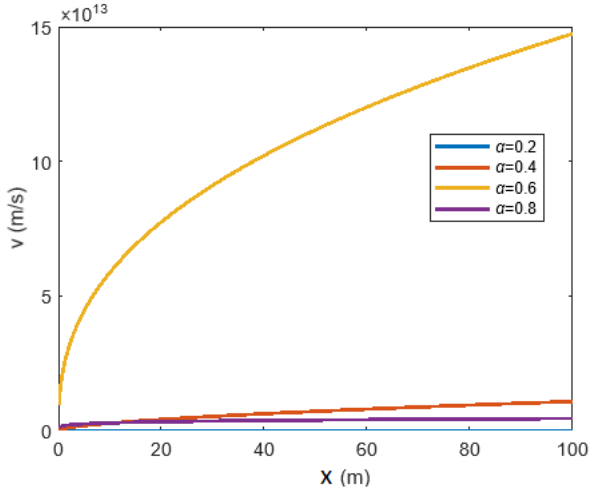

Fig. 2. Velocity versus x for $\alpha = 0.1, 0.4, 0.6, 0.8$

$$\frac{d\overrightarrow{\hat{\Pi}}}{dt} = \frac{\partial\overrightarrow{\hat{\Pi}}}{\partial t} + \frac{i}{\hbar}\left[\hat{\mathscr{H}}_\alpha, \overrightarrow{\hat{\Pi}}\right] = -e\frac{\partial\overrightarrow{A}}{\partial t} + \frac{i}{\hbar}\left[\hat{\mathscr{H}}_\alpha, \overrightarrow{\hat{\Pi}}\right], \tag{30}$$

consequently, the commutator is given by

$$\left[\hat{\mathscr{H}}_\alpha, \overrightarrow{\hat{\Pi}}\right] = \left[\hat{\mathscr{H}}_\alpha, \overrightarrow{\hat{p}}\right] - e\left[\hat{\mathscr{H}}_\alpha, \overrightarrow{A}\right]. \tag{31}$$

First, we compute the initial commutator in equation (31)

$$\begin{aligned}\left[\hat{\mathscr{H}}_\alpha, \overrightarrow{\hat{p}}\right] = c^\alpha\left[\overrightarrow{\hat{\alpha}}\cdot\overrightarrow{\hat{p}}_\alpha, \overrightarrow{\hat{p}}\right] - c^\alpha e\left[\overrightarrow{\hat{\alpha}}\cdot\overrightarrow{A}_\alpha, \overrightarrow{\hat{p}}\right] + e\left[\Phi_\alpha, \overrightarrow{\hat{p}}\right] \\ +m^\alpha c^{2\alpha}\left[\hat{\beta}, \overrightarrow{\hat{p}}\right],\end{aligned} \tag{32}$$

with $\left[\hat{\beta}, \overrightarrow{\hat{p}}\right] = \left[\overrightarrow{\hat{\alpha}}, \overrightarrow{\hat{p}}\right] = 0$ as $\hat{\beta}$ and $\overrightarrow{\hat{\alpha}}$ are independent of the spatial coordinates. Furthermore, we obtain

$$\left[\Phi_\alpha, \overrightarrow{\hat{p}}\right] = i\hbar\left[\overrightarrow{\nabla}, \Phi_\alpha\right] = i\hbar\left(\overrightarrow{\nabla}\Phi_\alpha - \Phi_\alpha\overrightarrow{\nabla}\right), \tag{33}$$

then making use of equation (33), we have

$$\left[\Phi_\alpha, \overrightarrow{\hat{p}}\right]\psi = i\hbar\left(\overrightarrow{\nabla}\Phi_\alpha - \Phi_\alpha\overrightarrow{\nabla}\right)\psi = i\hbar\left(\overrightarrow{\nabla}\Phi_\alpha\right)\psi, \tag{34}$$

and

$$\left[\overrightarrow{\hat{\alpha}}\cdot\overrightarrow{\hat{p}}_\alpha, \overrightarrow{\hat{p}}\right] = \frac{1}{\hbar}\hbar_\alpha^\alpha\left[|\hat{x}|^{1-\alpha}, \overrightarrow{\hat{p}}\right]\overrightarrow{\hat{\alpha}}\cdot\overrightarrow{\hat{p}}. \tag{35}$$

Also

$$\left[\overrightarrow{\hat{\alpha}}\cdot\overrightarrow{A}_\alpha, \overrightarrow{\hat{p}}\right] = -i\hbar\sum_{i,j}\hat{\alpha}_i\left[\left(A_\alpha\right)_i, \nabla_j\right]e_j, \tag{36}$$

then, taking into account the effect of equation (36) on ψ, we find

$$\left[\overrightarrow{\hat{\alpha}}\cdot\overrightarrow{A}_\alpha, \overrightarrow{\hat{p}}\right]\psi = i\hbar\sum_{i,j}\hat{\alpha}_i\left(\nabla_j\left(A_\alpha\right)_i\psi - \left(A_\alpha\right)_i\nabla_j\psi\right)e_j = i\hbar\sum_{i,j}\hat{\alpha}_i\left(\nabla_j\left(A_\alpha\right)_i\right)e_j\psi. \tag{37}$$

Now, we move on to the second commutator in equation (31), thus, we have

$$\begin{aligned}\left[\hat{\mathscr{H}}_{\alpha}, \overrightarrow{A}\right] = c^{\alpha}\left[\hat{\overrightarrow{\alpha}} \cdot \hat{\overrightarrow{p}}_{\alpha}, \overrightarrow{A}\right] - c^{\alpha} e\left[\hat{\overrightarrow{\alpha}} \cdot \overrightarrow{A}_{\alpha}, \overrightarrow{A}\right] + e\left[\Phi_{\alpha}, \overrightarrow{A}\right] \\ + m^{\alpha} c^{2\alpha}\left[\hat{\beta}, \overrightarrow{A}\right].\end{aligned} \tag{38}$$

Subsequently, we proceed to calculate each commutator in equation (38), starting with

$$\left[\hat{\overrightarrow{\alpha}} \cdot \hat{\overrightarrow{p}}_{\alpha}, \overrightarrow{A}\right] = -i\hbar_{\alpha}^{\alpha} \sum_{i,j} \hat{\alpha_i}\left[|\hat{x}|^{1-\alpha} \nabla_i, A_j\right] e_j, \tag{39}$$

and its act on ψ yields

$$\left[\hat{\overrightarrow{\alpha}} \cdot \hat{\overrightarrow{p}}_{\alpha}, \overrightarrow{A}\right] \psi = -i\hbar_{\alpha}^{\alpha} |\hat{x}|^{1-\alpha} \sum_{i,j} \hat{\alpha_i} \left(\nabla_i A_j\right) e_j \psi. \tag{40}$$

Note that in equations (34, 40), the gradient acts on $\overrightarrow{A}$ only. Then, we proceed with

$$\left[\hat{\beta}, \overrightarrow{A}\right] = \left[\hat{\overrightarrow{\alpha}}, \overrightarrow{A}\right] = 0, \tag{41}$$

and

$$\left[\Phi_{\alpha}, \overrightarrow{A}\right] = \left[\overrightarrow{A}_{\alpha}, \overrightarrow{A}\right] = 0. \tag{42}$$

Now, in total, we have

$$\begin{aligned}\frac{d\hat{\overrightarrow{\Pi}}}{dt} = -e\left\{\frac{\partial \overrightarrow{A}}{\partial t} + \left(\overrightarrow{\nabla} \Phi_{\alpha}\right)\right\} + ec^{\alpha} \sum_{i,j} \left(\hat{\alpha_i}\right)\left(\nabla_j \left(A_{\alpha}\right)_i - \frac{1}{\hbar}\hbar_{\alpha}^{\alpha} |\hat{x}|^{1-\alpha} \nabla_i A_j\right) e_j \\ + \frac{1}{\hbar}\hbar_{\alpha}^{\alpha} c^{\alpha}\left[|\hat{x}|^{1-\alpha}, \overrightarrow{\nabla}\right] \hat{\overrightarrow{\alpha}} \cdot \hat{\overrightarrow{p}}.\end{aligned} \tag{43}$$

Then, with

$$-\overrightarrow{E}_{\alpha} = \frac{\partial \overrightarrow{A}}{\partial t} + \overrightarrow{\nabla} \Phi_{\alpha}, \tag{44}$$

and if $A_{\alpha} = \frac{1}{\hbar}\hbar_{\alpha}^{\alpha} |\hat{x}|^{1-\alpha} \overrightarrow{A}$, one has

$$\frac{d\hat{\overrightarrow{\Pi}}}{dt} = e\overrightarrow{E}_{\alpha} + e\frac{1}{\hbar}\hbar_{\alpha}^{\alpha} c^{\alpha} |\hat{x}|^{1-\alpha} \sum_{i,j} \left(\hat{\alpha_i}\right)\left(\nabla_j A_i - \nabla_i A_j\right) e_j + \frac{1}{\hbar}\hbar_{\alpha}^{\alpha} c^{\alpha}\left[|\hat{x}|^{1-\alpha}, \overrightarrow{\nabla}\right] \hat{\overrightarrow{\alpha}} \cdot \hat{\overrightarrow{p}}. \tag{45}$$

By applying equation (28) and performing some simplifications, we obtain

$$\frac{1}{\hbar}\hbar_{\alpha}^{\alpha} c^{\alpha} |\hat{x}|^{1-\alpha} \sum_{i,j} \left(\hat{\alpha_i}\right)\left(\nabla_j A_i - \nabla_i A_j\right) e_j = \sum_{i,j} \left(v_i\right)\left(\nabla_j A_i - \nabla_i A_j\right) e_j = \overrightarrow{v} \times \operatorname{curl} \overrightarrow{A}. \tag{46}$$

Subsequently, we have

$$\frac{d\hat{\overrightarrow{\Pi}}}{dt} = e\left(\overrightarrow{E}_{\alpha} + \overrightarrow{v} \times \overrightarrow{B}\right) + \frac{1}{\hbar}\hbar_{\alpha}^{\alpha} c^{\alpha}\left[|\hat{x}|^{1-\alpha}, \overrightarrow{\nabla}\right] \hat{\overrightarrow{\alpha}} \cdot \hat{\overrightarrow{p}}, \tag{47}$$

with $\operatorname{curl} \overrightarrow{A} = \overrightarrow{B}$. As evident, equation (47) represents a α-Lorentz force in the classical case, describing the force exerted by the electromagnetic field on an electron with an electric charge e.

Similar to the velocity in equation (28), the impact of CFQM on the Lorentz force is prominently featured in equation (47). In the limit of $\alpha \to 1$, we obtain

$$\frac{d\overrightarrow{\hat{\Pi}}}{dt} = e\left(\overrightarrow{E} + \overrightarrow{v} \times \overrightarrow{B}\right), \tag{48}$$

which corresponds to the classical form of the Lorentz force.

Let us now turn to a discussion of our results. It is evident that $\overrightarrow{\hat{x}}$ does not adhere to classical equations of motion. However, a classical equation of motion can be determined for the operator $\overrightarrow{\hat{\Pi}}$. Interestingly, equation (47) formally resembles its classical counterpart, but it is important to note that expectation values from equation (48) are not practical due to the Zitterbewegung, with a reduction in velocity. At best, projecting the even contributions from (48) yields result relevant to a classical single-particle description. Equation (47) highlights how CFD alters the Lorentz force, introducing deformations as a result. Likewise, equation (28) shows that CFD also affects velocity. Notably, the application of CFQM are found to impact Ehrenfest's theorem.

4. Conformable fractional continuity equation

We define $\overline{\psi} \equiv \psi^{\dagger}\gamma^0$, where $\psi^{\dagger}$ is the complex conjugate of the row vector corresponding to the column vector ψ. Then, by taking the adjoint of equation (16):

$$\overline{\psi}\left\{-i\hbar^{\alpha}\gamma^0\partial_0^{\alpha} + i\hbar^{\alpha}\left(\gamma^k\right)^{\dagger}\overleftarrow{\partial}^{\alpha} - m^{\alpha}c^{\alpha}\right\} = 0, \tag{49}$$

with $\overleftarrow{\partial}^{\alpha} = \partial_k^{\alpha}$ acts from the right on $\overline{\psi}$, also, from the Hermicity of γ^{μ}, we have

$$(\gamma^{\mu})^{\dagger} = \gamma^0\gamma^{\mu}\gamma^0, \text{ and } \left(\alpha^k\right)^{\dagger} = \alpha^k. \tag{50}$$

Also, the Dirac equation and its adjoint can be obtained through the variation of the action using the conformable fractional Lagrangian density, which is expressed as follows

$$\mathcal{L}_{\alpha} = -i\hbar^{\alpha}c^{\alpha}\overline{\psi}\gamma^{\mu}\partial_{\mu}^{\alpha}\psi - m^{\alpha}c^{2\alpha}\overline{\psi}\psi. \tag{51}$$

Then, if one performs variation with respect to ψ, the result is the adjoint Dirac equation. Conversely, varying it with respect to $\overline{\psi}$ yields the Dirac equation. However, from equations (16), (49), we can obtain the following the α-continuity equation

$$\overline{\psi}\gamma^k\overleftarrow{\partial}^{\alpha}\psi - \overline{\psi}\gamma^0\partial_0^{\alpha}\psi + \overline{\psi}\gamma^0\partial_0^{\alpha}\psi - \overline{\psi}\gamma^k\partial_k^{\alpha}\psi = 0. \tag{52}$$

In a more elegant concise form, equation (52) becomes

$$D_{\mu}^{\alpha}\mathcal{J}_{\alpha}^{\mu} = D_t^{\alpha}\rho_{\alpha} + D_x^{\alpha}\mathcal{J}_{\alpha}^{k} = 0, \tag{53}$$

where the four-vector α-current density (the α-probability density and the α-probability flux) is given as follows

$$\mathcal{J}_{\alpha}^{\mu} : \begin{cases} \rho_{\alpha} = \overline{\psi}\gamma^0\psi = \psi^{\dagger}\psi = |\psi|^2, \\ \mathcal{J}_{\alpha}^{k} = \overline{\psi}\gamma^k\psi = \psi^{\dagger}\alpha^k\psi. \end{cases} \tag{54}$$

One can see from equation (54) that CFQM does not affect the four-vector current. However, the continuity equation itself is affected.

5. Correspondence principle in CFQM

The correspondence principle asserts that the behavior of systems described by the theory of quantum mechanics mirrors classical physics when quantum numbers become large. For example, at high energies, quantum calculations must align with classical counterparts. Here, we attempt examine how large quantum numbers can give rise to classical conduct. Consider the following conformable fractional quantum harmonic oscillator [39]:

$$E_n = \hbar\omega \left(2n + l + \frac{3}{2}\right)^{\frac{1}{\alpha}}, \tag{55}$$

n, l are quantum numbers, with ω is the angular frequency of the oscillator. The energy is usually described by the single quantum number $N = 2n + l$. ($N = 0, 1, 2, \dots$) But, the classical fractional harmonic oscillator in three dimensions is

$$E = \frac{1}{2} m^{\alpha} \omega^{2\alpha} \frac{x^{\alpha}}{\alpha}. \tag{56}$$

Thus, from equations (55) and (56), the quantum number has the value

$$N = \frac{x^{\alpha^2}}{\hbar^{\alpha} 2^{\alpha} \alpha^{\alpha}} m^{\alpha^2} \omega^{(2\alpha^2 - \alpha)} - \frac{3}{2}. \tag{57}$$

Now, for typical values m=1 Kg, $\omega = 1\,\mathrm{rad.s^{-1}}$, and x = 1m, one can get

$$N = \frac{1}{\hbar^{\alpha} 2^{\alpha} \alpha^{\alpha}} - \frac{3}{2}. \tag{58}$$

Then, for a better understanding the correspondence limit between quantum and classical harmonic oscillator, we plot equation (58).

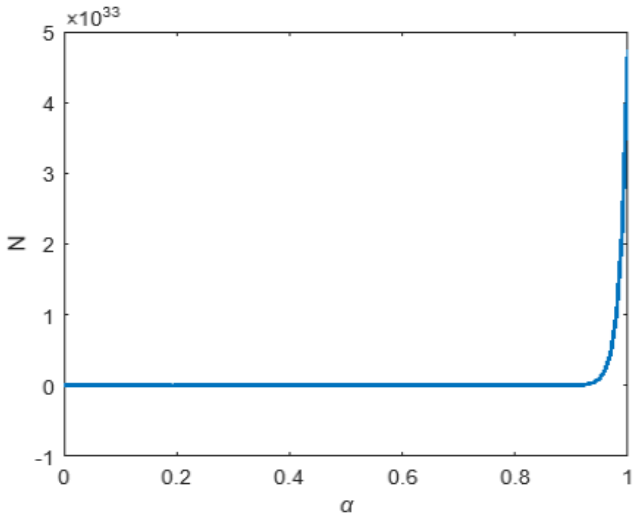

Fig. 3. N versus α (plot of equation (58))

In Fig. 3, we can see that only when the fractional parameter approaches unity, the system is in the correspondence limit, and for $\alpha = 1$,

$$N = \frac{1}{2\hbar} - \frac{3}{2} = 0.474126 \times 10^{34}, \tag{59}$$

which is a very large number; this, in turn confirms that the system is in the correspondence limit.

6. Conclusion and remarks

In this research, we have analytically investigated the classical limit of the Dirac equation interacting with electromagnetic potential within the CFQM, employing Ehrenfest's theorem. Our analysis successfully reveals the influence of the CFD on the classical limit, resulting in α-deformed classical equations. Our results confirm the feasibility of achieving the classical limit within the framework of CFDM. Once again, Ehrenfest's theorem proves effective in deriving classical limit of the Dirac equation, irrespective of the effects present in the relativistic system. Therefore, we emphasize the importance of such type of theorems. Moreover, it is shown that the inclusion of CFD does not alter the current density four-vector. Additionally, CFD appears to affect the correspondence limit between the quantum system and its classical counterpart.

Clearly, our findings serve as a valuable resource for further investigations, including nonrelativistic and semiclassical limits, as well as scenarios involving other types of fractional derivatives. Expanding this study to encompass more general cases, such as particles with arbitrary higher spins, would be a promising avenue for future research. Notably, in the limit as $\alpha \to 1$, the α-deformed Dirac and the obtained classical equations reduce to those of ordinary QM, confirming that our findings are consistent with and reducible to those found and discussed in the literature.

Funding

This research received no external funding.

Conflicts of Interest

The author declares no conflict of interest.

References

[1] Paul A.Tipler, Ralph A.Llewellyn, Modern Physics, (5ed.) W. H. Freeman and Company, 2008.

[2] N.Bohr, Über die Serienspektra der Elemente, *Z. Physik*, **423**(1920), no. 2, 423–469. DOI: 10.1007/BF01329978

[3] P.Ehrenfest, Bemerkung Über die angeдherte Gьltigkeit der klassischen Mechanik innerhalb der Quantenmechanik, *Z. Physik*, **45**(1927), 455. DOI: 10.1007/BF01329203

[4] G.Friesecke, M.Koppen, On the Ehrenfest theorem of quantum mechanics, *J. Math. Phys.*, **50**(2009), 082102. DOI: 10.1063/1.3191679

[5] Krьger, H. Classical limit of real Dirac theory: Quantization of relativistic central field orbits, *Found. Phys*, **23**(1993), 1265. DOI: 10.1007/BF01883679

[6] W. R.Greenberg, A.Klein, C.T.Li, Invariant tori and Heisenberg matrix mechanics: a new window on the quantum-classical correspondence, *Phys. Rep.*, **264**(1996), no. 1-5, 167. DOI: 10.1016/0370-1573(95)00036-4

[7] A.O.Bolivar, Classical limit of fermions in phase space, *J. Math. Phys.*, **42**(2001), no. 9, 4020. DOI: 10.1063/1.1386411

[8] I.Haouam, Ehrenfest's theorem for the Dirac equation in noncommutative Phase-Space, *Math. Comput. Sci.*, **4**(2024), no. 4, 53. DOI: 10.30511/mcs.2023.2013583.1143

[9] A.J.Makowski, Exact classical limit of quantum mechanics: Central potentials and specific states, *Phys. Rev. A*, **65**(2002), no. 3, 032103. DOI: 10.1103/PhysRevA.65.032103

[10] K.G.Kay, Exact wave functions from classical orbits. II. The Coulomb, Morse, Rosen-Morse, and Eckart systems, *Phys. Rev. A*, **65**(2002), no. 3, 03210. DOI: 10.1103/PhysRevA.65.032101

[11] R.Alicki, Search for a border between classical and quantum worlds, *Phys. Rev. A*, **65**(2002), no. 3, 034104. DOI: 10.1103/PhysRevA.65.034104

[12] I.Haouam, Classical limit and Ehrenfest's theorem versus non-relativistic limit of noncommutative Dirac equation in the presence of minimal uncertainty in momentum, *Int. J. Theor. Phys.*, **62**(2023), 189. DOI: 10.1007/s10773-023-05444-3

[13] M. L.Liang, Y.J.Sun, Quantum-classical correspondence of the relativistic equations, *Ann. Phys.*, (2004), no. 1, 314. DOI: 10.1016/j.aop.2004.06.006

[14] M.L.Liang, et al., Quantum-classical correspondence of the Dirac equation with a scalar-like potential, *Pramana. J. Phys.*, **72**(2009), 777. DOI: 10.1007/s12043-009-0070-3

[15] H.Spohn, Semiclassical limit of the Dirac equation and spin precession, *Ann. Phys.*, **282**(2000), no. 2, 420. DOI: 10.1006/aphy.2000.6039

[16] I.Haouam, L.Chetouani, The Foldy-Wouthuysen transformation of the Dirac equation in noncommutative phase-space, *J. Mod. Phys.*, **9**(2018), 2021. DOI: 10.4236/jmp.2018.911127

[17] I.Haouam, Foldy–Wouthuysen Transformation of Noncommutative Dirac Equation in the Presence of Minimal Uncertainty in Momentum, *Few-Body. Syst.*, **64**(2023), no. 9. DOI: 10.1007/s00601-023-01790-4

[18] J.T.Machado, et al,. Recent history of fractional calculus, *Commum. Nonlinear Sci. Numer. Simulat.*, **16**(2013), 1140. DOI: 10.1016/j.cnsns.2010.05.027

[19] R.Herrmann, Fractional Calculus: An Introduction for Physicists, World Sci. Publishing Singapore, 2011.

[20] J.T.Machado, et al., Fractional Calculus: Quo Vadimus? (Where are we Going?) *Frac. Calc. Appl. Anal.*, **18**(2015), 495. DOI: 10.1515/fca-2015-0031

[21] G.W.Leibniz, Letter from Hanover, Germany to G.F.A. L'Hospital, September 30, 1695, Leibniz Mathematis-che Schriften, Olms-Verlag, Hildesheim, Germany, 1962, 301–302, first published in 1849.

[22] J.Hadamard, *Journal de Mathmatiques Pures et Appliques*, **8**(1892), 101.

[23] M.Caputo, Linear models of dissipation whose Q is almost frequency independent–II. Geophys, *J. Int.*, **13**(1967), no. 5, 529. DOI: 10.1111/j.1365-246X.1967.tb02303.x

[24] Y.Povstenko, Essentials of Fractional Calculus, In: Fractional Thermoelasticity. Solid Mechanics and Its Applications, vol. 219, Springer, Cham., 2015. DOI: 10.1007/978-3-319-15335-3_1

[25] K.Oldham, J.Spanier, The fractional calculus: Theory and applications of differentiation and integration to arbitrary order, Elsevier, 1974.

[26] I.Podlubny, Fractional differential equations: an introduction to fractional derivatives, fractional differential equations, to methods of their solution and some of their applications, Elsevier, 1998.

[27] R.Hilfer, Applications of fractional calculus in physics, *World scientific Singapore*, **35**(2000), no. 12.

[28] A.A.Kilbas, H.M.Srivastava, J.J.Trujillo, Theory and Applications of Fractional Differential Equations, Elsevier, Amsterdam, vol. 204, 2006.

[29] I.Podlubny, Fractional Differential Equations. Academic Press, San Diego, 1999.

[30] R.Khalil, et al., A new definition of fractional derivative, *J. Comput. Appl. Math.*, **65**(2014), 264. DOI: 10.1016/j.cam.2014.01.002

[31] T.Abdeljawad, On conformable fractional calculus, *J. Comput. Appl. Math.*, 279, 57 (2015). DOI: 10.1016/j.cam.2014.10.016

[32] D.R.Anderson, Taylor's Formula and Integral Inequalities for Conformable Fractional Derivatives. In: Pardalos, P., Rassias, T. (eds) Contributions in Mathematics and Engineering. Springer, Cham., 2016. DOI: 10.1007/978-3-319-31317-7_2

[33] A.Atangana, D.Baleanu, A.Alsaedi, New properties of conformable derivative, *Open. Math.*, **13**(2015), no. 1, 000010151520150081. DOI: 10.1515/math-2015-0081

[34] E.Rabei, M.Al-Masaeed, A.Al-Jamel, Solution of the conformable angular equation of the Schrɳdinger equation, *Progress in fractional differentiation and applications*, **10**(2024), no. 1, 137. DOI: 10.18576/pfda/100113

[35] H.Karayer, D.Demirhan, F.Büyükkılıç, Conformable Fractional Nikiforov-Uvarov Method, *Comm. Theor. Phys.*, **66**(2016), 12. DOI: 10.1088/0253-6102/66/1/012

[36] Y.Zhang, et al., PT symmetry in a fractional Schrɳdinger equation, *Laser & Photonics Reviews*, **10**(2016), no. 3, 526. DOI: 10.1002/lpor.201600037

[37] D.R.Anderson, D.J.Ulness, Properties of the Katugampola fractional derivative with potential application in quantum mechanics, *J. Math. Phys.*, **56**(2015), 063502. DOI: 10.1063/1.4922018

[38] W.S.Chung, S.Zare, H.Hassanabadi. Investigation of conformable fractional schrɳdinger equation in presence of killingbeck and hyperbolic potentials, *Commun. Theor. Phys.*, **67**(2017), 250. DOI: 10.1088/0253-6102/67/3/250

[39] F.S.Mozaffari, et al., On the Conformable Fractional Quantum Mechanics, *J. Korean Phys. Soc.*, **72**(2018), 980. DOI: 10.3938/jkps.72.980

[40] M.Al-Masaeed, E.M.Rabei, A.Al-Jamel, Wkb approximation with conformable operator, *Mod. Phys. Lett. A*, **37**(2022), no. 22, 2250144. DOI: 10.1142/S0217732322501449

[41] U.N.Katugampola, (2014). A new fractional derivative with classical properties. arXiv preprint arXiv:1410.6535.

[42] W.S.Chung, I.Haouam, H.Hassanabadi, Quantum mechanics on a circle with a finite number of α-uniformly distributed points, *Phys. Lett. A*, **485**(2023), 129098. DOI: 10.1016/j.physleta.2023.129098

[43] Y.C.Enesiz, D.Baleanu, A.Kurt, O.Tasbozan, New exact solutions of Burgers' type equations with conformable derivative, *Waves Rand. Complex Media 27*, **103**(2017). DOI: 10.1080/17455030.2016.1205237

[44] H.W.Zhou, S.Yang, S.Q.Zhang, Conformable derivative approach to anomalous diffusion, *Physica A Stat. Mech. Appl.*, **491**(2018), 1001. DOI: 10.1016/j.physa.2017.09.101

[45] F.Mainardi, Fractional Calculus: Some Basic Problems in Continuum and Statistical Mechanics, Fractals and Fractional Calculus in Continuum mechanics, Springer-Verlag, New York, 1997.

[46] F.S.Mozaffari, et al., Investigation of the Dirac Equation by Using the Conformable Fractional Derivative, *J. Korean Phys. Soc.*, **72**(2018), 987. DOI: 10.3938/jkps.72.987

[47] W.S.Chung, Fractional Newton mechanics with conformable fractional derivative, *J. Comput. Appl. Math.*, **290**(2015), 150. DOI: 10.1016/j.cam.2015.04.049

[48] N.Ahmed, et al., New exact solutions to space–time fractional telegraph equation with conformable derivative, *Int. J. Mod. Phys. B*, **37**(2023), no. 31, 2350275. DOI: 10.1142/S0217979223502752

[49] M.J.Lazo, D.F.M.Torres, Variational calculus with conformable fractional derivatives, *IEEE/CAA Journal of Automatica Sinica*, **4**(2017), no. 2), 340. DOI: 10.1109/JAS.2016.7510160

[50] D.R.Anderson, E.Camrud, D.J.Ulness, On the nature of the conformable derivative and its applications to physics, *J. Fract. Calc. Appl.*, **10**(2019), no. 2, 92.

[51] I.Haouam, The non-relativistic limit of the DKP equation in noncommutative phase-space, *Symmetry*, **11**(2019), no. 2, 223. DOI: 10.3390/sym11020223

Классический аспект уравнения Дирака в контексте согласованной дробной производной

Ильяс Хауам
Лаборатория математической и субатомной физики (LMPPS)
Университет Братьев Ментури
Константин 25000, Алжир

Аннотация. В этой статье в контексте конформной дробной производной (CFD) и с использованием теоремы Эренфеста мы исследуем классический предел уравнения Дирака в рамках конформной дробной квантовой механики. Это приводит к получению деформированных классических уравнений. Здесь мы оцениваем эффективность теоремы Эренфеста при выводе классического предела с учетом CFD. Также мы исследуем принцип соответствия под влиянием CFD. Кроме того, мы получаем конформное дробное уравнение непрерывности.

Ключевые слова: согласованное дробное уравнение Дирака, согласованное дробное уравнение непрерывности, теорема Эренфеста, классический предел, принцип соответствия, согласованная квантовая механика.

EDN: QSNXSP
УДК 524.8

FRW Viscous Cosmological Model with Time Periodically Varying Deceleration Parameter In f(R, T)Gravity

M. Ramanamurty*
Rajamahanthi Santhikumar†
Aditya Institute of Technology and Management
K.Kotturu, Tekkali, Srikakulam Dist, Andhrapradesh-532201, India
K. Sobhanbabu‡
University Collage of Engineering-JNTUK
Narasaraopeta, Guntur, Andhra Pradesh-522616, India

Received 03.10.2024, received in revised form 09.12.2024, accepted 14.01.2025

Abstract. This research paper investigates the dynamics of a Friedmann–Robertson–Walker cosmological model characterized by perfect fluid pressure and barotropic bulk viscous pressure. By obtaining exact solutions to Einstein's field equations with a time-varying periodic deceleration parameter, the study reveals periodic behaviour in most parameters, attributed to the influence of a cosine function in the deceleration parameter. The analysis delves into the physical and dynamical implications of this model, particularly highlighting how negative pressure contributes to the late-time expansion of the universe.

Keywords: bulk viscous fluid, time period, decelerating parameter, accelerating expansion.

Citation: M. Ramanamurty, R. Santhikumar, K. Sobhanbabu, FRW Viscous Cosmological Model with Time Periodically Varying Deceleration Parameter In f(R,T)Gravity, J. Sib. Fed. Univ. Math. Phys., 2025, 18(2), 243–252. EDN: QSNXSP.

1. Introduction and preliminaries

Recent observational evidence, notably from Riess et al. (1998) [1] confirms that our universe is expanding at an accelerating rate. This accelerated expansion, particularly the "dark energy era"(Weinberg 1998) [2] , presents a significant cosmological puzzle. The driving force behind this acceleration is thought to be a mysterious entity with huge negative pressure. Numerous candidates have been proposed to explain dark energy, including the cosmological constant, quintessence, phantom energy, tachyon fields, and Chaplygin gas (Tegmark et al. 2004 [3]; Padmanabhan et al. 2002 [4]; Bento et al. 2002 [5]; Nojiri et al. 2003 [6]). Another intriguing epoch in the universe's history is the inflationary phase, a period of rapid expansion preceding the radiation-dominated era. Proposed in the early 1980s, inflation addresses shortcomings of the standard Big Bang model (Guth 1981 [7]; Linde 1983 [9], 1994 [8]). While Planck observations have provided constraints on inflationary parameters, direct observational evidence remains elusive. Modified gravity theories offer a compelling framework to explain both early and late-time acceleration. These theories, such as f(R) gravity, Gauss–Bonnet gravity (f(G)), and f(T) gravity, modify Einstein's general relativity. For instance, replacing the Einstein–Hilbert action with a function f(R) of the Ricci scalar R can yield cosmic acceleration. Copeland et al. provide a comprehensive review of f(R) gravity, while Bamba et al. [10]. review dark energy models with early

*ramanamurtymuddada@gmail.com https://orcid.org/0009-0009-4086-486X
†skrmahanthi@gmail.com https://orcid.org/0000-0001-5122-3800
‡ksobhanjntu@gmail.com https://orcid.org/0000-0002-2991-7651

inflation and late-time acceleration. Harko et al. (2011) [11] introduced f(R,T) gravity, a modified theory incorporating both the Ricci scalar R and the trace T of the energy-momentum tensor Reddy et al. (2012, 2013) [12, 13] investigated LRS Bianchi type-II and type-III cosmological models within this framework. Santhikumar et al. (2017) [15] studied accelerating cosmological model in f(R,T) gravity. Explaining the current accelerating expansion and the transition from a decelerating past is crucial in cosmological modeling. A varying deceleration parameter offers a mechanism to describe this phase transition in isotropic and anisotropic universe models. The deceleration parameter quantifies the rate at which the universe's expansion slows down. Studies of oscillating universe models with quintom matter demonstrate alternating phases of deceleration and acceleration, with a periodically varying Hubble parameter and keeps positive for time periodic deceleration parameter (TPVDP) (M. Shen and L. Zhao, 2014) [16]. Time periodically varying deceleration parameter models within f(R,T) gravity, investigated by Aktas and A?lin (2017) [17], show vanishing string tension density in a cyclic universe scenario. N. Ahmed and Alamri (2019) [18] suggest that the late-time acceleration could arise from a negative cosmological constant with a TPVDP. Hulka and Singh (2022) [19] find that positive energy density and negative pressure throughout the universe's evolution guarantee late-time expansion. Motivated by these investigations, this paper explores a Friedmann-Robertson-Walker viscous cosmological model with a TPVDP within the framework of f(R,T) gravity. The paper is structured as follows: Section 2: Brief reviews on f(R,T) gravity and its field equations of the model. Section 3: Presents solutions to the field equations. Section 4: Analyzes the physical properties of the model. Section 5: conclusions.

2. Brief reviews on f(R,T) gravity and its field equations of the model

Assuming the universe to be homogeneous and Isotropic, the FRW metric can be written as

$$ds^2 = -dt^2 + a^2(t)\left[\frac{dr^2}{1-kr^2} + r^2\left(\mathrm{d}\theta^2 + \sin^2\theta \mathrm{d}\varnothing^2\right)\right] \tag{1}$$

where a(t) is the scale factor of the universe and k = –1, 0, +1 represents the model for open, flat and closed universe respectively

The filed Eg. of f(R,T) gravity are driven from Hilbert–Einstein type variational principal by taking the action

$$S = \frac{1}{16k}\left[\int \{f(R,T) + L_m\}\sqrt{-g}\, d^4x\right] \tag{2}$$

where f(R,T) is an orbitrary function of the Ricci scalar "R"."T" is the trace of stress-energy tensor of the matter " T_{ij}" and "L_m" is the matter Lagrangian density

we define the stress energy tensor of the matter as

$$T_{\mathrm{ij}} = \frac{-2}{\sqrt{g}}\frac{\delta(\sqrt{-g}L_m)}{\delta 8^{\mathrm{ij}}} \tag{3}$$

And its trace by T = 8^{ij} T_{ij} respectively

By Assursing that $L_m$of matter depends only on the metric tensor components 8_{ij} and not on its derivatives, we obtain

$$T_{\mathrm{ij}} = g_{\mathrm{ij}}L_m - 2\frac{\partial L_m}{\partial 8^{\mathrm{ij}}} \tag{4}$$

Now by varying the action " S" of the gravitational field with respect to the metric tensor components g^{ij},we obtain the field equation of f(R,T) gravity as

$$f(R,T)R_{\mathrm{ij}} - \frac{1}{2}f(R,T)g_{\mathrm{ij}} + (g_{\mathrm{ij}}\,\boxdot - \nabla_i\nabla_j)\,f_R(R,T) = 8\pi T_{\mathrm{ij}} - f_T(R,T)T_{\mathrm{ij}} - f_T(R,T)\theta_{\mathrm{ij}} \quad (5)$$

$$\text{where } \theta_{\mathrm{ij}} = T_{\mathrm{ij}} + g_{\mathrm{ij}}L_m - 2g^{\mathrm{lk}}\frac{\partial^2 L_m}{\partial g^{\mathrm{ij}}\partial g^{\mathrm{lm}}} \quad (6)$$

$$\text{where } f_R = \frac{\delta f(R,T)}{?\mathrm{R}},\ f_{T=}\frac{\delta f(R,T)}{?\mathrm{T}} \ \text{ and } \ \boxdot = \nabla^i\nabla_i \quad (7)$$

∇_i is the covariant derivative and T_{ij} is the standard matter energy-momentum tensor derived from Lagrawgian L_m. It may be noted that when f(R,T)≡ f(R) the eq. 5 yields, the field equation of f(R) gravity.

The problem of the perfect fluid described by an energy density ρ, effective pressure and four velocity-u^i is complicated since that is no unique definition of the matter Lagrangian. However, here, we assume that the stress energy tensor of the matter is given below

and the matter Lagrangian can be taken as $L_m = -\overrightarrow{p}$ and we have

$$u^i\nabla_i\nabla_j = 0,\ u^iu_j = 1 \quad (8)$$

With the use of equation (6) , we obtain for the variation of stress energy tensor of perfect fluid the expression

$$\theta_{\mathrm{ij}} = -2T_{\mathrm{ij}} - \overrightarrow{p}\,g_{\mathrm{ij}} \quad (9)$$

Generally, the field equations also depends through the tensor θ_{ij}, on the physical nature of the matter field. Hence, in the case of f(R,T) gravity depends on the nature matter source,we obtain serval theoretical models corresponding to each choice of f(R,T)

Assusing

$$f(R,T) = R + 2f(T) \quad (10)$$

as a first choice where f(T) is an arbitrary function of the trace of stress-energy of matter.

We get the gravitational field equation of f(R,T) gravity from equation (5) as

$$R_{\mathrm{ij}} - \frac{1}{2}Rg_{\mathrm{ij}} = 8\pi T_{\mathrm{ij}} - 2f^1(T)T_{\mathrm{ij}} - 2f^1(T)\theta_{\mathrm{ij}+f(T)g_{\mathrm{ij}}} \quad (11)$$

Where the prime denotes differentiation with respect to the argument.

If the matter source is a perfect fluid then the field equations become

$$R_{\mathrm{ij}} - \frac{1}{2}g_{\mathrm{ij}}R = 8\pi T_{\mathrm{ij}} + 2f^1(T)T_{\mathrm{ij}} + \left[2\overrightarrow{p}\,f^{'}(T) + f(T)\right]g_{\mathrm{ij}} \quad (12)$$

Using co-moving coordinates and particular choice of the function given by (Herko et. al. 2011)

$$f(T) = \mu T,\ \mu \text{ is constant} \quad (13)$$

$$R_{\mathrm{ij}} - \frac{1}{2}8_{\mathrm{ij}}R = 8\pi T_{\mathrm{ij}} + 2\mu T_{\mathrm{ij}} + [2\overrightarrow{p}\,\mu + \mu T]\,g_{\mathrm{ij}} \quad (14)$$

3. Field equations

Using Equation & we obtain

$$2\frac{\ddot{a}}{a} + \left(\frac{\dot{a}}{a}\right)^2 + \frac{k}{a^2} = (8\pi + 3\mu)\overrightarrow{p} - \mu\rho \quad (15)$$

$$3\left(\frac{\dot{a}}{a}\right)^2 + 3\left(\frac{k}{a^2}\right) = -(8\pi + 3\mu)\rho + \mu\overrightarrow{p} \tag{16}$$

where an overhead dot denotes differentials with respect to t.

Solution and the Model

From the above two independent field Equations & the field equations are highly non-linear in nature and therefore we use the following placesible physical condition

(i) For baratropic fluid the combined effect of proper pressure and the barotropic bulk viscous pressure can be expressed as

$$\overrightarrow{p} = p - 3H = \epsilon\rho \tag{17}$$

$$\text{where } p = \in_0 \rho, \quad 0 \leqslant \in_0 \leqslant 1 \tag{18}$$

(ii) We use the time periodically varying decleration parameter (TPVDP) of the form [16]

$$q = m\,Cos(nt) - 1 \tag{19}$$

where m and n are positive constants. This type of deceleration parameter is known as TPVDP. The deceleration parameter play a role in determine the nature of the constructed

models of the Universe i.e decelerating (or) accelerating in nature. According to the range values of "q" the universe exhibits the expansion in the following way [20, N.Hulke et.al (2020)], [21, G.P.Singh et.al (2020)].

$q > 0$: Decelerating expansion

$q = 0$: Expansion with constant rate

$-1 < q < 0$: Accelerating power law expansions

$q = -1$: Exponential expansion / de sitter expansion

$q < -1$: Super exponential expansion.

From the consideration form of "q" in Eg(20), the deceleration parameter shows periodic nature due to the presence of cos(nt).

The deceleration parameter "q" lies in the interval $-(m+1) \leqslant q \leqslant (m-1)$.

Here we observed that

(i) For m=0, the deceleration parameter q=–1 and the universe exhibits exponential expansion de sitter expansion.

(ii) For m $\in (0, 1)$, the deceleration parameter "q" becomes negative and leades to decelerated expansion in the periodic way.

(iii) For m=1, q lies in the interval $[-2, 0]$ it indicates that the universe enolves from expension with constant rate to super exponential expansion in a periodic way followed by accelerating power law expansion to de sitter expansion.

(iv) For $m > 1$, phase transition taken place from deceleratives phase to accelerations phase in a periodic way where the universe starts will a deceleratives expansion and evolves to super exponential expansion.

By N. Hulke (2022) [19] the following are rang of the parameter m for fixed "n" values.

n	0.01	0.02	0.03	0.04	0.05	0.06	0.07	0.08	0.09	0.10
Inter	$0.34 \leqslant$	$0.35 \leqslant$	$0.37 \leqslant$	$0.39 \leqslant$	$0.43 \leqslant$	$0.49 \leqslant$	$0.59 \leqslant$	$0.74 \leqslant$	$1.02 \leqslant$	$1.70 \leqslant$
of	$m \leqslant$	$m \leqslant$	$m \leqslant$	$m \leqslant$	$m \leqslant$	$m \leqslant$	$m \leqslant$	$m \leqslant$	$m \leqslant$	$m \leqslant$
m	0.64	0.66	0.69	0.74	0.82	0.94	1.11	1.39	1.93	3.20

Clearly for n=0.01 & $0.34 \leqslant m \leqslant 0.64$ reshows us $q < 0$ it represent the model is accelerating in nature for n=0.10 & $1.70 \leqslant m \leqslant 3.20$, the model show phase transion from decelerating phase to accelerating phase. Here q is from positive to negative. Hence the complete phase transition scenario of the model is discussed in this range only. In order to obtaion the Hubble parameter from equation we used the relation between Hubble parameter and deceleration parameter on

$$q = \frac{1}{\mathrm{dt}}\left(\frac{1}{H}\right) - 1 \tag{20}$$

Hubble parameter

$$H = \frac{\dot{a}}{a} \tag{21}$$

Deceleration parameter

$$q = \frac{-\mathrm{a}\ddot{\mathrm{a}}}{\dot{a}^2} \tag{22}$$

By Eq (19) & (21) we have

$$H = \frac{w}{m\mathrm{Sin}(\mathrm{nt}) + nl} \tag{23}$$

where "l" is integration constant and we obtain

$$a(t) = c \cdot \exp\left\{\frac{2}{\sqrt{nlm - m^2}} \tan^{-1}\left(\frac{nl\tan\left(\frac{\mathrm{nt}}{2}\right) + m}{\sqrt{nlm - m^2}}\right)\right\} \tag{24}$$

where c is integration constant

$$\mathrm{ds}^2 = -\mathrm{dt}^2 + c^2 \cdot \exp\left\{\frac{4}{\sqrt{nlm - m^2}} \tan^{-1}\left(\frac{nl\tan\left(\frac{\mathrm{nt}}{2}\right) + m}{\sqrt{nlm - m^2}}\right)\right\} \times \times \left[\frac{\mathrm{dr}^2}{1 - kr^2} + r^2\left(\mathrm{d}\theta^2 + \sin^2\theta d\varnothing^2\right)\right] \tag{25}$$

4. Physical properties of the model

Eq (25) represents FRW Viscous fluid model. Using equation (15)–(18) & (23), (24) Density

$$\rho = \left[\frac{1}{\varepsilon - (8\pi + 3\mu)}\right]\left[3\left(\frac{\dot{a}}{a}\right)^2 + 3\left(\frac{k}{a^2}\right)\right] \tag{26}$$

$$\rho = \left[\frac{3}{\varepsilon - (8\pi + 3\mu)}\right]\left[\left(\frac{n}{n\,\sin nt + nl}\right)^2\right] + + k\left[\mathrm{c} \cdot \exp\left\{\frac{2}{\sqrt{nlm - m^2}} \tan^{-1}\left(\frac{nl\tan\left(\frac{\mathrm{nt}}{2}\right) + m}{\sqrt{nlm - m^2}}\right)\right\}\right]^{-1} \tag{27}$$

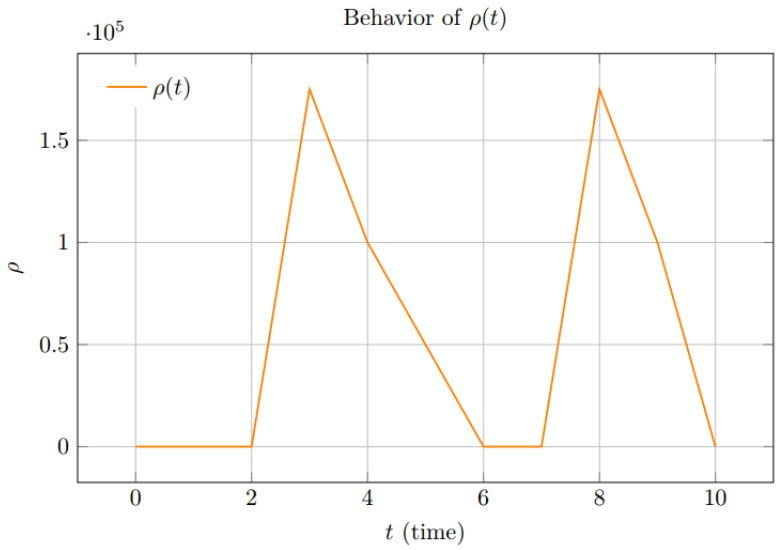

Fig. 1. Energy Density ρ Vs. Time t

The behavior energy density ρ(t) of from the Fig. 1 is the term involving sin(nt) introduces oscillations in the function. The exponential term in the denominator influences the decay or growth, depending on the parameter values. Certain values of t may lead to singularities (e. g., when the denominator of trigonometric terms approaches zero).

Bulk viscour pressure

$$\overrightarrow{p} = \varepsilon\left(\left(\frac{3}{\varepsilon-(8\pi+3\mu)}\right)\left[\left(\frac{n}{n\sin \mathrm{nt}+\mathrm{nl}}\right)^2\right]+ \right. \\ \left. +\,\mathrm{k}\left[c\cdot\exp\left\{\frac{2}{\sqrt{\mathrm{nlm}-m^2}}\tan^{-1}\left(\frac{\mathrm{nl}\tan\left(\frac{\mathrm{nt}}{2}\right)+m}{\sqrt{\mathrm{nlm}-m^2}}\right)\right\}\right]^{-1}\right) \quad (28)$$

Pressure

$$p=\varepsilon_0\rho=\varepsilon_0\left(\left[\frac{3}{\varepsilon-(8\pi+3\mu)}\right]\left[\left(\frac{n}{n\sin \mathrm{nt}+nl}\right)^2\right]+ \right. \\ \left. +\,k\left[\mathrm{c}\cdot\exp\left\{\frac{2}{\sqrt{nlm-m^2}}\tan^{-1}\left(\frac{\mathrm{nl}\tan\left(\frac{\mathrm{nt}}{2}\right)+m}{\sqrt{nlm-m^2}}\right)\right\}\right]^{-1}\right) \quad (29)$$

The Behavior of p(t) from the Fig. 2 is the sine term causes periodic oscillations, which dominate the behavior at certain intervals. The exponential term in the denominator moderates the magnitude of pressure, depending on the constants $\mathrm{n}, \mathrm{l}, \mathrm{m}, \mathrm{n}$. Singularities may arise at specific t values due to the denominators in the equation becoming close to zero.

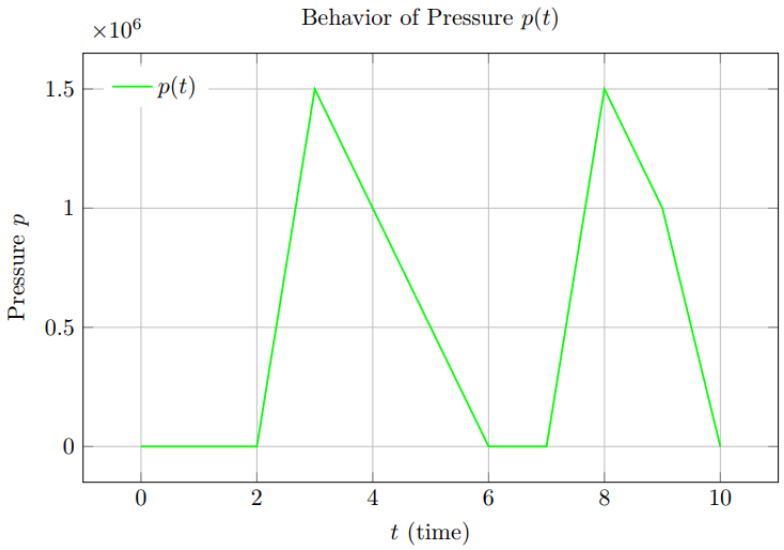

Fig. 2. Pressure p Vs. Time

Bulk viscous coefficient

$$\xi = \left(\frac{p-\varepsilon\rho}{3H}\right) = (\varepsilon_0 - \varepsilon) \times \times \left(\frac{\left[\frac{3}{\varepsilon-(8\pi+3\mu)}\right]\left[\left(\frac{n}{n\sin nt+nl}\right)^2\right] + k\left[\mathrm{c}\cdot\exp\left\{\frac{2}{\sqrt{nlm-m^2}}\tan^{-1}\left(\frac{\mathrm{nl}\tan\left(\frac{\mathrm{nt}}{2}\right)+m}{\sqrt{nlm-m^2}}\right)\right\}\right]^{-1}}{3\,\frac{w}{\mathrm{m}\sin(\mathrm{nt})+nl}} \right) \tag{30}$$

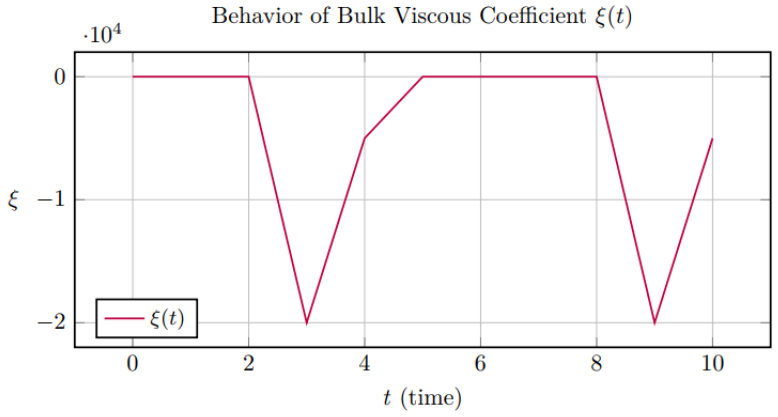

Fig. 3. Bulk viscous coefficient $\xi(t)$ Vs. Time t

The Behaviour of Bulk Viscous Coefficient $\xi(t)$, from the Fig. 3 is the interplay of pressure p , density ρ, and the oscillatory nature of sin(nt) introduces both periodic and nonlinear variations. The denominator msin(nt)+nl may approach zero at specific points, leading to spikes or

singularities in $\xi(t)$. The exponential term moderates the coefficient, while the sin(nt) dependent term introduces periodicity.

Now we discuss the physical nature of the universe represented by eq. (26)–(30). In these two cases universe has a finite life time. It starts a Big bang at t=0. The energy density the scale factor of the universe diverse on finite time, so that the universe has a Big**gd** (Caldwel et al., 2003) [22]. Also as $t \longrightarrow \infty$ the energy density, Pressure, the hubbles parameter, Coefficient of Bulk viscous, viscous pressure vanish. It can be seen that the late times the deceleration parameter because negative. So that the universe accelerates which is in accordance with the recent scenario of accelerated expansion of the universe. It may also be observed that the energy density is always positive irrespective of the fact that the curvature k is positive (or) not.

5. Conclusion

This paper investigated a Friedmann–Robertson–Walker cosmological model within the framework of f(R,T) gravity, as formulated by Harko et al. The model incorporates a time-periodically varying deceleration parameter and considers the pressure of a perfect fluid. Exact solutions to the field equations were obtained using the time-periodically varying deceleration parameter proposed by Ming and Lang. A barotropic equation of state relating the metric potential and bulk viscous pressure was employed to obtain a determinate solution. The resulting cosmological model describes a spatially expanding, non-rotating, and non-singular universe. By fixing the constant parameter n, we observed distinct behaviours of the deceleration parameter. For n = 0.01, the deceleration parameter remains negative throughout the universe's evolution, indicating perpetual acceleration. Conversely, for n = 0.10, the universe undergoes periodic transitions between decelerating and accelerating phases. The Hubble parameter was calculated based on the deceleration parameter, reflecting the universe's expansion history. The key findings of this study are: The choice of a time-periodically varying deceleration parameter leads to periodic behavior in almost all cosmological parameters investigated. The model demonstrates the possibility of a universe transitioning between phases of deceleration and acceleration. The specific behaviour of the universe's expansion is sensitive to the choice of model parameters, highlighting the importance of observational constraints. Future work could explore the implications of this model for structure formation, the cosmic microwave background radiation, and the nature of dark energy.

References

[1] A.G.Riess, A.V.Filippenko, P.Challis, A.Clocchiatti, A.Diercks, P. M.Garnavich, et al., Observational evidence from supernovae for an accelerating universe and a cosmological constant, *The Astronomical Journal*, **116**(1998), no. 3, 1009.

[2] S.Weinberg, The cosmological constant problem, *Reviews of Modern Physics*, **61**(1989), no. 1.

[3] M.Tegmark, M.A.Strauss, M.R.Blanton, AK.bazajian, S.Dodelson, H.Sandvik,et al., Cosmological parameters from SDSS and WMAP, *Physical Review D*, **69**(2004), no. 10, 103501. DOI: 10.1103/PhysRevD.69.103501

[4] T.Padmanabhan, Accelerated expansion of the universe driven by tachyonic matter, *Physical Review D*, **66**(2002), no. 2, 021301. DOI: 10.1103/PhysRevD.66.021301

[5] M.C.Bento, O.Bertolami, A.A.Sen, Generalized Chaplygin gas, accelerated expansion, and dark-energy-matter unification, *Physical Review D*, **66**(2002), no. 4, 043507. DOI: 10.1103/PhysRevD.66.043507

[6] S. I.Nojiri, S. D.Odintsov, Modified gravity with negative and positive powers of curvature: Unification of inflation and cosmic acceleration, *Physical Review D*, **68**(2003), no. 12, 123512. DOI: 10.1103/PhysRevD.68.123512

[7] A. H.Guth, Inflationary universe: A possible solution to the horizon and flatness problems, *Physical Review D*, **23**(1981), no. 7, 347.

[8] A.Linde, Hybrid inflation, *Physical Review D*, **49**(1994), no. 2, 748.

[9] A.D.Linde, Chaotic inflation, *Physics Letters B*, **129**(1983), no. 3-4, 177–181.

[10] K.Bamba, S.Capozziello, S.I.Nojiri, S.D.Odintsov, Dark energy cosmology: the equivalent description via different theoretical models and cosmography tests, *Astrophysics and Space Science*, **342**(2011), no. 2, 155–228.

[11] T.Harko, F.S.Lobo, S.I.Nojiri, S.D.Odintsov, f(R, T) gravity, *Physical Review D. Particles, Fields, Gravitation, and Cosmology*, **84**(2011), no. 2, 024020. DOI: 10.1103/PhysRevD.84.024020

[12] D.R.Reddy, R.Santikumar, R.L.Naidu, Bianchi type-III cosmological model in f(R, T) theory of gravity. *Astrophysics and Space Science*, **342**(2012), 249–252. DOI: 10.1007/s10509-012-1158-7

[13] D.R.K.Reddy, SR.anthikumar, T. V.Pradeep Kumar, Bianchi type-III dark energy model in f(R, T) gravity, *International Journal of Theoretical Physics*, **52**(2013), 239–245. DOI: 10.1007/s10773-012-1325-1

[14] D.R.K.Reddy, R.Santhi Kumar, Some anisotropic cosmological models in a modified theory of gravitation. *Astrophysics and Space Science*, **344**(2013), 253–257. DOI: 10.1007/s10509-012-1304-2

[15] R.Santhikumar, B.Satyannarayana, Accelerating anisotropic cosmological model in f(R, T) theory of gravity. *Indian Journal of Physics*, **91**(2017), no. 10, 1293–1296. DOI: 10.1007/s12648-017-1017-z

[16] M.Shen, L.Zhao, Oscillating quintom model with time periodic varying deceleration parameter. C*hinese Physics Letters*, **31**(2014), no. 1, 010401. DOI:10.1088/0256-307X/31/1/010401

[17] C.Akta, S.Aygün, *Curr. Res. Int*, **11**(2017), no. 1.

[18] N.Ahmed, S.Z.Alamri, A cyclic universe with varying cosmological constant in f(R, T) gravity, *Canadian Journal of Physics*, **97**(2019), no. 10, 1075–1082.

[19] N.Hulke, G.P.Singh, B.K.Bishi, Bianchi-I cosmology with generalised Chaplygin gas and periodic deceleration parameter, *Indian Journal of Physics*, **96**(2022), no. 13, 4033–4049. DOI: 10.1007/s12648-022-02315-1

[20] N.Hulke, G.P.Singh, B.K.Bishi, Variable Chaplygin gas cosmologies in f(R, T) gravity with particle creation, *New Astronomy*, **77**(2020), no. 13, 101357.

[21] G. P.Singh, N.Hulke, A.Sing, Cosmological study of particle creation in higher derivative theory, *Indian Journal of Physics*, **94**(2020), no. 1, 127–141. DOI: 10.1007/s12648-019-01426-6

[22] R.R.Caldwell, M.Doran, Cosmic microwave background and supernova constraints on quintessence: concordance regions and target models, *Physical Review D*, **69**(2004), no. 10, 103517. DOI: 10.1103/PhysRevD.69.103517

Вязкая космологическая модель FRW с периодически изменяющимся во времени параметром замедления в f(R, T)гравитации

М. Раманамурти
Раджамаханти Сантикумар
Институт технологии и менеджмента Адитьи, Теккали
Шрикакулам, Андхра-Прадеш, Индия-532203
К. Собханбабу
Университетский инженерный колледж-JNTUK, Нарасараопет
Андхра-Прадеш-Индия-522616

Аннотация. В этой исследовательской работе изучается динамика космологической модели Фридмана–Робертсона–Уокера, характеризующейся давлением идеальной жидкости и баротропным объемным вязким давлением. Получая точные решения уравнений поля Эйнштейна с изменяющимся во времени периодическим параметром замедления, исследование выявляет периодическое поведение большинства параметров, приписываемое влиянию косинусной функции в параметре замедления. Анализ углубляется в физические и динамические следствия этой модели, в частности, подчеркивая, как отрицательное давление способствует расширению Вселенной в поздние времена.

Ключевые слова: объемная вязкая жидкость, период времени, параметр замедления, ускоренное расширение.

EDN: UBPBHA
УДК 517.9

Filtration of Two Immiscible Liquids in a Viscoelastic Porous Medium

Margarita A. Tokareva*
Alexander A. Papin†
Altai State University
Barnaul, Russian Federation

Received 19.10.2024, received in revised form 02.12.2024, accepted 09.01.2025

Abstract. Governing equations for the motion of two immiscible fluids in a poroelastic skeleton are obtained within the framework of the theory of interacting continua. The stability of the steady-state solution of the system is investigated.

Keywords: poroelasticity, two-phase filtration, Darcy's law, stability, viscoelasticity.

Citation: M.A. Tokareva, A.A. Papin, Filtration of Two Immiscible Liquids in a Viscoelastic Porous Medium, J. Sib. Fed. Univ. Math. Phys., 2025, 18(2), 253–261. EDN: UBPBHA.

Introduction

The problem of global warming is one of the most important modern scientific problems. The emission of CO2 is one of the causes leading to global changes in the Earth's climate.

Geological storage of carbon dioxide in deep geological formations is considered a key transition method for reducing greenhouse gas emissions into the atmosphere and, therefore, their feedback on the climate. Such method has been used for several decades in applications related to enhanced oil recovery. A number of industrial, demonstration and pilot projects are underway, and the processes and techniques associated with geological carbon dioxide storage have been theoretically and experimentally studied. Deep saline formations are geological units that are estimated to have the highest storage potential due to their worldwide distribution. Methods for modelling and monitoring CO2 storage in such formations are rapidly developing in many parts of the world. The basic assumption underlying the modelling of such processes is that after CO2 injection, the void space within the formation is occupied by two fluids: natural brine and injected CO2 [1].

Two-phase models are also applied to describe CO2 sequestration in producing gas fields. In [2], CO2 sequestration scenarios through three injection wells in a producing gas field located in the river Po sedimentary basin (Italy) are modeled with the ultimate goal of understanding the geomechanical consequences of CO2 injection. The process is analyzed from a geomechanical point of view, with the following main issues being addressed: prediction of possible vertical uplift of the earth and the corresponding impact on the surface infrastructure; assessment of the stress state induced in the reservoir with possible formation of fractures and analysis of the risk of activation of existing faults.

*tma25@mail.ru https://orcid.org/0000-0002-7162-342X
†papin@math.asu.ru https://orcid.org/0000-0001-7510-9164

In the paper [3] a poromechanical model is developed to determine how chemical carbonation reactions can affect the mechanical behavior of well cement in the context of CO2 storage. A multiphase model is also considered, in which the pore fluid consists of dissolved components and a solvent (water).

Thus, the mathematical model of two-phase filtration in a poroelastic medium is quite relevant and describes well the processes of CO2 storage. A large number of works are devoted to mathematical modeling of the process of carbon dioxide burial under various conditions. Most of the known models do not take into account the variable porosity of the solid skeleton. Usually porosity is a given function or is assumed to be constant. However, taking into account variable porosity seems important, since it can lead to the detection of cracks and the release of CO2 to the surface during burial. The mathematical model we consider takes into account the compressibility of the solid skeleton and its poroelastic properties, i.e. variable porosity.

Work using variable porosity has been conducted since the 1920s. A relationship was discovered between the burial depth of sedimentary rocks and porosity. In particular, there is an exponential dependence of porosity on depth [4]. One of the first tools for constructing models of poroelastic media was the Terzaghi effective stress concept, which takes into account the mobility of the skeleton and its poroelastic properties [5]. Further, the theory of poroelasticity was developed in the works of Bio [6], where porosity was also a function of effective pressure. Porosity depended on pressure (but the deformation of the porous skeleton was not considered) in [7]. A model of two-phase filtration in a deformable porous medium was proposed in [8], in which the motion of a solid skeleton was described based on an analogue of Terzaghi's principle and a modified linear Hooke's law. The justification issues were not considered in this work. This was done in works [9,10], where particular solutions were constructed in models of zero and first approximations. In the case of single-phase filtration in a deformable porous medium, the mathematical theory of the process was constructed in works [11–13].

1. Governing equations

We consider a system of differential equations describing the motion of two immiscible fluids in a deformable viscoelastic medium. The continuity equations for each phase, taking into account variable porosity in the absence of phase transitions, are as follows [15]:

$$\frac{\partial(\rho_1 s_1\phi)}{\partial t} + \nabla\cdot(\rho_1\phi s_1\vec{v}_1) = 0, \quad \frac{\partial(\rho_2 s_2\phi)}{\partial t} + \nabla\cdot(\rho_2\phi s_2\vec{v}_2) = 0, \quad s_2 + s_1 = 1, \\ \frac{\partial(1-\phi)\rho_3}{\partial t} + \nabla\cdot((1-\phi)\rho_3\vec{v}_3) = 0. \tag{1}$$

Here $\rho_1, \rho_2, \rho_3, \vec{v}_1, \vec{v}_2, \vec{v}_3$ are true phase densities and velocities, respectively (1 is the wetting fluid, 2 is the non-wetting fluid, 3 is the solid deformable skeleton), s_1, s_2 are fluid saturations, ϕ is the porosity.

Instead of the equations of conservation of momentum in the theory of two-phase filtration, a generalized Darcy law for liquid phases is used, taking into account the motion of a solid skeleton [16, 17]:

$$s_1\phi(\vec{v}_1 - \vec{v}_3) = -K_0(\phi)\frac{k_{01}(s_1)}{\mu_1}(\nabla p_1 - \rho_1\vec{g}), \tag{2}$$

$$s_2\phi(\vec{v}_2 - \vec{v}_3) = -K_0(\phi)\frac{k_{02}(s_2)}{\mu_2}(\nabla p_2 - \rho_2\vec{g}), \tag{3}$$

where p_1, p_2 are fluid pressures, $k_{01}(s_1), k_{02}(s_2)$ are permeabilities, μ_1, μ_2 are dynamic viscosities, $\vec{g}$ is the acceleration vector of gravity. Taking into account capillary forces means that the phase pressures p_2 and p_1 differ by the magnitude of the capillary jump: $p_2 - p_1 = p_c(s_1)$, $p_c(s_1)$ is the capillary pressure (is a given function).

The system of equations (1)–(3) with respect to the sought functions of pressures, phase velocities and saturations of immiscible liquids moving in a non-deformable porous medium, in the isothermal case (the temperature in the flow is constant) is closed either by the assumption of incompressibility of liquids, i.e. the densities are assumed to be constant, or by an equation of state relating the densities and pressures of the phases.

The resulting mathematical model in the case of a stationary porous medium $\vec{v}_3 = 0$ is called the Musket–Leverett model (in the case of the absence of a capillary jump — the Buckley–Leverett model). The mathematical theory of the process for the Musket–Leverett model was justified in the monograph [18].

The fundamental point is to take into account the compressibility of the porous medium. Work using variable porosity began in the 1920s in connection with attempts to mathematically model filtration processes in sedimentary rocks [4]. At first, simple dependences of porosity on depth were used (see review in [19]]), obtained on the basis of experimental data. Then more complex dependences appeared for porosity through effective pressure [5], which, according to Terzaghi's concept, is defined as the difference between the total pressure and the fluid pressure. This position reflects the fact that the fluid bears part of the load. In this approach, the relationship between the deformation of the skeleton of the solid matrix and the processes of fluid flow is fundamental. Experimental data on unknown porosity are contained in the works of [20, 21].

The Maxwell-type relationship between porosity and effective pressure p_e is as follows [22–24]:

$$\nabla \cdot \vec{v}_3 = -(\alpha(\phi)p_e + \beta(\phi)\frac{dp_e}{dt}), \tag{4}$$

where $\alpha(\phi), \beta(\phi)$ are given functions that depend on porosity (parameters of the medium that are responsible for viscosity and elasticity, respectively), $\dfrac{d}{dt} = \dfrac{\partial}{\partial t} + (\vec{v}_3 \cdot \nabla)$ is the material derivative. The effective pressure p_e and the pressures in the liquid phases p_1, p_2 and the solid p_3 phases are related by the relations:

$$p_{tot} = \phi p_f + (1-\phi)p_3, \quad p_e = (1-\phi)(p_3 - p_f), \quad p_f = s_1 p_1 + s_2 p_2. \tag{5}$$

The balance equation of forces for the system as a whole has the form [22, 23, 25]:

$$\nabla p_{tot} = \rho_{tot}\vec{g} + \nabla \cdot \left((1-\phi)\eta \left(\frac{\partial \vec{v}_3}{\partial \vec{x}} + \left(\frac{\partial \vec{v}_3}{\partial \vec{x}} \right)^* \right) \right), \;\; \rho_{tot} = \phi\rho_f + (1-\phi)\rho_3, \;\; \rho_f = s_1\rho_1 + s_2\rho_2, \tag{6}$$

where p_{tot} is the total pressure, ρ_{tot} is the total density, η is the viscosity of the porous skeleton, $*$ is the symbol for the transposition operation. Here, the approach is used in which the deviator of the stress tensor in the liquid phase is neglected, because the viscosity of the liquid is much smaller than the shear viscosity of the skeleton.

Thus, the system of equations (1)–(6), describing the motion of two immiscible liquids in a deformable porous medium, takes the form [14]:

$$\begin{gathered} \frac{\partial(\rho_1 s_1 \phi)}{\partial t} + \nabla \cdot (\rho_1 \phi s_1 \vec{v}_1) = 0, \quad \frac{\partial(\rho_2 s_2 \phi)}{\partial t} + \nabla \cdot (\rho_2 \phi s_2 \vec{v}_2) = 0, \\ \frac{\partial(1-\phi)\rho_3}{\partial t} + \nabla \cdot ((1-\phi)\rho_3 \vec{v}_3) = 0, \end{gathered} \tag{7}$$

$$
\begin{aligned}
s_1\phi(\vec{v}_1-\vec{v}_3) &= -K_0(\phi)\frac{k_{01}(s_1)}{\mu_1}(\nabla p_1-\rho_1\vec{g}),\\
s_2\phi(\vec{v}_2-\vec{v}_3) &= -K_0(\phi)\frac{k_{02}(s_2)}{\mu_2}(\nabla p_2-\rho_2\vec{g}),
\end{aligned}
\tag{8}
$$

$$
\nabla\cdot\vec{v}_3 = -(\alpha(\phi)p_e+\beta(\phi)\frac{dp_e}{dt}),\quad \frac{d}{dt}=\frac{\partial}{\partial t}+(\vec{v}_3\cdot\nabla),
\tag{9}
$$

$$
p_{tot}=\phi p_f+(1-\phi)p_3,\quad p_e=(1-\phi)(p_3-p_f),\quad p_2-p_1=p_c(s_1),
\tag{10}
$$

$$
\nabla p_{tot}=\rho_{tot}\vec{g}+div\left((1-\phi)\eta\left(\frac{\partial\vec{v}_3}{\partial\vec{x}}+\left(\frac{\partial\vec{v}_3}{\partial\vec{x}}\right)^*\right)\right),\quad \rho_{tot}=\phi\rho_f+(1-\phi)\rho_3.
\tag{11}
$$

This model is quite complex for investigation, relatively new and has not been studied in sufficient detail. In the paper [26] a similar system of equations is investigated, for which some exact solutions are obtained in the thin layer approximation in the model case. In the paper [14] the solvability of the model problem in the Hele–Shaw cell approximation for the equations (7)–(11) is established. In the one-dimensional case for the system (7)–(11) at a constant temperature and single-phase filtration, the dependence of the liquid phase density on the pressure and in the absence of phase transitions, local solvability is established in [11]. With constant densities, global solvability is proved in [12]. In the papers [27, 28] the problems of two-phase filtration in a deformable medium with known porosity are considered. The purpose of this work is to study the stability of the stationary solution of the general system of equations (7)–(11).

2. A study of the stability of the problem of the motion of two immiscible fluids in a poroelastic medium

2.1. Steady-state solution of the system

To find an analytical solution to the system (7)–(11) we will use the following hypotheses:

•fluids and solid skeletons are incompressible, that is, $\rho_i^0 = const\,(i=1,2,3)$;

• gravity acceleration and capillary jump are equal to zero: $\overrightarrow{g}=0,\quad p_c=0.$

We consider a stationary solution in which the phase velocities are zero ($\vec{v}_1=\vec{v}_2=\vec{v}_3=0$), and the porosity and saturation are constant:

$$
\phi=\phi^0,\quad s_1=s_1^0,\quad s_2=s_2^0,\quad (\phi^0,s_1^0,s_2^0)\in(0,1).
$$

From the equation (11) it follows that $p_{tot}=h=const$.

From the absence of a capillary jump it follows that $p_1=p_2$.

Under these assumptions, equations (7)–(11) are satisfied automatically. From equation (9) it follows that $p_e=0$. From the equation for effective pressure: $p_e=p_{tot}-p_f$ we establish that $p_{tot}=p_f=p_1=p_2=p_3=h$.

Thus, the steady-state solution has the form:

$$
s_1=s_1^0,\quad s_2=s_2^0,\quad \vec{v}_1=\vec{v}_2=\vec{v}_3=0,\quad \phi=\phi^0,\quad p_1=p_2=p_3=h.
$$

2.2. Perturbed solution

The perturbed solution of the system (7)–(11) is sought in the vicinity of the stationary one and has the following form [29]:

$$\vec{v}_1 = \vec{\bar{v}}_1, \quad \vec{v}_2 = \vec{\bar{v}}_2, \quad \vec{v}_3 = \vec{\bar{v}}_3, \quad s_1 = s_1^0 + \bar{s}_1, \quad s_2 = s_2^0 + \bar{s}_2,$$
$$\phi = \phi^0 + \bar{\phi}, \quad s_1^0 + s_2^0 = 1, \quad \bar{s}_1 + \bar{s}_2 = 0,$$
$$p_1 = \bar{p}_1 + h, \quad p_2 = \bar{p}_2 + h, \quad p_3 = \bar{p}_3 + h, \quad \bar{p}_2 = \bar{p}_1.$$

where the functions $\overline{v_3}, \overline{v_1}, \overline{v_2}, \overline{p_1}, \overline{p_2}, \overline{p_3}, \overline{s_1}, \overline{s_2}, \overline{\phi}$ are small and have continuous derivatives. The functional parameters $K_0(\phi), k_{01}(s_1), k_{02}(s_2)$ can be represented as:

$$K_0(\phi) = K_0(\phi^0) + K_0'(\phi^0)\overline{\phi},$$
$$k_{01}(s_1) = k_{01}(s_1^0) + k_{01}'(s_1^0)\overline{s_1},$$
$$k_{02}(s_2) = k_{02}(s_2^0) + k_{02}'(s_2^0)\overline{s_2},$$
$$\alpha(\phi) = \alpha(\phi^0) + \alpha'(\phi^0)\bar{\phi}, \quad \beta(\phi) = \beta(\phi^0) + \beta'(\phi^0)\bar{\phi}.$$

Substituting the perturbed solution into the system (7)–(11) and discarding the nonlinear terms, we arrive at the following linear system (for convenience, we omit the dashes from above):

$$\frac{\partial(1-\phi)}{\partial t} + (1-\phi^0)\nabla\cdot\vec{v}_3 = 0, \tag{12}$$

$$\phi^0\frac{\partial(s_1)}{\partial t} + s_1^0\frac{\partial(\phi)}{\partial t} + \phi^0 s_1^0\nabla\cdot\vec{v}_1 = 0, \tag{13}$$

$$\phi^0\frac{\partial(s_2)}{\partial t} + s_2^0\frac{\partial(\phi)}{\partial t} + \phi^0 s_2^0\nabla\cdot\vec{v}_2 = 0, \tag{14}$$

$$s_1^0\phi^0(\vec{v}_1 - \vec{v}_3) = -K_0(\phi^0)\frac{k_{01}(s_1^0)}{\mu_1}\nabla p_1, \tag{15}$$

$$s_2^0\phi^0(\vec{v}_2 - \vec{v}_3) = -K_0(\phi^0)\frac{k_{02}(s_2^0)}{\mu_2}\nabla p_2, \tag{16}$$

$$\nabla\cdot\vec{v}_3 = (1-\phi^0)\left(\alpha(\phi^0)(p_3-p_1) + \beta(\phi^0)\frac{\partial(p_3-p_1)}{\partial t}\right), \tag{17}$$

$$(1-\phi^0)\nabla p_3 + \phi^0\nabla p_1 = \eta(1-\phi^0)(\Delta\vec{v}_3 + \nabla(\nabla\cdot\vec{v}_3)). \tag{18}$$

To find $\vec{v}_3$ we add the continuity equations (12)–(14). We get:

$$\nabla\cdot\vec{v}_3 = -\frac{\phi^0}{1-\phi^0}\left(s_1^0\nabla\cdot\vec{v}_1 + s_2^0\nabla\cdot\vec{v}_2\right). \tag{19}$$

After adding the equations (15), (16), and apply the *div* operator to both parts of the resulting equality we get:

$$\nabla\cdot(\phi^0 s_1^0\vec{v}_1 + s_2^0\phi^0\vec{v}_2) - \phi^0\nabla\cdot\vec{v}_3 = -K_0(\phi^0)\left(\frac{k_{01}(s_1^0)}{\mu_1} + \frac{k_{02}(s_2^0)}{\mu_2}\right).$$

Taking into account the relation (19), we obtain

$$\nabla\cdot\vec{v}_3 = K_0(\phi^0)\left(\frac{k_{01}(s_1^0)}{\mu_1} + \frac{k_{02}(s_2^0)}{\mu_2}\right)\Delta p_1. \tag{20}$$

Taking the *div* operator to both parts of the equation (18) and, taking into account the previous equality, we obtain

$$(1-\phi^0)\Delta p_3 = 2\eta\tilde{K}(1-\phi^0)\Delta^2 p_1 - \phi^0\Delta p_1. \tag{21}$$

Equation (17) taking into account (20) will take the form

$$\tilde{K}\Delta p_1 = (1-\phi^0)\left(\alpha(\phi^0)(p_3-p_1) + \beta(\phi^0)\frac{\partial(p_3-p_1)}{\partial t}\right),$$

where $\tilde{K} = K_0(\phi^0)\left(\frac{k_{01}(s_1^0)}{\mu_1} + \frac{k_{02}(s_2^0)}{\mu_2}\right)$. Taking the operator Δ to the previous equation, we get

$$\tilde{K}\Delta^2 p_1 = \alpha(\phi^0)((1-\phi^0)\Delta p_3) - \alpha(\phi^0)(1-\phi^0)\Delta p_1 + \beta(\phi^0)\frac{\partial}{\partial t}((1-\phi^0)\Delta p_3) - \beta(\phi^0)(1-\phi^0)\frac{\partial}{\partial t}(\Delta p_1).$$

Taking into account equation (21), we have the equation for p_1

$$\frac{\partial}{\partial t}(\Delta p_1) - A\Delta^2 p_1 - B\frac{\partial}{\partial t}(\Delta^2 p_1) + C\Delta p_1 = 0, \tag{22}$$

where

$$A = \tilde{K}\frac{2\alpha(\phi^0)\eta(1-\phi^0)-1}{\beta(\phi^0)},\ B = 2\eta\tilde{K}(1-\phi^0),\ C = \frac{\alpha(\phi^0)}{\beta(\phi^0)},\ \tilde{K} = K_0(\phi^0)\left(\frac{k_{01}(s_1^0)}{\mu_1} + \frac{k_{02}(s_2^0)}{\mu_2}\right).$$

Let us describe the scheme for finding all the desired functions. After finding p_1 from the equation (22) we find p_2, since $p_c = 0$ and, therefore, $p_1 = p_2$. We also obtain $divv_3$ from (20). We find p_3 from (21), and then we find v_3 from (18). We can find v_1 and v_2 from (15), (16), and ϕ from (12). From (13) we find s_1, and, therefore, s_2, since $s_1 + s_2 = 1$.

We now seek a plane wave solution of the form [30]

$$p_1 = \hat{p}_1 \exp(st)\exp(i\mathbf{k}\cdot\mathbf{x}), \quad s = \xi - i\bar{\eta},$$

where $\mathbf{k}$ is the wave vector of the plane wave, $\bar{\eta}$ is related to the velocity of propagation V by $V = \bar{\eta}/|\mathbf{k}|$, where $|\mathbf{k}|$ is the wave number.

Substituting this representation into (22), we obtain

$$\hat{p}_1 k^2(s + Ak^2 + Bsk^2 + C) = 0.$$

The solutions $\hat{p}_1 = 0$ represent transverse waves. We also have that

$$\xi = -\frac{k^2\tilde{K}(2\alpha(\phi^0)\eta(1-\phi^0)-1) + \alpha(\phi^0)}{\beta(\phi^0)(1 + 2\eta\tilde{K}(1-\phi^0)k^2)}. \tag{23}$$

From this equation we obtain the relationship between the degree of growth of the harmonic ξ perturbations and its wavelength (wave number $|\mathbf{k}| = 2\pi/\lambda$). For $\xi > 0$ the perturbations grow exponentially and, therefore, the initial solution is unstable, for $\xi < 0$ the perturbations decay and the solution is stable. It is easy to see that $\xi > 0$ for $|\mathbf{k}| \in (0, k_c)$, where

$$k_c = \left(\frac{\alpha(\phi^0)}{\tilde{K}(1 - 2\alpha(\phi^0)\eta(1-\phi^0))}\right)^{1/2},$$

if the condition $1 > 2\alpha\eta(1-\phi^0)$ is satisfied.

Note that in the absence of viscosity in the skeleton and the prevalence of its elastic properties, i.e., when $\alpha = 0$, we have unstable perturbations, since it is easy to see from the equality (23) that $\xi > 0$ for any initial data of the equations. In the presence of viscosity and when the condition is satisfied

$$1 < 2\eta\alpha(1 - \phi^0) \tag{24}$$

the process will be stable, since there are no real k_c. Therefore, viscosity can stabilize the process under consideration. In the absence of skeleton elasticity ($\beta = 0$) we have $k_c = \infty$ and the solution is always unstable. Therefore, elasticity also contributes to the stabilization of the process. In other words, the process will be stable if the (24) condition is met and the skeleton has viscoelastic properties.

The study was supported by the Russian Science Foundation grant no. 23-71-10045, https://rscf.ru/project/23-71-10045/.

References

[1] Geological Storage of CO2 in Deep Saline Formations, Springer, Editor: Niemi, Bear and Bensabat, 2016.

[2] M.Ferronato, G.Gambolati, C.Janna, P.Teatini, Geomechanical issues of anthropogenic CO2 sequestration in exploited gas fields, *Energy Conversion and Management*, **51**(2010), 1918–1928.

[3] A.Fabbri, N.Jacquemet, D.M.Seyedi, A chemo-poromechanical model of oilwell cement carbonation under CO2 geological storage conditions, *Cement and Concrete Research*, **42**(2012), 8–19.

[4] L.F.Athy, Density, porosity, and compaction of sedimentary rocks, *Amer. Ass. Petrol. Geol. Bull.*, **14**(1930), 1–24.

[5] K.Terzaghi, Theoretical Soil Mechanics, Wiley J., New York, 1943.

[6] M.A.Biot, General theory of three-dimensional consolidation, *J. Appl. Phys.*, **12**(1941), no. 2, 155–164.

[7] O.B.Bocharov, On the filtration of two immiscible liquids in a compressible formation, *Dynamics of continuous media: Coll. scientific papers / USSR Academy of Sciences. Siberian Branch. Institute of Hydrodynamics*, **50**(1981), 15–36 (in Russian).

[8] V.V.Vedernikov, V.N.Nikolaevskii, Mechanics equations for porous medium saturated by a twophase liquid, *Izvestiya Akademii Nauk SSSR, Mekhanika Zhidkosti i Gaza*, **5**(1978), 769–773.

[9] O.B.Bocharov, V.Ya.Rudyak, A.V.Seryakov, The simplest models of deformation of a poroelastic medium saturated with fluids, *Physical and technical problems of mineral development*, **2**(2014), 54–68. (in Russian)

[10] V.Ya.Rudyak, O.B.Bocharov, A.V.Seryakov, Hierarchical sequence of models and deformation peculiarities of porous media saturated with fluids, Proceedings of the XLI Summer School-Conference Advanced Problems in Mechanics (APM-2013), 1-6 July , St-Petersburg, 2013, 183–190.

[11] A.A.Papin, M.A.Tokareva, On local solvability of the system of the equations of one dimensional motion of magma, *Journal of Siberian Federal Universit. Mathematics and Physics*, **10**(2017), no. 3, 385–395.

[12] M.A.Tokareva, A.A.Papin, Global solvability of a system of equations of one-dimensional motion of a viscous fluid in a deformable viscous porous medium, *Journal of Applied and Industrial Mathematics*, **13**(2019), no. 2, 350–362.

[13] M.A.Tokareva, A.A.Papin, On the existence of global solution of the system of equations of one-dimensional motion of a viscous liquid in a deformable viscous porous medium, *Siberian Electronic Mathematical Reports*, **18**(2021), no. 2, 1397–1422.

[14] P.V.Gilev, A.A.Papin, Filtration of two immiscible incompressible fluids in a thin poroelastic layer, *Journal of Applied and Industrial Mathematics*, **18**(2024), 234–245.

[15] R.I.Nigmatulin, Fundamentals of the Mechanics of Heterogeneous Media, Moscow, Izdatel'stvo Nauka, 1978 (in Russian).

[16] J.Bear, A.H.D.Cheng, Modeling Groundwater Flow and Contaminant Transport, Springer Science & Business Media, Berlin, 2010.

[17] F.Schneider, J.L.Potdevin, S.Wolf, I.Faille, Vechanical and chemical compaction model for sedimentary bsasin simulation, *Tectonophysics*, **263** (1996), 307–317.

[18] S.N.Antontsev, A.V.Kazhikhov, V.N.Monakhov, Boundary Value Problems in Mechanics of Nonhomogeneous Fluids, North-Holland, 1989.

[19] J.JE.Lee, Modelling and Simulation of Compacting Sedimentary Basins, University of Oxford, 2019.

[20] P.A.Waldner, M.Schneebeli, U.Schultze-Zimmermann, H.Fluhler, Effect of snow structure on water flow and solute transport, *Hydrological Processes*, **18**(2008), no. 7, 1271–1290. DOI:10.1002/hyp.1401

[21] R.R.Khasanov, A.R.Smirnova, Experimental research of physical characteristics of preliminary compressed clay soil at moistening, *International Research Journal*, **12**(2017), no. 66, 178–182. DOI: 10.23670/IRJ.2017.66.130

[22] A.Fowler, Mathematical Geoscience Springer-Verlag London Limited, 2011.

[23] C.Morency et al., A numerical model for coupled fluid flow and matrix deformation with applications to disequilibrium compaction and delta stability, *Journal of Geophysical Research: Solid Earth*, **112**(2007), no. B10.

[24] J.A.D.Connolly, Y.Y.Podladchikov, Compaction-driven fluid flow in viscoelastic rock, *Geodin. Acta*, **11**(1998), 55–84.

[25] O.Coussy, Poromechanics, John Wiley & Sons, 2004.

[26] M.A.Tokareva, A.A.Papin, A.A.Beregovykh, Two-phase filtration in a thin poroelastic layer, *AIP Conference Proceedings*, **2528**(2022), 020008. DOI: 10.1063/5.0106334

[27] V.V.Shelukhin, A poroelastic medium saturated by a two-phase capillary fluid, *Contin. Mech. Thermodyn*, **26**(2014), no. 5, 619–638. DOI: 10.1007/s00161-013-0321-x

[28] A.Jardani, A.Revil, Seismoelectric couplings in a poroelastic material containing two immiscible fluid phases, *Geophys. J. Int.*, **202**(2015), no. 2, 850–870. DOI: 10.1093/gji/ggv176

[29] A.A.Glushkova, A.A.Papin, Stability of two-phase flows in a poroelastic medium, *Proceedings of the Seminar on Geometry and Mathematical Modeling*, **5**(2019), 55–59 (in Russian).

[30] S.K.Garg, J.W.Pritchett, Dynamics of gasfluidized beds, *Journal of Applied Physics*, **46**(1975), 4493.

Фильтрация двух несмешивающихся жидкостей в вязкоупругой пористой среде

Маргарита А. Токарева
Александр А. Папин
Алтайский государственный университет
Барнаул, Российская Федерация

Аннотация. В рамках теории взаимодействующих континуумов получены определяющие уравнения для движения двух несмешивающихся жидкостей в пороупругом скелете. Исследована устойчивость стационарного решения системы.

Ключевые слова: пороупругость, двухфазная фильтрация, закон Дарси, устойчивость, вязкоупругость.

EDN: OTALKL
УДК 517

Properties of $m\mathcal{H}$-compact Sets in Hereditary m-Spaces

Ahmad Al-Omari*
Department of Mathematics
Faculty of Sciences
Al al-Bayt University
Mafraq 25113, Jordan
Takashi Noiri†
Yatsushiro-shi, Kumamoto-ken, Japan

Received 01.10.2024, received in revised form 06.11.2024, accepted 10.01.2025

Abstract. Let $(X, m, \mathcal{H})$ be a hereditary m-space. A subset A of X is said to be $\mathcal{H}$-compact relative to X if for every cover $\mathcal{U}$ of A by m-open sets of X, there exists a finite subset $\mathcal{U}_0$ of $\mathcal{U}$ such that $A \setminus \cup \mathcal{U}_0 \in \mathcal{H}$. We obtain several properties of these sets. And also, we define and investigate two kinds of strong forms of $\mathcal{H}$-compact relative to X.

Keywords: hereditary m-space, $\mathcal{H}$-compactness, strong $\mathcal{H}$-compactness, super $\mathcal{H}$-compactness.

Citation: A. Al-Omari, T. Noiri, Properties of $m\mathcal{H}$-compact Sets in Hereditary m-Spaces, J. Sib. Fed. Univ. Math. Phys., 2025, 18(2), 262–272. EDN: OTALKL.

Introduction

In 1967, Newcomb [11] introduced the notion of compactness modulo an ideal. Rančin [16] and Hamlett and Janković [6] further investigated this notion and obtained some more properties of compactness modulo an ideal. Császár [5] introduced the notion of hereditary classes as a generalization of ideals. In [13], a minimal structure and a minimal space (X, m) are introduced and investigated. Recently, the present authors [1,3,4] introduced and studied the notions related to compactness modulo hereditary classes.

In this paper, we define a subset A of a hereditary m-space $(X, m, \mathcal{H})$ to be m-$\mathcal{H}$-compact relative to X if for every cover $\mathcal{U}$ of A by m-open sets of X, there exists a finite subset $\mathcal{U}_0$ of $\mathcal{U}$ such that $A \setminus \cup \mathcal{U}_0 \in \mathcal{H}$. We obtain several properties of these sets. And also, we define and investigate two kinds of strong forms of $\mathcal{H}$-compact relative to X. Moreover, for a function $f : (X, m, \mathcal{H}) \to (Y, n)$ we define a hereditry class $J_H = \{B \subset Y : f^{-1}(B) \in \mathcal{H}\}$ and by using hereditry classes $f(\mathcal{H})$ and J_H on Y we obtain several preservation theorems.

1. Preliminaries

Definition 1.1. A subfamily m of the power set $\mathcal{P}(X)$ of a nonempty set X is called a *minimal structure* (briefly *m-structure*) [13] on X if $\emptyset \in m$ and $X \in m$.

*omarimutah1@yahoo.com https://orcid.org/0000-0002-6696-1301
†t.noiri@nifty.com https://orcid.org/0000-0002-0862-5297

By (X, m), we denote a nonempty set X with a minimal structure m on X and call it an *m-space*. Each member of m is said to be *m-open* and the complement of an m-open set is said to be *m-closed*. For a point $x \in X$, the family $\{U : x \in U \text{ and } U \in m\}$ is denoted by $m(x)$.

Definition 1.2. Let (X, m) be an m-space and A a subset of X. The *m-closure* $\mathrm{mCl}(A)$ and $\mathrm{mInt}(A)$ of A [10] are defined as follows:
(1) $\mathrm{mCl}(A) = \cap\{F \subset X : A \subset F, X \setminus F \in m\}$,
(2) $\mathrm{mInt}(A) = \cup\{U \subset X : U \subset A, U \in m\}$.

Lemma 1.3. (Maki et al. [10]). *Let X be a nonempty set and m a minimal structure on X. For subsets A and B of X, the following properties hold:*
(1) $A \subset \mathrm{mCl}(A)$ and $\mathrm{mCl}(A) = A$ if A is m-closed,
(2) $\mathrm{mCl}(\emptyset) = \emptyset$, $\mathrm{mCl}(X) = X$,
(3) If $A \subset B$, then $\mathrm{mCl}(A) \subset \mathrm{mCl}(B)$,
(4) $\mathrm{mCl}(A) \cup \mathrm{mCl}(B) \subset \mathrm{mCl}(A \cup B)$,
(5) $\mathrm{mCl}(\mathrm{mCl}(A)) = \mathrm{mCl}(A)$.

Definition 1.4. A minimal structure m of a set X is said to have *property $\mathcal{B}$* [10] if the union of any collection of elements of m is an element of m,

Lemma 1.5. (Popa and Noiri [13]). *Let (X, m) be an m-space and A a subset of X.*
(1) $x \in \mathrm{mCl}(A)$ if and only if $U \cap A \neq \emptyset$ for every $U \in m(x)$.
(2) Let m have property $\mathcal{B}$. Then the following properties hold:
(i) A is m-closed if and only if $\mathrm{mCl}(A) = A$,
(ii) A is m-open if and only if $\mathrm{mInt}(A) = A$.

Definition 1.6. A nonempty subfamily $\mathcal{H}$ of $\mathcal{P}(X)$ is called a *hereditary class* on X [5] if it satisfies the following properties: $A \in \mathcal{H}$ and $B \subset A$ implies $B \in \mathcal{H}$. A hereditary class $\mathcal{H}$ is called an *ideal* [9], [17] if it satisfies the additional condition: $A \in \mathcal{H}$ and $B \in \mathcal{H}$ implies$A \cup B \in \mathcal{H}$.

A minimal space (X, m) with a hereditary class $\mathcal{H}$ on X is called a *hereditary minimal space* (briefly *hereditary m-space*) and is denoted by $(X, m, \mathcal{H})$. The notion of ideals has been introduced in [9] and [17] and further investigated in [8].

Lemma 1.7. [11] *For a function $f : (X, \tau) \to (Y, \sigma)$ and ideals I and J, the following properties hold:*
(1) if f is surjective and I is an ideal on X, then $f(I) = \{f(A) : A \in I\}$ is an ideal on Y,
(2) if f is injective and J is an ideal on Y, then $f^{-1}(J) = \{f^{-1}(B) : B \in J\}$ is an ideal on X.

Lemma 1.8. *Let $(X, m, \mathcal{H})$ be a hereditary m-space, $f : (X, m, \mathcal{H}) \to (Y, n)$ a function and $J_H = \{B \subset Y : f^{-1}(B) \in \mathcal{H}\}$. Then the following properties hold:*
(1) J_H is a hereditary class on Y,
(2) if f is injective, then $\mathcal{H} \subset f^{-1}(J_H)$,
(3) if f is surjective, then $J_H \subset f(\mathcal{H})$,
(4) if f is bijective, then $J_H = f(\mathcal{H})$.

Proof. (1) Let $A \subset B$ and $B \in J_H$, then $f^{-1}(A) \subset f^{-1}(B) \in \mathcal{H}$. Hence $f^{-1}(A) \in \mathcal{H}$ and $A \in J_H$. Therefore, J_H is a hereditary class on Y.

(2) Since f is injective, for any $A \in \mathcal{H}$, $f^{-1}(f(A)) = A \in \mathcal{H}$ and $f(A) \in J_H$. Therefore, $A \in f^{-1}(J_H)$ and $\mathcal{H} \subset f^{-1}(J_H)$.

(3) For any $B \in J_H, f^{-1}(B) \in \mathcal{H}$. Since f is surjective, $B = f(f^{-1}(B)) \in f(\mathcal{H})$ and hence $J_H \subset f(\mathcal{H})$.

(4) The proof is obvious by (2) and (3). □

Definition 1.9. Let (X, m) be m-space. A subset A of X is said to be *m-compact relative to X* [14] if for each cover $\{U_\alpha : \alpha \in \Delta\}$ of A by m-open sets of X, there exists a finite subset Δ_0 of Δ such that $A \subset \cup\{U_\alpha : \alpha \in \Delta_0\}$.

Definition 1.10. A m-space (X, m) is said to be *m-compact* [14] if the set X is m-compact relative to X.

Definition 1.11. A function $f : (X, m) \to (Y, n)$ is said to be

(1) *M-continuous* [13] if for each $x \in X$ and each n-open set V containing $f(x)$, there exists an m-open set U containing x such that $f(U) \subset V$,

(2) *M-open* if $f(U)$ is n-open in (Y, n) for every m-open set U of (X, m).

Lemma 1.12 ([13]). *Let m have property $\mathcal{B}$. Then a function $f : (X, m) \to (Y, n)$ is M-continuous if and only if $f^{-1}(V) \in m$ for every $V \in n$.*

2. On m-$\mathcal{H}$-compact spaces

Definition 2.1. Let $(X, m, \mathcal{H})$ be a hereditary m-space.

(1) A subset A of X is said to be *m-$\mathcal{H}$-compact relative to X* if for every cover $\{U_\alpha : \alpha \in \Delta\}$ of A by m-open sets of X, there exists a finite subset Δ_0 of Δ such that $A \setminus \cup\{U_\alpha : \alpha \in \Delta_0\} \in \mathcal{H}$.

(2) $(X, m\ \mathcal{H})$ is called an *m-$\mathcal{H}$-compact space* if X is m-$\mathcal{H}$-compact relative to X.

Remark 2.2. Let $(X, m, \mathcal{H})$ be a hereditary m-space. If $\mathcal{H} = \{\emptyset\}$, then "$m$-$\mathcal{H}$-compact relative to X" coincides with "m-compact relative to X".

Theorem 2.3. *Let $(X, m, \mathcal{H})$ be a hereditary m-space. For a subset A of X, the following properties are equivalent:*

(1) A is m-$\mathcal{H}$-compact relative to X;

(2) for every family $\{F_\alpha : \alpha \in \Delta\}$ of m-closed sets of X such that $A \cap (\cap\{F_\alpha : \alpha \in \Delta\}) = \emptyset$, there exists a finite subset Δ_0 of Δ such that $A \cap (\cap\{F_\alpha : \alpha \in \Delta_0\}) \in \mathcal{H}$.

Proof. (1) $\Rightarrow$ (2): Let $\{F_\alpha : \alpha \in \Delta\}$ be a family of m-closed sets of X such that $A \cap (\cap\{F_\alpha : \alpha \in \Delta\}) = \emptyset$. Then, we have $A \subset X \setminus (\cap\{F_\alpha : \alpha \in \Delta\}) = \cup\{X \setminus F_\alpha : \alpha \in \Delta\}$. Since $X \setminus F_\alpha$ is m-open for each $\alpha \in \Delta$, by (1) there exists a finite subset Δ_0 of Δ such that $A \setminus (\cup\{X \setminus F_\alpha : \alpha \in \Delta_0\}) \in \mathcal{H}$. Therefore, we have

$$A \cap (\cap\{F_\alpha : \alpha \in \Delta_0\}) = A \cap [X \setminus \cup\{(X \setminus F_\alpha : \alpha \in \Delta_0\})] = A \setminus (\cup\{X \setminus F_\alpha : \alpha \in \Delta_0\}) \in \mathcal{H}.$$

(2) $\Rightarrow$ (1): Let $\{U_\alpha : \alpha \in \Delta\}$ be any cover of A by m-open sets of X. Then $A \cap (X \setminus \cup\{U_\alpha : \alpha \in \Delta\}) = A \cap (\cap\{X \setminus U_\alpha : \alpha \in \Delta\}) = \emptyset$. Since $X \setminus U_\alpha$ is m-closed for each $\alpha \in \Delta$, by (2) there exists a finite subset Δ_0 of Δ such that $A \cap (\cap\{X \setminus U_\alpha : \alpha \in \Delta_0\}) \in \mathcal{H}$. Therefore, we have

$$A \cap (\cap\{X \setminus U_\alpha : \alpha \in \Delta_0\}) = A \cap (X \setminus \cup\{U_\alpha : \alpha \in \Delta_0\}) = A \setminus \cup\{U_\alpha : \alpha \in \Delta_0\} \in \mathcal{H}.$$

This shows that A is m-$\mathcal{H}$-compact relative to X. □

Corollary 2.4. *For a hereditary m-space $(X, m, \mathcal{H})$, the following properties are equivalent:*

(1) $(X, m, \mathcal{H})$ is m-$\mathcal{H}$-compact;

(2) for every family $\{F_\alpha : \alpha \in \Delta\}$ of m-closed sets of X such that $\cap\{F_\alpha : \alpha \in \Delta\} = \emptyset$, there exists a finite subset Δ_0 of Δ such that $\cap\{F_\alpha : \alpha \in \Delta_0\} \in \mathcal{H}$.

Definition 2.5. Let $(X, m, \mathcal{H})$ be a hereditary m-space. A subset A of X is said to be

(1) *$\mathcal{H}mg$-closed* [2] if $\mathrm{mCl}(A) \subset U$ whenever $A \setminus U \in \mathcal{H}$ and U is m-open,

(2) *mg-closed* [12] if $\mathrm{mCl}(A) \subset U$ whenever $A \subset U$ and U is m-open.

Remark 2.6. We note the following:
(1) If $\mathcal{H} = \{\emptyset\}$, then $\{\emptyset\}mg$-closed and mg-closed are coincide.
(2) If A is $\mathcal{H}mg$-closed, then A is mg-closed. The converse is not always true as shown by the following example due to [15].

Example 2.7. Let $X = \mathbf{R}$, $m = \{\emptyset, R\} \cup \{(r, \infty) : r \in R\}$ and $\mathcal{H} = \{H : H \subseteq Q \cap [0, \infty)$ or $H \subseteq Q \cap (-\infty, 0]\}$. If $A = Q$, then
(1) A is mg-closed because if $A \subseteq U$ and $U \in m$, then $U = R$ and $\mathrm{mCl}(A) = R \subseteq U$.
(2) A is not $\mathcal{H}mg$-closed because if $U = (0, \infty)$, then $U \in m$ and $A \setminus U = Q \setminus (0, \infty) = Q \cap (-\infty, 0] \in \mathcal{H}$ but $\mathrm{mCl}(A) = R$ is not contained in $(0, \infty)$.

Theorem 2.8. *Let $(X, m, \mathcal{H})$ be a hereditary m-space, m have property $\mathcal{B}$ and A, B subsets of X such that $A \subset B \subset \mathrm{mCl}(A)$, then the following properties are hold:*
(1) if A is m-$\mathcal{H}$-compact relative to X and $\mathcal{H}mg$-closed, then B is m-compact relative to X,
(2) if B is m-$\mathcal{H}$-compact relative to X and A is mg-closed, then A is m-$\mathcal{H}$-compact relative to X.

Proof. (1): Suppose that A is m-$\mathcal{H}$-compact relative to X and A is $\mathcal{H}mg$-closed. Let $\{U_\alpha : \alpha \in \Delta\}$ be any cover of B by m-open sets of X. Then $\{U_\alpha : \alpha \in \Delta\}$ is a cover of A by m-open sets of X. Since A is m-$\mathcal{H}$-compact relative to X, there exists a finite subset Δ_0 of Δ such that $A \setminus \cup\{U_\alpha : \alpha \in \Delta_0\} \in \mathcal{H}$. Since A is $\mathcal{H}mg$-closed , $\mathrm{mCl}(A) \subset \cup\{U_\alpha : \alpha \in \Delta_0\}$. Since $B \subset \mathrm{mCl}(A)$, we have $B \subset \cup\{U_\alpha : \alpha \in \Delta_0\}$. Therefore, B is m-compact relative to X.
(2): Suppose that B is m-$\mathcal{H}$-compact relative to X and A is mg-closed. Let $\{U_\alpha : \alpha \in \Delta\}$ be any cover of A by m-open sets of X. Since A is mg-closed, we have $B \subset \mathrm{mCl}(A) \subset \cup\{U_\alpha : \alpha \in \Delta\}$. Since B is m-$\mathcal{H}$-compact relative to X, there exists a finite subset Δ_0 of Δ such that $B \setminus \cup\{U_\alpha : \alpha \in \Delta_0\} \in \mathcal{H}$. Since $A \subset B, A \setminus \cup\{U_\alpha : \alpha \in \Delta_0\} \in \mathcal{H}$. Therefore, A is m-$\mathcal{H}$-compact relative to X. □

Corollary 2.9. *Let $(X, m, \mathcal{H})$ be a hereditary m-space. If A is $\mathcal{H}mg$-closed and $A \subset B \subset \mathrm{mCl}(A)$, then the following properties are equivalent:*
(1) A is m-$\mathcal{H}$-compact relative to X;
(2) B is m-$\mathcal{H}$-compact relative to X.

Theorem 2.10. *Let $(X, m, \mathcal{H})$ be an ideal m-space. If subsets A and B of X are m-$\mathcal{H}$-compact relative to X, then $A \cup B$ is m-$\mathcal{H}$-compact relative to X.*

Proof. Let $\mathcal{U} = \{U_\alpha : \alpha \in \Delta\}$ be any cover of $A \cup B$ by m-open sets of X. Then $\mathcal{U}$ is a cover of A and B by m-open sets of X. Since A and B are m-$\mathcal{H}$-compact relative to X, there exist finite subsets Δ_A and Δ_B of Δ and subsets H_A and H_B of $\mathcal{H}$ such that $A \subset \cup\{U_\alpha : \alpha \in \Delta_A\} \cup H_A$ and $B \subset \cup\{U_\alpha : \alpha \in \Delta_B\} \cup H_B$. Hence we have $A \cup B \subset \cup\{U_\alpha : \alpha \in \Delta_A \cup \Delta_B\} \cup (H_A \cup H_B)$. Since $\mathcal{H}$ is an ideal, we have $(A \cup B) \setminus \cup\{U_\alpha : \alpha \in \Delta_A \cup \Delta_B\} \in \mathcal{H}$. This shows that $A \cup B$ is m-$\mathcal{H}$-compact relative to X. □

The assumption "*ideal* m-space" in Theorem 3.10 can not be replaced by "*hereditary* m-space" as shown by the following example which is due to Qahis et at. [15].

Example 2.11. Let $X = \mathbf{R}$ be the real numbers, $m = \tau$ the usual topology, and $\mathcal{H} = \{H \subseteq \mathbf{R} : H \subseteq (0, 1)$ or $H \subseteq (1, 2)\}$. If $A = (0, 1)$ and $B = (1, 2)$, then
(1) A and B are m-$\mathcal{H}$-compact relative to X.
(2) $A \cup B$ is not m-$\mathcal{H}$-compact relative to X.

Proof. (1) The proof is obvious.
(2) The family $\{(1/n, 2 - 1/n) : n \in Z^+\}$, where $\mathbf{Z}^+$ is the family of positive integers,

is a cover of $A \cup B$ by m-open sets of X. For any finite subsets $\{n_1, n_2, \ldots, n_i\}$ of $\mathbf{Z}^+$, put $N = \max\{n_1, n_2, \ldots, n_i\}$. Then we have $(A \cup B) \setminus \cup\{(1/n, 2 - 1/n) : 1 \leqslant i \leqslant n\} = (A \cup B) \setminus (1/N, 2 - 1/N) = (0, 1/N] \cup [2 - 1/N, 2) \notin \mathcal{H}$. Therefore, $A \cup B$ is not m-$\mathcal{H}$-compact relative to X. □

Theorem 2.12. *Let $(X, m, \mathcal{H})$ be a hereditary m-space, and A, B be subsets of X. If A is m-$\mathcal{H}$-compact relative to X and B is m-closed, then $A \cap B$ is m-$\mathcal{H}$-compact relative to X.*

Proof. Let $\{U_\alpha : \alpha \in \Delta\}$ be a cover of $A \cap B$ by m-open sets of X. Then $A \setminus B \subset X \setminus B$ and $X \setminus B$ is m-open. Then $\{U_\alpha : \alpha \in \Delta\} \cup \{X \setminus B\}$ is a cover of A by m-open sets of X. Since A is m-$\mathcal{H}$-compact relative to X, there exists a finite subset Δ_0 of Δ such that $A \subset (\cup\{U_\alpha : \alpha \in \Delta_0\}) \cup \{X \setminus B\} \cup H_0$, where $H_0 \in \mathcal{H}$. Then we have

$$(A \cap B) \subset (\cup\{U_\alpha \cap B : \alpha \in \Delta_0\}) \cup (H_0 \cap B) \subset \cup\{U_\alpha : \alpha \in \Delta_0\} \cup H_0.$$

Therefore, $(A \cap B) \setminus \cup\{U_\alpha : \alpha \in \Delta_0\} \subset H_0 \in \mathcal{H}$. This shows that $A \cap B$ is m-$\mathcal{H}$-compact relative to X.

Corollary 2.13. *If a hereditary m-space $(X, m, \mathcal{H})$ is m-$\mathcal{H}$-compact and B is m-closed, then B is m-$\mathcal{H}$-compact relative to X.*

Theorem 2.14. *If $f : (X, m, \mathcal{H}) \to (Y, n, f(\mathcal{H}))$ is a surjective M-continuous function and A is m-$\mathcal{H}$-compact relative to X, then $f(A)$ is n-$f(\mathcal{H})$-compact relative to Y.*

Proof. Suppose that A is m-$\mathcal{H}$-compact relative to X. Let $\{V_\alpha : \alpha \in \Delta\}$ be any cover of $f(A)$ by n-open sets of Y. For each $x \in A$, there exists $\alpha(x) \in \Delta$ such that $f(x) \in V_{\alpha(x)}$. Since f is M-continuous, there exists an m-open set U_x containing x such that $f(x) \in f(U_x) \subset V_{\alpha(x)}$. Since $\{U_x : x \in A\}$ is an m-open cover of A and A is m-$\mathcal{H}$-compact relative to X, there exists a finite subset A_0 of A such that $A \subset \cup\{U_x : x \in A_0\} \cup H_0$, where $H_0 \in \mathcal{H}$ and hence $f(A) \subset \cup\{f(U_x) : x \in A_0\} \cup f(H_0) \subset \cup\{V_{\alpha(x)} : x \in A_0\} \cup f(H_0)$. Therefore, $f(A) \setminus \cup\{V_{\alpha(x)} : x \in A_0\} \subset f(H_0) \in f(\mathcal{H})$. Therefore, we have $f(A) \setminus \cup\{V_{\alpha(x)} : x \in A_0\} \in f(\mathcal{H})$. This shows that $f(A)$ is n-$f(\mathcal{H})$-compact relative to Y. □

Corollary 2.15. *If $f : (X, m, \mathcal{H}) \to (Y, n, f(\mathcal{H}))$ is a surjective M-continuous function and $(X, m, \mathcal{H})$ is m-$\mathcal{H}$-compact, then $(Y, n, f(\mathcal{H}))$ is n-$f(\mathcal{H})$-compact.*

Theorem 2.16. *Let $f : (X, m) \to (Y, n, \mathcal{J})$ be an M-open bijective function. If B is n-$\mathcal{J}$-compact relative to Y, then $f^{-1}(B)$ is m-$f^{-1}(J)$-compact relative to X.*

Proof. Since $f^{-1} : (Y, n, \mathcal{J}) \to (X, m)$ is an M-continuous bijection, by Theorem 3.14 the proof is obvious. □

Corollary 2.17. *Let $f : (X, m) \to (Y, n, \mathcal{J})$ be an M-open bijective function and $(Y, n, \mathcal{J})$ is n-$\mathcal{J}$-compact, then $(X, m, f^{-1}(\mathcal{J}))$ is m-$f^{-1}(\mathcal{J})$-compact.*

Theorem 2.18. *If $f : (X, m, \mathcal{H}) \to (Y, n)$ is an injective M-continuous function and A is m-$\mathcal{H}$-compact relative to X, then $f(A)$ is n-$\mathcal{J}_H$-compact relative to Y.*

Proof. Let $\{V_\alpha : \alpha \in \Delta\}$ be any cover of $f(A)$ by n-open sets of Y. For each $x \in A$, there exists $\alpha(x) \in \Delta$ such that $f(x) \in V_{\alpha(x)}$. Since f is M-continuous, there exists an m-open set U_x containing x such that $f(U_x) \subset V_{\alpha(x)}$. Then $\{U_x : x \in A\}$ is an m-open cover of A. Since A is m-$\mathcal{H}$-compact relative to X, there exists a finite subset A_0 of A such that $A \subset \cup\{U_x : x \in A_0\} \cup H_0$ for some $H_0 \in \mathcal{H}$ and $f(A) \subset \cup\{f(U_x) : x \in A_0\} \cup f(H_0)$ for some $H_0 \in \mathcal{H}$. Therefore, $f(A) \subset \cup\{V_{\alpha(x)} : x \in A_0\} \cup f(H_0)$. Since f is injective, $f^{-1}(f(H_0)) = H_0 \in \mathcal{H}$ and $f(H_0) \in \mathcal{J}_H$. Consequently, we obtain $f(A) \setminus \cup\{V_{\alpha(x)} : x \in A_0\} \in \mathcal{J}_H$. This shows that $f(A)$ is n-$\mathcal{J}_H$-compact relative to Y.

3. Strongly m-$\mathcal{H}$-compact spaces

Definition 3.1. Let $(X, m, \mathcal{H})$ be a hereditary m-space.

(1) A subset A of X is said to be *strongly m-$\mathcal{H}$-compact relative to X* if for every family $\{U_\alpha : \alpha \in \Delta\}$ of m-open sets of X such that $A \setminus \cup\{U_\alpha : \alpha \in \Delta\} \in \mathcal{H}$, there exists a finite subset Δ_0 of Δ such that $A \setminus \cup\{U_\alpha : \alpha \in \Delta_0\} \in \mathcal{H}$.

(2) $(X, m, \mathcal{H})$ is said to be *strongly m-$\mathcal{H}$-compact* if X is *strongly m-$\mathcal{H}$-compact relative to X*.

Theorem 3.2. *Let $(X, m, \mathcal{H})$ be a hereditary m-space. For a subset A of X, the following properties are equivalent:*

(1) A is strongly m-$\mathcal{H}$-compact relative to X;

(2) for every family $\{F_\alpha : \alpha \in \Delta\}$ of m-closed sets of X such that $A \cap (\cap\{F_\alpha : \alpha \in \Delta\}) \in \mathcal{H}$, there exists a finite subset Δ_0 of Δ such that $A \cap (\cap\{F_\alpha : \alpha \in \Delta_0\}) \in \mathcal{H}$.

Proof. (1) $\Rightarrow$ (2): Let $\{F_\alpha : \alpha \in \Delta\}$ be a family of m-closed sets of X such that $A \cap (\cap\{F_\alpha : \alpha \in \Delta\}) \in \mathcal{H}$. Then $A \setminus \cup\{X \setminus F_\alpha : \alpha \in \Delta\}) = A \setminus (X \setminus \cap\{F_\alpha : \alpha \in \Delta\}) = A \cap (\cap\{F_\alpha : \alpha \in \Delta\}) \in \mathcal{H}$. Since $X \setminus F_\alpha$ is m-open for each $\alpha \in \Delta$ and A is strongly m-$\mathcal{H}$-compact relative to X by (1), there exists a finite subset Δ_0 of Δ such that $A \setminus \cup\{X \setminus F_\alpha : \alpha \in \Delta_0\} \in \mathcal{H}$. This implies that $A \cap (\cap\{F_\alpha : \alpha \in \Delta_0\}) = A \setminus (X \setminus (\cap\{F_\alpha : \alpha \in \Delta_0\})) = A \setminus \cup\{X \setminus F_\alpha : \alpha \in \Delta_0\} \in \mathcal{H}$.

(2) $\Rightarrow$ (1): Let $\{U_\alpha : \alpha \in \Delta\}$ be a family of m-open sets of X such that $A \setminus \cup\{U_\alpha : \alpha \in \Delta\} \in \mathcal{H}$. Then $\{X \setminus U_\alpha : \alpha \in \Delta\}$ is a family of m-closed sets of X and also $A \setminus \cup\{U_\alpha : \alpha \in \Delta\} = A \cap (X \setminus \cup\{U_\alpha : \alpha \in \Delta\}) = A \cap (\cap\{X \setminus U_\alpha : \alpha \in \Delta\}) \in \mathcal{H}$. Thus by (2) there exists a finite subset Δ_0 of Δ such that $A \cap (\cap\{X \setminus U_\alpha : \alpha \in \Delta_0\}) \in \mathcal{H}$. Therefore, we have $A \setminus \cup\{U_\alpha : \alpha \in \Delta_0\} = A \cap (X \setminus \cup\{U_\alpha : \alpha \in \Delta_0\}) = A \cap (\cap\{X \setminus U_\alpha : \alpha \in \Delta_0\}) \in \mathcal{H}$. This shows that A is strongly m-$\mathcal{H}$-compact relative to X. □

Corollary 3.3. *For a hereditary m-space $(X, m, \mathcal{H})$, the following properties are equivalent:*

(1) $(X, m, \mathcal{H})$ is strongly m-$\mathcal{H}$-compact;

(2) for every family $\{F_\alpha : \alpha \in \Delta\}$ of m-closed sets of X such that $\cap\{F_\alpha : \alpha \in \Delta\} \in \mathcal{H}$, there exists a finite subset Δ_0 of Δ such that $\cap\{F_\alpha : \alpha \in \Delta_0\} \in \mathcal{H}$.

Theorem 3.4. *Let $(X, m, \mathcal{H})$ be a hereditary m-space and m have property $\mathcal{B}$. If A is $\mathcal{H}mg$-closed and $A \subset B \subset \mathrm{mCl}(A)$, then the following properties are equivalent:*

(1) A is strongly m-$\mathcal{H}$-compact relative to X;

(2) B is strongly m-$\mathcal{H}$-compact relative to X.

Proof.(1) $\Rightarrow$ (2): Suppose that A is strongly m-$\mathcal{H}$-compact relative to X. Let $\{U_\alpha : \alpha \in \Delta\}$ be a family of m-open sets of X such that $B \setminus \cup\{U_\alpha : \alpha \in \Delta\} \in \mathcal{H}$. Then $A \setminus \cup\{U_\alpha : \alpha \in \Delta\} \in \mathcal{H}$. Since A is strongly m-$\mathcal{H}$-compact relative to X, there exists a finite subset Δ_0 of Δ such that $A \setminus \cup\{U_\alpha : \alpha \in \Delta_0\} \in \mathcal{H}$. Since A is $\mathcal{H}mg$-closed, $\mathrm{mCl}(A) \subset \cup\{U_\alpha : \alpha \in \Delta_0\}$. Since $B \subset \mathrm{mCl}(A)$, we have $B \setminus \cup\{U_\alpha : \alpha \in \Delta_0\} \subset \mathrm{mCl}(A) \setminus \cup\{U_\alpha : \alpha \in \Delta_0\} = \emptyset \in \mathcal{H}$. Therefore, B is strongly m-$\mathcal{H}$-compact relative to X.

(2) $\Rightarrow$ (1): Suppose that B is strongly m-$\mathcal{H}$-compact relative to X. Let $\{U_\alpha : \alpha \in \Delta\}$ be any family of m-open sets of X such that $A \setminus \cup\{U_\alpha : \alpha \in \Delta\} \in \mathcal{H}$. Since A is $\mathcal{H}mg$-closed, we have $B \subset \mathrm{mCl}(A) \subset \cup\{U_\alpha : \alpha \in \Delta\}$. Since B is strongly m-$\mathcal{H}$-compact relative to X, there exists a finite subset Δ_0 of Δ such that $B \setminus \cup\{U_\alpha : \alpha \in \Delta_0\} \in \mathcal{H}$. Since $A \subset B, A \setminus \cup\{U_\alpha : \alpha \in \Delta_0\} \in \mathcal{H}$. Hence, A is strongly m-$\mathcal{H}$-compact relative to X. □

Theorem 3.5. *Let $(X, m, \mathcal{H})$ be an ideal m-space. If subsets A and B of X are strongly m-$\mathcal{H}$-compact relative to X, then $A \cup B$ is strongly m-$\mathcal{H}$-compact relative to X.*

Proof. Let $\{U_\alpha : \alpha \in \Delta\}$ be any family of m-open sets of X such that $(A \cup B) \setminus \cup\{U_\alpha : \alpha \in \Delta\} \in \mathcal{H}$. Then $A \setminus \cup\{U_\alpha : \alpha \in \Delta\} \in \mathcal{H}$ and $B \setminus \cup\{U_\alpha : \alpha \in \Delta\} \in \mathcal{H}$. Since A and B are strongly m-$\mathcal{H}$-compact relative to X, there exist finite subsets Δ_A and Δ_B of Δ and subsets H_A and H_B of $\mathcal{H}$ such that $A \subset \cup\{U_\alpha : \alpha \in \Delta_A\} \cup H_A$ and $B \subset \cup\{U_\alpha : \alpha \in \Delta_B\} \cup H_B$. Hence we have $(A \cup B) \subset \cup\{U_\alpha : \alpha \in \Delta_A \cup \Delta_B\} \cup (H_A \cup H_B)$. Since $\mathcal{H}$ is an ideal, we have $(A \cup B) \setminus \cup\{U_\alpha : \alpha \in \Delta_A \cup \Delta_B\} \in \mathcal{H}$. This shows that $A \cup B$ is strongly m-$\mathcal{H}$-compact relative to X. □

Theorem 3.6. *Let $(X, m, \mathcal{H})$ be a hereditary m-space and A, B be subsets of X. If A is strongly m-$\mathcal{H}$-compact relative to X and B is m-closed, then $A \cap B$ is strongly m-$\mathcal{H}$-compact relative to X.*

Proof. Let $\{U_\alpha : \alpha \in \Delta\}$ be a family of m-open sets of X such that $(A \cap B) \setminus \cup\{U_\alpha : \alpha \in \Delta\} \in \mathcal{H}$. Then $\{U_\alpha : \alpha \in \Delta\} \cup \{X \setminus B\}$ is a family of m-open sets of X such that $A \setminus [(X \setminus B) \cup (\cup\{U_\alpha : \alpha \in \Delta\})] \in \mathcal{H}$. Since A is strongly m-$\mathcal{H}$-compact relative to X, there exists a finite subset Δ_0 of Δ such that $A \subset \cup[\{U_\alpha : \alpha \in \Delta_0\} \cup \{X \setminus B\}] \cup H_0$, where $H_0 \in \mathcal{H}$. Then we have

$$(A \cap B) \subset [\cup\{U_\alpha \cap B : \alpha \in \Delta_0\}] \cup (H_0 \cap B) \subset [\cup\{U_\alpha : \alpha \in \Delta_0\}] \cup H_0.$$

Therefore, $(A \cap B) \setminus \cup\{U_\alpha : \alpha \in \Delta_0\} \subset H_0 \in \mathcal{H}$. This shows that $A \cap B$ is strongly m-$\mathcal{H}$-compact relative to X. □

Corollary 3.7. *If a hereditary m-space $(X, m, \mathcal{H})$ is strongly m-$\mathcal{H}$-compact and B is m-closed, then B is strongly m-$\mathcal{H}$-compact relative to X.*

Theorem 3.8. *If $f : (X, m, \mathcal{H}) \to (Y, n)$, where m has property $\mathcal{B}$, is a bijective M-continuous function and A is strongly m-$\mathcal{H}$-compact relative to X, then $f(A)$ is strongly n-$f(\mathcal{H})$-compact relative to Y.*

Proof. Suppose that A is strongly m-$\mathcal{H}$-compact relative to X. Let $\{V_\alpha : \alpha \in \Delta\}$ be any family of n-open sets in Y such that $f(A) \setminus \cup\{V_\alpha : \alpha \in \Delta\} \in f(\mathcal{H})$. Then $f(A) \subset \cup\{V_\alpha : \alpha \in \Delta\} \cup f(H_0)$ for some $H_0 \in \mathcal{H}$. Since f is bijective, $A = f^{-1}(f(A)) \subset \cup\{f^{-1}(V_\alpha) : \alpha \in \Delta\} \cup H_0$ and hence $A \setminus \cup\{f^{-1}(V_\alpha) : \alpha \in \Delta\} \in \mathcal{H}$. Since f is M-continuous, by Lemma 2.12 $\{f^{-1}(V_\alpha) : \alpha \in \Delta\}$ is a family of m-open sets of X. Since A is strongly m-$\mathcal{H}$-compact relative to X, there exists a finite subset Δ_0 of Δ such that $A \setminus \cup\{f^{-1}(V_\alpha) : \alpha \in \Delta_0\} \in \mathcal{H}$. Hence we have $A \subset \cup\{f^{-1}(V_\alpha) : \alpha \in \Delta_0\} \cup H_A$, where $H_A \in \mathcal{H}$ and $f(A) \subset \cup\{V_\alpha : \alpha \in \Delta_0\} \cup f(H_A)$. Therefore, we have $f(A) \setminus \cup\{V_\alpha : \alpha \in \Delta_0\} \in f(\mathcal{H})$. This shows that $f(A)$ is strongly n-$f(\mathcal{H})$-compact relative to Y. □

Corollary 3.9. *If $f : (X, m, \mathcal{H}) \to (Y, n)$, where m has property $\mathcal{B}$, is a bijective M-continuous function and $(X, m, \mathcal{H})$ is strongly m-$\mathcal{H}$-compact, then $(Y, n, f(\mathcal{H}))$ is strongly n-$f(\mathcal{H})$-compact.*

Theorem 3.10. *If $f : (X, m, \mathcal{H}) \to (Y, n)$, where m has property $\mathcal{B}$, is an M-continuous injective function and A is strongly m-$\mathcal{H}$-compact relative to X, then $f(A)$ is strongly n-J_H-compact relative to Y.*

Proof. Suppose that A is strongly m-$\mathcal{H}$-compact relative to X. Let $\{V_\alpha : \alpha \in \Delta\}$ be any family of n-open sets in Y such that $f(A) \setminus \cup\{V_\alpha : \alpha \in \Delta\} \in J_H$. Then $f(A) \subset \cup\{V_\alpha : \alpha \in \Delta\} \cup J_0$ for some $J_0 \in J_H$. Then $A \subset f^{-1}(f(A)) \subset \cup\{f^{-1}(V_\alpha) : \alpha \in \Delta\} \cup f^{-1}(J_0)$ and hence $A \setminus \cup\{f^{-1}(V_\alpha) : \alpha \in \Delta\} \in \mathcal{H}$. Since f is M-continuous, $\{f^{-1}(V_\alpha) : \alpha \in \Delta\}$ is a family of m-open sets of X. Since A is strongly m-$\mathcal{H}$-compact relative to X, there exists a finite subset Δ_0 of Δ such that $A \setminus \cup\{f^{-1}(V_\alpha) : \alpha \in \Delta_0\} \in \mathcal{H}$. Hence we have $A \subset \cup\{f^{-1}(V_\alpha) : \alpha \in \Delta_0\} \cup H_0$, where $H_0 \in \mathcal{H}$ and $f(A) \subset \cup\{V_\alpha : \alpha \in \Delta_0\} \cup f(H_0)$. Since f is injective, we have $f(A) \setminus \cup\{V_\alpha : \alpha \in \Delta_0\} \in J_H$ and hence $f(A)$ is strongly n-J_H-compact relative to Y. □

Corollary 3.11. *If $f : (X, m, \mathcal{H}) \to (Y, n)$, where m has property $\mathcal{B}$, is a bijective M-continuous function and $(X, m, \mathcal{H})$ is strongly m-$\mathcal{H}$-compact, then (Y, n) is strongly n-J_H-compact.*

4. Super m-$\mathcal{H}$-compact spaces

Definition 4.1. Let $(X, m, \mathcal{H})$ be a hereditary m-space.

(1) A subset A of X is said to be *super m-$\mathcal{H}$-compact relative to X* if for every family $\{U_\alpha : \alpha \in \Delta\}$ of m-open sets of X such that $A \setminus \cup\{U_\alpha : \alpha \in \Delta\} \in \mathcal{H}$, there exists a finite subset Δ_0 of Δ such that $A \subset \cup\{U_\alpha : \alpha \in \Delta_0\}$.

(2) $(X, m, \mathcal{H})$ is said to be *super m-$\mathcal{H}$-compact* if the set X is super m-$\mathcal{H}$-compact relative to X.

Theorem 4.2. *Let $(X, m, \mathcal{H})$ be a hereditary m-space. For a subset A of X, the following properties are equivalent:*

(1) A is super m-$\mathcal{H}$-compact relative to X;

(2) for every family $\{F_\alpha : \alpha \in \Delta\}$ of m-closed sets of X such that $A \cap (\cap\{F_\alpha : \alpha \in \Delta\}) \in \mathcal{H}$, there exists a finite subset Δ_0 of Δ such that $A \cap (\cap\{F_\alpha : \alpha \in \Delta_0\}) = \emptyset$.

Proof. (1) $\Rightarrow$ (2): Let $\{F_\alpha : \alpha \in \Delta\}$ be a family of m-closed sets of X such that $A \cap (\cap\{F_\alpha : \alpha \in \Delta\}) \in \mathcal{H}$. Then $\{X \setminus F_\alpha : \alpha \in \Delta\}$ is a family of m-open sets of X. Then $A \setminus \cup\{(X \setminus F_\alpha) : \alpha \in \Delta\} = A \cap [X \setminus (X \setminus \cap\{F_\alpha : \alpha \in \Delta\})] = A \cap (\cap\{F_\alpha : \alpha \in \Delta\}) \in \mathcal{H}$. Since $A \setminus \cup\{(X \setminus F_\alpha) : \alpha \in \Delta\} \in \mathcal{H}$, by (1) there exists a finite subset Δ_0 of Δ such that $A \subset \cup\{(X \setminus F_\alpha) : \alpha \in \Delta_0\}$. This implies that $A \cap (\{F_\alpha : \alpha \in \Delta_0\}) = \emptyset$.

(2) $\Rightarrow$ (1): Let $\{U_\alpha : \alpha \in \Delta\}$ be a family of m-open sets of X such that $A \setminus \cup\{U_\alpha : \alpha \in \Delta\} \in \mathcal{H}$. Then $\{X \setminus U_\alpha : \alpha \in \Delta\}$ is a family of m-closed sets of X and $A \cap (\cap\{X \setminus U_\alpha : \alpha \in \Delta\}) = A \cap (X \setminus \cup\{U_\alpha : \alpha \in \Delta\}) \in \mathcal{H}$. Thus by (2) there exists a finite subset Δ_0 of Δ such that $A \cap (\cap\{X \setminus U_\alpha : \alpha \in \Delta_0\}) = \emptyset$; hence $A \subset \cup\{U_\alpha : \alpha \in \Delta_0\}$. This shows that $(X, m, \mathcal{H})$ is super m-$\mathcal{H}$-compact. □

Corollary 4.3. *For a hereditary m-space $(X, m, \mathcal{H})$, the following properties are equivalent:*

(1) $(X, m, \mathcal{H})$ is super m-$\mathcal{H}$-compact;

(2) for every family $\{F_\alpha : \alpha \in \Delta\}$ of m-closed sets of X such that $\cap\{F_\alpha : \alpha \in \Delta\} \in \mathcal{H}$, there exists a finite subset Δ_0 of Δ such that $\cap\{F_\alpha : \alpha \in \Delta_0\} = \emptyset$.

Theorem 4.4. *Let $(X, m, \mathcal{H})$ be a hereditary m-space, where m has property $\mathcal{B}$, and A, B subsets of X such that $A \subset B \subset \mathrm{mCl}(A)$, then the following properties are hold:*

(1) if A is super m-$\mathcal{H}$-compact relative to X and mg-closed, then B is super m-$\mathcal{H}$-compact relative to X,

(2) if A is strongly m-$\mathcal{H}$-compact relative to X and $\mathcal{H}mg$-closed, then B is super m-$\mathcal{H}$-compact relative to X,

(3) if B is m-compact relative to X and A is $\mathcal{H}mg$-closed, then A is super m-$\mathcal{H}$-compact relative to X.

Proof. (1): Suppose that A is super m-$\mathcal{H}$-compact relative to X and mg-closed. Let $\{U_\alpha : \alpha \in \Delta\}$ be a family of m-open sets of X such that $B \setminus \cup\{U_\alpha : \alpha \in \Delta\} \in \mathcal{H}$. Then $A \setminus \cup\{U_\alpha : \alpha \in \Delta\} \in \mathcal{H}$. Since A is super m-$\mathcal{H}$-compact relative to X, there exists a finite subset Δ_0 of Δ such that $A \subset \cup\{U_\alpha : \alpha \in \Delta_0\}$. Since A is mg-closed, $\mathrm{mCl}(A) \subset \cup\{U_\alpha : \alpha \in \Delta_0\}$. Since $B \subset \mathrm{mCl}(A)$, we have $B \subset \cup\{U_\alpha : \alpha \in \Delta_0\}$. Therefore, B is super m-$\mathcal{H}$-compact relative to X.

(2): Suppose that A is strongly m-$\mathcal{H}$-compact relative to X and $\mathcal{H}mg$-closed. Let $\{U_\alpha : \alpha \in \Delta\}$ be a family of m-open sets of X such that $B \setminus \cup\{U_\alpha : \alpha \in \Delta\} \in \mathcal{H}$. Then $A \setminus \cup\{U_\alpha : \alpha \in \Delta\} \in$

$\mathcal{H}$. Since A is strongly m-$\mathcal{H}$-compact relative to X, there exists a finite subset Δ_0 of Δ such that $A \setminus \cup\{U_\alpha : \alpha \in \Delta_0\} \in \mathcal{H}$. Since A is $\mathcal{H}mg$-closed, $\mathrm{mCl}(A) \subset \cup\{U_\alpha : \alpha \in \Delta_0\}$. Since $B \subset \mathrm{mCl}(A)$, we have $B \subset \cup\{U_\alpha : \alpha \in \Delta_0\}$. Therefore, B is super m-$\mathcal{H}$-compact relative to X.

(3): Suppose that B is m-compact relative to X and A is $\mathcal{H}mg$-closed. Let $\{U_\alpha : \alpha \in \Delta\}$ be any family of m-open sets of X such that $A \setminus \cup\{U_\alpha : \alpha \in \Delta\} \in \mathcal{H}$. Since A is $\mathcal{H}mg$-closed, we have $B \subset \mathrm{mCl}(A) \subset \cup\{U_\alpha : \alpha \in \Delta\}$. Since B is m-compact relative to X, there exists a finite subset Δ_0 of Δ such that $B \subset \cup\{U_\alpha : \alpha \in \Delta_0\}$. Since $A \subset B, A \subset \cup\{U_\alpha : \alpha \in \Delta_0\}$. Therefore, A is super m-$\mathcal{H}$-compact relative to X. □

Corollary 4.5. *Let $(X, m, \mathcal{H})$ be a hereditary m-space and m have property $\mathcal{B}$. If A is $\mathcal{H}mg$-closed and $A \subset B \subset \mathrm{mCl}(A)$, then the following properties are equivalent:*

(1) A is super m-$\mathcal{H}$-compact relative to X;

(2) B is super m-$\mathcal{H}$-compact relative to X.

Theorem 4.6. *Let $(X, m, \mathcal{H})$ be a hereditary m-space. If subsets A and B of X are super m-$\mathcal{H}$-compact relative to X, then $A \cup B$ is super m-$\mathcal{H}$-compact relative to X.*

Proof. Let $\{U_\alpha : \alpha \in \Delta\}$ be any family of m-open sets of X such that $(A \cup B) \setminus \cup\{U_\alpha : \alpha \in \Delta\} \in \mathcal{H}$. Then $A \setminus \cup\{U_\alpha : \alpha \in \Delta\} \in \mathcal{H}$ and $B \setminus \cup\{U_\alpha : \alpha \in \Delta\} \in \mathcal{H}$. Since A and B are super m-$\mathcal{H}$-compact relative to X, there exist finite subsets Δ_A and Δ_B of Δ such that $A \subset \cup\{U_\alpha : \alpha \in \Delta_A\}$ and $B \subset \cup\{U_\alpha : \alpha \in \Delta_B\}$. Hence we have $(A \cup B) \subset \cup\{U_\alpha : \alpha \in \Delta_A \cup \Delta_B\}$. This shows that $A \cup B$ is super m-$\mathcal{H}$-compact relative to X. □

Theorem 4.7. *Let $(X, m, \mathcal{H})$ be a hereditary m-space and A, B be subsets of X. If A is super m-$\mathcal{H}$-compact relative to X and B is m-closed, then $A \cap B$ is super m-$\mathcal{H}$-compact relative to X.*

Proof. Let $\{U_\alpha : \alpha \in \Delta\}$ be a family of m-open sets of X such that $(A \cap B) \setminus \cup\{U_\alpha : \alpha \in \Delta\} \in \mathcal{H}$. Then $\{U_\alpha : \alpha \in \Delta\} \cup \{X \setminus B\}$ is a family of m-open sets of X such that $A \subset [(X \setminus B) \cup (\cup\{U_\alpha : \alpha \in \Delta\})] \cup H_0$, where $H_0 \in \mathcal{H}$. Since A is super m-$\mathcal{H}$-compact relative to X, there exists a finite subset Δ_0 of Δ such that $A \subset [\cup\{U_\alpha : \alpha \in \Delta_0\}] \cup \{X \setminus B\}$. Then we have $(A \cap B) \subset \cup\{U_\alpha \cap B : \alpha \in \Delta_0\} \subset \cup\{U_\alpha : \alpha \in \Delta_0\}$. This shows that $A \cap B$ is super m-$\mathcal{H}$-compact relative to X. □

Corollary 4.8. *If a hereditary m-space $(X, m, \mathcal{H})$ is super m-$\mathcal{H}$-compact and B is m-closed, then B is super m-$\mathcal{H}$-compact relative to X.*

Theorem 4.9. *If $f : (X, m, \mathcal{H}) \to (Y, n)$, where m has property $\mathcal{B}$, is a bijective M-continuous function and A is super m-$\mathcal{H}$-compact relative to X, then $f(A)$ is super n-$f(\mathcal{H})$-compact relative to Y.*

Proof. Suppose that A is super m-$\mathcal{H}$-compact relative to X. Let $\{V_\alpha : \alpha \in \Delta\}$ be any family of n-open sets in Y such that $f(A) \setminus \cup\{V_\alpha : \alpha \in \Delta\} \in f(\mathcal{H})$. Then $f(A) \subset \cup\{V_\alpha : \alpha \in \Delta\} \cup f(H_0)$ for some $H_0 \in \mathcal{H}$. Since f is bijective, $A = f^{-1}(f(A)) \subset \cup\{f^{-1}(V_\alpha) : \alpha \in \Delta\} \cup H_0$ and hence $A \setminus \cup\{f^{-1}(V_\alpha) : \alpha \in \Delta\} \in \mathcal{H}$. Since f is M-continuous, $\{f^{-1}(V_\alpha) : \alpha \in \Delta\}$ is a family of m-open sets of X. Since A is super m-$\mathcal{H}$-compact relative to X, there exists a finte subset Δ_0 of Δ such that $A \subset \cup\{f^{-1}(V_\alpha) : \alpha \in \Delta_0\}$. Hence we have $f(A) \subset \cup\{V_\alpha : \alpha \in \Delta_0\}$ and hence $f(A)$ is super n-$f(\mathcal{H})$-compact relative to Y. □

Corollary 4.10. *If $f : (X, m, \mathcal{H}) \to (Y, n)$, where m has property $\mathcal{B}$, is a bijective M-continuous function and $(X, m, \mathcal{H})$ is super m-$\mathcal{H}$-compact, then $(Y, n, f(\mathcal{H}))$ is super n-$f(\mathcal{H})$-compact.*

Theorem 4.11. *If $f : (X, m, \mathcal{H}) \to (Y, n)$, where m has property $\mathcal{B}$, is an M-continuous function and A is super m-$\mathcal{H}$-compact relative to X, then $f(A)$ is super n-$\mathcal{J}_H$-compact relative to Y.*

Proof. Suppose that A is super m-$\mathcal{H}$-compact relative to X. Let $\{V_\alpha : \alpha \in \Delta\}$ be any family of n-open sets in Y such that $f(A) \setminus \cup\{V_\alpha : \alpha \in \Delta\} \in \mathcal{J}_H$. Then $f(A) \subset \cup\{V_\alpha : \alpha \in \Delta\} \cup J_0$ for some $J_0 \in \mathcal{J}_H$. Then $A \subset f^{-1}(f(A)) \subset \cup\{f^{-1}(V_\alpha) : \alpha \in \Delta\} \cup f^{-1}(J_0)$ and hence $A \setminus \cup\{f^{-1}(V_\alpha) : \alpha \in \Delta\} \subset f^{-1}(J_0) \in \mathcal{H}$. Since f is M-continuous, $\{f^{-1}(V_\alpha) : \alpha \in \Delta\}$ is a family of m-open sets of X. Since A is super m-$\mathcal{H}$-compact relative to X, there exists a finte subset Δ_0 of Δ such that $A \subset \cup\{f^{-1}(V_\alpha) : \alpha \in \Delta_0\}$. Hence we have $f(A) \subset \cup\{f(f^{-1}(V_\alpha)) : \alpha \in \Delta_0\} \subset \cup\{V_\alpha : \alpha \in \Delta_0\}$. Therefore, $f(A)$ is super n-$\mathcal{J}_H$-compact relative to Y. □

Corollary 4.12. *If $f : (X, m, \mathcal{H}) \to (Y, n)$, where m has property $\mathcal{B}$, is a surjective M-continuous function and $(X, m, \mathcal{H})$ is super m-$\mathcal{H}$-compact, then (Y, n) is super n-$\mathcal{J}_H$-compact.*

Remark 4.13. We have the following relationships:

$$\begin{array}{ccc} \text{super } m\text{-}\mathcal{H}\text{-compact relative to } X & \Rightarrow & \text{strongly } m\text{-}\mathcal{H}\text{-compact relative to } X, \\ \Downarrow & & \Downarrow \\ m\text{-compact relative to } X & \Rightarrow & m\text{-}\mathcal{H}\text{-compact relative to } X. \end{array}$$

Remark 4.14. The following examples show that "m-compact relative to X" and "strongly m-$\mathcal{H}$-compact relative to X" are independent of each other.

Example 4.15. Let $\mathcal{R}$ be the set of real numbers with the usual topology, $X = [1, 2]$ and $m = \{X \cap (a, b) : a < b, a, b \in \mathcal{R}\}$. Then it is clear that (X, m) is a topological space and an m-space. Let $\mathcal{H} = \{\emptyset, \{1\}, \{2\}\}$. Observe that (X, m) is m-compact relative to X but $(X, m, \mathcal{H})$ is not strongly m-$\mathcal{H}$-compact relative to X. In fact if $U_n = (1 + \frac{1}{n}, 2]$ for all integer number $n > 1$, then $X \setminus \cup_{n>1} U_n = \{1\} \in \mathcal{H}$. If we take $N = \max\{n_1, n_2, \cdots, n_k\}$, $k \in \mathbf{Z}$ and $n_1, n_2, \cdots, n_k$ are integer numbers then $X \setminus \cup_{i=1}^{k} U_{n_i} = X \setminus (1 + \frac{1}{N}, 2] = [1, 1 + \frac{1}{N}] \notin \mathcal{H}$.

Example 4.16. Let $\mathcal{R}$ be the set of real numbers with the usual topology τ. Let $X = (0, 1)$, m the relative topology of τ on X and $\mathcal{H} = \{A : A \subseteq (0, 1)\}$ then $(X, m, \mathcal{H})$ is strongly m-$\mathcal{H}$-compact relative to X but (X, m) is not m-compact relative to X. Because an m-open cover $\{(0 + \frac{1}{n}, 1 - \frac{1}{n}) : n \in \mathbf{Z}^+\}$ of X has no finite subcover.

References

[1] A.Al-Omari, T.Noiri, Properties of $\gamma\mathcal{H}$-compact spaces with hereditary classes, *Atti Accad. Pelor. Peric. Cl. Sci. Fis. Mat. Natur.*, **98**(2020), no. 2, A4-1-A4-11.

[2] A.Al-Omari, T.Noiri, Generalizations of Lindelöf spaces via hereditary classes, *Acta Univ. Sapientie Math.*, **13**(2021), no. 2, 281-291.

[3] A.Al-Omari, T.Noiri, Properties of θ-$\mathcal{H}$-compact sets in hereditary m-spaces, *Acta Comment. Univ. Tartu. Math.*, **26**(2022), 193–206

[4] A.Al-Omari, T.Noiri, Super and strong $\gamma\mathcal{H}$-compactness in Hereditary m-spaces, *Commun. Korean Math. Soc.*, **39**(2024), no. 3, 775–784. DOI: 10.4134/CKMS.C230199

[5] Á.Császár, Modification of generalized topologies via hereditary classes, *Acta Math. Hungar.*, **115**(1-2), (2007), 29-35.

[6] T.R.Hamlett, D.Janković, Compactness with respect to an ideal, *Boll. Un. Mat. Ital.*, **4**-B (1990), no. 7, 849–861.

[7] S.Jafari, T Noiri, V.Popa, On θ-compactness in ideal topological spaces, *Ann. Univ. Sci. Budapest.*, **52**(2009), 123–130.

[8] D.Janković, T.R.Hamlett, New topologies from old via ideals, *Amer. Math. Monthly*, **97**(1990), no. 4, 295–310.

[9] K.Kuratowski, Topology, Vol. I, Academic Press, New York, 1966.

[10] H.Maki, K.C.Rao, A.Nagoor Gani, On generalizing semi-open and preopen sets, *Pure Appl. Math. Sci.*, **49**(1999), 17–29.

[11] R.L.Newcomb, Toplogies which are compact modulo an ideal, Ph. D. Dissertation, Univ. of Cal. at Santa Barbara, 1967

[12] T.Noiri, A unified theory of modifications of g-closed sets, *Rend. Circ. Mat. Palermo*, **56**(2007), no. 2, 171–184.

[13] V.Popa, T.Noiri, On M-continuous functions, *An. Univ. "Dunarea de Jos" Galati, Ser. Mat. Fiz. Mec. Teor.*, **43**(**23**)(2000), 31–41.

[14] V.Popa, T.Noiri, A unified theory of weak continuity for functions, *Rend. Circ. Mat. Palermo*, **51**(2002), no. 2, 439–464.

[15] A.Qahis, H.H.Al-Jarrah, T.Noiri, Weakly μ-compact via a herediatary class, *Bol. Soc. Paran. Mat.*, **39**(2021), no. 3, 123–135.

[16] D.V.Rančin, Compactness modulo an ideal, *Soviet Math. Dokl.*, **13**(1972), 193–197.

[17] R.Vaidyanathaswani, The localization theory in set-topology, *Proc. Indian Acad. Sci.*, **20**(1945), 51–62.

Свойства $m\mathcal{H}$-компактов в наследственных m-пространствах

Ахмад Аль-Омари
Университет Аль-аль-Байт
Мафрак 25113, Иордания
Такаши Ноири
Яцусиро-си, Кумамото-кен, Япония

Аннотация. Пусть $(X, m, \mathcal{H})$ — наследственное m-пространство. Подмножество A из X называется $\mathcal{H}$-компактным относительно X, если для любого покрытия $\mathcal{U}$ из A m-открытыми множествами из X существует конечное подмножество $\mathcal{U}_0$ из $\mathcal{U}$ такое, что $A \setminus \cup\, \mathcal{U}_0 \in \mathcal{H}$. Мы получаем несколько свойств этих множеств. А также мы определяем и исследуем два вида сильных форм $\mathcal{H}$-компактности относительно X.

Ключевые слова: наследственное m-пространство, $\mathcal{H}$-компактность, сильная $\mathcal{H}$-компактность, супер $\mathcal{H}$-компактность.

EDN: ZDRWXS
УДК 519

Novel Results on Positive Solutions for Nonlinear Caputo-Hadamard Fractional Volterra-Fredholm Integro Differential Equations

Abdulrahman A. Sharif*
Department of Mathematics
Hodeidah University
AL-Hudaydah, Yemen
Maha M. Hamood†
Department of Mathematics
Taiz University
Taiz, Yemen
Kirtiwant P. Ghadle‡
Department of Mathematics
Dr. Babasaheb Ambedkar Marathwada University
Aurangabad-431 004 (M.S.), India

Received 10.08.2024, received in revised form 15.09.2024, accepted 24.10.2024

Abstract. In this paper, we establish the existence and uniqueness of positive solutions for fractional Volterra-Fredholm integro-differential equation. This equation incorporates Caputo–Hadamard fractional derivatives and is defined with initial conditions. Our proof methodology relies on the Schauder fixed point theorem, the Banach contraction principle, upper and lower solution concepts, and their applications. To illustrate the significance of our theoretical findings, we also present a compelling example.

Keywords: fractional Volterra–Fredholm integro-differential equation, positive solutions, fixed point method

Citation: A.A. Sharif, M.M. Hamood, K.P. Ghadle, Novel Results on Positive Solutions for Nonlinear Caputo-Hadamard Fractional Volterra-Fredholm Integro Differential Equations, J. Sib. Fed. Univ. Math. Phys., 2025, 18(2), 273–282. EDN: ZDRWXS.

1. Introduction and preliminaries

Fractional calculus introduces the extension of derivative and integral concepts to non-integer orders, representing a relatively recent area of exploration. Noteworthy contributions in this domain have been made by researchers like Kilbas et al. [17] and Podlubny [23], among others. The investigation of equations involving fractional differentiation and integration holds particular significance due to their broad applicability in various scientific and technological fields, spanning both natural and engineering domains. It's worth mentioning that many researchers have focused

*abdul.sharef1985@gmail.com https://orcid.org/0000-0001-9076-3615
†mahamgh1@gmail.com https://orcid.org/0000-0003-0657-2093
‡ghadle.maths@bamu.ac.in https://orcid.org/0000-0003-3205-5498

on studying the positivity properties of solutions for these equations, as evidenced by numerous references [1–6, 8, 9, 13–16] and the citations therein.

In recent times, the examination of Hadamard Fractional Differential Equations (Hadamard FDEs) has gained considerable significance. Notably, there has been substantial progress in the understanding of Hadamard derivatives in the context of differential equations. For a comprehensive exploration of the Hadamard fractional derivative, please refer to the following sources: [7, 10, 12, 18, 19].

In [20], we study the solutions of the nonlinear fractional differential equation involving the Caputo–Hadamard operator.

This paper study of the existence and uniqueness of positive solutions of the fractional Caputo–Hadamard nonlinear Volterra–Friedholm integrol-differential equations,

$$ {}^{C}\mathfrak{D}_{1}^{\mathfrak{w}}\mathfrak{u}(\mathfrak{r}) = \kappa(\mathfrak{r},\mathfrak{u}(\mathfrak{r})) + \int_{1}^{\mathfrak{r}} \mathbb{k}_0(\mathfrak{r},\varpi,\mathfrak{u}(\varpi))d\varpi + \int_{1}^{\xi} \mathbb{k}_1(\mathfrak{r},\varpi,\mathfrak{u}(\varpi))d\varpi + \mathfrak{D}_{1}^{\mathfrak{w}-1}\hbar(\mathfrak{r},\mathfrak{u}(\mathfrak{r})), \quad \mathfrak{r}\in\psi. \quad (1) $$

The Initial Conditions

$$ \mathfrak{u}(1) = \lambda_0, \quad \mathfrak{u}'(1) = \lambda_1 > 0, \quad \psi = [1,\xi] \quad (2) $$

where $1 < \mathfrak{w} \leqslant 2$, $\kappa : \psi \times \mathfrak{N} \times \mathfrak{N} \times \mathfrak{N} \to \mathfrak{N}$, and two additional functions $\hbar : \psi \times \mathfrak{N} \to \mathfrak{N}$ and $\zeta : \psi \to \mathfrak{N}$ are introduced as continuous functions. It is important to note that $\hbar$ exhibits a non-decreasing behavior on the set $\mathfrak{u}$ and $\lambda_1 \geqslant \hbar(1,\lambda_0)$.

This paper is organized as follows. In Sect. 2., we introduce fundamental definitions and results. In Sect. 3., we present the existence and uniqueness of positive solution for problem (1)–(2). In Sect. 4., we provide an example to illustrate our results.

2. Auxiliary results

Before presenting our primary results, we offer the essential definitions, preliminary details and assumptions that will be employed in our subsequent discourse. For see [11, 21, 22, 24–30].

Consider the set ψ defined as $\psi = (1,\xi]$. Let $\mathbb{C}(\psi)$ represent the Banach space comprising all continuous functions defined on ψ, equipped with the norm defined as:

$$ \|\mathfrak{u}\| = \sup\{|\mathfrak{u}(\mathfrak{r})| : \mathfrak{r}\in\psi\}. $$

Furthermore, let $\mathfrak{B}$ be a nonempty closed subset of $\mathbb{C}(\psi)$, which can be defined as:

$$ \mathfrak{B} = \{\mathfrak{u}(\mathfrak{r}) \in \mathbb{C}(\psi) : \mathfrak{u}(\mathfrak{r}) \geqslant 0, \quad \forall \mathfrak{r}\in\psi\}. $$

Definition 2.1 ([13]). *The Hadamard fractional integral of order* $\mathfrak{w}$ *, is defined as*

$$ \mathfrak{I}_{1}^{\mathfrak{w}}\mathfrak{u}(\mathfrak{r}) = \frac{1}{\Gamma(\mathfrak{w})}\int_{1}^{\mathfrak{r}} \Big(\ln\frac{\mathfrak{r}}{\varpi}\Big)^{\mathfrak{w}-1}\mathfrak{u}(\varpi)\frac{d\varpi}{\varpi}, \ \mathfrak{w} > 0. \quad (3) $$

Definition 2.2 ([27]). *The definition of the Caputo–Hadamard fractional derivative of order* $\mathfrak{w}$ *is given, where* $\mathfrak{u} : [1,\infty) \longrightarrow \mathfrak{N}$.

$$ \mathfrak{D}_{1}^{\mathfrak{w}}\mathfrak{u}(\mathfrak{r}) = \frac{1}{\Gamma(\upsilon-\mathfrak{w})}\int_{1}^{\mathfrak{r}} \Big(\ln\frac{\mathfrak{r}}{\varpi}\Big)^{\upsilon-\mathfrak{w}-1}\Big(\mathfrak{r}\frac{d}{d\mathfrak{r}}\Big)^{\upsilon}\mathfrak{u}(\varpi)\frac{d\varpi}{\varpi}, \ \upsilon-1 < \mathfrak{w} < \upsilon. \quad (4) $$

Lemma 2.3 ([27]). *Let* $\upsilon - 1 < \mathfrak{w} \leqslant \upsilon,\ \upsilon \in \mathbb{N}$ *and* $\mathfrak{u} \in \mathbb{C}^{\upsilon}(\psi)$. *Then the Caputo–Hadamard fractional differential equation*

$$(\mathfrak{I}^{\mathfrak{w}}\mathfrak{D}^{\mathfrak{w}}\mathfrak{u})(\mathfrak{r}) = \mathfrak{u}(\mathfrak{r})$$

$$(\mathfrak{I}_1^{\mathfrak{w}}\mathfrak{D}_1^{\mathfrak{w}}\mathfrak{u})(\mathfrak{r})) = \mathfrak{u}(\mathfrak{r}) - \sum_{j=0}^{\upsilon-1} \frac{\mathfrak{u}^j(1)}{\Gamma(j+1)}(\ln \mathfrak{r})^j.$$

Theorem 2.4 (Schauder's [28]). *Consider a non-empty, closed, and convex subset* Ω *within a Banach space denoted as* $\mathfrak{s}$. *Let* $\aleph : \Omega \to \Omega$ *be a continuous, compact operator. In such a scenario, it can be asserted that* $\aleph$ *possesses a fixed point within the set* Ω.

Theorem 2.5 ("Banach's fixed point theorem" [28]). *Let* Ω *be a non-empty complete metric space and* $\kappa : \Omega \to \Omega$, *is contraction mapping. Then, there exists a unique point* $\varpi \in \Omega$ *such that* $\Phi(\varpi) = \varpi$.

Definition 2.6. *Let* $\mathfrak{a}, \mathfrak{a}_0 \in \mathfrak{N}^+$, *and* $\mathfrak{a}_0 > \mathfrak{a}$ *For any* $\mathfrak{u} \in [\mathfrak{a}, \mathfrak{a}_0]$, *we define the upper-control function* $\mathbb{U}(\mathfrak{r}, \mathfrak{u}) = \sup_{\mathfrak{d} \leqslant \tau \leqslant \mathfrak{u}} \kappa(\mathfrak{r}, \tau)$ *and lower-control function* $\mathbb{L}(\mathfrak{r}, \mathfrak{u}) = \inf_{\mathfrak{u} \leqslant \tau \leqslant \mathfrak{d}_0} \kappa(\mathfrak{r}, \tau)$ *Obviously,* $\mathbb{U}(\mathfrak{r}, \mathfrak{u})$ *and* $\mathbb{L}(\mathfrak{r}, \mathfrak{u})$ *are monotonous non-decreasing on* $[\mathfrak{a}, \mathfrak{a}_0]$ *and*

$$\mathbb{L}(\mathfrak{r}, \mathfrak{u}) \leqslant \kappa(\mathfrak{r}, \mathfrak{u}) \leqslant \mathbb{U}(\mathfrak{r}, \mathfrak{u})$$

3. Principal findings

In this section, we will present the results pertaining to the existence and uniqueness of Eq. (1), subject to the condition (2). Prior to delving into the proof of our primary findings, we will introduce the following set of hypotheses:

(Δ_1) Let $\mathfrak{u}^*, \mathfrak{u}_* \in \mathfrak{B}$ such that $\mathfrak{a} \leqslant \mathfrak{u}_*(\mathfrak{r}) \leqslant \mathfrak{u}_*(\mathfrak{r}) \leqslant \mathfrak{a}_0$ such that

$$\mathfrak{D}^{\mathfrak{w}}\mathfrak{u}^*(\mathfrak{r}) - \int_1^{\mathfrak{r}} \Bbbk_0(\mathfrak{r}, \varpi, \mathfrak{u}^*(\varpi))d\varpi - \int_1^{\xi} \Bbbk_1(\mathfrak{r}, \varpi, \mathfrak{u}^*(\varpi))d\varpi - \mathfrak{D}^{\mathfrak{w}-1}\hbar(\mathfrak{r}, \mathfrak{u}^*(\mathfrak{r})) \geqslant \mathbb{U}(\mathfrak{r}, \mathfrak{u}^*(\mathfrak{r}))$$

$$\mathfrak{D}^{\mathfrak{w}}\mathfrak{u}_*(\mathfrak{r}) - \int_1^{\mathfrak{r}} \Bbbk_0(\mathfrak{r}, \varpi, \mathfrak{u}_*(\varpi))d\varpi - \int_1^{\xi} \Bbbk_1(\mathfrak{r}, \varpi, \mathfrak{u}_*(\varpi))d\varpi - \mathfrak{D}^{\mathfrak{w}-1}\hbar(\mathfrak{r}, \mathfrak{u}_*(\mathfrak{r})) \leqslant \mathbb{L}(\mathfrak{r}, \mathfrak{u}_*(\mathfrak{r}))$$

(Δ_2) There exist positive constants $\delta_\kappa, \delta_{\Bbbk_0}, \delta_{\Bbbk_1}$ and $\delta_\hbar$ such that

$$\|\kappa(\mathfrak{r}, \mathfrak{u}(\mathfrak{r})) - \kappa(\mathfrak{r}, \mathfrak{u}_0(\mathfrak{r}))\| \leqslant \delta_\kappa \|\mathfrak{u} - \mathfrak{u}_0\|,\ \mathfrak{r} \in \psi,\ \mathfrak{u}, \mathfrak{u}_0 \in \mathfrak{N}$$

$$\|\hbar(\mathfrak{r}, \mathfrak{u}(\mathfrak{r})) - \hbar(\mathfrak{r}, \mathfrak{u}_0(\mathfrak{r}))\| \leqslant \delta_\hbar \|\mathfrak{u} - \mathfrak{u}_0\|,\ \mathfrak{r} \in \psi,\ \mathfrak{u}, \mathfrak{u}_0 \in \mathfrak{N}$$

$$\|\Bbbk_0(\mathfrak{r}, \varpi, \mathfrak{u}(\varpi)) - \Bbbk_0(\mathfrak{r}, \varpi, \mathfrak{u}_0(\varpi))\| \leqslant \delta_{\Bbbk_0} \|\mathfrak{u} - \mathfrak{u}_0\|$$

$$\|\Bbbk_1(\mathfrak{r}, \varpi, \mathfrak{u}(\varpi)) - \Bbbk_1(\mathfrak{r}, \varpi, \mathfrak{u}_0(\varpi))\| \leqslant \delta_{\Bbbk_1} \|\mathfrak{u} - \mathfrak{u}_0\|,\quad (\mathfrak{r}, \varpi) \in \mathcal{G},\quad \mathfrak{u},\ \mathfrak{u}_0 \in \mathfrak{N}$$

where $\mathcal{G} = \{(\mathfrak{r}, \varpi) :\ 0 \leqslant \varpi \leqslant \mathfrak{r} \leqslant \xi\}$.

The functions $\mathfrak{u}^*$ and $\mathfrak{u}_*$ are respectively called the pair of upper and lower solutions for the problem (1)–(2).

Lemma 3.1. *If* $\mathfrak{u} \in \mathbb{C}(\psi)$, $\mathfrak{u}^{(2)}$ *and* $\dfrac{\partial \hbar}{\partial \mathfrak{r}}$ *exists, then* $\mathfrak{u}$ *is a solution to problem* (1)–(2) *if and only if*

$$\begin{aligned} \mathfrak{u}(\mathfrak{r}) \ =\ & \frac{1}{\Gamma(\mathfrak{w})} \int_1^{\mathfrak{r}} \big(\ln \frac{\mathfrak{r}}{\mathfrak{q}}\big)^{\mathfrak{w}-1} \Big[\kappa(\mathfrak{q}, \mathfrak{u}(\mathfrak{q})) + \int_1^{\mathfrak{q}} \Bbbk_0(\mathfrak{q}, \varpi, \mathfrak{u}(\varpi))d\varpi + \int_1^{\xi} \Bbbk_1(\mathfrak{q}, \varpi, \mathfrak{u}(\varpi))d\varpi\Big] \frac{d\mathfrak{q}}{\mathfrak{q}} + \\ +\ & \lambda_0 + (\lambda_1 - \hbar(1, \lambda_0)) \ln \mathfrak{r} + \int_1^{\mathfrak{r}} \hbar(\mathfrak{q}, \mathfrak{u}(\mathfrak{q})) \frac{d\mathfrak{q}}{\mathfrak{q}} \end{aligned} \tag{5}$$

Proof. Let $\mathfrak{u}(\mathfrak{r})$ be a solution of (1)–(2). First we write this equation as

$$\mathfrak{I}_1^{\mathfrak{w}}\mathfrak{D}_1^{\mathfrak{w}}\mathfrak{u}(\mathfrak{r}) \;=\; \mathfrak{I}_1^{\mathfrak{w}}\Big[\kappa(\mathfrak{r},\mathfrak{u}(\mathfrak{r})) + \int_1^{\mathfrak{r}} \Bbbk_0(\mathfrak{r},\varpi,\mathfrak{u}(\varpi))d\varpi + \int_1^{\xi} \Bbbk_1(\mathfrak{r},\varpi,\mathfrak{u}(\varpi))d\varpi + \mathfrak{D}^{\mathfrak{w}-1}\hbar(\mathfrak{r},\mathfrak{u}(\mathfrak{r})\Big]$$

In view of Lemma 2.3, we get

$$\begin{aligned}
\mathfrak{u}(\mathfrak{r}) &= \mathfrak{u}(1) + \mathfrak{u}'(1)\ln\mathfrak{r} + \mathfrak{I}_1^{\mathfrak{w}}\mathfrak{D}^{\mathfrak{w}-1}\hbar(\mathfrak{r},\mathfrak{u}(\mathfrak{r}))+\\
&+ \mathfrak{I}_1^{\mathfrak{w}}\Big[\kappa(\mathfrak{r},\mathfrak{u}(\mathfrak{r})) + \int_1^{\mathfrak{r}} \Bbbk_0(\mathfrak{r},\varpi,\mathfrak{u}(\varpi))d\varpi + \int_1^{\xi} \Bbbk_1(\mathfrak{r},\varpi,\mathfrak{u}(\varpi))d\varpi\Big] =\\
&= \mathfrak{I}^1\mathfrak{I}_1^{\mathfrak{w}-1}\mathfrak{D}^{\mathfrak{w}-1}\hbar(\mathfrak{r},\mathfrak{u}(\mathfrak{r}))+\\
&+ \mathfrak{I}_1^{\mathfrak{w}}\Big[\kappa(\mathfrak{r},\mathfrak{u}(\mathfrak{r})) + \int_1^{\mathfrak{r}} \Bbbk_0(\mathfrak{r},\varpi,\mathfrak{u}(\varpi))d\varpi + \int_1^{\xi} \Bbbk_1(\mathfrak{r},\varpi,\mathfrak{u}(\varpi))d\varpi\Big]+\\
&+ \mathfrak{I}^1\big(\hbar(\mathfrak{r},\mathfrak{u}(\mathfrak{r}) - \hbar(1,\mathfrak{u}(1))\big)+\\
&+ \mathfrak{I}_1^{\mathfrak{w}}\Big[\kappa(\mathfrak{r},\mathfrak{u}(\mathfrak{r})) + \int_1^{\mathfrak{r}} \Bbbk_0(\mathfrak{r},\varpi,\mathfrak{u}(\varpi))d\varpi + \int_1^{\xi} \Bbbk_1(\mathfrak{r},\varpi,\mathfrak{u}(\varpi))d\varpi\Big] =\\
&= \mathfrak{u}(1) + \mathfrak{u}'(1)\ln\mathfrak{r} - \hbar(1,\mathfrak{u}(1))\ln\mathfrak{r} + \int_1^{\mathfrak{r}} \hbar(\mathfrak{q},\mathfrak{u}(\mathfrak{q}))\frac{d\mathfrak{q}}{\mathfrak{q}}+\\
&+ \frac{1}{\Gamma(\mathfrak{w})}\int_1^{\mathfrak{r}}\Big(\ln\frac{\mathfrak{r}}{\mathfrak{q}}\Big)^{\mathfrak{w}-1}\Big[\kappa(\mathfrak{q},\mathfrak{u}(\mathfrak{q})) + \int_1^{\mathfrak{q}} \Bbbk_0(\mathfrak{q},\varpi,\mathfrak{u}(\varpi))d\varpi + \int_1^{\xi} \Bbbk_1(\mathfrak{q},\varpi,\mathfrak{u}(\varpi))d\varpi\Big]\frac{d\mathfrak{q}}{\mathfrak{q}} =\\
&= \frac{1}{\Gamma(\mathfrak{w})}\int_1^{\mathfrak{r}}\Big(\ln\frac{\mathfrak{r}}{\mathfrak{q}}\Big)^{\mathfrak{w}-1}\Big[\kappa(\mathfrak{q},\mathfrak{u}(\mathfrak{q})) + \int_1^{\mathfrak{q}} \Bbbk_0(\mathfrak{q},\varpi,\mathfrak{u}(\varpi))d\varpi + \int_1^{\xi} \Bbbk_1(\mathfrak{q},\varpi,\mathfrak{u}(\varpi))d\varpi\Big]\frac{d\mathfrak{q}}{\mathfrak{q}}+\\
&+ \lambda_0 + (\lambda_1 - \hbar(1,\lambda_0))\ln\mathfrak{r} + \int_1^{\mathfrak{r}} \hbar(\mathfrak{q},\mathfrak{u}(\mathfrak{q}))\frac{d\mathfrak{q}}{\mathfrak{q}}
\end{aligned}$$

Conversely, suppose $\mathfrak{u}$ satisfies (5), then applying ${}^{C}\mathfrak{D}^{\mathfrak{w}}$ to both sides of(5), we obtain

$$\begin{aligned}
\mathfrak{D}_1^{\mathfrak{w}}\mathfrak{u}(\mathfrak{r}) &= \mathfrak{D}_1^{\mathfrak{w}}\bigg(\frac{1}{\Gamma(\mathfrak{w})}\int_1^{\mathfrak{r}}\Big(\ln\frac{\mathfrak{r}}{\mathfrak{q}}\Big)^{\mathfrak{w}-1}\Big[\kappa(\mathfrak{q},\mathfrak{u}(\mathfrak{q})) + \int_1^{\mathfrak{q}} \Bbbk_0(\mathfrak{q},\varpi,\mathfrak{u}(\varpi))d\varpi + \int_1^{\xi} \Bbbk_1(\mathfrak{q},\varpi,\mathfrak{u}(\varpi))d\varpi\Big]\frac{d\mathfrak{q}}{\mathfrak{q}}+\\
&+ \int_1^{\mathfrak{r}} \hbar(\mathfrak{q},\mathfrak{u}(\mathfrak{q}))\frac{d\mathfrak{q}}{\mathfrak{q}} + \lambda_0 + (\lambda_1 - \hbar(1,\lambda_0))\ln\mathfrak{r}\bigg) =\\
&= \mathfrak{D}_1^{\mathfrak{w}}\mathfrak{I}_1^{\mathfrak{w}}\Big[\kappa(\mathfrak{q},\mathfrak{u}(\mathfrak{q})) + \int_1^{\mathfrak{q}} \Bbbk_0(\mathfrak{q},\varpi,\mathfrak{u}(\varpi))d\varpi + \int_1^{\xi} \Bbbk_1(\mathfrak{q},\varpi,\mathfrak{u}(\varpi))d\varpi\Big] + \mathfrak{D}_1^{\mathfrak{w}}\mathfrak{I}_1^{\mathfrak{w}}\hbar(\mathfrak{q},\mathfrak{u}(\mathfrak{q}))\frac{d\mathfrak{q}}{\mathfrak{q}}+\\
&+ \mathfrak{D}_1^{\mathfrak{w}}\Big(\lambda_0 + (\lambda_1 - \hbar(1,\lambda_0))\ln\mathfrak{r}\Big) =\\
&= \kappa(\mathfrak{r},\mathfrak{u}(\mathfrak{r})) + \int_1^{\mathfrak{r}} \Bbbk_0(\mathfrak{r},\varpi,\mathfrak{u}(\varpi))d\varpi + \int_1^{\xi} \Bbbk_1(\mathfrak{r},\varpi,\mathfrak{u}(\varpi))d\varpi + \mathfrak{D}_1^{\mathfrak{w}-1}\hbar(\mathfrak{r},\mathfrak{u}(\mathfrak{r}))
\end{aligned}$$

Moreover, the initial conditions $\mathfrak{u}(1) = \lambda_0,$ and $\mathfrak{u}'(1) = \lambda_1$ hold. This completes the proof $\square$

To transform (5) for compatibility with Schauder's fixed point theorem, we introduce the operator $\aleph : \Omega \longrightarrow \Omega$ as follows:

$$\begin{aligned}
(\aleph\mathfrak{u})(\mathfrak{r}) \;&=\; \frac{1}{\Gamma(\mathfrak{w})}\int_1^{\mathfrak{r}}\Big(\ln\frac{\mathfrak{r}}{\mathfrak{q}}\Big)^{\mathfrak{w}-1}\Big[\kappa(\mathfrak{q},\mathfrak{u}(\mathfrak{q})) + \int_1^{\mathfrak{q}} \Bbbk_0(\mathfrak{q},\varpi,\mathfrak{u}(\varpi))d\varpi + \int_1^{\xi} \Bbbk_1(\mathfrak{q},\varpi,\mathfrak{u}(\varpi))d\varpi\Big]\frac{d\mathfrak{q}}{\mathfrak{q}} +\\
&+ \int_1^{\mathfrak{r}} \hbar(\mathfrak{q},\mathfrak{u}(\mathfrak{q}))\frac{d\mathfrak{q}}{\mathfrak{q}} + \lambda_0 + (\lambda_1 - \hbar(1,\lambda_0))\ln\mathfrak{r} \qquad (6)
\end{aligned}$$

Theorem 3.2. *Assuming that conditions* $(\Delta_1)-(\Delta_2)$ *are satisfied, it can be deduced that there is at least one positive solution to the problem described by equations* (1)–(2).

Proof. Consider the set Φ defined as follows: $\Phi = \{\mathfrak{u} \in \mathfrak{B} : \mathfrak{u}_*(\mathfrak{r}) \leqslant \mathfrak{u}(\mathfrak{r}) \leqslant \mathfrak{u}^*(\mathfrak{r}),\ \mathfrak{r} \in \psi\}$. This set is equipped with the norm $|\mathfrak{u}| = \{\max_{\mathfrak{r}\in\psi} |\mathfrak{u}(\mathfrak{r})| : |\mathfrak{u}| \leqslant \ell\}$. As a result, we have that $\aleph$ represents a convex, bounded, and closed subset of the Banach space $\mathbb{C}(\psi)$. It's worth noting that the continuity of the operator $\aleph$ can be inferred from the continuity of the functions $\kappa, \hbar_0, \hbar_1$, and $\hbar$. Additionally, if $\mathfrak{u} \in \Phi$, it implies the existence of positive constants $\Upsilon_\kappa, \Upsilon_{\Bbbk_0}, \Upsilon_{\Bbbk_1}$, and $\Upsilon_\hbar$. such that

$$\max\{\kappa(\mathfrak{r}, \mathfrak{u}(\mathfrak{r})) : \mathfrak{u}(\mathfrak{r}) \leqslant \ell\} \leqslant \Upsilon_\kappa$$
$$\max\{\hbar(\mathfrak{r}, \mathfrak{u}(\mathfrak{r})) : \mathfrak{u}(\mathfrak{r}) \leqslant \ell\} \leqslant \Upsilon_\hbar$$
$$\max\{\Bbbk_0(\mathfrak{r}, \varpi, \mathfrak{u}(\varpi)) : \mathfrak{r},\ \varpi \in \psi, \mathfrak{u}(\varpi) \leqslant \ell\} \leqslant \Upsilon_{\Bbbk_0}$$
$$\max\{\Bbbk_1(\mathfrak{r}, \varpi, \mathfrak{u}(\varpi)) : \mathfrak{r},\ \varpi \in \psi, \mathfrak{u}(\varpi) \leqslant \ell\} \leqslant \Upsilon_{\Bbbk_1}$$

Then

$$|(\aleph\mathfrak{u})(\mathfrak{r})| = \frac{1}{\Gamma(\mathfrak{w})}\int_1^{\mathfrak{r}}\Big(\ln\frac{\mathfrak{r}}{\mathfrak{q}}\Big)^{\mathfrak{w}-1}\Big[|\kappa(\mathfrak{q}, \mathfrak{u}(\mathfrak{q}))| + \int_1^{\mathfrak{q}}|\Bbbk_0(\mathfrak{q}, \varpi, \mathfrak{u}(\varpi))d\varpi| + \int_1^{\xi}|\Bbbk_1(\mathfrak{q}, \varpi, \mathfrak{u}(\varpi))d\varpi|\Big]\frac{d\mathfrak{q}}{\mathfrak{q}} +$$
$$+ \int_1^{\mathfrak{r}}|\hbar(\mathfrak{q}, \mathfrak{u}(\mathfrak{q}))|\frac{d\mathfrak{q}}{\mathfrak{q}} + |\lambda_0 + (\lambda_1 - \hbar(1, \lambda_0))\ln\mathfrak{r}| \leqslant$$
$$\leqslant \frac{\Upsilon_\kappa(\ln\xi)^{\mathfrak{w}}}{\Gamma(\mathfrak{w}+1)} + \frac{(\Upsilon_{\Bbbk_0} + \Upsilon_{\Bbbk_1})(\ln\xi)^{\mathfrak{w}+1}}{\Gamma(\mathfrak{w}+2)} + \lambda_0 + \big(\lambda_1 + \zeta^* + \Upsilon_\hbar\big)\ln\xi$$

where $\zeta^* = |\hbar(1, \lambda_0)|$, thus

$$\|(\aleph\mathfrak{u})(\mathfrak{r})\| \leqslant \frac{\Upsilon_\kappa(\ln\xi)^{\mathfrak{w}}}{\Gamma(\mathfrak{w}+1)} + \frac{(\Upsilon_{\Bbbk_0} + \Upsilon_{\Bbbk_1})(\ln\xi)^{\mathfrak{w}+1}}{\Gamma(\mathfrak{w}+2)} + \lambda_0 + \big(\lambda_1 + \zeta^* + \Upsilon_\hbar\big)\ln\xi$$

Consequently, the set $\aleph(\Phi)$ is uniformly bounded.
Now, we proceed to establish the equicontinuity of $\aleph(\Phi)$. For each $\mathfrak{u} \in \Phi$. Then for $\mathfrak{r}_1, \mathfrak{r}_2 \in [1.\xi]$ with $\mathfrak{r}_1 < \mathfrak{r}_2$, we have

$$|(\aleph\mathfrak{u})(\mathfrak{r}_1) - (\aleph\mathfrak{u})(\mathfrak{r}_2)| =$$
$$= \frac{1}{\Gamma(\mathfrak{w})}\int_1^{\mathfrak{r}_1}\left[\Big(\ln\frac{\mathfrak{r}_1}{\mathfrak{q}}\Big)^{\mathfrak{w}-1} - \Big(\ln\frac{\mathfrak{r}_2}{\mathfrak{q}}\Big)^{\mathfrak{w}-1}\right]|\kappa(\mathfrak{q}, \mathfrak{u}(\mathfrak{q}))|\frac{d\mathfrak{q}}{\mathfrak{q}} + \frac{1}{\Gamma(\mathfrak{w})}\int_{\mathfrak{r}_1}^{\mathfrak{r}_2}\Big(\ln\frac{\mathfrak{r}_2}{\mathfrak{q}}\Big)^{\mathfrak{w}-1}|\kappa(\mathfrak{q}, \mathfrak{u}(\mathfrak{q}))|\frac{d\mathfrak{q}}{\mathfrak{q}} +$$
$$+ \frac{1}{\Gamma(\mathfrak{w})}\int_1^{\mathfrak{r}_1}\left[\Big(\ln\frac{\mathfrak{r}_1}{\mathfrak{q}}\Big)^{\mathfrak{w}-1} - \Big(\ln\frac{\mathfrak{r}_2}{\mathfrak{q}}\Big)^{\mathfrak{w}-1}\right]\left[\int_1^{\mathfrak{q}}|\Bbbk_0(\mathfrak{q}, \varpi, \mathfrak{u}(\varpi))|d\varpi + \int_1^{\xi}|\Bbbk_1(\mathfrak{q}, \varpi, \mathfrak{u}(\varpi))|d\varpi\right]\frac{d\mathfrak{q}}{\mathfrak{q}} +$$
$$+ \frac{1}{\Gamma(\mathfrak{w})}\int_{\mathfrak{r}_1}^{\mathfrak{r}_2}\Big(\ln\frac{\mathfrak{r}_2}{\mathfrak{q}}\Big)^{\mathfrak{w}-1}\left[\int_1^{\mathfrak{q}}|\Bbbk_0(\mathfrak{q}, \varpi, \mathfrak{u}(\varpi))|d\varpi + \int_1^{\xi}|\Bbbk_1(\mathfrak{q}, \varpi, \mathfrak{u}(\varpi))|d\varpi\right]\frac{d\mathfrak{q}}{\mathfrak{q}} +$$
$$+ \int_{\mathfrak{r}_1}^{\mathfrak{r}_2}|\hbar(\mathfrak{q}, \mathfrak{u}(\mathfrak{q}))|\frac{d\mathfrak{q}}{\mathfrak{q}} + (\lambda_1 + \zeta^*)(\ln\mathfrak{r}_2 - \ln\mathfrak{r}_1) \leqslant$$
$$\leqslant \frac{\Upsilon_\kappa}{\Gamma(\mathfrak{w}+1)}\left[2\Big[\ln\frac{\mathfrak{r}_2}{\mathfrak{r}_1}\Big]^{\mathfrak{w}} + \big[\ln\mathfrak{r}_1\big]^{\mathfrak{w}} - \big[\ln\mathfrak{r}_2\big]^{\mathfrak{w}}\right] + \frac{(\Upsilon_{\Bbbk_0} + \Upsilon_{\Bbbk_1})}{\Gamma(\mathfrak{w}+2)}\left[2\Big[\ln\frac{\mathfrak{r}_2}{\mathfrak{r}_1}\Big]^{\mathfrak{w}+1} + \Big[\ln\mathfrak{r}_1\Big]^{\mathfrak{w}+1} -\right.$$
$$\left. - \big[\ln\mathfrak{r}_2\big]^{\mathfrak{w}+1}\right] + \Upsilon_\hbar\Big[\ln\frac{\mathfrak{r}_2}{\mathfrak{r}_1}\Big] + (\lambda_1 + \zeta^*)\Big[\ln\frac{\mathfrak{r}_2}{\mathfrak{r}_1}\Big] \leqslant$$
$$\leqslant \frac{2\Upsilon_\kappa}{\Gamma(\mathfrak{w}+1)}\Big[\ln\frac{\mathfrak{r}_2}{\mathfrak{r}_1}\Big]^{\mathfrak{w}} + \frac{2(\Upsilon_{\Bbbk_0} + \Upsilon_{\Bbbk_1})}{\Gamma(\mathfrak{w}+2)}\Big[\ln\frac{\mathfrak{r}_2}{\mathfrak{r}_1}\Big]^{\mathfrak{w}+1} + (\lambda_1 + \zeta^* + \Upsilon_\hbar)\Big[\ln\frac{\mathfrak{r}_2}{\mathfrak{r}_1}\Big]$$

$$\longrightarrow \quad 0 \quad \text{as } \mathfrak{r}_1 \longrightarrow \mathfrak{r}_2$$

The convergence is independent of of $\mathfrak{u}$ within Φ, indicating that $\aleph(\Phi)$ is uniformly equicontinuous. By invoking the Arzela-Ascoli theorem, we can conclude that $\aleph : \Phi \longrightarrow \mathfrak{B}$ is a compact operator. To apply the Schauder fixed point theorem, the only remaining requirement is to demonstrate that $\aleph(\Phi) \subset \Phi$. For any $\mathfrak{u} \in \Phi$, then $\mathfrak{u}_*(\mathfrak{r}) \leqslant \mathfrak{u}(\mathfrak{r}) \leqslant \mathfrak{u}^*(\mathfrak{r})$ and by (Δ_1), we have

$$\begin{aligned}
(\aleph\mathfrak{u})(\mathfrak{r}) &= \frac{1}{\Gamma(\mathfrak{w})}\int_1^{\mathfrak{r}}\Big(\ln\frac{\mathfrak{r}}{\mathfrak{q}}\Big)^{\mathfrak{w}-1}\Big[\kappa(\mathfrak{q},\mathfrak{u}(\mathfrak{q}))+\int_1^{\mathfrak{q}}\Bbbk_0(\mathfrak{q},\varpi,\mathfrak{u}(\varpi))d\varpi+\int_1^{\xi}\Bbbk_1(\mathfrak{q},\varpi,\mathfrak{u}(\varpi))d\varpi\Big]\frac{d\mathfrak{q}}{\mathfrak{q}}+\\
&+\int_1^{\mathfrak{r}}\hbar(\mathfrak{q},\mathfrak{u}(\mathfrak{q}))\frac{d\mathfrak{q}}{\mathfrak{q}}+\lambda_0+(\lambda_1-\hbar(1,\lambda_0))\ln\mathfrak{r}\leqslant\\
&\leqslant\frac{1}{\Gamma(\mathfrak{w})}\int_1^{\mathfrak{r}}\Big(\ln\frac{\mathfrak{r}}{\mathfrak{q}}\Big)^{\mathfrak{w}-1}\Big[\mathbb{U}(\mathfrak{q},\mathfrak{u}(\mathfrak{q}))+\int_1^{\mathfrak{q}}\Bbbk_0(\mathfrak{q},\varpi,\mathfrak{u}(\varpi))d\varpi+\int_1^{\xi}\Bbbk_1(\mathfrak{q},\varpi,\mathfrak{u}(\varpi))d\varpi\Big]\frac{d\mathfrak{q}}{\mathfrak{q}}+\\
&+\int_1^{\mathfrak{r}}\hbar(\mathfrak{q},\mathfrak{u}(\mathfrak{q}))\frac{d\mathfrak{q}}{\mathfrak{q}}+\lambda_0+(\lambda_1-\hbar(1,\lambda_0))\ln\mathfrak{r}\leqslant\\
&\leqslant\frac{1}{\Gamma(\mathfrak{w})}\int_1^{\mathfrak{r}}\Big(\ln\frac{\mathfrak{r}}{\mathfrak{q}}\Big)^{\mathfrak{w}-1}\Big[\mathbb{U}(\mathfrak{q},\mathfrak{u}^*(\mathfrak{q}))+\int_1^{\mathfrak{q}}\Bbbk_0(\mathfrak{q},\varpi,\mathfrak{u}^*(\varpi))d\varpi+\int_1^{\xi}\Bbbk_1(\mathfrak{q},\varpi,\mathfrak{u}^*(\varpi))d\varpi\Big]\frac{d\mathfrak{q}}{\mathfrak{q}}+\\
&+\lambda_0+(\lambda_1-\hbar(1,\lambda_0))\ln\mathfrak{r}+\int_1^{\mathfrak{r}}\hbar(\mathfrak{q},\mathfrak{u}^*(\mathfrak{q}))\frac{d\mathfrak{q}}{\mathfrak{q}}\leqslant\\
&\leqslant\mathfrak{u}^*(\mathfrak{r})
\end{aligned}$$

and

$$\begin{aligned}
(\aleph\mathfrak{u})(\mathfrak{r}) &= \frac{1}{\Gamma(\mathfrak{w})}\int_1^{\mathfrak{r}}\Big(\ln\frac{\mathfrak{r}}{\mathfrak{q}}\Big)^{\mathfrak{w}-1}\Big[\kappa(\mathfrak{q},\mathfrak{u}(\mathfrak{q}))+\int_1^{\mathfrak{q}}\Bbbk_0(\mathfrak{q},\varpi,\mathfrak{u}(\varpi))d\varpi+\int_1^{\xi}\Bbbk_1(\mathfrak{q},\varpi,\mathfrak{u}(\varpi))d\varpi\Big]\frac{d\mathfrak{q}}{\mathfrak{q}}+\\
&+\int_1^{\mathfrak{r}}\hbar(\mathfrak{q},\mathfrak{u}(\mathfrak{q}))\frac{d\mathfrak{q}}{\mathfrak{q}}+\lambda_0+(\lambda_1-\hbar(1,\lambda_0))\ln\mathfrak{r}\geqslant\\
&\geqslant\frac{1}{\Gamma(\mathfrak{w})}\int_1^{\mathfrak{r}}\Big(\ln\frac{\mathfrak{r}}{\mathfrak{q}}\Big)^{\mathfrak{w}-1}\Big[\mathbb{L}(\mathfrak{q},\mathfrak{u}(\mathfrak{q}))+\int_1^{\mathfrak{q}}\Bbbk_0(\mathfrak{q},\varpi,\mathfrak{u}(\varpi))d\varpi+\int_1^{\xi}\Bbbk_1(\mathfrak{q},\varpi,\mathfrak{u}(\varpi))d\varpi\Big]\frac{d\mathfrak{q}}{\mathfrak{q}}+\\
&+\int_1^{\mathfrak{r}}\hbar(\mathfrak{q},\mathfrak{u}(\mathfrak{q}))\frac{d\mathfrak{q}}{\mathfrak{q}}+\lambda_0+(\lambda_1-\hbar(1,\lambda_0))\ln\mathfrak{r}\geqslant\\
&\geqslant\frac{1}{\Gamma(\mathfrak{w})}\int_1^{\mathfrak{r}}\Big(\ln\frac{\mathfrak{r}}{\mathfrak{q}}\Big)^{\mathfrak{w}-1}\Big[\mathbb{L}(\mathfrak{q},\mathfrak{u}_*(\mathfrak{q}))+\int_1^{\mathfrak{q}}\Bbbk_0(\mathfrak{q},\varpi,\mathfrak{u}_*(\varpi))d\varpi+\int_1^{\xi}\Bbbk_1(\mathfrak{q},\varpi,\mathfrak{u}_*(\varpi))d\varpi\Big]\frac{d\mathfrak{q}}{\mathfrak{q}}+\\
&+\lambda_0+(\lambda_1-\hbar(1,\lambda_0))\ln\mathfrak{r}+\int_1^{\mathfrak{r}}\hbar(\mathfrak{q},\mathfrak{u}_*(\mathfrak{q}))\frac{d\mathfrak{q}}{\mathfrak{q}}\geqslant\\
&\geqslant\mathfrak{u}_*(\mathfrak{r})
\end{aligned}$$

As a result, we have $\mathfrak{u}(\mathfrak{r}) \leqslant (\aleph\mathfrak{u})(\mathfrak{r}) \leqslant \mathfrak{u}^(\mathfrak{r})$, which means that $\aleph(\Phi) \subset \Phi$. In accordance with the Schauder fixed point theorem, the operator $\aleph$ possesses at least one fixed point, denoted as $\mathfrak{u} \in \Phi$. Consequently, problem (1)–(2) has at least one positive solution. □

Theorem 3.3. *Assume that* (Δ_2) *is satisfied and*

$$\Delta=\left[\frac{\delta_\kappa(\ln\xi)^{\mathfrak{w}}}{\Gamma(1+\mathfrak{w})}+\frac{(\delta_{\Bbbk_0}+\delta_{\Bbbk_1})(\ln\xi)^{1+\mathfrak{w}}}{\Gamma(2+\mathfrak{w})}+\delta_\hbar(\ln\xi)\right]<1 \tag{7}$$

Then problem (1)–(2) *has a unique positive solution.*

Proof. It follows from Theorem 3.2 that problems(1)–(2) have at least one positive solution. Therefore, all that remains is for us to demonstrate that the operator defined in (6) is a contraction in Φ. In actuality, we have for each $\mathfrak{u}, \mathfrak{u}_0 \in \Phi$,

$$|(\aleph\mathfrak{u})(\mathfrak{r})-(\aleph\mathfrak{u}_0)(\mathfrak{r})| = \frac{1}{\Gamma(\mathfrak{w})}\int_1^{\mathfrak{r}}\Big(\ln\frac{\mathfrak{r}}{\mathfrak{q}}\Big)^{\mathfrak{w}-1}\Big|\kappa(\mathfrak{q},\mathfrak{u}(\mathfrak{q}))-\kappa(\mathfrak{q},\mathfrak{u}_0(\mathfrak{q}))\Big|\frac{d\mathfrak{q}}{\mathfrak{q}}+$$

$$
\begin{aligned}
&+ \quad \frac{1}{\Gamma(\mathfrak{w})}\int_1^{\mathfrak{r}}\Big(\ln\frac{\mathfrak{r}}{\mathfrak{q}}\Big)^{\mathfrak{w}-1}\Bigg(\int_1^{\mathfrak{q}}\big|\Bbbk_0(\mathfrak{q},\varpi,\mathfrak{u}(\varpi))-\Bbbk_0(\mathfrak{q},\varpi,\mathfrak{u}_0(\varpi))\big|d\varpi+\\
&+ \quad \int_1^{\xi}\big|\Bbbk_1(\mathfrak{q},\varpi,\mathfrak{u}(\varpi))-\Bbbk_1(\mathfrak{q},\varpi,\mathfrak{u}_0(\varpi))\big|d\varpi\Bigg)\frac{d\mathfrak{q}}{\mathfrak{q}}+\\
&+ \quad \int_1^{\mathfrak{r}}\big|\hbar(\mathfrak{q},\mathfrak{u}(\mathfrak{q}))-\hbar(\mathfrak{q},\mathfrak{u}_0(\mathfrak{q}))\big|\frac{d\mathfrak{q}}{\mathfrak{q}}\leqslant\\
&\leqslant \quad \left[\frac{\delta_\kappa(\ln\xi)^{\mathfrak{w}}}{\Gamma(\mathfrak{w}+1)}+\frac{(\delta_{\Bbbk_0}+\delta_{\Bbbk_1})(\ln\xi)^{\mathfrak{w}+1}}{\Gamma(\mathfrak{w}+2)}+\delta_\hbar(\ln\xi)\right]\|\mathfrak{u}-\mathfrak{u}_0\|
\end{aligned}
$$

The contraction $\aleph$ is derived from (7). According to Theorem 2.5, it asserts the existence of a unique fixed point for the equation $\aleph$, which corresponds to the sole positive solution of the equations (1)–(2). With this, we conclude the proof. □

4. An application

As an application of our result, With an integral boundary condition, we examine the fractional Volterra-Fredholm integro-differential equation as follows:

$$
\begin{aligned}
\mathfrak{D}_1^{\frac{4}{3}}\mathfrak{u}(\mathfrak{r})-\mathfrak{D}_1^{\frac{1}{3}}\left[\frac{\mathfrak{u}(\mathfrak{r})}{3e^{\mathfrak{r}-1}}\right]=&\frac{\cos(\mathfrak{r})}{9+e^{\mathfrak{r}^2-1}}\left(\frac{\mathfrak{u}(\mathfrak{r})}{|\mathfrak{u}|+1}\right)+\frac{1}{5}\int_1^{\mathfrak{r}}e^{-2(\varpi^2-\mathfrak{r}^2)}\mathfrak{u}(\varpi)d\varpi+\int_1^{e}\frac{e^{-\varpi^2\mathfrak{r}}}{20}\mathfrak{u}(\varpi)d\varpi\\
&\mathfrak{u}(1)=1,\quad \mathfrak{u}'(1)=1
\end{aligned}
\tag{8}
$$

Since κ is continuous positive functions, $\Bbbk_0,\Bbbk_1$ and $\hbar$ are non-decreasing on $\Bbbk$. For $\Bbbk,\Bbbk_0\in\mathfrak{N}^+$ and $\mathfrak{r}\in(1,e]$ we have:

$$
\begin{aligned}
|\kappa(\mathfrak{r},\mathfrak{u})-\kappa(\mathfrak{r},\mathfrak{u}_0)|&=\left|\frac{\cos(\mathfrak{r})}{9+e^{\mathfrak{r}^2-1}}\left(\frac{|\mathfrak{u}|}{|\mathfrak{u}|+1}-\frac{\mathfrak{u}_0}{|\mathfrak{u}_0|+1}\right)\right|\leqslant\\
&\leqslant\frac{1}{9+e^{\mathfrak{r}^2-1}}\left(\frac{|\mathfrak{u}-\mathfrak{u}_0|}{(|\mathfrak{u}|+1)(|\mathfrak{u}_0|+1)}\right)\leqslant\\
&\leqslant\frac{1}{10}|\mathfrak{u}-\mathfrak{u}_0|
\end{aligned}
$$

$$
\begin{aligned}
|\hbar(\mathfrak{r},\mathfrak{u})-\hbar(\mathfrak{r},\mathfrak{u}_0)|&=\left|\frac{|\mathfrak{u}|}{3e^{\mathfrak{r}-1}}-\frac{|\mathfrak{u}_0|}{3e^{\mathfrak{r}-1}}\right|\leqslant\frac{1}{3e^{\mathfrak{r}-1}}|\mathfrak{u}-\mathfrak{u}_0|\leqslant\\
&\leqslant\frac{1}{3}|\mathfrak{u}-\mathfrak{u}_0|
\end{aligned}
$$

$$
\begin{aligned}
|\Bbbk_0(\mathfrak{r},\varpi,\mathfrak{u}(\varpi))-\Bbbk_0(\mathfrak{r},\varpi,\mathfrak{u}_0(\varpi))|&=\left|\frac{|\mathfrak{u}|}{5e^{(\varpi^2-\mathfrak{r}^2)}}\frac{|\mathfrak{u}_0|}{5e^{2(\varpi^2-\mathfrak{r}^2)}}\right|\leqslant\frac{1}{5e^{2(\varpi^2-\mathfrak{r}^2)}}|\mathfrak{u}-\mathfrak{u}_0|\leqslant\\
&\leqslant\frac{1}{10}|\mathfrak{u}-\mathfrak{u}_0|
\end{aligned}
$$

and

$$
\begin{aligned}
|\Bbbk_1(\mathfrak{r},\varpi,\mathfrak{u}(\varpi))-\Bbbk_1(\mathfrak{r},\varpi,\mathfrak{u}_0(\varpi))|&=\left|\frac{|\mathfrak{u}|}{5e^{(\varpi^2-\mathfrak{r}^2)}}\frac{|\mathfrak{u}_0|}{10e^{(\varpi^2\mathfrak{r})}}\right|\leqslant\frac{1}{10e^{(\varpi^2\mathfrak{r})}}|\mathfrak{u}-\mathfrak{u}_0|\leqslant\\
&\leqslant\frac{1}{20}|\mathfrak{u}-\mathfrak{u}_0|
\end{aligned}
$$

Currently, the conditions $(\Delta_1) - (\Delta_3)$ is fulfilled, given that

$$\mathfrak{w} = \frac{4}{3}, \quad \xi = e, \quad \delta_\kappa = \frac{1}{10}, \quad \delta_\hbar = \frac{1}{3}, \quad \delta_{\mathbb{k}_0} = \frac{1}{10}, \quad \delta_{\mathbb{k}_1} = \frac{1}{20}.$$

subsequently, through a series of calculations, it is determined that.

$$\begin{aligned}\Delta &= \left[\frac{\delta_\kappa(\ln\xi)^{\mathfrak{w}}}{\Gamma(1+\mathfrak{w})} + \frac{(\delta_{\mathbb{k}_0}+\delta_{\mathbb{k}_1})(\ln\xi)^{1+\mathfrak{w}}}{\Gamma(2+\mathfrak{w})} + \delta_\hbar(\ln\xi)\right] \\ &\cong 0.314 < 1\end{aligned}$$

Then by Theorem 3.3, the equation (8) has a unique positive solution.

References

[1] B.Tellab, A.Boulfoul, A.Ghezal, Existence and uniqueness results for nonlocal problem with fractional integro-differential equation in Banach Space, *Thai Journal of Mathematics*, **21**(2023), no. 1, 53–65.

[2] A.A.Hamoud, A.A.Sharif, Existence, Uniqueness and Stability Results for Nonlinear Neutral Fractional Volterra-Fredholm Integro-Differential Equations, *Discontinuity, Nonlinearity, and Complexity*, **12**(2023), no. 2, 381–398.

[3] A.Lachouri, N.Gouri, Existence and Uniqueness of Positive Solutions for a Class of Fractional Integro-Differential Equations, *Palestine Journal of Mathematics*, **11**(2022), no. 3, 167–174.

[4] A.Ardjouni, A.Djoudi, Existence and Uniqueness of Positive Solutions for First-Order Nonlinearliouville-Caputo Fractional Differential Equations, *Sao Paulo J. Math. Sci.*, **14**(2020), 381–390. DOI: 10.1007/s40863-019-00147-2

[5] C.Wang, L.Gao, Q.Dou, Existence and uniqueness of positive solution for a nonlinear multi-order fractional differential equations, *British Journal of Mathematics & Computer Science*, **4**(2014), no. 15, 2137. DOI: 10.9734/BJMCS/2014/10719

[6] A.Lachouri, A.Ardjouni, A.Djoudi, Positive Solutions of a Fractional Integro-Differential Equation With Integral Boundary Conditions, *Communications in Optimization Theory*, **2020**(2020), 1–9.

[7] F.Mainardi, Fractional Calculus and Waves in Linear Viscoelasticity: An Introduction to Mathematical Models, Imperial College Press, London, 2010.

[8] J.Klafter, S.C.Lim, R.Metzler, Fractional Dynamics in Physics Recent Advances, World Scientific, Singapore, 2011.

[9] J.A.Tenreiro-Machado, V.Kiryakova, F.Mainardi, Recent history of fractional calculus, *Commun. Nonlin. Sci. Numer. Sim.*, **16**(2011), 1140–1153.
DOI: 10.1016/j.cnsns.2010.05.027

[10] S.Das, Functional Fractional Calculus, Springer-Verlag, Berlin, Heidelberg, 2011.

[11] A.Hamoud, A.Sharif, K.Ghadle, Existence and Stability of Solutions for a Nonlinear Fractional Volterra-Fredholm Integro-Differential Equation in Banach Spaces, *Journal of Mahani Mathematical Research Center*, (2021), 2645–4505.

[12] P.Butzer, A.Kilbas, J.Trujillo, Compositions of Hadamard-Type Fractional Integration Operators and the Semigroup Property, *J. Math. Anal. Appl.*, **269**(2002), 387–400. DOI: 10.1016/S0022-247X(02)00049-5

[13] A.Kilbas, Hadamard-type fractional calculus, *J. Korean Math. Soc.*, **38**(2001), 1191–1204.

[14] C.Wang, H.Zhang, S.Wang, Positive Solution of a Nonlinear Fractional Differential Equationinvolving Caputo Derivative, *Discrete Dyn. Nat. Soc.*, **2012**(2012), 425–408.

[15] J.Wang, Y.Zhou, M.Medved, Existence and Stability of Fractional Differential Equations Withhadamard Derivative, *Topological Methods in Nonlinear Analysis*, **41**(2013), no. 1, 113–133.

[16] A.Ardjouni, A.Djoudi, Positive solutions for nonlinear Caputo-Hadamard fractional differential equations with integral boundary conditions,*Open J. Math. Anal.*, **3**(2019), no. 1, 62–69.

[17] A.A.Kilbas, H.M.Srivastava, J.J.Trujillo, Theory and Applications of Fractional Differential Equations, Elsevier Science B. V, Amsterdam, 2006.

[18] S.Das, Functional Fractional Calculus for System Identification and Controls, Springer-Verlag, Berlin, Heidelberg, 2008.

[19] V.Lakshmikantham, A.S.Vatsala, Basic Theory of Fractional Differential Equations, *Nonlinear Anal.*, **69**(2008), 2677–2682. DOI: 10.1016/J.NA.2007.08.042

[20] A.Ardjouni, Existence and Uniqueness of Positive Solutions for Nonlinear Caputo-Hadamard Fractional Differential Equation, *Proyecciones Journal of Mathematics*, **40**(2021), no. 1, 139–152. DOI: 10.22199/issn.0717-6279-2021-01-0009

[21] A.Lachouri, A.Ardjouni, A.Djoudi, Existence and Ulam Stability Results for Nonlinear Hybrid Implicit Caputo Fractional Differential Equations, *Math. Morav*, **24**(2020), no. 1, 109–122. DOI: 10.5937/MatMor2001109L

[22] K.S.Miller, B.Ross, An Introduction to the Fractional Calculus and Differential Equations, John Wiley, New York, 1993.

[23] I.Podlubny, Fractional Differential Equations, Academic Press, San Diego, 1999.

[24] A.A.Sharif, M.M.Hamood, K.P.Ghadle, Existence and Uniqueness Theorems for Integro-Differential Equations With CAB-Fractional Derivative, *Acta Universitatis Apuleius*, **72**(2022), 59–78. DOI: 10.17114/j.aua.2022.72.05

[25] A.Sharif, A.Hamoud, On ψ-Caputo Fractional Nonlinear Volterra-Fredholm Integro-Differential Equations, *Discontinuity, Nonlinearity, and Complexity*, **11**(2022), no. 1, 97–106. DOI: 10.5890/DNC.2022.03.008

[26] X.Wang, L.Wang, Q.Zeng, Fractional Differential Equations With Integral Boundary Conditions, *J. of Nonlinear Sci. Appl*, **8**(2015), 309–314.

[27] F.Jarad, T.Abdeljawad, D.Baleanu, Caputo-Type Modification of the Hadamard Fractional Derivatives, *Adv. Diff. Equa.*, **142**(2012), 1–8. DOI: 10.1186/1687-1847-2012-142

[28] D.R.Smart, Fixed Point Theorems, Cambridge Tracts in Mathematics, *Cambridge University Press*, London, New York, 1974.

[29] D.Idczak, R.Kamocki, On the Existence and Uniqueness and Formula for the Solution of R-L Fractional Cauchy Problem in $\mathbb{R}^n$, *Fract. Calc. Appl. Anal.*, **14**(2011), no. 4, 538–553. DOI: 10.2478/s13540-011-0033-5

[30] K.Balachandran, J.J.Trujillo, The Nonlocal Cauchy Problem for Nonlinear Fractional Integrodifferential Equations in Banach Spaces, *Nonlinear Analysis: Th. Meth. Appl.*, **72**(2010), 4587–4593. DOI: 10.1016/j.na.2010.02.035

Новые результаты по положительным решениям для нелинейных дробных производных Капуто-Адамара интегро-дифференциальных уравнений Вольтерра-Фредгольма

Абдулрахман А. Шариф
Факультет математики
Университет Ходейда
AL-Ходайда, Йемен
Маха М. Хамуд
Факультет математики
Университет Таиз
Таиз, Йемен
Киртивант П. Гэдл
Кафедра математики
Университет доктора Бабасахеба Амбедкара Маратвады
Аурангабад-431 004 (MS), Индия

Аннотация. В этой статье мы устанавливаем существование и единственность положительных решений для дробного интегро-дифференциального уравнения Вольтерра-Фредгольма. Это уравнение включает дробные производные Капуто–Адамара и определяется начальными условиями. Наша методология доказательства опирается на теорему Шаудера о неподвижной точке, принцип сокращения Банаха, концепции верхнего и нижнего решения и их приложения. Чтобы проиллюстрировать значимость наших теоретических выводов, мы также приводим убедительный пример.

Ключевые слова: дробное интегро-дифференциальное уравнение Вольтерра–Фредгольма, положительные решения, метод неподвижной точки

Journal of Siberian Federal University. Mathematics & Physics 2025, 18(2), 283–288

EDN: UCXSVG
УДК 517.55

Another Proof of Puiseux's Theorem on Algebraic Functions

Maxim I. Buzurnyy*
Ilya A. Lopatin†
Siberian Federal University
Krasnoyarsk, Russian Federation

Received 12.10.2024, received in revised form 04.11.2024, accepted 27.12.2024

Abstract. The paper gives a simpler proof of Puiseux's theorem on the algebraic function for polynomials of a special form.

Keywords: Newton diagram, Puiseux series, singular point, Weierstrass polynomial.

Citation: M.I. Buzurnyy, I.A. Lopatin, Another proof of Puiseux's Theorem on Algebraic Functions, J. Sib. Fed. Univ. Math. Phys., 2025, 18(2), 283–288. EDN: UCXSVG.

Introduction

Isaac Newton, in a letter to Oldenburg [1], outlined the idea of an algorithm for finding a solution to an algebraic equation $F(z,w)=0$ in the form of a series with a fractional exponent of the variable z. Now it is called the Newton diagram method. It should be noted that Newton did not consider the question of the convergence of the resulting series. For the first time, the fact that the solutions obtained by the Newton diagram method converge in a certain neighborhood of zero was proved by Victor Puiseux in [2]. This fact is called Puiseux's theorem.

The next stage in the development of interest in this issue were works using techniques equivalent to resolving the singularities of algebraic curves in modern terminology. Namely, for an algebraic curve V, defined by the equation $F(w,z)=0$, are constructed a non-singular curve $\bar{V}$ and a map $\phi:\bar{V}\to V$ such that the restriction $\phi:\bar{V}\setminus\phi^{-1}(V_{sing})\to V\setminus V_{sing}$ is a birational isomorphism. The map ϕ is a composition of blow-ups of singular points ($\sigma-$processes). For a non-singular curve $\bar{V}$ identification of regular branches in a neighborhood of points from $\phi^{-1}(V_{sing})$ is possible due to the implicit function theorem. These branches are mapped by ϕ into solutions of the equation $F(z,w)=0$, which are given by convergent series. A thorough presentation of this approach to finding solutions to the equation $F(z,w)=0$, in the language of modern algebraic geometry is given in the [3, 5, chapter 2], as well as in [4, section 8.4].

Puiseux's theorem can also be obtained from other considerations, for example, from the expansion of the polynomial $F(z,w)$ into the product of irreducible Weierstrass polynomials with respect to the variable z. By considering each irreducible polynomial separately, it is possible to construct a local parameterization of the branch of the curve it defines. Each of the formal solutions of the equation $F(z,w)=0$ coincides with one of the obtained parameterizations, and is thus convergent. A detailed proof of this fact can be found in the monograph [4, section 8.3].

For some classes of equations, the proof of Puiseux's theorem can be obtained without using the constructions discussed above. This paper presents one such class of equations whose coefficients are convergent Puiseux series. It is shown that all convergent solutions can be obtained immediately from the Newton diagram of the original equation, and, in particular, intermediate resolutions of singularities can be omitted. Thus, the proposed method is of interest for assessing the theoretical complexity of solving equations of the form $F(z,w)=0$.

*a.chigur@inbox.ru
†lopatin@mi-ras.ru

1. Newton's diagram and statement of the main theorem

In this paper we consider an arbitrary equation of two complex variables

$$F(z,w)=\sum_{(\beta,\alpha)\subset A\subset\mathbb{N}^2} a_{\beta\alpha}z^{\alpha}w^{\beta}=\sum_{\beta}A_{\beta}(z)w^{\beta}=0, \tag{1}$$

where $A_\beta(z)\in\mathbb{C}[z]$.

Definition 1. *A Puiseux series in one variable is a formal algebraic expression of the form*

$$f(z)=\sum_{n=n_0}^{+\infty}a_n z^{\frac{n}{m}},$$

where n_0 is an integer, m is natural (for $m=1$ the result is a Laurent series), coefficients a_n taken from some ring R.

Definition 2. *Newton's diagram $N(F)$ of equation (1) is the set of compact faces of the unbounded polyhedron c.h. $(\cup P_\beta)$, where $P_\beta=\{(\beta,s):s\geqslant\alpha\}$ (c.h. denotes the convex hull).*

Let us give a brief description of Newton's algorithm.
It is necessary to find all solutions $w=w(z)$ of equation (1) in the form of Puiseux's series:

$$F(z,w(z))=0.$$

The strategy for finding solutions $w(z)$ is the following:
Let $w(z)=cz^{\sigma}+\widetilde{w}(z)$, where $\widetilde{w}$ is a series of monomials of degree $>\sigma$ and let $\sigma=\dfrac{p}{q}$. Then

$$F(z,w(z))=\sum_{(\beta,\alpha)\in A}a_{\beta\alpha}z^{\alpha}(cz^{\sigma}+\widetilde{w})^{\beta}=\sum_{(\beta,\alpha)\in A}(a_{\beta\alpha}c^{\beta}z^{\alpha+\frac{p}{q}\beta}+o(z^{\sigma\beta+\alpha})).$$

In order for $F(z,w(z))\equiv 0$, it is necessary that the quantity

$$\alpha+\frac{p}{q}\beta=\frac{1}{q}(\alpha q+p\beta)$$

reaches a minimum on A in at least two points, i.e. on some edge $\tau\subset N(F)$. So, the condition on $\sigma=\dfrac{p}{q}$ is as follows:

(1) $N(F)$ has an edge τ with the slope σ, i.e. with the directing vector (q,p).
And the condition on c:

(2) c is a nonzero solution to the equation

$$\sum_{(\beta,\alpha)\in\tau}a_{\alpha\beta}c^{\beta}=0.$$

The number of such roots (taking into account multiplicity) is equal to the length of the projection τ onto the β axis.

Let us formulate the main result of this work.

Theorem. Let the equation $F(z,w)=0$ be such that each edge of its Newton diagram does not contain integer points other than the vertices. Then each of its solutions, obtained using Newton's algorithm, is a convergent Puiseux series.

2. Auxiliary statements

We precede the proof of the theorem with several auxiliary statements.

Lemma 1. *Let $G \subset \mathbb{C}$ be a bounded domain with piecewise smooth boundary and let $f \in \mathcal{O}(\bar{G})$ have a unique zero $a \in G$ in $\bar{G}$ of multiplicity 1. Then for any $\varphi \in \mathcal{O}(\bar{G})$ the following formula holds:*

$$\frac{1}{2\pi i}\int_{\partial G}\varphi\frac{df}{f} = \varphi(a) \tag{2}$$

Proof. It follows immediately from Cauchy's theorem and the residue formula for a meromorphic function at a simple pole:

$$\frac{1}{2\pi i}\int_{\partial G}\varphi\frac{df}{f} = res_{z=a}\frac{\varphi f'}{f} = \frac{\varphi(a)f'(a)}{f'(a)} = \varphi(a).$$

Note: If in the lemma we assume that f has a finite number of simple zeros $a_1, a_2, \ldots, a_N \in G$ in $\bar{G}$, then by the residue theorem and formula (2) we get

$$\frac{1}{2\pi i}\int_{\partial G}\varphi\frac{df}{f} = \sum_{i=1}^{N}\varphi(a_j). \tag{3}$$

In particular, when $\varphi \equiv 1$, we obtain a formula known from the complex analysis course

$$\frac{1}{2\pi i}\int_{\partial G}\frac{df}{f} = N.$$

Let us now assume that a is a zero of f of multiplicity μ, i.e. in a neighborhood U of point a

$$f(z) = (z-a)^{\mu}\psi(z), \qquad \psi(a) \neq 0.$$

Then, for any sufficiently small complex ξ, the function $f(z) - \xi$ has in U exactly μ simple roots $z_j(\xi)$, tending to a as $\xi -> 0$. Indeed, let us make the biholomorphic change $(\xi - z)\psi^{\frac{1}{\mu}}(z) = w$ (here is a branch of the radical $\psi^{\frac{1}{mu}}(z)$ can be chosen in U since $\psi(a) \neq 0$). Then the function $f(z) - \xi$ takes the form $w^{\mu} - \xi$, which shows that it has μ simple roots tending to zero as $\xi -> 0$.

According to (1) and (2)

$$\frac{1}{2\pi i}\int_{\partial U}\varphi(z)\frac{df(\xi)}{f(\xi)} = \frac{1}{2\pi i}\lim_{\xi->0}\int_{\partial U}\varphi(z)\frac{d[f(\xi)-\xi]}{f(\xi)-\xi} = \lim_{\xi->0}\sum_{j=1}^{\mu}\varphi(z_j(\xi)) = \mu\varphi(a).$$

From here, using the residue theorem, we get

Theorem 1 (on logarithmic residue)**.** *Let $G \subset \mathbb{C}$ be a bounded domain with piecewise smooth boundary and $f \in \mathcal{O}(\bar{G})$ has a finite number of zeros $a_j \in G$ of multiplicities in $\bar{G}$ μ_j. Then for any $\varphi \in \mathcal{O}(\bar{G})$*

$$\frac{1}{2\pi i}\int_{\partial G}\varphi\frac{df}{f} = \sum_{j}\mu_j\varphi(a_j).$$

In particular, for $\varphi \equiv 1$ the integral on the left is equal to the number of zeros of the function f, taking into account their multiplicities.

Consider a function in $(\zeta, z) \in \mathbb{C}^2$ holomorphic at the origin and having a Taylor expansion of the form

$$\Phi(\zeta, z) = zP(\zeta, z) + \sum_{i+j>d} a_{ij}z^i\zeta^j, \tag{4}$$

where $d \geqslant 2$, P is a homogeneous polynomial of degree $d-1$, and $P(\zeta, 0) \neq 0$, that is, P has a monomial of the form $a\zeta^{d-1}$.

Theorem 2 (A. P. Yuzhakov)**.** *The equation $\Phi(\zeta, z) = 0$ has a solution (branch) of the form*

$$z = z(\zeta) = \sum_{k \geqslant 2} c_k \zeta^k.$$

Proof. Let us choose the weight with respect to which the monomial $az\zeta^{d-1}$ has minimal degree in expansion (3). As such a weight we can take $\left(\frac{3}{2}, 1\right)$. Since each monomial $z^i\zeta^j$ with respect to this weight has a degree

$$\frac{3}{2}i + j = \frac{1}{2}i + (i + j),$$

and it is easy to see that on the Newton diagram it reaches its minimum value at a single point $(i, j) = (1, d - 1)$.

Let us denote $\theta(\zeta, z) = \Phi(\zeta, z) - az\zeta^{d-1}$. Then on the skeleton $|z| = r^{\frac{3}{2}}, |\zeta| = r$ we have
$|az\zeta^{d-1}| = |a|r^{d+\frac{1}{2}}$;
$|\theta(\zeta, z)| = r^{\frac{1}{2}+d+\epsilon}\alpha(r)$,
where $\epsilon > 0$ and $\alpha(r)$ is bounded. Consequently, for a sufficiently small r on the set $\left\{|z| = r^{\frac{3}{2}}\right\} \times \left\{\frac{r}{2} \leqslant |\zeta| \leqslant r\right\}$ there is an inequality

$$|az\zeta^{d-1}| > |\theta(\zeta, z)| \tag{5}$$

Considering $\Phi(\zeta, z)$ as a function of z in the circle $|z| \leqslant r^{\frac{3}{2}}$ with parameter ζ from the ring $K = \left\{\frac{r}{2} \leqslant |\zeta| \leqslant r\right\}$, according to Rouche's principle, we obtain that it has a single zero in the indicated circle $z = z(\zeta)$.

By the logarithmic residue formula $\big($applied to $G = \left\{|z| < r^{\frac{3}{2}}\right\}$, $\phi(z) = z\big)$:

$$z(\zeta) = \frac{1}{2\pi i} \int\limits_{|z|=r^{\frac{3}{2}}} \frac{z\Phi'_z(\zeta, z)}{\Phi(\zeta, z)} dz.$$

As an integral over the compact set $|z| = r^{\frac{3}{2}}$ of a continuous integrand that holomorphically depends on the parameter ζ from the ring K, the function $z(\zeta)$ is holomorphic in this ring.

Let $z(\zeta) = \sum\limits_{k=-\infty}^{+\infty} c_k\zeta^k$ be the Laurent expansion for $z(\zeta)$, convergent at least in the ring K. The coefficient c_k is represented by the integral

$$c_k = \frac{1}{2\pi i} \int\limits_{|\zeta|=\rho} \frac{z(\zeta)}{\zeta^{k+1}} d\zeta = \frac{1}{(2\pi i)^2} \int\limits_{\substack{|\zeta|=\rho \\ |z|=r^{\frac{3}{2}}}} \frac{z\Phi'_z(\zeta, z)}{\zeta^{k+1}\Phi(\zeta, z)} dz d\zeta, \tag{6}$$

where $\frac{r}{2} \leqslant |\rho| \leqslant r$.

Recall that

$$\Phi(\zeta, z) = az\zeta^{d-1} + \theta(\zeta, z),$$

where θ is a series in $z^i\zeta^j$, for which $i + j \geqslant d$.

Due to the inequality (4) on the skeleton $|\zeta| = \rho, |z| = r^{\frac{1}{2}}$ there is an expansion into a series of geometric progression

$$\frac{1}{\Phi} = \frac{1}{az\zeta^{d-1}(1 + \frac{\theta}{az\zeta^{d-1}})} = \sum_{l=0}^{\infty} (-1)^l \frac{\theta^l}{(az\zeta^{d-1})^{l+1}},$$

convergent uniformly on the skeleton. The integrand expression will then expand into the series

$$\sum_{l=0}^{\infty}(-1)^l\frac{\zeta^{-k-1}z\Phi'_z\theta^l}{(az\zeta^{d-1})^{l+1}}.$$

The degree of the numerator is equal to $-k-1+d+dl=-k-1+d(l+1)$, and the degree of the denominator is equal to $d(l+1)$. Therefore, the integral of each term is equal to zero if $-k-1>-2$, that is, if $k<1$.

Thus, $\forall k<1$ the Laurent coefficient $c_k=0$, thereby $z(\zeta)$ is holomorphic at zero, and $z(0)=0$. It is easy to show (taking into account the form of $\theta=z^2p'+\theta'$, where p' is homogeneous of degree $d-2$, and $ord\theta'\geqslant d+1$), so $c_1=0$.

3. Proof of Puiseux's theorem

Now we prove the main theorem of two-dimensional algebraic geometry.

Let $F(z,w)$ be a polynomial of two variables whose Newton diagram $N(F)$ has an edge with ends $(\alpha,p+\beta)$ and $(q+\alpha,\beta)$.

We also assume that the edge has no other integer points, so F has the form

$$(az^p+bw^q)w^\alpha z^\beta+\sum_{ip+jq>\alpha p+(p+\beta)q}a_{ij}w^iz^j.$$

The selected two terms can be normalized so that $a=1,b=-1$:

$$(z^p-w^q)w^\alpha z^\beta+\sum_{ip+jq>\alpha p+(p+\beta)q}a_{ij}w^iz^j.$$

The change $z^p=\xi^q,\ z=\xi^{\frac{q}{p}}$ gives

$$(z^p-w^q)w^\alpha\xi^{\frac{\beta q}{p}}+\sum_{ip+jq>\alpha p+(p+\beta)q}a_{ij}w^i\xi^{\frac{pj}{q}}.$$

But $\xi^q-w^q=(\xi-w)(\xi^{q-1}+\xi^{q-2}w+\cdots+w^{q-1})$, which means function F will look like

$$(\xi-w)P(\xi,w)+\sum_{ip+jq>\alpha p+(p+\beta)q}a_{ij}w^i\xi^{\frac{pj}{q}}.$$

After the change $\xi-w=u$ we get

$$uP(\xi,\xi-u)+\sum_{ip+jq>\alpha p+(p+\beta)q}a_{ij}w^i\xi^{\frac{pj}{q}}.$$

But according to Yuzhakov's theorem there is a solution (holomorphic) $u=u(\xi)$,
therefore, $w=\xi-u(\xi)=z^{\frac{p}{q}}+$ series in powers of $z^{\frac{1}{q}}$.

4. Comparison with the singularity method

Let us illustrate with an example when the proven theorem leads to the goal faster than the technique of resolving the singularities of algebraic curves. Thus, the given result can be considered as an interesting fact for assessing the theoretical complexity of solving an equation of the form $F(z,w)=0$.

Consider an equation of the form

$$G(z,w) = az^{\alpha}w^{\beta} + \sum_{i+j>\alpha+\beta} a_{ij}z^{i}w^{j} = 0$$

and satisfying the conditions of Theorem 1. This function has a singular point $(0,0)$ of order $\alpha+\beta$. Recall that a σ-process centered at the point $(0,0)$ is (for the case of a plane curve) a transformation which in the affine part of the projective plane is a mapping $\phi : \mathbb{C}^2 \to \mathbb{C}^2$, which in coordinates has the form: $(u,v) \to (u,uv)$. After substituting $z = u$, $w = vu$ we get:

$$u^{\alpha+\beta}(av^{\beta} + \sum_{i+j>d} u^{i+j-(\alpha+\beta)}v^{j}) = u^{\alpha+\beta}\widetilde{G}(u,v) = 0,$$

from which it is clear that the point $(0,0)$ remains singular for the function $\widetilde{G}(u,v)$. This is due to the fact that the tangent cone at the point $(0,0)$ for the curve $G(z,w)$ has multiple components (a component $z=0$ of multiplicity α and a component $w=0$ of multiplicity β). According to the construction of the resolution, it is necessary to continue blow up the singular point, i.e. at least more than one step is required. At the same time, the use of Theorem 1 immediately allows us to obtain a convergent solution.

The authors express their gratitude to their scientific supervisor August Karlovich Tsikh for posing the problem and comprehensive assistance in the work.

This work was supported by the Krasnoyarsk Mathematical Center, funded by the Ministry of Education and Science of the Russian Federation (Agreement 075-02-2024-1429).

References

[1] I.Newton, Letter to Oldenburg dated 1676 Oct. 24, The correspondence of Isaac Newton. II, Cambridge University press, 1960.

[2] V.Puiseux, Recherches sur les fonctions algébriques, *J. Math. Pures Appl.*, **15**(1850).

[3] J.L.Coolidge, A treatise on algebraic plane curves, *The American Mathematical Monthly*, Oxford, **39**(1932), no. 5, 293-295.

[4] E.Brieskorn, H.Knörrer, Plane algebraic curves, Birkhäuser Verlag, Basel, 1986.

[5] N.G.Chebotarev, Theory of algebraic functions, Moscow, GITTL, 1948 (in Russian).

Еще одно доказательство теоремы Пьюизо об алгебраической функции

Максим И. Бузурный
Илья А. Лопатин
Сибирский федеральный университет
Красноярск, Российская Федерация

Аннотация. В работе дано более простое доказательство теоремы Пьюизо об алгебраической функции для многочленов специального вида.

Ключевые слова: диаграмма Ньютона, ряд Пьюизо, особая точка, полином Вейерштрасса.